APPLYING A MOLECULAR PHARMACEUTICS FRAMEWORK TO THE STUDY OF ULTRASOUND CONTRAST AGENTS

Samantha M. Fix

A dissertation submitted to the faculty at the University of North Carolina at Chapel Hill in partial fulfillment of the requirements for the degree of Doctor of Philosophy in the Eshelman School of Pharmacy.

Chapel Hill
2018

Approved by:

Paul A. Dayton

Michael Jay

Samuel K. Lai

Autumn J. McRee

Yuliya Pylayeva-Gupta

ABSTRACT

SAMANTHA M. FIX: Applying a molecular pharmaceutics framework to the study of ultrasound contrast agents.
(Under the direction of Paul A. Dayton)

Several decades ago, stabilized microbubbles (MBs) were developed as vascular contrast agents for ultrasound imaging, and since then, the physics of MB oscillation and the unique acoustic signatures that MBs create have been relatively well characterized. Less well understood are considerations regarding how MBs interact with biological systems and how they can be exploited for therapeutic purposes. As the diagnostic and therapeutic applications of contrast agents continue to become more sophisticated, these considerations are ever more important. Thus, the purpose of this thesis is to study contrast agents from a new perspective, applying concepts from molecular pharmaceutics to enhance our understanding of contrast agent behavior and therapeutic potential.

First, we characterize changes in MB clearance that occur over the course of longitudinal studies that involve repeated MB administrations over several weeks. We show that MB clearance becomes dramatically faster over time, which is associated with an immune response against polyethylene glycol (PEG), a common component of clinical and pre-clinical MB formulations. The effect we demonstrate has important implications for quantitative contrast-enhanced ultrasound imaging studies as well as therapeutic ultrasound applications that require consistent intravascular concentrations of MBs over the course of repeated administrations.

Next, we explore the potential of MBs being repurposed for the controlled delivery of therapeutic gases. We thoroughly review the literature surrounding this topic and subsequently show that administering oxygen-filled MBs to rat fibrosarcoma tumors temporarily relieves tumor hypoxia and increases the efficacy of subsequent radiotherapy.

Finally, we explore how ultrasound-stimulated contrast agents can be used to enhance drug delivery. Various biological barriers hamper efficient drug accumulation in tissues or cells of interest, presenting a major challenge in pharmaceutics research. Through the final portion of this thesis, we

use a new class of contrast agents – phase change contrast agents (PCCAs) – in conjunction with ultrasound to physically manipulate these biological barriers. *In vitro,* we show that ultrasound stimulated PCCAs can transiently disrupt cell membranes and epithelial monolayers for improved intracellular and transepithelial drug delivery, respectively. We envision *in vivo* applications of this work focused on enhancing drug delivery to solid tumors and improving gastrointestinal delivery of biologics.

ACKNOWLEDGEMENTS

I owe a great deal of thanks to my loving friends and family who have supported me at every step. To my parents, Eric and Jackie, and brother, Paul: thank you for showing me the value of a strong worth ethic and for teaching me to have the stick-to-it-ness that grad school required. To my closest friends, Ariel and Trina, thank you for constantly making me laugh and for always being there for me. Benjamin, my grad school experience would have been a lot different without your support. I appreciate you always providing a listening ear when I struggled and for celebrating my success when things went well. Also, thank you for patiently editing of every essay, research proposal, and anxiety-provoking email that I have written over the past 4.5 years.

I am fortunate to have been taught by wonderful mentors at UNC, all of whom contributed to the research presented in this thesis. This work would not have been possible without the expertise and advice from my advisor, Paul Dayton, and the rest of my thesis committee: Michael Jay, Sam Lai, Autumn McRee, and Yuliya Pylayeva-Gupta. Thank you all for sharing your unique perspectives and for helping me troubleshoot difficult projects. Paul, I am especially grateful for your mentorship. It is clear that you always have your students' best interest in mind. Thank you for providing me the flexibility to explore my own ideas and pursue the projects I found most interesting in the lab. Also, thank you for encouraging me to apply for fellowships, take time away from the lab for eye-opening internships, and travel to present my work. To all of the Dayton lab members who have served as mentors for me, thank you for your patience and coaching. Anthony and Chris, you provided me with a great foundation and am a grateful for your thorough training when I joined the lab. Virginia, I have had such a wonderful time working with you. You constantly inspire me be a better scientist, and I am so happy to have you as a mentor and friend.

I have found great friends in my Dayton lab colleagues; thank you all for making every day in the lab so much fun. Gloria, from our gourmet Ye Ole Waffle breakfasts on the Duke bus to our many

travel faux pas, navigating grad school with you has been an absolute blast. Thank you for all of the laughs, for passionately venting with me when experiments failed, and for being the ultimate travel partner.

Finally, I am grateful for the support I have received from the National Institutes of Health through a Predoctoral Fellowship (F31CA220970). This award has provided me with extra flexibility in pursuing the research I found most interesting.

TABLE OF CONTENTS

LIST OF FIGURES

LIST OF TABLES

LIST OF ABBREVIATIONS

3D	Three dimensional
Ab	Antibody
ABC	Accelerated blood clearance
ADV	Acoustic droplet vaporization
Akt	Protein kinase B
Ar	Argon
ATCC	American type culture collection
AUC	Area under the curve
B-mode	Brightness mode
BBB	Blood brain barrier
BDNF	Brain-derived neurotrophic factor
BF	Bifunctionally targeted
BLM	Bleomycin
b.p.	Boiling point
BRIJ 100	Polyoxyethylene (100) stearyl ether
Caco-2	Colorectal adenocarcinoma
CH	Cholesterol
CPS	Contrast pulse sequence
DBPC	Dibehenoylphosphatidylcholine
DC-CH·HCl	3β-[N-(N',N'-dimethylaminoehane)-carbamoyl] cholesterol hydrochloride
DDFP	Dodecafluoropentane
DFB	Decafluorobutane
DLS	Dynamic light scattering
DMEM	Dulbecco's modified eagle's medium
DMF	Dose modifying factor
DOPC	1,2-dioleoyl-sn-glycero-3-phosphocholine

DOTAP	N-[1-(2,3-dioleoyloxy) propyl]-N,N,N-trimethylammonium
DPPC	1,2-dipalmitoyl-sn-glycero-3-phosphatidylcholine
DPPE	1,2-dipalmitoyl-sn-glycero-3-phosphoethanolamine
DPPE-PEG2000	1,2-dipalmitoyl-sn-glycero-3-phosphoethanolamine-N-[methoxy(polyethylene glycol)-2000]
DPPG	1,2-dipalmitoyl-sn-glycero-3- [phosphor-rac-1-glycerol]
DSPC	1,2-distearoyl-sn-glycero-3- phosphocholine
DSPE	1,2-distearoyl-sn- glycero-3-phosphoethanolamine
DSPE-PEG2000	1,2-distearoyl-sn- glycero-3-phosphoethanolamine-N-[methoxy(polyethyleneglycol)-2000]
DSPE-PEGfolate	1,2-distearoyl-sn- glycero-3-phosphoethanolamine-N-[folate(polyethyleneglycol)-2000]
DVT	Deep vein thrombosis
EDPPC	1,2-dipalmitoyl-sn-glycero-3-ethylphosphocholine
EDRF	Endothelium-derived relaxing factor
Egg-PC	Egg phosphocholine
ELIP	Echogenic liposome
ELISA	Enzyme-linked immunosorbent assay
EPC	L-α-phosphatidylcholine
EPR	Enhanced permeability and retention
FBS	Fetal bovine serum
FDA	U.S. Food and Drug Administration
FITC	Fluorescein isothiocyanate
FSA	Fibrosarcoma
GI	Gastrointestinal
HIF-1α	Hypoxia inducible factor-1α
HIFU	High intensity focused ultrasound
HT-29	Human colon adenocarcinoma cells
ICD	Inertial cavitation dose

Ig	Immunoglobulin
IP	Intraperitoneal
IV	Intravenous
IVUS	Intravascular ultrasound
k_e	Elimination rate
LOM	Lipidic oxygen-containing microbubble
MAPK	Mitogen-activated protein kinase
MB	Microbubble
MI	Mechanical index
mPEG-DSPE	1,2-distearoyl-*sn*-glycero-3-phosphoethanolamine-N-methoxy(polyethylene-glycol)-2000
mpk	Milligrams per kilogram body weight
MSC	Mesenchymal stem cell
NMB	Nitrogen microbubble
NMDA	*N*-methyl-D-aspartate
NO	Nitric oxide
NOS	Nitric oxide synthase
O_2	Oxygen
OFP	Octofluoropropane
OMB	Oxygen microbubble
PANC-1	Human pancreatic adenocarcinoma cells
PBS	Phosphate-buffered saline
PC	Phosphatidylcholine
PCCA	Phase-change ultrasound contrast agent
PEG	Polyethylene glycol
PEG-40S	polyoxyethylene-40 stearate
PEG2000-PE	1,2-dipalmitoyl-sn-glycero-3-phosphoethanolamine-N-[methoxy(polyethylene glycol)-2000]
PFC	Perfluorocarbon

PI	Propidium iodide
PNP	Peak negative pressure
PRF	Pulse repetition frequency
PTX	Paclitaxel
PVP	Polyvinylpyrrolidone
RB	Rose Bengal
RBC	Red blood cell
ROI	Region of interest
ROS	Reactive oxygen species
RT	Radiation therapy
SBRT	Stereotactic body radiotherapy
SCD	Stable cavitation dose
SD	Standard deviation
SDT	sonodynamic therapy
SF_6	Sulfur hexafluoride
SRS	Stereotactic radiosurgery
$t_{1/2}$	Half-life
TEER	Transepithelial electrical resistance
TIC	Time intensity curve
TPGS	Alpha tocopheryl polyethylene glycol succinate
US	Ultrasound
VSMC	Vascular smooth muscle cells
Xe	Xenon

CHAPTER 1

INTRODUCTION

1.1 MEDICAL ULTRASOUND IMAGING AND THERAPEUTIC ULTRASOUND

Ultrasound is a widely used diagnostic imaging modality, most well-known for its applications in obstetrics (fetal imaging) [1] and cardiology (echocardiography) [2]. To build ultrasound images, high frequency (>20 kHz) sound waves are transmitted into the body using a piezoelectric transducer. When the pressure wave encounters a tissue boundary, a portion of the signal is reflected due to differences in the density of and speed of sound through various tissues. These echoes are received by the transducer and processed to build the familiar brightness-mode (B-mode) images common in fetal imaging, where pixel brightness reflects the magnitude of the received echo. Standard B-mode imaging is a portable and inexpensive method to create anatomical images in real time without exposing patients to ionizing radiation, and as such, ultrasound is a staple bedside diagnostic imaging modality.

Beyond imaging, ultrasound can be used to elicit a wide range of biological effects depending on the intensity of the applied beam (collectively referred to here as therapeutic ultrasound). At the high end of the intensity spectrum, ultrasound can be used thermally ablate diseased tissue noninvasively and with high spatial precision. Internal tissue is heated only where the acoustic waves are focused, thus sparing surrounding tissues in the beam path [3]. The clinical impact of high intensity focused ultrasound (HIFU) technology can be seen in the treatment of uterine fibroids [4], where HIFU is used to noninvasively destroy the fibroids while causing minimal discomfort for the patient. Indeed, patients can be awake during the treatment and are typically able to return to work and an active lifestyle 1-3 days later [4, 5]. This is in contrast to the approximate 6-week recovery time reported for women undergoing standard hysterectomy treatment for their uterine fibroids [4, 5].

With reduced acoustic intensity, therapeutic ultrasound can be used to non-destructively heat tissue by a modest 2-5°C [3]. This mode of therapeutic ultrasound has been used for decades in the field of physical therapy with the goal of eliciting biological effects ranging from decreased joint stiffness to increased blood flow, albeit with modest or uncertain benefit to the patient [6, 7]. Ultrasound hyperthermia has also been proposed as an adjuvant treatment in oncology in combination with radiation or chemotherapy [8]. More recently, this technology has been used to trigger the release of drugs from temperature sensitive liposomes and control therapeutic gene expression via heat-sensitive promoters [3].

Finally, low intensity ultrasound can be used to transiently disrupt biological barriers. Unlike the previously described examples which rely on heating, barrier disruption is largely driven by mechanical forces. When fluid or tissue is exposed to ultrasound of sufficient amplitude, vapor cavities will be created through a process called cavitation. These gas pockets will then stably oscillate with the acoustic wave (stable cavitation) or, at sufficient acoustic amplitudes, they will violently collapse upon themselves (inertial cavitation) [9]. These physical phenomena apply mechanical stress on nearby biological structures, transiently influencing their integrity. This mode of therapeutic ultrasound is most often used to enhance drug delivery through challenging biological barriers, such as the stratum corneum (skin) [10, 11], gastrointestinal epithelium [12, 13], or blood brain barrier [14]. Exogenous cavitation nuclei (ultrasound contrast agents) are often used in this technique to reduce the acoustic energy required for inducing cavitation-mediated bioeffects.

1.2 ULTRASOUND CONTRAST AGENTS

1.2.1 MICROBUBBLES

The signal-enhancing capability of bubbles was discovered by chance when a cardiologist noticed transient increases in ultrasound signal while injecting indocyanine green dye into the left ventricle during an echocardiography [15, 16]. The signal enhancement was later attributed to the formation of bubbles on the catheter tip, which sparked interest in developing microbubbles as intravenous ultrasound contrast agents. This lead to the discovery that blood components could stabilize air bubbles, ultimately leading to the commercial development of Albunex™, an albumin-

shelled air-filled microbubble formulation [15, 17]. Since these initial discoveries, decades of research have resulted in the development of sophisticated ultrasound contrast agents and contrast-specific imaging methods.

Modern microbubbles comprise two key components: a gas core and a stabilizing shell. All commercially-available microbubble formulations contain either sulfur hexafluoride or a perfluorocarbon gas [17]. These high molecular weight gases are poorly soluble in the blood stream, which limits microbubble dissolution and enhances their persistence. Protein, polymers, or lipids are often used for the stabilizing shell, which protects the microbubble from dissolution and dictates how the microbubble will respond to ultrasound [17]. Finally, a stealth polymer called polyethylene glycol is often included in the shell forming material to impart the microbubbles with a steric shield, limiting microbubble coalescence and clearance by scavenging immune cells [18].

Microbubbles respond to ultrasound in a unique manner. Their gas cores are highly compressible, and they expand and contract with passing acoustic waves [19]. At very low amplitudes, these oscillations are primarily linear, with symmetric oscillations around a stable resting diameter. As amplitude is increased, microbubble oscillations become asymmetric with unequal expansion and contraction phases [20]. As amplitude is further increased, microbubble fragmentation and destruction occur. These unique behaviors create echoes with a wide range of frequency content that is unique from the ultrasound transmission frequency and the response of tissue [19, 21]. As a result, it is possible to isolate microbubble signals from that of tissue/fluid, which has given rise to contrast specific imaging techniques.

Due to their micron-range size distributions (1-10 μm), microbubbles are confined to the vascular space after intravenous administration [20]. This, combined with the ability to perform contrast-specific imaging, makes microbubbles ideal blood pool markers, and has given rise to a number of ultrasound imaging techniques centered on evaluating vascular structure, blood flow, and tissue perfusion [20, 21]. These techniques are especially powerful in the context of cancer, where chaotic angiogenesis is a hallmark feature and common treatment target. Indeed, a technique called acoustic angiography has been used to map tumor associated vasculature and quantify its distinct

morphology [22]. Furthermore, this technique shows promise as a novel method to provide early detection of tumor response to radiation therapy [23].

More recently, microbubbles have been adopted by the therapeutic ultrasound field where they are used to enhance biological effects. Microbubble oscillation and collapse can cause flow disturbances in surrounding fluid, create shock waves, and even produce microjets of fluid toward nearby boundaries, which all exert physical stress on surrounding biological structures [19, 24]. There is particular interest in combining microbubbles with low intensity therapeutic ultrasound to open the blood brain barrier or tumor-associated vasculature to enhance the accumulation and efficacy of various drugs [25-27].

1.2.2 PHASE-CHANGE ULTRASOUND CONTRAST AGENTS

Phase-change ultrasound contrast agents (PCCAs) are liquid perfluorocarbon nanoemulsions that are stabilized by shells similar in composition to those of microbubbles. In the liquid state, PCCAs do not provide ultrasound contrast, but they can be vaporized into acoustically active microbubbles with ultrasound stimulation of sufficient amplitude [28]. Once vaporized, the resultant microbubbles can provide contrast for imaging purposes or be exploited for therapeutic purposes much like the conventional microbubbles described in the previous section.

Early PCCAs were formulated with perfluorocarbons that had bulk boiling points near body temperature (e.g., dodecafluoropentane, DDFP, bulk b.p. = 29°C). These agents are stable in the liquid state at room temperature, but even at 37°C, nanoscale DDFP PCCAs require high acoustic pressures for vaporization (3-6 MPa [29, 30]). This raises concerns of undesirable biological effects being induced by the high-pressure activation pulse for diagnostic imaging or low intensity therapeutic ultrasound applications.

Sheeran et al. invented low boiling point PCCAs filled with decafluorobutane (DFB, bulk b.p. = -2°C) [31] or octofluoropropane (OFP, bulk b.p. = -36.7°C) liquid [32]. These PCCAs are fabricated through microbubble condensation, where precursor microbubbles are exposed to low temperatures and high pressures until their gaseous DFB or OFP cores condense into a liquid. They remain metastable in the liquid state at room and body temperature, and importantly, they can be

vaporized into microbubbles with acoustic parameters in line with what is used for clinical diagnostic imaging and with existing clinical hardware. This provides a substantial advantage over higher boiling point formulations.

Motivation to use PCCAs rather than microbubbles is driven largely by their reduced size distribution. With sizes ranging from 100-300 nm, it has been postulated that PCCAs may be able to extravasate from leaky tumor-associated vasculature via the enhanced permeability and retention effect [33]. This, in theory, may allow extravascular imaging capabilities and expanded utility for therapeutic ultrasound applications compared to microbubbles that are confined to the vascular space.

1.3 DISSERTATION SCOPE AND OBJECTIVES

Historically, microbubbles have been characterized from a contrast imaging perspective, with emphasis placed on elucidating microbubble physics, their unique acoustic signatures, and optimal contrast-specific imaging techniques. Less well understood are details regarding (1) how biological systems respond to these chemical entities and (2) how microbubbles/PCCAs can be used to therapeutically manipulate biological features. Through this thesis, we study microbubbles and PCCAs from a molecular pharmaceutics perspective, gaining a better understanding of contrast agent behavior and therapeutic potential.

Similar to drugs and drug delivery vehicles, microbubbles are chemical entities that will interact with biological milieu and the immune system when administered systemically. Chapter 2 explores how these interactions may influence microbubble pharmacokinetics, particularly when microbubbles are administered repeatedly to the same animal over a one-month period. Understanding how microbubble pharmacokinetics may change as a result of anti-microbubble immune responses is important for many emerging applications of contrast-enhanced ultrasound imaging and therapeutic ultrasound that involve repeated administration of microbubbles to the same patient.

A major theme of pharmaceutics research is that clever formulations can be designed to deliver therapeutic payloads that are otherwise limited by poor aqueous solubility or instability in

biological environments. In chapters 3 and 4, we apply this concept to microbubbles, exploring their potential as therapeutic gas delivery vehicles. Specifically, in chapter 4, we study the use of microbubbles to deliver molecular oxygen to hypoxic tumors to overcome hypoxia-induced resistance to radiation therapy.

Efficient and specific drug delivery to the desired site of action is often hampered by nuanced biological barriers. Through the final chapters of this work (chapters 5-8), we explore how ultrasound-stimulated PCCAs can be used to overcome some of these biological barriers through *in vitro* experimentation. Chapter 5 provides an introduction to mechanisms and applications of ultrasound-mediated drug delivery. Through chapter 6, we demonstrate the ability of low boiling point PCCAs to be used to permeabilize individual cell membranes, which we apply to the delivery of bleomycin into chemo-resistant cancer cells in chapter 7. Finally, in chapter 8, we explore to potential of PCCAs to disrupt epithelial barriers towards applications in gastrointestinal drug delivery.

REFERENCES

1. Papp, Z. and T. Fekete, *The evolving role of ultrasound in obstetrics/gynecology practice.* Int J Gynaecol Obstet, 2003. **82**(3): p. 339-46.

2. Maragiannis, D. and S.H. Little, *Interventional imaging: the role of echocardiography.* Methodist Debakey Cardiovasc J, 2014. **10**(3): p. 172-7.

3. Wang, S., V. Zderic, and V. Frenkel, *Extracorporeal, low-energy focused ultrasound for noninvasive and nondestructive targeted hyperthermia.* Future Oncol, 2010. **6**(9): p. 1497-511.

4. Taran, F.A., et al., *Magnetic resonance-guided focused ultrasound (MRgFUS) compared with abdominal hysterectomy for treatment of uterine leiomyomas.* Ultrasound Obstet Gynecol, 2009. **34**(5): p. 572-8.

5. Stewart, E.A., et al., *Clinical outcomes of focused ultrasound surgery for the treatment of uterine fibroids.* Fertility and Sterility, 2006. **85**(1): p. 22-29.

6. Miller, D.L., et al., *Overview of therapeutic ultrasound applications and safety considerations.* J Ultrasound Med, 2012. **31**(4): p. 623-34.

7. Robertson, V.J. and K.G. Baker, *A review of therapeutic ultrasound: effectiveness studies.* Phys Ther, 2001. **81**(7): p. 1339-50.

8. Marchal, C., et al., *Treatment of superficial human cancerous nodules by local ultrasound hyperthermia.* Br J Cancer Suppl, 1982. **5**: p. 243-5.

9. Mitragotri, S., *Healing sound: the use of ultrasound in drug delivery and other therapeutic applications.* Nat Rev Drug Discov, 2005. **4**(3): p. 255-60.

10. Mitragotri, S. and J. Kost, *Low-frequency sonophoresis: a review.* Adv Drug Deliv Rev, 2004. **56**(5): p. 589-601.

11. Tachibana, K. and S. Tachibana, *Transdermal delivery of insulin by ultrasonic vibration.* J Pharm Pharmacol, 1991. **43**(4): p. 270-1.

12. Schoellhammer, C.M., et al., *Ultrasound-mediated gastrointestinal drug delivery.* Sci Transl Med, 2015. **7**(310): p. 310ra168.

13. Schoellhammer, C.M. and G. Traverso, *Low-frequency ultrasound for drug delivery in the gastrointestinal tract.* Expert Opin Drug Deliv, 2016. **13**(8): p. 1045-8.

14. Wu, S.Y., et al., *Characterizing Focused-Ultrasound Mediated Drug Delivery to the Heterogeneous Primate Brain In Vivo with Acoustic Monitoring.* Sci Rep, 2016. **6**: p. 37094.

15. Calliada, F., et al., *Ultrasound contrast agents: basic principles.* Eur J Radiol, 1998. **27 Suppl 2**: p. S157-60.

16. Gramiak, R. and P.M. Shah, *Echocardiography of the aortic root.* Invest Radiol, 1968. **3**(5): p. 356-66.

17. Paefgen, V., D. Doleschel, and F. Kiessling, *Evolution of contrast agents for ultrasound imaging and ultrasound-mediated drug delivery.* Front Pharmacol, 2015. **6**.

18. Abou-Saleh, R.H., et al., *Poly(ethylene glycol) lipid-shelled microbubbles: abundance, stability, and mechanical properties.* Langmuir, 2014. **30**(19): p. 5557-63.

19. Ferrara, K., R. Pollard, and M. Borden, *Ultrasound microbubble contrast agents: fundamentals and application to gene and drug delivery.* Annu Rev Biomed Eng, 2007. **9**: p. 415-47.

20. Cosgrove, D., *Ultrasound contrast agents: an overview.* Eur J Radiol, 2006. **60**(3): p. 324-30.

21. Martin, K.H. and P.A. Dayton, *Current status and prospects for microbubbles in ultrasound theranostics.* Wiley Interdiscip Rev Nanomed Nanobiotechnol, 2013. **5**(4): p. 329-45.

22. Shelton, S.E., et al., *Quantification of Microvascular Tortuosity during Tumor Evolution Using Acoustic Angiography.* Ultrasound Med Biol, 2015. **41**(7): p. 1896-904.

23. Kasoji, S.K., et al., *Early Assessment of Tumor Response to Radiation Therapy using High-Resolution Quantitative Microvascular Ultrasound Imaging.* Theranostics, 2018. **8**(1): p. 156-168.

24. Lentacker, I., et al., *Understanding ultrasound induced sonoporation: definitions and underlying mechanisms.* Adv Drug Deliv Rev, 2014. **72**: p. 49-64.

25. Park, J., et al., *Evaluation of permeability, doxorubicin delivery, and drug retention in a rat brain tumor model after ultrasound-induced blood-tumor barrier disruption.* J Control Release, 2017. **250**: p. 77-85.

26. Kotopoulis, S., et al., *Sonoporation-enhanced chemotherapy significantly reduces primary tumour burden in an orthotopic pancreatic cancer xenograft.* Mol Imaging Biol, 2014. **16**(1): p. 53-62.

27. Dimcevski, G., et al., *A human clinical trial using ultrasound and microbubbles to enhance gemcitabine treatment of inoperable pancreatic cancer.* J Control Release, 2016. **243**: p. 172-181.

28. Sheeran, P.S. and P.A. Dayton, *Phase-Change Contrast Agents for Imaging and Therapy.* Curr Pharm Des, 2012. **18**(15): p. 2152-65.

29. Williams, R., et al., *Characterization of submicron phase-change perfluorocarbon droplets for extravascular ultrasound imaging of cancer.* Ultrasound Med Biol, 2013. **39**(3): p. 475-89.

30. Burgess, M.T. and T.M. Porter, *Acoustic cavitation-mediated delivery of small interfering ribonucleic acids with phase-shift nanoemulsions.* Ultrasound in medicine & biology, 2015. **41**(8): p. 2191-2201.

31. Sheeran, P.S., et al., *Formulation and acoustic studies of a new phase-shift agent for diagnostic and therapeutic ultrasound.* Langmuir, 2011. **27**(17): p. 10412-20.

32. Sheeran, P.S., et al., *Design of ultrasonically-activatable nanoparticles using low boiling point perfluorocarbons.* Biomaterials, 2012. **33**(11): p. 3262-9.

33. Rapoport, N., et al., *Ultrasound-mediated tumor imaging and nanotherapy using drug loaded, block copolymer stabilized perfluorocarbon nanoemulsions.* J Control Release, 2011. **153**(1): p. 4-15.

CHAPTER 2[1]

ACCELERATED BLOOD CLEARANCE OF PEGYLATED MICROBUBBLES

2.1 MOTIVATION AND OVERVIEW

Many emerging applications of microbubbles in ultrasound imaging and therapy involve repeated interrogation over several weeks. For example, quantitative contrast-enhanced imaging has been proposed as a method to provide early detection of tumor response to therapy [1, 2]. Here, microbubbles are used as blood pool markers, and quantification of microbubble flow or overall microbubble signal density can be related to tumor perfusion or degree of vascularity. Thus, changes in these imaging metrics over the course of treatment are assumed to reflect changes in tumor vascular physiology (e.g., decreased vascularization) and are used to predict treatment efficacy.

In terms of therapeutic ultrasound, microbubbles are often combined with low intensity ultrasound to enhance drug delivery to a target region. When used to enhance chemotherapeutic accumulation in solid tumors, this ultrasound-enhanced treatment is repeated over the course of several weeks in accordance with standard chemotherapy dosing timelines [3]. Treatment efficacy is sensitive to microbubble concentration, and it is essential for microbubbles be present during the entire ultrasound exposure (e.g., after a bolus dose).

In each of these examples, the concentration of microbubbles in circulation is critical, and a fundamental assumption is that microbubble persistence (pharmacokinetics) remains constant from day to day. However, we and others have noticed that the clearance of microbubbles becomes faster

[1]This chapter previously appeared as an article in Ultrasound in Medicine and Biology. The original citation is as follows: Fix, S. M., Nyankima, A.G., McSweeney, M.D., Tsuruta, J.K., Lai, S.K., Dayton, P.A. (2018). "Accelerated Clearance of Ultrasound Contrast Agents Containing Polyethylene Glycol is Associated with the Generation of Anti-Polyethylene Glycol Antibodies." Ultrasound in Medicine & Biology **44**(6): 1266-1280.

during the course of longitudinal studies. We hypothesized that this phenomenon may be related to the development of an immune response against polyethylene glycol (PEG), a common component of many lipid-shelled microbubble formulations.

The purpose of this chapter is to evaluate the generation of an anti-PEG immune response following a single dose or multiple doses of homemade PEGylated microbubbles over a one-month period and to characterize associated changes in microbubble pharmacokinetics. A secondary aim of this study was to characterize anti-PEG immunity and accelerated clearance following multiple doses of two clinically-approved microbubble formulations: PEGylated Definity® and non-PEGylated Optison™.

2.2 BACKGROUND

PEG is used ubiquitously in biomedical research to enhance the *in vivo* stability and circulatory persistence of various particles. The high conformational flexibility and hydrophilicity of PEG makes interactions with blood proteins energetically unfavorable [4]. Therefore, PEGylation creates a steric shield surrounding the particle, reducing opsonization and subsequent clearance by the reticuloendothelial system [5]. This approach has been used to endow therapeutic proteins [6-8], drug-carrying nanoparticles [4, 9, 10], and imaging contrast agents [11-14] with improved pharmacokinetics, and several of these agents have been translated to clinical use [15, 16].

Many microbubbles are formulated with PEG to stabilize their phospholipid shell [17, 18]. PEG-mediated stabilization is typically achieved through the use of PEGylated surfactants (e.g., polyethylene glycol stearate) or PEGylated phospholipids [18-20]. In both cases, the PEGylated molecules incorporate into the microbubble monolayer shell and stabilize the particles against coalescence with other microbubbles and interaction with blood plasma proteins [18, 19]. Inclusion of these PEGylated molecules has been shown to drastically enhance microbubble stability *in vitro*, prolonging formulation lifetime from approximately 13 min (without PEGylated lipids) to 60 min (with 5% PEGylated lipids) [18]. Two of the three FDA approved microbubble formulations contain PEG. Lumason®/SonoVue® contains PEG-4000 as a stabilizer in the suspending medium [21] and

Definity® contains PEGylated phospholipid as a shell component [22]. The third FDA-approved formulation, Optison™, is stabilized by a human albumin-based shell and does not contain PEG [23].

Paradoxically, the immune system is able to generate specific antibodies that bind to PEG, the molecule originally exploited for its resistance to protein absorption and immunological shielding [24, 25]. In rodents, anti-PEG immunity is characterized by robust but transient production of anti-PEG IgM, which peaks in concentration approximately one-week following the initial dose of PEGylated agents [25]. Conversely, in humans, anti-PEG IgG antibodies are more prevalent, suggesting evidence for a potential anti-PEG memory response [26]. Furthermore, recent evidence suggests up to 72% of the general population (not previously exposed to PEGylated therapeutics) possess detectable pre-existing anti-PEG antibodies [26], possibly due to repeated low-level exposure to PEG-containing household goods such as foods, toothpastes, and skin care products.

The pharmacokinetics of PEGylated particles are altered in the presence of anti-PEG antibodies. This so-called 'accelerated blood clearance (ABC) phenomenon' has been associated with >10-fold reductions in particle half-lives in preclinical species [27-29]. The ABC phenomenon has been observed in a variety of animals and for PEGylated agents ranging from proteins to liposomes [30-32]. Additionally, the presence of anti-PEG antibodies in humans has been correlated with increased incidence of adverse events and reductions in the therapeutic efficacy of PEGylated proteins in clinical trials, including pegloticase (indicated for severe treatment-refractory gout) and pegaspargase (part of multidrug therapy used to treat acute lymphoblastic leukemia) [33-35].

We and other researchers have observed accelerated microbubble clearance in the later stages of studies that involve repeat contrast imaging over several days [36], and the role of anti-PEG immunity in this observation will be explored through this chapter.

2.3 MATERIALS AND METHODS

2.3.1 HOMEMADE MICROBUBBLE FABRICATION AND CHARACTERIZATION

To form lipid-shelled microbubbles (referred to as house-MBs), 1,2-distearoyl-*sn*-glycero-3-phosphocholine (DSPC) and 1,2-distearoyl-*sn*-glycero-3-phosphoethanolamine-N-methoxy(polyethylene-glycol)-2000 (mPEG-DSPE) (Avanti Polar Lipids, Alabaster, AL, USA) were

combined in a 9:1 molar ratio and dissolved in a phosphate-buffered saline (PBS)-based solution containing 15% (v/v) propylene glycol and 5% (v/v) glycerol for a final lipid concentration of 1.0 mg/mL. Lipid solubilization was achieved using a previously described method [37]. One and one half milliliter aliquots of the lipid solution were then dispensed into 3.0 mL glass vials. The vial headspace air was replaced with decafluorobutane gas (Fluoromed, Round Rock, TX, USA), and microbubbles were generated by vigorous shaking of the vial using a VialMix (Bristol-Myers-Squibb, New York, NY, USA). House-MB size distributions and concentrations were characterized via single particle optical sizing (Accusizer 780AD, Particle Sizing Systems, Port Richey, FL, USA). House-MBs were characterized by a polydisperse size distribution. The average concentration and number-weighted mean diameter of these microbubbles were found to be $(1.0 \pm 0.3) \times 10^{10}$ microbubbles/mL and 1.00 $\pm$ 0.02 μm, respectively (N=3 vials).

2.3.2 COMMERCIALLY AVAILABLE MICROBUBBLES

Definity (Lantheus Medical Imaging, Billerica, MA, USA) and Optison (GE Healthcare, Princeton, NJ, USA) used throughout this study were purchased from the Hospital Pharmacy at the University of North Carolina at Chapel Hill.

2.3.3 ANIMAL PREPARATION

All animal experiments were approved and performed in accordance with the University of North Carolina at Chapel Hill Institutional Animal Care and Use Committee. First, female Fischer 344 rats were anesthetized via inhaled isoflurane (induced at 5% and maintained at 2% isoflurane in oxygen). A 24 G catheter was inserted into the tail vein and used to collect blood samples for PEG-specific antibody detection. The catheter was then flushed with a small volume of heparinized saline to prevent clot formation and catheter blockage. Next, the animals' abdominal regions were shaved with an electric clipper and a disposable razor, and ultrasound gel was used to couple the imaging transducer to the animals' skin.

2.3.4 ULTRASOUND IMAGE ACQUISITION

An Acuson Sequoia 512 clinical imaging system equipped with a 14 MHz linear array transducer was used throughout this study (15-L8, Siemens, Mountain View, CA, USA). Anesthetized animals were positioned on their left sides and secured to a heated platform using surgical tape to minimize movement during imaging. The kidney was chosen as our imaging target due to its high vascularity, its proximity to the skin's surface, and because it is not a suspected clearance organ for intact microbubbles [38, 39]. The largest transverse plane of right kidney was located via B-mode imaging at 14 MHz and 0.61 mechanical index with an imaging frame rate of 17 Hz. Contrast specific imaging in Cadence™ Contrast Pulse Sequencing (CPS) mode was then initiated with a frequency of 7.0 MHz, mechanical index of 0.18, CPS gain of -10 dB, imaging frame rate of 20 Hz, and dynamic range of 80 dB. Twenty-minute CPS-mode clips were recorded using a capture frame rate of 1.0 Hz. Ten seconds into CPS clip storage, a bolus dose of microbubbles providing approximately 6.7×10^8 microbubbles/kg body weight (see experimental protocols below for more detail) was rapidly administered through the tail vein catheter followed immediately by a 200 μL flush of sterile saline. Image data were exported from the ultrasound machine in DICOM format and analyzed offline using MATLAB (Mathworks Inc., Natick, MA, USA) and ImageJ software (NIH, Bethesda, MD, USA).

2.3.5 EXPERIMENT 1 – CHANGE IN CIRCULATORY PERSISTENCE OF PEGYLATED HOUSE-MBS OVER 28 DAYS

A total of 11 female Fischer 344 rats (average weight 150.5 g) were divided into the experimental groups outlined below and underwent ultrasound imaging (or sham treatment) on days 0, 1, 2, 3, 7, 14, and 28 of this study. For each contrast imaging session, approximately 1×10^8 house-MBs were administered in 90 μL sterile saline followed by a saline flush.

1. **Sham (n=2):** These animals underwent ultrasound imaging without contrast administration at each time point. Instead of house-MBs, these animals received a bolus dose of sterile saline. Serum collected from these animals served as a control for anti-PEG antibody expression at each time point.

2. **Single contrast dose (n=4)**: This group was used to study the generation of anti-PEG antibodies following a single dose of PEGylated contrast. These animals were imaged with contrast on day 0. At each subsequent time point, they underwent sham treatment involving catheter insertion, administration of sterile saline, and imaging in the absence of contrast agents. After the final blood collection on day 28, these animals received follow-up contrast imaging to evaluate the effect of a single dose of contrast on the clearance of house-MBs administered 28 days later.
3. **Multiple contrast doses (n=5):** These animals received contrast imaging at each time point (days 0, 1, 2, 3, 7, 14, and 28) to study the generation of an anti-PEG antibody response and altered house-MB clearance kinetics during repeat imaging schedules. One animal from this group died on day 14, and data collected up until that point was included in this study. We believe this animal's death was unrelated to the experiment and was likely due to isoflurane sensitivity.

2.3.6 Experiment 2 – Free PEG competition to recover circulatory persistence of house-MBs

We performed a free PEG competition experiment to explore the causal relationship between anti-PEG antibodies and accelerated clearance of house-MBs. A total of 7 female Fischer 344 rats (average weight 93.7 g) were divided into Control and Free PEG Competition groups. These animals were smaller than those used for experiment 1, and the contrast dose was proportionally reduced to approximately 6.2×10^7 house-MBs administered in 90 μL of sterile saline. All animals received a dose of house-MBs on day 0 and underwent contrast imaging to capture initial microbubble circulation kinetics. On days 1, 2, and 3, all animals received an additional dose of house-MBs to stimulate the accelerated blood clearance effect. On days 7 and 24, Control or Free PEG Competition protocols were performed as detailed below. On day 22, all animals underwent contrast imaging to ensure that the free PEG dose on day 7 did not stimulate further acceleration in MB clearance for animals in the competition group. The timeline of this study is depicted in Figure 2.1.

1. **Control (n=3):** On day 7, control animals received an injection of sterile saline equal in volume to that of the free PEG dose administered for the competition group. Approximately 3 hours later, house-MBs were administered and circulation kinetics were captured by contrast ultrasound imaging. This sequence of saline injection followed by contrast imaging was repeated on day 24.

Serum was collected on day 0, day 7 (before and ~3hr after saline injection), and day 24 (before and ~3hr after saline injection) to characterize anti-PEG antibody levels.

2. **Free PEG Competition (n=4):** On day 7, animals in the competition group received a 550 mg per kg body weight (mpk) dose of sterile free PEG in PBS (20 kDa molecular weight, PEG20 kDa) (Sigma-Aldrich, St. Louis, MO, USA). Approximately 3 hours later, house-MBs were administered and contrast ultrasound imaging was performed. This free PEG competition sequence was repeated on day 24 with an increased dose of PEG20 kDa (2,200 mpk). Serum collected on day 0, day 7 (before and ~3hr after PEG injection), and day 24 (before and ~3hr after PEG injection) was used to characterize anti-PEG antibody levels. Serum was collected before and after PEG injection to determine if the free PEG was able to bind a substantial portion of circulating anti-PEG antibodies and therefore decrease detectable antibody concentrations.

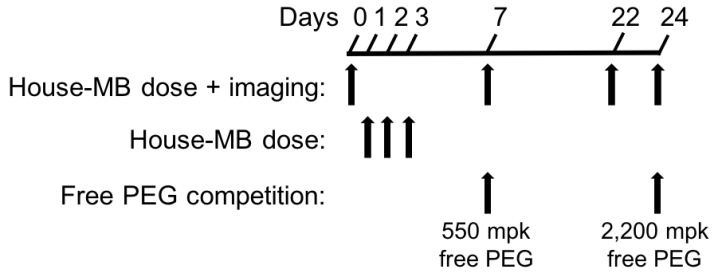

Figure 2.1: Timeline detailing experiment two. Free PEG competition to recover circulatory persistence of house-MBs. On days 0, 7, 22, and 24, animals underwent contrast ultrasound imaging to quantify microbubble circulatory persistence. On days 1, 2, and 3, animals received a dose of house-MBs without imaging to induce the ABC effect. On days 7 and 24, free PEG (or saline) was administered prior to the house-MB dose and contrast imaging.

2.3.7 EXPERIMENT 3 – CHANGE IN CIRCULATORY PERSISTENCE OF DEFINITY AND OPTISON WITH MULTIPLE DOSING OVER 30 DAYS

The purpose of this experiment was to study changes in the circulatory persistence of two clinically-approved microbubble formulations - Definity and Optison - when administered multiple times over a 30-day period. Definity is a lipid-based microbubble formulation, which contains mPEG5000-DPPE as a shell component. Conversely, Optison microbubbles are stabilized by a human albumin shell, and the formulation does not contain PEG.

A total of 15 Fischer 344 rats (average weight 146.8 g) were divided into Sham (n=4), Optison (n=6), and Definity (n=5) groups and underwent contrast imaging (or sham treatment) on days 0, 1, 2, 3, 7, 14, and 30 as described for experiment 1 (see procedures for 'Sham' and 'Multiple contrast doses'). Approximately 1×10^8 microbubbles were administered at each time point, according to the stock concentrations reported on the Definity and Optison package inserts [22, 23]. Serum was collected from all animals at each time point and tested for anti-PEG antibodies.

2.3.8 QUANTIFICATION OF MICROBUBBLE PERSISTENCE

B-mode images and CPS videos were imported into MATLAB and converted from DICOM to TIFF and AVI formats, respectively. Each converted file was then opened in ImageJ where a relatively small region of interest (ROI, 60×30 pixel oval) was drawn in the upper half of the kidney. A small ROI was chosen to minimize artifacts due to shadowing in the lower regions of the kidney [40]. Mean pixel intensity within the ROI was plotted over time, providing contrast time intensity curves (TICs) for further analysis. After microbubble administration, contrast intensity peaked rapidly and was followed by plateau and washout phases.

From the TICs, three metrics were calculated to quantify the circulatory kinetics of the microbubbles: area under the curve (AUC), elimination rate (k_e), and half-life ($t_{1/2}$). First, baseline intensity (average of the first 5 frames) was subtracted from the TIC and AUC were calculated in GraphPad Prism 6.0h (GraphPad Software, Inc., La Jolla, CA, USA). Additionally, a one-phase exponential decay equation was fit to the TIC washout phase, which was used to calculate the exponential decay constant referred to here as elimination rate (k_e, min^{-1}) and microbubble half-live ($t_{1/2}$, min) using GraphPad. All curve fits were associated with R^2 values between 0.90-0.99. AUC, k_e, and $t_{1/2}$ values were averaged among animals at each time point and are reported here as mean ± standard deviation.

For experiment 2, image collection on day 24 was erroneously terminated before the 20-min end point. Therefore, AUC values calculated from 0 – 7 min ($AUC_{0\text{-}7min}$) were compared among groups for this experiment. One-phase exponential decays were fit to the shortened curves on day 24 with strong R^2 values >0.96 and used to calculate $t_{1/2}$ and k_e values.

2.3.9 DETECTION OF PEG-SPECIFIC ANTIBODIES

For all experiments, blood was collected as described in the 'Animal Preparation' section and allowed to clot at room temperature for 15-60 min. Serum was then isolated by centrifugation at 2,000 g for 10 min and stored at −60°C for future use.

Serum concentrations of anti-PEG IgM or anti-PEG IgG antibodies were analyzed separately using their respective enzyme-linked immunosorbent assay (ELISA) kits (Life Diagnostics, Inc., West Chester, PA, USA) performed according to the manufacturer's protocol. For all experiments, serum samples were diluted 100× for the anti-PEG IgG assay. For experiment 1, serum samples were diluted 1000× for the anti-PEG IgM assay. Serum dilution was reduced to 250× for the anti-PEG IgM assay for experiments 2 and 3. Upon completion of the assay, optical density at 450 nm was read using an HTS 7000 Bioassay Plate Reader (PerkinElmer, Waltham, MA, USA) and the absorbance of a blank well was subtracted from all experimental values. All serum samples were tested in duplicate, and standard curves generated in duplicate on each ELISA plate were used to calculate the relative concentration of anti-PEG IgM or anti-PEG IgG in the samples in arbitrary units per milliliter. Please note that since the concentration of IgM and IgG standards were provided in arbitrary units, relative quantities of experimental anti-PEG antibody can only be compared within each isotype.

For experiment 1, samples from the time points showing maximal antibody concentration (day 7 for IgM and day 14 for IgG) were used in competitive ELISAs to confirm antibody specificity for the PEG component of house-MBs. Anti-PEG IgM and anti-PEG IgG ELISA kits were used as described above except serum samples were diluted with a solution containing the PEGylated lipid component of our microbubbles (DSPE-mPEG2000, 0.9-0.99 mg/mL). The relative quantity of anti-PEG IgM and anti-PEG IgG detected through the competition assay was compared with that observed in the standard ELISA.

2.3.10 STATISTICAL ANALYSES

All statistical analyses were performed in GraphPad. For each experiment, metrics describing microbubble circulatory kinetics (AUC, k_e, $t_{1/2}$) were compared using one-way ANOVA followed by Sidak's multiple comparison testing on significant results. AUC, k_e, and $t_{1/2}$ values describing later

time points were compared to the respective initial values calculated on day 0. For experiment 1, kinetic parameters calculated on day 28 were also compared between those animals that had received multiple contrast doses throughout the study and those that had received a single contrast dose on day 0 and follow-up contrast imaging on day 28.

For experiments 1 and 3, mean anti-PEG IgM and anti-PEG IgG levels for each experimental group (i.e., multiple and single dosing for experiment 1, and Definity and Optison for experiment 3) were compared to the respective control mean at each time point using two-way ANOVA with respect to time. Dunnet's multiple comparison testing was then performed on significant results. For experiment 1, the concentrations of IgM and IgG antibodies detected in the competitive ELISA assay were compared to the respective concentrations detected in the non-competitive ELISA using a paired student's t-test. Throughout this study, p-values < 0.05 were considered statistically significant.

For experiment 3, remarkably high anti-PEG IgG values of 3,380 and 5,320 U/mL were detected in one of four control animals on days 14 and 30, respectively. This is in comparison to the 400 ± 200 and 400 ± 300 U/mL IgG detected in the remaining control animals on days 14 and 30, respectively. Therefore, Grubbs' tests were performed, and it was determined that both IgG measurement values from this animal were significant outliers. As such, these data points were excluded from the analysis. Note: this outlying control animal did not demonstrate unusually high anti-PEG IgM concentrations at any time point.

2.4 RESULTS AND DISCUSSION

2.4.1 EXPERIMENT 1 – CHANGE IN CIRCULATORY PERSISTENCE OF HOUSE-MBS OVER 28 DAYS

Microbubbles are unable to escape the vascular space due to their relatively large size. By avoiding the measurement of signal in organs that are involved in active microbubble uptake and elimination (liver and spleen), we assumed that any signal observed in contrast-specific imaging was the result of microbubbles in circulation. Thus, microbubble blood clearance following an intravenous bolus dose was measured via quantification of contrast intensity over time.

Here, we imaged circulating microbubbles for 20 min following bolus administration using the kidney as an imaging target. The microbubbles were found to wash into the kidney vasculature within 5 s of the injection (Figure 2.2 B, 2.2 G, 2.2 L), and the high concentration of microbubbles caused shadowing in some cases (white arrow heads in Figure 2.2 C and 2.2 H).

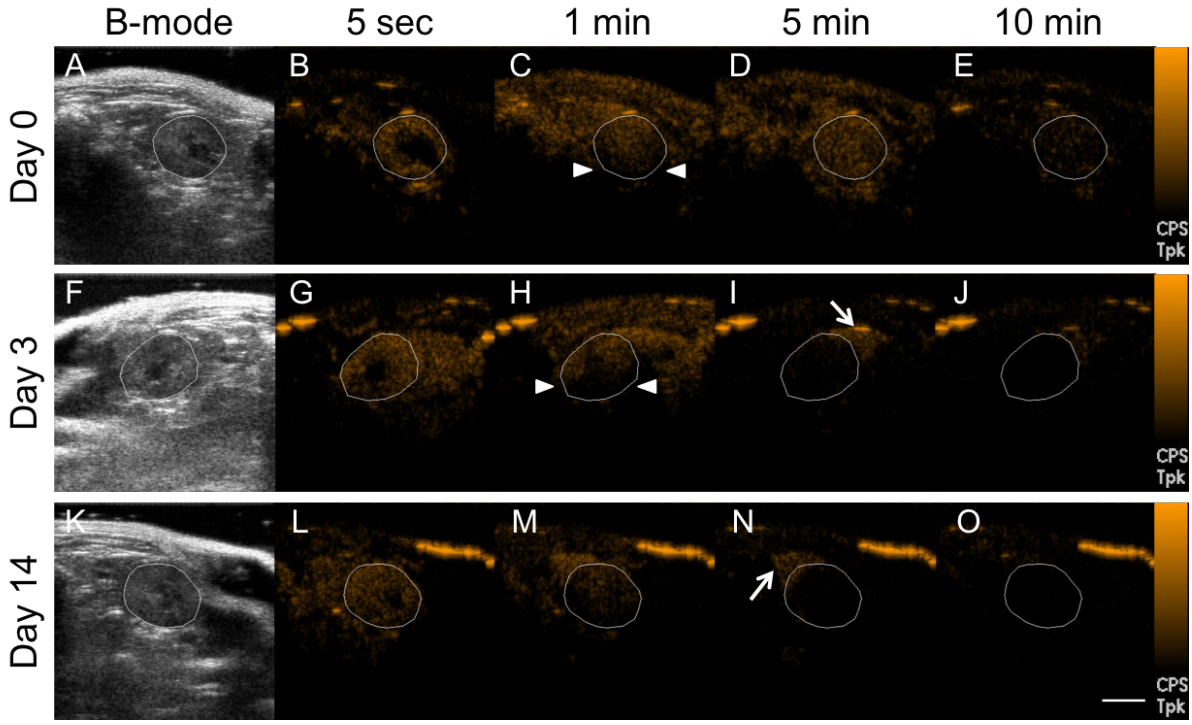

Figure 2.2: Representative B-mode and contrast images of rat kidneys from experiment one. Kidneys are outlined in white. As shown in the day 0 panel, contrast washes out uniformly from all visible tissues in naïve rats, and some signal from the house-MBs is still observable at the 10-min time point. The ABC effect becomes apparent on day 3 and persists throughout the study. At these later time points we see rapid washout of contrast from the kidney, and redistribution into the liver (white arrows). Shadowing was observed post-contrast injection and is noted with white arrowheads. Bar = 5 mm.

When microbubbles were administered to naïve animals on day 0, contrast was observable for greater than 10 min post-injection (Figure 2.2 A-E). Additionally, contrast intensity faded uniformly throughout the images. Accelerated blood clearance (ABC) of the microbubbles became apparent on day 2, and by day 3, the kidney appeared devoid of contrast signal by 5-min post-injection (Figure 2.2 F-J). The ABC effect continued throughout the remainder of the study (through day 28). Interestingly, we observe that strong signal intensity in the liver persisted well beyond microbubble signal detected in the kidney and surrounding tissue, as designated by white arrows in Figure 2.2 I

and 2.2 N. Such an effect was never observed for the first contrast dose in naïve animals, and this qualitative observation suggests that ABC could be associated with more active liver uptake and clearance of the microbubbles. If the ABC is indeed due to the binding of multiple antibodies per microbubble, we suspect that clearance might be mediated by FcγRIIb receptors on liver sinusoidal endothelial cells and by Kupffer cells, as has been reported for other immune complexes [41-43] and microbubbles [44, 45]. Clearance to the liver and spleen may also be guided by erythrocytes following binding of opsonized microbubbles by complement receptor one [46].

Contrast intensity was quantified in ImageJ and used to generate the time-intensity curves (TICs) presented in Figure 2.3. Corresponding with our qualitative observations, a leftward shift in the TICs was first observed 2 days after the initial microbubble dose (Figure 2.3 A). This effect continued to become more dramatic throughout the study, reaching a maximum on day 14 that was matched at day 28. This observation is reflected quantitatively in terms of elimination rate (k_e), half-life ($t_{1/2}$) and area under curve (AUC) (Table 1 and Figure 2.4). k_e rates calculated on days 14 and 28 were approximately 4-times faster than that of the initial dose. Similarly, $t_{1/2}$ and AUC decreased throughout the study, reaching a minimum on day 14, which was approximately matched on day 28. Half-lives and AUCs at these time points were approximately 4- and 6.5-times less than those of the initial dose, respectively.

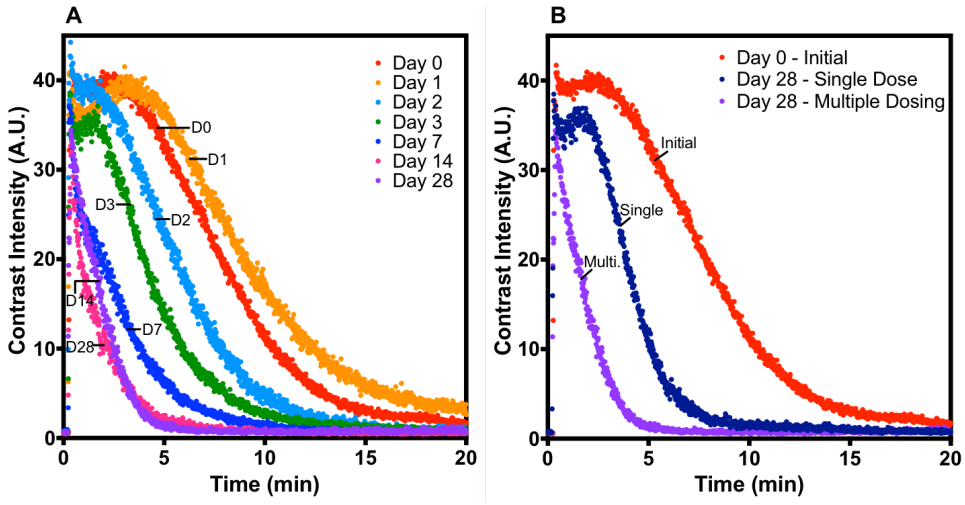

Figure 2.3: Average time intensity curves from experiment one. (A) Time intensity curves obtained from animals receiving repeat doses of polyethylene glycol (PEG)-containing house-MBs over 28 days. Curve labels (D0-D28) indicate time in days since the initial dose. (B) Comparison of the initial contrast time intensity curve to those obtained 28 days later in animals that received multiple doses of contrast (purple) and those that received a single prior dose (blue).

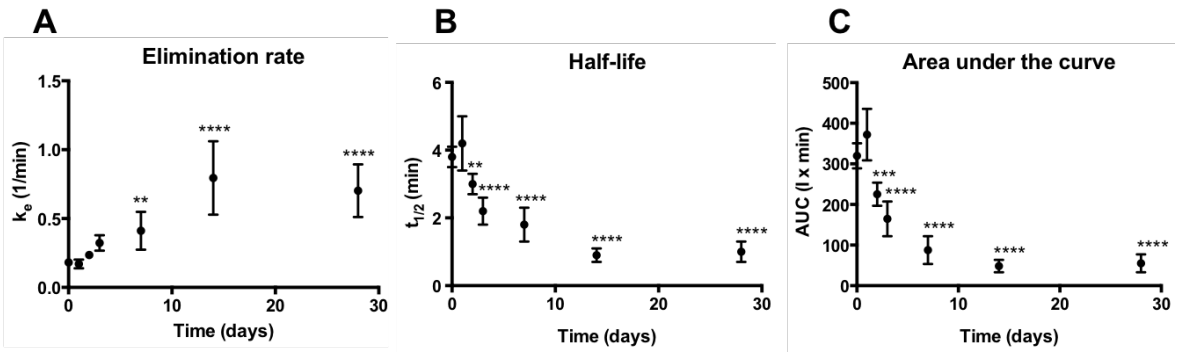

Figure 2.4: Changes in house-MB pharmacokinetic parameters over 30 days of repeat dosing. A) Elimination rate (k_e); B) Half-life ($t_{1/2}$); C) Area under the curve (AUC). Symbol key: ** $p \leq 0.01$; *** $p \leq 0.001$; **** $p \leq 0.0001$

ABC was also observed on day 28 for animals that had received a single prior dose of microbubbles. However, the effect was not as dramatic as that seen on the 28th day in animals that had received multiple microbubble doses over 28 days (Figure 2.3 B). In the single dose group, k_e was found to increase by 2.3-times, while $t_{1/2}$ and AUC were both found to decrease by approximately 2-times compared to the initial dose. However, k_e was found to be significantly lower and AUC significantly higher in the single dose animals compared to the animals that received multiple dosing throughout the study ($p \leq 0.01$ for both). These data indicate that cumulative microbubble exposure as well as dosing interval may be important in determining the magnitude of the ABC effect for PEGylated microbubbles.

Table 2.1: Summary of key parameters describing the persistence of house-MBs in circulation from experiment one. Multiple = animals that received a house-MB dose at each time point, Single = animals that received house-MB dosing only on days 0 and 28 of the study, k_e = elimination rate, $t_{1/2}$ = half-life, AUC = area under the curve, House-MB = homemade polyethylene glycol-containing microbubbles, SD = standard deviation. Not significant (ns) $p > 0.05$; * $p \leq 0.05$; ** $p \leq 0.01$; *** $p \leq 0.001$; **** $p \leq 0.0001$

	k_e (min^{-1})		$t_{1/2}$ (min)		AUC (l × min)	
Treatment day	**Avg. ± SD**	**Different from initial?**	**Avg. ± SD**	**Different from initial?**	**Avg. ± SD**	**Different from initial?**
Day 0	0.18 ± 0.02	--	3.8 ± 0.3	--	320 ± 30	--
Day 1	0.17 ± 0.03	No - ns	4.2 ± 0.8	No - ns	370 ± 60	No - ns
Day 2	0.24 ± 0.02	No - ns	3.0 ± 0.3	Yes **	230 ± 30	Yes ***
Day 3	0.32 ± 0.06	No - ns	2.2 ± 0.4	Yes ****	160 ± 40	Yes ****
Day 7	0.4 ± 0.1	Yes **	1.8 ± 0.5	Yes ****	90 ± 30	Yes ****
Day 14	0.8 ± 0.3	Yes ****	0.9 ± 0.2	Yes ****	50 ± 20	Yes ****
Day 28 - Multiple	0.7 ± 0.2	Yes ****	1.0 ± 0.3	Yes ****	50 ± 20	Yes ****
Day 28 - Single	0.42 ± 0.04	Yes *	1.7 ± 0.1	Yes ****	150 ± 20	Yes ****

2.4.2 EXPERIMENT 1 – GENERATION OF A PEG SPECIFIC IMMUNE RESPONSE IN RESPOSE TO HOUSE-MB DOSING

Commercially available ELISA kits were used to compare serum anti-PEG IgM and anti-PEG IgG levels between sham-treated control animals and animals that received either multiple house-MB dosing over 28 d or a single house-MB dose on day 0. As expected, we did not see any changes in anti-PEG IgM levels in sham-treated control animals throughout the study. However, we did see a slight increase in anti-PEG IgG on day 3 in sham control animals (Figure 2.5 A). Since such an elevation in anti-PEG IgG levels was not found in sham control animals at any subsequent time point, we consider the increase on day 3 to be insignificant to the interpretation of this study.

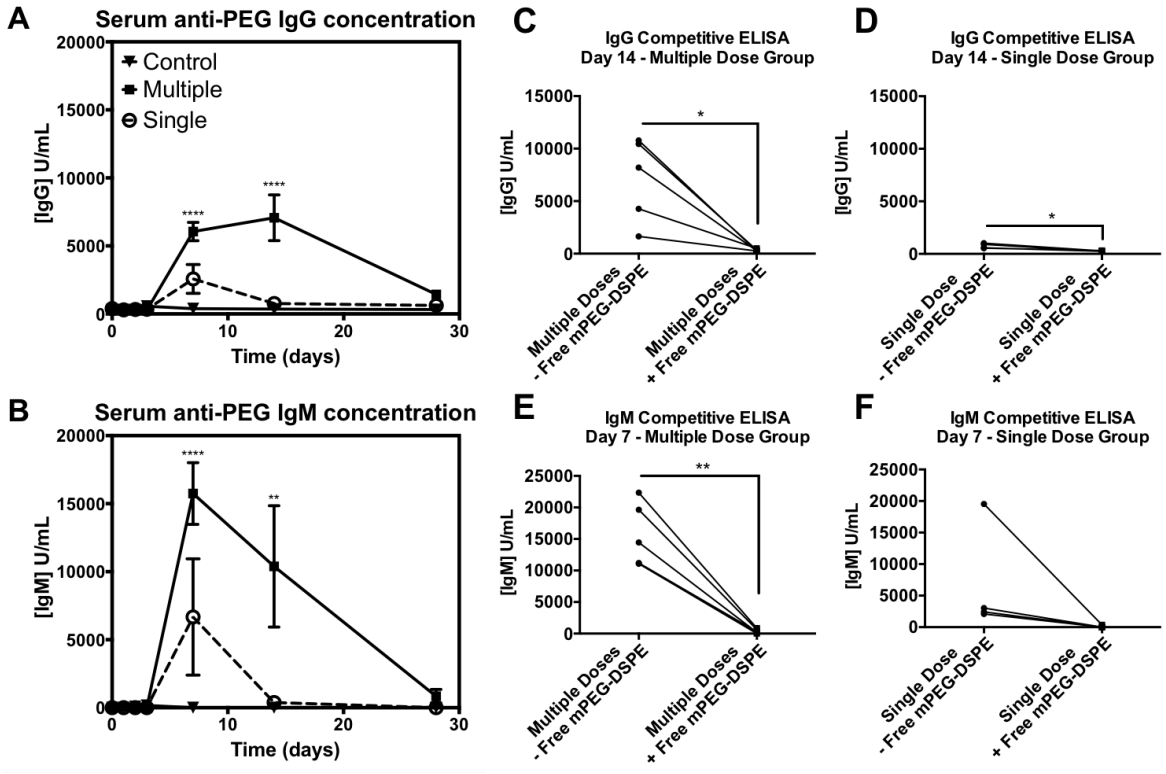

Figure 2.5: Quantification of serum anti-PEG antibody levels and results of a competitive ELISA using free mPEG-DSPE (experiment one). (A) Serum anti-PEG IgG is shown to peak 7-14 days after the initial dose of house-MBs and decrease by the 28-day time point. (B) Serum anti-PEG IgM is shown to peak on day 7 for multiple and single dose groups. Anti-PEG IgM was found to decrease at subsequent time points. C and D) For those samples showing high anti-PEG IgM or anti-PEG IgG antibody expression, a competitive ELISA assay was performed to confirm PEG specificity. IgM and IgG binding to the PEG-coated ELISA plate was shown to decrease substantially when serum was incubated in the presence of free mPEG-DSPE (0.9-0.99 mg/ml). * $p \leq 0.05$; ** $p \leq 0.01$; **** $p \leq 0.0001$. ELISA = enzyme-linked immunosorbent assay, Ig = immunoglobulin, mPEG-DSPE = 1,2,-distearoyl-sn-glycero-3-phosphoethanolamine-N-methoxy(polyethylene-glycol)-2000.

Statistically significant elevations in anti-PEG IgG concentrations were detected on days 7 and 14 in animals that had received multiple microbubble doses (Figure 2.5 A). Anti-PEG IgG peaked in these animals on day 14, and decreased considerably by day 28. As expected, the levels of anti-PEG IgG were lower in the animals that had received a single microbubble dose compared to those that received multiple microbubble doses. Although anti-PEG IgG concentration did not reach statistical significance for animals in the single dose group compared to that of the sham controls, we do note that quantifiable levels of antibody were observed on day 7 (Figure 2.5 A).

Serum anti-PEG IgM concentrations peaked 7 days after the initial microbubble dose for both groups of animals that received microbubbles. In animals that received multiple doses, anti-PEG IgM concentrations were also detected on day 14 but diminished substantially by day 28 (Figure 2.5 B). The elevation in anti-PEG IgM concentration on days 7 and 14 in the multiple dosing group showed statistical significance when compared to the IgM concentration of sham controls at the same time point. Elevation in anti-PEG IgM concentrations did not reach statistical significance at any time point for animals that had received a single microbubble dose; however, detectable levels of antibody were observed on day 7.

To confirm that the detected antibodies were specific for the PEG component of our microbubbles, a competitive ELISA was performed where free mPEG-DSPE was added to compete for antibody binding. Competition was performed on serum samples that showed high antibody expression (i.e., day 7 for anti-PEG IgM and day 14 for anti-PEG IgG). Free mPEG-DSPE competition reduced the detected anti-PEG IgM concentration by 97.4% and 98.7% in the multiple and single dose groups, respectively (Figure 2.5 E-F). Similarly, a 95.3% decrease in apparent anti-PEG IgG concentration was found in the multiple dosing group following free mPEG-DSPE competition (Figure 2.5 C). A lower (64.8%), yet statistically significant, reduction in anti-PEG IgG antibody concentration was found for the single dose group due to the already low antibody levels present without competition (Figure 2.5 D). These data indicate mPEG-DSPE-specificity of the detected IgM and IgG antibodies. Furthermore, we performed additional ELISA assays using plates coated with our microbubble components (DSPC and mPEG-DSPE) instead of the PEG-BSA coated plates provided in the ELISA kit. We observed similar trends in serum IgM and IgG levels using the

plates coated with microbubble components compared to the kit-provided plates. This confirmed the presence of microbubble-specific antibodies in our serum samples (Appendix A.1, Figure A.1).

The time course of initial anti-PEG antibody production coincides with the observed changes in house-MB clearance, both peaking 7-14 days after the initial dose. Furthermore, animals that had received multiple microbubble doses demonstrated a more robust anti-PEG immune response compared to animals receiving a single dose. This corresponds with the more dramatic increase in microbubble clearance for the multiple versus single dose group.

However, we do not see a strong correlation between detected anti-PEG antibody concentration and the rate of microbubble clearance. For example, kinetic parameters describing house-MB clearance are nearly identical on days 14 and 28. Conversely, anti-PEG IgM and anti-PEG IgG levels are considerably greater on day 14 than day 28. We hypothesize that antibody-microbubble binding is not a rate-limiting step in the microbubble clearance pathway and that even on day 28 (when antibody concentrations had declined below the limit of quantification for our ELISA) we have a sufficient molar excess of antibodies to drive maximally accelerated clearance.

Here, we have administered microbubble doses containing approximately 1.0×10^{8} house-MBs resulting in a rat blood concentration of ~1.66×10^{-14} M. Unfortunately, the lower limits of detection of the commercial anti-PEG IgM and anti-PEG IgG ELISA kits used in this study are unknown. However, we note that ELISA assays for anti-PEG antibodies can have lower limits of detection in the range of 2 – 15 ng/mL [26]. This implies that serum antibody concentrations near the detection limits of our assays may correspond to an antibody molar excess of >800 antibodies per microbubble. Thus, antibody concentrations well below our ELISA's probable lower limit of detection would likely be sufficient to induce the accelerated clearance of this dose of microbubbles as immune complexes.

2.4.3 EXPERIMENT 2 – FREE PEG COMPETITION TO RECOVER CIRCULATORY PERSISTENCE OF HOUSE-MBS

A competition experiment was performed to explore the mechanistic connection between anti-PEG antibody generation and accelerated clearance of PEGylated house-MBs. We dosed rats

with house-MBs on days 0, 1, 2, and 3 to induce anti-PEG antibody production and accelerated microbubble clearance. On day 7, we administered free PEG20 kDa at a dose of 550 mpk in hopes of occupying the circulating anti-PEG antibodies. We subsequently administered house-MBs and characterized their circulatory persistence. This competition protocol did not provide recovery of house-MB dwell time compared to control animals that had received a saline injection prior to the house-MB dose. The initial $t_{1/2}$ on day 0 was found to be 8 ± 3 min, whereas Control and Competition groups on day 7 where characterized by $t_{1/2}$ values of 2.5 ± 0.5 min and 2 ± 0.7 min, respectively. ELISA analysis demonstrated high anti-PEG IgM and anti-PEG IgG concentrations before the PEG20 kDa dose (similar to that found on day 7 in experiment 1 (Figure 2.5)), which did not decrease after the PEG20kDa injection (Appendix A.2, Figure A.2). This indicates that a PEG20 kDa dose of 550 mpk was not sufficient to bind a substantial fraction of the high anti-PEG antibody concentration present on day 7, explaining why free PEG competition did not result in prolonged microbubble dwell time. A competitive ELISA experiment confirmed that free PEG20 kDa is able to compete for antibody-plate binding at a concentration of 0.9 mg/ml for both anti-PEG IgG and anti-PEG IgM (Appendix A.2, Figure A.2). This *in vitro* concentration of free PEG would be approximately equal to an *in vivo* free PEG dose of 6,000-15,000 mpk (taking into consideration the 100-250× serum dilution used in the ELISAs and assuming a blood volume of 6.5 ml for a 100 g rat). Therefore, PEG20 kDa would theoretically have been a successful competition agent *in vivo* if administered in at a high enough dose.

From experiment 1, we know that anti-PEG antibody concentrations decrease between days 14 – 28 in our model. Therefore, we repeated the competition experiment using a higher dose of free PEG20 kDa (2,200 mpk) at a later time point (day 24) when the serum anti-PEG antibody concentrations were lower. With the revised competition protocol, we did observe a significant prolongation of house-MB dwell time in animals that received free PEG20 kDa compared to control animals that received a saline injection (Figure 2.6 A). Microbubble elimination kinetics (k_e and $t_{1/2}$) after competition matched that of the initial contrast dose. However, the peak intensity of the competition TIC remained slightly lower than that of the initial TIC (day 0). These observations are displayed quantitatively in terms of k_e, $t_{1/2}$, and AUC in Figure 2.6 B-D.

Without competition, k_e was 3.6× faster on day 24 than on day 0. With free-PEG competition, elimination rate was reduced to a value that was statistically insignificantly different than that seen on day 0. Similarly, half-life recovered to a value that was insignificantly different from the initial value after free PEG competition. AUC did not reach that of the initial TIC, due to the lower initial peak intensity found for the competition curve. However, competition significantly increased AUC compared to that of the control TIC on day 24. Collectively, these data support our hypothesis that anti-PEG antibodies are mechanistically involved in the accelerated clearance of our PEGylated house-MBs.

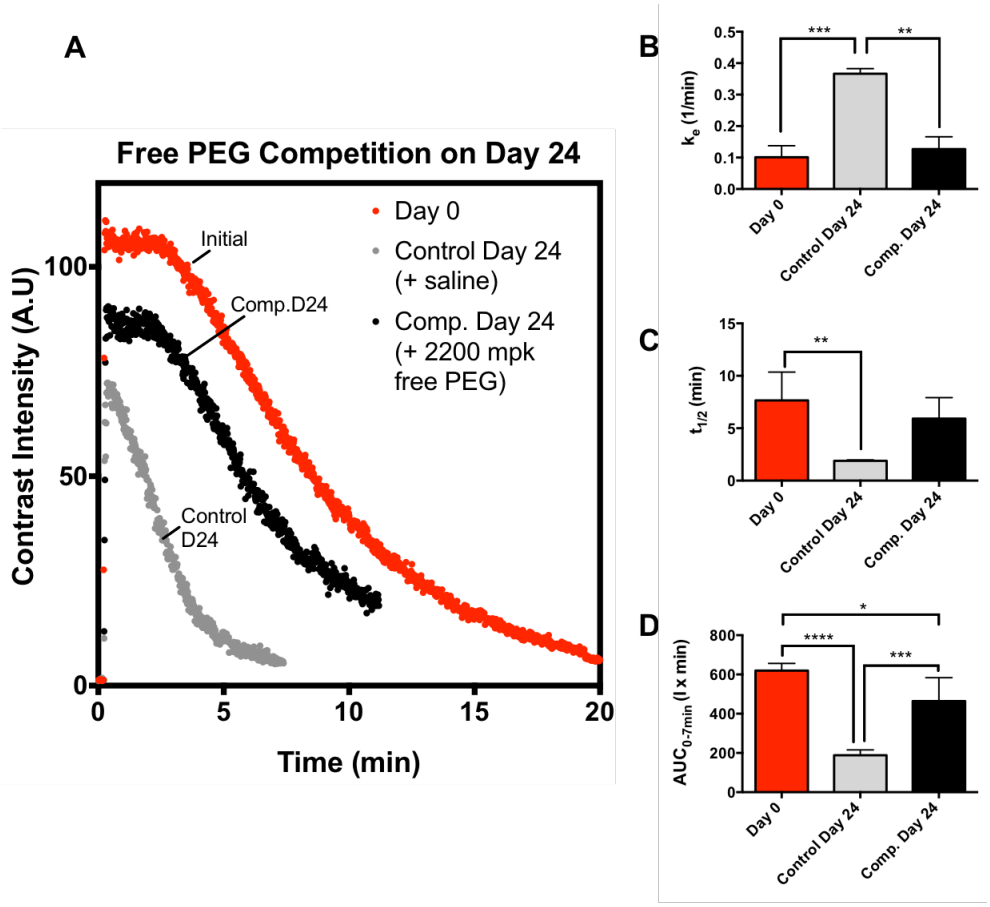

Figure 2.6: Competition with 2,200 mpk free PEG20 kDa prolongs house-MB circulation in animals exhibiting the ABC effect. (A) Initial time intensity curve of house-MBs (red) shows slow clearance compared to that of control animals on day 24 (grey). When animals were pre-dosed with 2,200 mpk free PEG, the microbubble time intensity curve (black) showed a long circulation profile similar to that seen on day 0, indicating successful competition of binding between anti-PEG antibodies and microbubbles. (B-D) After competition on day 24, k_e and $t_{1/2}$ values were not statistically different from their respective initial values. After competition on day 24, AUC was still significantly lower than the initial value, however, competition did significantly increase AUC compared to control animals that received saline injections on day 24. * $p \leq 0.05$; ** $p \leq 0.01$; *** $p \leq 0.001$; **** $p \leq 0.0001$

Our data is consistent with the current literature describing the mechanism of the ABC phenomenon for PEGylated liposomes [25, 47-49]. The binding of IgM or IgG to PEGylated particles is thought to activate the complement system through the classical, antibody-mediated pathway. Such activation leads to particle opsonization by complement proteins, followed by binding/trafficking by erythrocytes (mediated by complement receptor one [46]) or direct accumulation in liver-resident scavenger cells such as liver sinusoidal endothelial cells and Kupffer cells [25]. This mechanism is in line with the data presented throughout this manuscript showing (1) anti-PEG antibody detection coinciding with accelerated microbubble clearance, (2) competition with free PEG resulting in recovered microbubble circulation kinetics, and (3) our observation suggesting the possibility of enhanced microbubble accumulation in the liver following clearance from the blood stream (experiment 1).

2.4.4 EXPERIMENT 3 – CHANGE IN CIRCULATORY PERSISTENCE OF DEFINITY AND OPTISON WITH MULTIPLE DOSING OVER 30 DAYS

FDA-approved Definity microbubbles are stabilized by a PEGylated lipid shell. These microbubbles are similar in composition to our house-MBs, and therefore, we hypothesized that repeat administration of Definity over several weeks would result in anti-PEG antibody production and accelerated clearance. Indeed, we observe a leftward shift in Definity TICs over 30 days (Figure 2.7 A), which corresponded to significant decreases in AUC and $t_{1/2}$ and a significant increase in k_e (Figure 2.8 A-C). A maximum change of 2.1× was found on day 7 for both k_e and $t_{1/2}$. The maximum change in AUC was found on day 14 were AUC was 2.6× lower than the initial value.

The 2.1-2.6× changes in AUC, $t_{1/2}$, and k_e found for Definity are modest compared to the 4-6.5× changes found for our house-MBs when administered with the same dosing schedule. We believe that this discrepancy is due to the relatively faster clearance of Definity at baseline compared to our house-MBs. The half-lives of Definity and house-MBs on day 0 were 2.0 ± 0.3 and 3.8 ± 0.3 min, respectively, but both formulations were characterized by the same minimum half-life of 0.9 min when maximally accelerated clearance was exhibited.

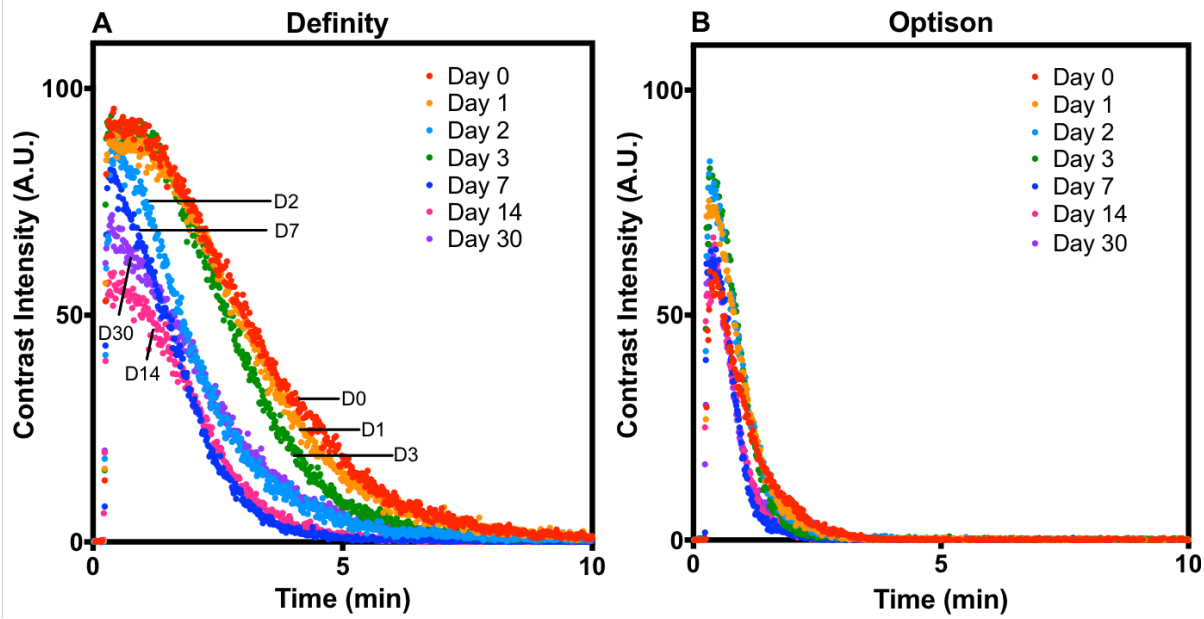

Figure 2.7: Average time intensity curves of commercial microbubbles. (A) Average time intensity curves obtained from animals receiving multiple injections of Definity over 30 days. Curve labels (D0-D30) indicate time in days since the initial dose. (B) Average time intensity curves from animals receiving multiple injections of Optison over 30 days.

Accelerated Definity clearance was associated with the generation of anti-PEG IgM and to a lesser extent anti-PEG IgG (Figure 2.9). Antibody production followed a similar trend to that observed with house-MB dosing. Highest antibody concentrations were observed on day 7, and antibody levels decreased substantially by the study endpoint.

Optison microbubbles are stabilized by a shell of human albumin and do not contain PEG. Therefore, we were hypothesized that this formulation would not undergo PEG-associated accelerated clearance when administered repeatedly over 30 days. Indeed, Optison administration did not result in the generation of anti-PEG antibodies (Figure 2.9). However, we did observe a slight shift in TICs towards the end of the 30-day period (Figure 2.7 B). Optison microbubbles were rapidly cleared at baseline (initial $t_{1/2}$ of 0.5 ± 0.3 min), and $t_{1/2}$ decreased by a modest 1.75× on day 30 (Figure 2.8 E). Similarly, a 1.59× increase in k_e was found on day 30 (Figure 2.8 F). While statistically significant, the experimental relevance of the small changes in Optison $t_{1/2}$ and k_e values warrants further investigation (i.e., Will a decrease in $t_{1/2}$ from 0.5 ± 0.3 min to 0.3 ± 0.1 min change the interpretation of longitudinal contrast enhanced ultrasound studies?). The shift in Optison TICs did not result in a significant change in AUC at any time point (Figure 2.8 D).

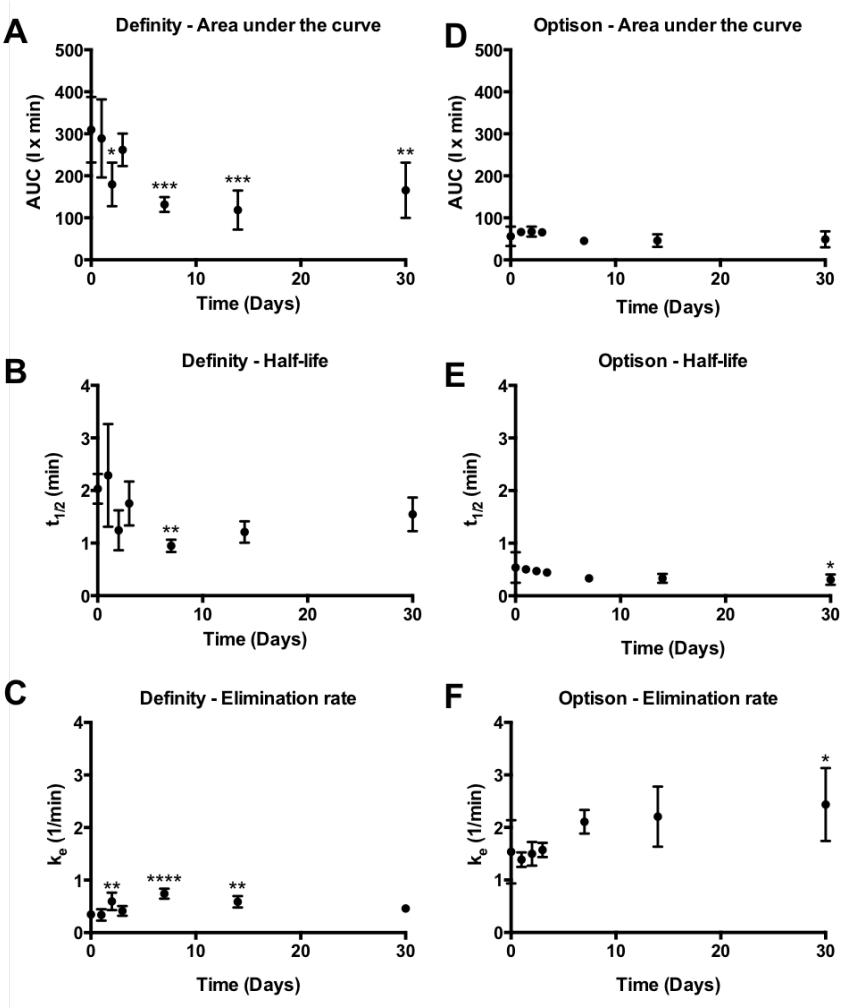

Figure 2.8: Changes in commercial microbubble pharmacokinetic parameters over 30 days of repeat dosing. Change in areas under the curves (A), half-lives (B), elimination rates (C) through time for Definity when administered repeatedly over a 30-day period. Change in areas under the curves (D), half-lives (E), elimination rates (F) through time for Optison when administered repeatedly over a 30-day period. * $p \leq 0.05$; ** $p \leq 0.01$; *** $p \leq 0.001$; **** $p \leq 0.0001$

The shift in Optison TICs suggests that physical or immunological effects beyond anti-PEG immunity may be involved in the accelerated clearance of microbubbles, especially those that are non-PEGylated. Human serum albumin (the shell material of Optison) is immunogenic in rodents [50, 51], and liposomes decorated with foreign albumin molecules (bovine serum albumin or ovalbumin) have been shown to induce anti-albumin antibody generation and accelerated liposome clearance in rodents [52-54]. We hypothesize that the observed shift in Optison TICs during our study is related to an immune response to human albumin in rats or the generation of other opsonizing serum factors in response to the initial microbubble doses. Others have reported that high doses of conventional

liposomes (i.e., liposomes not containing PEG or foreign albumin) induce accelerated clearance of subsequently administered PEGylated liposomes [55]. This indicates that serum factors generated in response to an initial dose of particles may opsonize subsequent particles and trigger accelerated clearance by Kuppfer cells in the liver [55]. The exact mechanism of accelerated clearance in the case of Optison warrants further investigation. However, these results do suggest that the accelerated blood clearance effect is an important consideration for all microbubble formulations, not only those containing PEG.

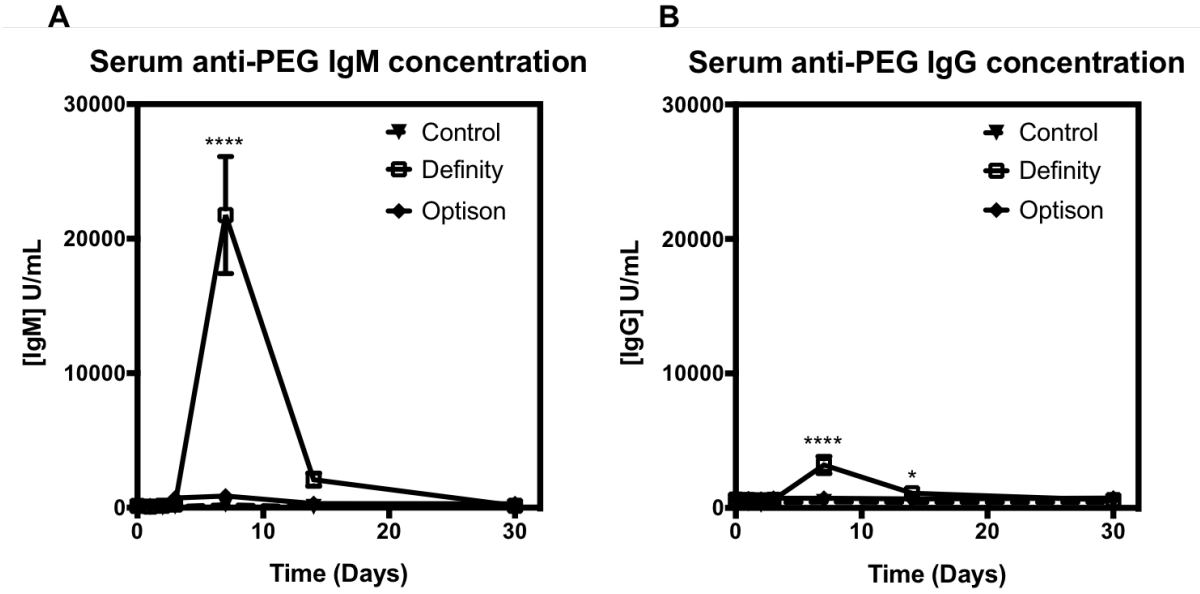

Figure 2.9: Enzyme-linked immunosorbent assay detection of serum anti-PEG antibodies for animals that had received commercial microbubbles. Anti-PEG IgM (A) and anti-PEG IgG (B) antibody levels for animals repeatedly dosed with Definity or Optison over 30 days. PEG = polyethylene glycol; Ig = immunoglobulin

2.4.5 IMPACT FOR CONTRAST-ENHANCED IMAGING

Any ultrasound imaging study that involves the repeated administration of PEGylated microbubbles over multiple days is likely to induce the production of anti-PEG antibodies and result in accelerated microbubble clearance. Furthermore, non-PEGylated microbubbles may induce accelerated clearance through other immunological mechanisms. Acceleration of microbubble clearance may become an important consideration for the interpretation of ultrasound imaging studies

that involve multiple imaging sessions. For example, several reports have demonstrated the potential of ultrasound time intensity curve (TIC) analysis for monitoring tumor response to chemotherapy in human patients [1, 56, 57]. In such studies, TICs (similar to those in Figure 2.3) are generated from images of a tumor region periodically throughout the course of treatment. Changes in TIC features are then correlated with therapeutic outcome. In this example, it is critical that changes in the TICs are due to changes in tumor physiology (e.g., decreased vascularization) and not due to fundamental antibody-mediated alterations in the microbubble clearance.

The field of ultrasound molecular imaging (UMI) may also be affected if accelerated clearance is realized for targeted microbubbles. UMI can be used to interrogate disease- or tissue-specific targets and has applications in diagnosis [58-61], evaluation of tumor biomarker expression [62-65], and monitoring treatment response [66, 67]. Regardless of application, molecular imaging is often repeated on multiple days and changes in microbubble binding are assumed to reflect physiological changes in target/receptor expression rather than altered pharmacokinetics of the microbubbles themselves. Accelerated microbubble clearance will likely be correlated with reduced microbubble binding, which should be considered when interpreting the results of UMI studies. Indeed, there is one report of accelerated microbubble clearance being associated with reduced target binding in UMI [36].

It is also important to consider the presence of pre-existing anti-PEG antibodies in human patients. A recent study has found low levels of pre-existing anti-PEG antibodies in over 70% of the general human population (i.e., individuals not previously exposed to PEGylated therapeutics) [26]. While reported mean anti-PEG IgG and anti-PEG IgM concentrations were only 52 ng/mL and 22 ng/mL, respectively, these antibody concentrations may be sufficient to influence the circulation kinetics of PEGylated microbubbles. For example, the recommended dose of Definity provides an approximate blood concentration of ~2.6×10^{-15} M particles to an 80 kg patient. In the same example patient, the reported average anti-PEG IgM and anti-PEG IgG concentrations would equate to approximate molar excesses of 5,000× and 74,000×, respectively (assuming a plasma volume of 3.4 L, IgM molecular weight of 950 kDa, and IgG molecular weight of 150 kDa). The concentration of anti-PEG antibodies required for inducing clinically significant changes in the pharmacokinetics of

PEGylated agents remains undetermined. However, the potential influence of low-level, pre-existing anti-PEG antibodies on contrast-enhanced ultrasound imaging studies warrants consideration and further exploration.

Finally, the safety implications of anti-PEG antibodies (pre-existing or generated in response to an initial microbubble dose) are important to consider with the clinical use of PEGylated ultrasound contrast agents. Previous research regarding PEGylated protein therapies demonstrates that circulating anti-PEG antibodies increase the risk of injection reactions in human patients [34, 35]. Although the reported incidence of adverse effects following administration of microbubble contrast agents is minute and is often reported as less than other contrast agent types [68, 69], clinicians should be aware of this risk when administering PEGylated microbubbles to patients who have suspected hypersensitivity to PEGylated microbubbles or therapeutics. This will require increased awareness of anti-PEG antibodies among relevant physician subsets. A recent study of physicians who prescribe PEGylated therapeutics found that only one quarter of prescribers were aware of anti-PEG antibodies [70].

2.5 CONCLUSIONS

We have demonstrated that the circulatory kinetics of homemade PEGylated microbubbles change dramatically when administered repeatedly over a one-month period in otherwise untreated animals. PEGylated microbubbles appear to be subject to the same ‘accelerated blood clearance (ABC) phenomenon’ observed following the repeated administration of PEGylated proteins and liposomes. Here we show that the magnitude of accelerated microbubble clearance is related to cumulative microbubble exposure. Microbubble clearance at the study endpoint was faster for those animals that had received 6 prior doses of house-MBs compared to those animals that had only received one prior dose. Furthermore, we detected both anti-PEG IgM and anti-PEG IgG antibodies in all animals that received house-MBs. Once the ABC response had been mounted, dosing animals with free-PEG as a competition agent prior to house-MB administration resulted in recovery of microbubble intravascular dwell time. Therefore, we conclude that the accelerated clearance of PEGylated microbubbles is significantly related to an anti-PEG immune response. Similar trends in

accelerated clearance and generation of anti-PEG antibodies were also observed with commercial Definity microbubbles. Interestingly, studies repeated with Optison also illustrated as slight change in clearance rate, which was necessarily independent from PEG-related immunity. We hypothesize that clearance changes in repeatedly administered Optison may have been associated with immunogenicity of the human albumin shell in rats.

In conclusion, it is important to understand the immunogenicity of microbubble shell materials and how this may impact microbubble circulation kinetics during contrast-enhanced ultrasound imaging studies that involve multiple microbubble doses over several days to weeks. Any changes in microbubble circulation driven by anti-PEG or other immune responses should be considered when interpreting the results of longitudinal contrast-enhanced imaging results.

REFERENCES

1. Schirin-Sokhan, R., et al., *Response evaluation of chemotherapy in metastatic colorectal cancer by contrast enhanced ultrasound.* World J Gastroenterol, 2012. **18**(6): p. 541-5.

2. Kasoji, S.K., et al., *Early Assessment of Tumor Response to Radiation Therapy using High-Resolution Quantitative Microvascular Ultrasound Imaging.* Theranostics, 2018. **8**(1): p. 156-168.

3. Dimcevski, G., et al., *A human clinical trial using ultrasound and microbubbles to enhance gemcitabine treatment of inoperable pancreatic cancer.* J Control Release, 2016. **243**: p. 172-181.

4. Salmaso, S. and P. Caliceti, *Stealth properties to improve therapeutic efficacy of drug nanocarriers.* J Drug Deliv, 2013. **2013**: p. 374252.

5. Butcher, N.J., G.M. Mortimer, and R.F. Minchin, *Drug delivery: Unravelling the stealth effect.* Nat Nanotechnol, 2016. **11**(4): p. 310-1.

6. Hirotsu, T., et al., *Self-Assembly PEGylation Retaining Activity (SPRA) Technology via a Host-Guest Interaction Surpassing Conventional PEGylation Methods of Proteins.* Mol Pharm, 2017.

7. Liu, Z., et al., *In vivo anti-tumor activity of polypeptide HM-3 modified by different polyethylene glycols (PEG).* Int J Mol Sci, 2011. **12**(4): p. 2650-63.

8. Nie, Q., et al., *Conjugation to 10 kDa Linear PEG Extends Serum Half-Life and Preserves the Receptor-Binding Ability of mmTRAIL with Minimal Stimulation of PEG-Specific Antibodies.* Mol Pharm, 2017.

9. Haynes, M.T. and L. Huang, *Maximizing the Supported Bilayer Phenomenon: Liposomes Comprised Exclusively of PEGylated Phospholipids for Enhanced Systemic and Lymphatic Delivery.* ACS Appl Mater Interfaces, 2016. **8**(37): p. 24361-7.

10. Liu, D., et al., *Preparation and in vivo safety evaluations of antileukemic homoharringtonine-loaded PEGylated liposomes.* Drug Dev Ind Pharm, 2017: p. 1-9.

11. Garg, S., A.A. Thomas, and M.A. Borden, *The effect of lipid monolayer in-plane rigidity on in vivo microbubble circulation persistence.* Biomaterials, 2013. **34**(28): p. 6862-70.

12. Malinge, J., et al., *Liposomes for PET and MR Imaging and for Dual Targeting (Magnetic Field/Glucose Moiety): Synthesis, Properties, and in Vivo Studies.* Mol Pharm, 2017.

13. Zhou, B., et al., *PEGylated polyethylenimine-entrapped gold nanoparticles loaded with gadolinium for dual-mode CT/MR imaging applications.* Nanomedicine (Lond), 2016. **11**(13): p. 1639-52.

14. Borden, M.A., et al., *Ultrasound radiation force modulates ligand availability on targeted contrast agents.* Mol Imaging, 2006. **5**(3): p. 139-47.

15. Appis, A.W., M.J. Tracy, and S.B. Feinstein, *Update on the safety and efficacy of commercial ultrasound contrast agents in cardiac applications.* Echo Res Pract, 2015. **2**(2): p. R55-62.

16. Marchal, S., et al., *Anticancer Drug Delivery: An Update on Clinically Applied Nanotherapeutics.* Drugs, 2015. **75**(14): p. 1601-11.

17. Martin, K.H. and P.A. Dayton, *Current Status and Prospects for Microbubbles in Ultrasound Theranostics.* Wiley interdisciplinary reviews. Nanomedicine and nanobiotechnology, 2013. **5**(4): p. 10.1002/wnan.1219.

18. Abou-Saleh, R.H., et al., *Poly(ethylene glycol) lipid-shelled microbubbles: abundance, stability, and mechanical properties.* Langmuir, 2014. **30**(19): p. 5557-63.

19. Borden, M.A., et al., *Surface phase behavior and microstructure of lipid/PEG-emulsifier monolayer-coated microbubbles.* Colloids Surf B Biointerfaces, 2004. **35**(3-4): p. 209-23.

20. Paefgen, V., D. Doleschel, and F. Kiessling, *Evolution of contrast agents for ultrasound imaging and ultrasound-mediated drug delivery.* Front Pharmacol, 2015. **6**.

21. LUMASON®, *[package insert]. Bracco Diagnostics Inc., Monroe Twp., NJ. 2014.*

22. DEFINITY®, *[package insert]. Lantheus Medical Imaging, Inc. North Billerica, MA. October, 2011.* .

23. OPTISON™. *[package insert]. GE Healthcare Inc., Princeton, NJ. May 2012*. November 24, 2017]; Available from: https://www.accessdata.fda.gov/drugsatfda_docs/label/2012/020899s015lbl.pdf.

24. Abu Lila, A.S., H. Kiwada, and T. Ishida, *The accelerated blood clearance (ABC) phenomenon: clinical challenge and approaches to manage.* J Control Release, 2013. **172**(1): p. 38-47.

25. Yang, Q. and S.K. Lai, *Anti-PEG immunity: emergence, characteristics, and unaddressed questions.* Wiley Interdiscip Rev Nanomed Nanobiotechnol, 2015. **7**(5): p. 655-77.

26. Yang, Q., et al., *Analysis of pre-existing IgG and IgM antibodies against polyethylene glycol (PEG) in the general population.* Anal Chem, 2016.

27. Dams, E.T., et al., *Accelerated blood clearance and altered biodistribution of repeated injections of sterically stabilized liposomes.* J Pharmacol Exp Ther, 2000. **292**(3): p. 1071-9.

28. Kaminskas, L.M., et al., *Differences in colloidal structure of PEGylated nanomaterials dictate the likelihood of accelerated blood clearance.* J Pharm Sci, 2011. **100**(11): p. 5069-77.

29. Suzuki, T., et al., *Accelerated blood clearance of PEGylated liposomes containing doxorubicin upon repeated administration to dogs.* Int J Pharm, 2012. **436**(1-2): p. 636-43.

30. Sroda, K., et al., *Repeated injections of PEG-PE liposomes generate anti-PEG antibodies.* Cell Mol Biol Lett, 2005. **10**(1): p. 37-47.

31. Xu, H., et al., *Influence of phospholipid types and animal models on the accelerated blood clearance phenomenon of PEGylated liposomes upon repeated injection.* Drug Deliv, 2015. **22**(5): p. 598-607.

32. Zhang, C., et al., *Impact of large aggregated uricases and PEG diol on accelerated blood clearance of PEGylated canine uricase.* PLoS One, 2012. **7**(6): p. e39659.

33. Armstrong, J.K., et al., *Antibody against poly(ethylene glycol) adversely affects PEG-asparaginase therapy in acute lymphoblastic leukemia patients.* Cancer, 2007. **110**(1): p. 103-11.

34. Ganson, N.J., et al., *Control of hyperuricemia in subjects with refractory gout, and induction of antibody against poly(ethylene glycol) (PEG), in a phase I trial of subcutaneous PEGylated urate oxidase.* Arthritis Research & Therapy, 2006. **8**(1): p. R12-R12.

35. Hershfield, M.S., et al., *Induced and pre-existing anti-polyethylene glycol antibody in a trial of every 3-week dosing of pegloticase for refractory gout, including in organ transplant recipients.* Arthritis Res Ther, 2014. **16**(2): p. R63.

36. Zhang, H., et al., *Ultrasound molecular imaging of tumor angiogenesis with a neuropilin-1-targeted microbubble.* Biomaterials, 2015. **56**: p. 104-113.

37. Marshalek, J.P., et al., *Intracellular delivery and ultrasonic activation of folate receptor-targeted phase-change contrast agents in breast cancer cells in vitro.* Journal of Controlled Release, 2016. **243**: p. 69-77.

38. Tartis, M.S., et al., *Dynamic microPET imaging of ultrasound contrast agents and lipid delivery.* Journal of controlled release : official journal of the Controlled Release Society, 2008. **131**(3): p. 160-166.

39. Walday, P., et al., *Biodistributions of air-filled albumin microspheres in rats and pigs.* Biochemical Journal, 1994. **299**(Pt 2): p. 437-443.

40. Chen, C.C., S.R. Sirsi, and M.A. Borden, *EFFECT OF SURFACE ARCHITECTURE ON IN VIVO ULTRASOUND CONTRAST PERSISTENCE OF TARGETED SIZE-SELECTED MICROBUBBLES.* Ultrasound in medicine & biology, 2012. **38**(3): p. 492-503.

41. Ganesan, L.P., et al., *FcgammaRIIb on liver sinusoidal endothelium clears small immune complexes.* J Immunol, 2012. **189**(10): p. 4981-8.

42. Jenne, C.N. and P. Kubes, *Immune surveillance by the liver.* Nat Immunol, 2013. **14**(10): p. 996-1006.

43. Steffan, A.M., et al., *Phagocytosis, an unrecognized property of murine endothelial liver cells.* Hepatology, 1986. **6**(5): p. 830-6.

44. Yanagisawa, K., et al., *Phagocytosis of ultrasound contrast agent microbubbles by Kupffer cells.* Ultrasound Med Biol, 2007. **33**(2): p. 318-25.

45. Iijima, H., et al., *Ultrasound contrast agent, Levovist microbubbles are phagocytosed by Kupffer cells-In vitro and in vivo studies.* Hepatol Res, 2006. **35**(4): p. 235-7.

46. Pascual, M. and J.A. Schifferli, *Another function of erythrocytes: transport of circulating immune complexes.* Infusionsther Transfusionsmed, 1995. **22**(5): p. 310-5.

47. Ishida, T., et al., *Spleen plays an important role in the induction of accelerated blood clearance of PEGylated liposomes.* Journal of Controlled Release, 2006. **115**(3): p. 243-250.

48. Ishida, T. and H. Kiwada, *Accelerated blood clearance (ABC) phenomenon upon repeated injection of PEGylated liposomes.* International Journal of Pharmaceutics, 2008. **354**(1–2): p. 56-62.

49. Kawanishi, M., et al., *Comprehensive analysis of PEGylated liposome-associated proteins relating to the accelerated blood clearance phenomenon by combination with shotgun analysis and conventional methods.* Biotechnol Appl Biochem, 2015. **62**(4): p. 547-55.

50. Britton, S. and F. Celada, *Immunogenicity of human serum albumin: decay in the normal mouse.* Immunology, 1968. **14**(4): p. 503-9.

51. Dahlman-Höglund, A., et al., *Bystander suppression of the immune response to human serum albumin in rats fed ovalbumin.* Immunology, 1995. **86**(1): p. 128-133.

52. Shek, P.N. and T.D. Heath, *Immune response mediated by liposome-associated protein antigens. III. Immunogenicity of bovine serum albumin covalently coupled to vesicle surface.* Immunology, 1983. **50**(1): p. 101-6.

53. Shek, P.N., N.G. Lopez, and T.D. Heath, *Immune response mediated by liposome-associated protein antigens. IV. Modulation of antibody formation by vesicle-encapsulated methotrexate.* Immunology, 1986. **57**(1): p. 153-7.

54. Tardi, P.G., et al., *An immune response to ovalbumin covalently coupled to liposomes is prevented when the liposomes used contain doxorubicin.* J Immunol Methods, 1997. **210**(2): p. 137-48.

55. Ishida, T., et al., *Accelerated blood clearance of PEGylated liposomes following preceding liposome injection: effects of lipid dose and PEG surface-density and chain length of the first-dose liposomes.* J Control Release, 2005. **105**(3): p. 305-17.

56. Lassau, N., et al., *Metastatic renal cell carcinoma treated with sunitinib: early evaluation of treatment response using dynamic contrast-enhanced ultrasonography.* Clin Cancer Res, 2010. **16**(4): p. 1216-25.

57. Ueda, N., et al., *Contrast-Enhanced Ultrasonography in Evaluation of the Therapeutic Effect of Chemotherapy for Patients with Liver Metastases.* Yonago Acta Med, 2016. **59**(4): p. 255-261.

58. McCarty, O.J., et al., *Molecular imaging of activated von Willebrand factor to detect high-risk atherosclerotic phenotype.* JACC Cardiovasc Imaging, 2010. **3**(9): p. 947-55.

59. Dayton, P.A. and K.W. Ferrara, *Targeted imaging using ultrasound.* J Magn Reson Imaging, 2002. **16**(4): p. 362-77.

60. Davidson, B.P., et al., *Ischemic memory imaging in nonhuman primates with echocardiographic molecular imaging of selectin expression.* J Am Soc Echocardiogr, 2014. **27**(7): p. 786-793 e2.

61. Machtaler, S., et al., *Assessment of Inflammation in an Acute on Chronic Model of Inflammatory Bowel Disease with Ultrasound Molecular Imaging.* Theranostics, 2015. **5**(11): p. 1175-86.

62. Shelton, S.E., et al., *Molecular Acoustic Angiography: A New Technique for High-resolution Superharmonic Ultrasound Molecular Imaging.* Ultrasound Med Biol, 2016. **42**(3): p. 769-81.

63. Lindsey, B.D., et al., *Assessment of Molecular Acoustic Angiography for Combined Microvascular and Molecular Imaging in Preclinical Tumor Models.* Mol Imaging Biol, 2016.

64. Spivak, I., et al., *Low-Dose Molecular Ultrasound Imaging with E-Selectin-Targeted PBCA Microbubbles.* Mol Imaging Biol, 2016. **18**(2): p. 180-90.

65. Zhang, H., et al., *Ultrasound molecular imaging of tumor angiogenesis with a neuropilin-1-targeted microbubble.* Biomaterials, 2015. **56**: p. 104-13.

66. Palmowski, M., et al., *Molecular profiling of angiogenesis with targeted ultrasound imaging: early assessment of antiangiogenic therapy effects.* Mol Cancer Ther, 2008. **7**(1): p. 101-9.

67. Streeter, J.E., et al., *A comparative evaluation of ultrasound molecular imaging, perfusion imaging, and volume measurements in evaluating response to therapy in patient-derived xenografts.* Technol Cancer Res Treat, 2013. **12**(4): p. 311-21.

68. Abdelmoneim, S.S., et al., *Safety of contrast agent use during stress echocardiography: a 4-year experience from a single-center cohort study of 26,774 patients.* JACC Cardiovasc Imaging, 2009. **2**(9): p. 1048-56.

69. Caschera, L., et al., *Contrast agents in diagnostic imaging: Present and future.* Pharmacol Res, 2016. **110**: p. 65-75.

70. McSweeney, M.D., et al., *Physician Awareness of Immune Responses to Polyethylene Glycol-Drug Conjugates.* Clinical and Translational Science: p. n/a-n/a.

CHAPTER 3[1]

THERAPEUTIC GAS DELIVERY VIA MICROBUBBLES AND LIPOSOMES

3.1 MOTIVATION AND OVERVIEW

In general, therapeutic gases have physiochemical characteristics drastically different from those of classic small molecule drugs, offering unique therapeutic advantages and challenges. For instance, these gases are far smaller than classic drugs and are able to easily diffuse across membranes and through the blood brain barrier. Gases are rapidly excreted via expiration, which reduces toxicity and bioaccumulation concerns compared to classic drugs. A major hurdle, however, is the controlled and site-specific delivery of gases. This chapter provides a comprehensive overview of how ultrasound contrast agents (microbubbles and echogenic liposomes) can be adapted to address this unique delivery challenge. In particular, the delivery of oxygen (O_2), nitric oxide (NO), and xenon (Xe) will be reviewed.

3.2 BACKGROUND

3.2.1 OXYGEN: THERAPEUTIC POTENTIAL IN THE REVERSAL OF OXYGEN DEPLETION

It is estimated that at least 50-60% of advanced solid tumors contain hypoxic or anoxic tissue, typically due to irregularities in the tumor microcirculation [1]. Tumor hypoxia is associated with a number of adverse effects, including resistance to chemotherapy and radiation treatment and an increased risk of metastasis. Correspondingly, tumor hypoxia leads to poor prognosis in cancer

[1]This chapter previously appeared as an article in the Journal of Controlled Release. The original citation is as follows: Fix, S. M., Borden, M.A., Dayton, P.A. (2015). "Therapeutic gas delivery via microbubbles and liposomes." J Control Release **209**: 139-149.

patients. For example, pancreatic cancer, which is characterized by poorly vascularized tumors, is one of the deadliest human cancers, with a five-year survival rate of less than 6% [2].

Several approaches have been tested in effort to exploit reoxygenation for radiosensitizing hypoxic tumors. Early work involved combining hyperbaric oxygenation with radiation. This approach improved five-year survival rates, but also produced toxicity in healthy tissue [3]. Additional studies have investigated increasing red blood cell count to increase O_2 carrying capacity of blood and therefore increase pO_2 levels in tumors. This approach provided no benefit to head and neck cancer patients [4]. To date, there are no clinically approved methods for increasing tumor oxygen levels for radiosensitzation.

Hypoxemia often presents in cases of severe lung injury, airway obstruction, and acute respiratory distress syndrome, and is associated with increased mortality rates in these patients [5]. Severe hypoxemia is often treated with inspired oxygen, intubation, and mechanical ventilation, however if adequate re-oxygenation is not rapidly achieved, cardiac arrest, organ damage, and death may ensue [6]. In cases of acute blood loss, there is a drastic decrease in systemic oxygen supply and there is a need to restore oxygen delivery to tissues. For this purpose, significant efforts have been made towards developing artificial blood substitutes. These are typically perfluorocarbon emulsions or hemoglobin-based oxygen carriers [7, 8]. These systems are designed to scavenge oxygen in the high O_2 environment of the lungs and release O_2 content in hypoxic regions, repeating this process as they persist in circulation. A disadvantage of these oxygen delivery platforms is that they require an intact pulmonary function and may not be useful in cases of severe lung injury or airway obstruction.

3.2.2 NITRIC OXIDE: EXPLOITATION OF SECOND MESSENGER EFFECTS FOR THERAPEUTIC PURPOSES

In 1980, it was discovered that relaxation of vascular smooth muscle cells in response to acetylcholine is dependent on an intact endothelium. Furchgott and Zawadzki defined the molecule responsible ‘endothelium-derived relaxing factor’ (EDRF) [9]. Several years later, in the late ‘80s, it was shown that EDRF is nitric oxide (NO) [10, 11]. This discovery sparked intensive research

regarding the biological roles of this molecule. It is now known that NO is synthesized endogenously from L-arginine by NO synthases (NOS) of which there are three isoforms: inducible NOS (iNOS), endothelial NOS (eNOS), and neuronal NOS (nNOS) [12].

NO mediates pleiotropic physiological processes through complex and coordinated interactions with multiple cellular targets. NO plays a critical role in the vascular physiology and the cardiovascular system, acting as a vasodilator and inhibiting platelet aggregation [13, 14]. NO mediates vascular remodeling, and deficits in NOS/NO pathways may be involved the development of hypertension and atherosclerosis [15].

NO signaling plays an important role in the central nervous system. It mediates cerebral blood flow, provides neuroprotection, and influences pathophysiological processes post-brain injury [16]. Cerebral NO synthesized in various concentrations and locations elicit diverse and sometimes opposing effects. For example, eNOS-derived NO provides neuroprotection following injury. Whereas, NO derived from iNOS has been shown to exacerbate neuronal injury [16].

The role of NO in cancer biology exemplifies another dichotomy in NO signaling. At low concentrations NO may promote tumor cell growth by stimulating angiogenesis while at high concentrations, NO is cytotoxic and may be a useful chemotherapeutic agent [17].

NO holds therapeutic potential for many conditions including atherosclerosis, hypertension, stroke and cancer. However, the concentration and tissue dependence of response is a challenge and presents risk of side effects. Current approaches to deliver NO include inhalation, intravenous or oral delivery of prodrugs, and the administration of spontaneously releasing chemical donors, among others [18]. There is an extensive body of research surrounding the therapeutic exploitation of endogenous gases; for a comprehensive review of clinical and preclinical investigations readers are referred to Szabo and Abraham [18].

3.2.3 XENON: THERAPEUTIC BIOLOGICAL EFFECTS DESPITE CHEMICAL INERTNESS

Xenon, among other noble gases, elicits significant biological effects. Xenon induces anesthesia through inhibition of *N*-methyl-D-aspartate (NMDA) receptor signaling and is thought to exert analgesic effects through the same mechanism. Following traumatic brain injury or stroke, over-

activation of NMDA receptors triggers biochemical cascades resulting in neuronal death and sustained injury [19]. By inhibiting the NMDA pathway, xenon also provides neuroprotection [20]. Xenon shows promise as a medical gas with potential applications in neuroprotection against stroke or traumatic brain injury and cardioprotection for patients with myocardial infarction. However, adequate delivery is a major hurdle for its clinical translation. The main route of administration currently employed for *in vivo* studies is via inhalation. For noticeable neuroprotective effects, Xe must be inhaled at concentrations of 50-70%, which would critically limit the fraction of inspired oxygen and lead to hypoxic tissue damage [21].

3.3 MICROBUBBLES AND LIPOSOMES FOR THERAPEUTIC GAS DELIVERY

3.3.1 PROTECTION FROM ENDOGENOUS SCAVENGERS

The bubble or liposomal shell protects the contained gas from endogenous scavengers. This feature is particularly attractive for the delivery of NO, which rapidly reacts with hemoglobin (reaction rate of $3\text{-}5\times10^{7}\ M^{-1}s^{-1}$) and consequently has a short half-life in circulation [22]. The particle shell protects NO from scavenging until NO is released (passively or actively via ultrasound stimulation). However, once NO is released it must travel to the target site (i.e., endothelium) prior to being consumed by red blood cells (RBCs). There is a RBC-free zone near the endothelium within vessels where NO is able to persist without being consumed by RBCs [22]. According to calculations by Postema et al., targeting NO release in the RBC-free layer may enhance the effectiveness of NO therapy [23]. This may be accomplished by targeting the NO-containing particle to the endothelium using ligands or antibodies or by exploiting acoustic radiation force to push the particles into the RBC-free zone. This will be discussed in more detail later in this chapter.

3.3.2 DIFFERENCES BETWEEN MICROBUBBLES AND ECHOGENIC LIPOSOMES

An important difference between microbubbles and liposomes is their gas loading capacity. Microbubbles comprise a solid gas core and offer a high loading capacity. Conversely, liposomes can only carry approximately 10% gas by volume [24]. This low loading capacity is sufficient when

delivering potent bioactive gases, such as NO and Xe. However, liposomes are not suitable for the delivery of O_2, which is typically required in high concentrations for a therapeutic effect.

The second important difference between MBs and ELIPs is their size and their potential to extravasate. In healthy blood vessels, inter-endothelial pores are approximately 6.5-7.5 nm [25]. Tumor vasculature is typically characterized by large pore sizes with upper limits between 380-780 nm. This allows for enhanced permeability and retention of large molecules within tumors [26]. Therapeutic microbubbles are typically 1-4 μm in diameter and are therefore unable to extravasate from either healthy or leaky tumor vasculature. This would be a limitation when using microbubbles in situations where tissue penetration is required for a therapeutic effect. In general, liposomes can be fabricated on the nanoscale and have been shown to preferentially extravasate into tumor tissue [26, 27]. However, loading gas into liposomes increases their size. The ELIPs presented here have average sizes ranging from 800 nm to several microns. These particles are on average smaller than microbubbles but still may be too large to extravasate from tumor vasculature. However, it may be possible to reduce the size these liposomes; liposomes loaded with non-therapeutic gases have been fabricated with particle sizes between 400-600 nm [28, 29].

3.3.3 AN OPPORTUNITY FOR TARGETED DELIVERY

The microbubble shell provides mechanical stability for the particle and enables persistence of the bubble in circulation. Lipids, which form a monolayer around the gas core, are a popular choice of shell material, Figure 3.1 A. The internal structure of ELIPs is not well established. One hypothesis is that lipid-monolayer stabilized pockets of gas are contained within the liposome core [30, 31]. Alternatively, gas may form pockets within the lipid bilayer, as in Figure 3.1 B [30, 31]. Bubbles and liposomes are commonly stabilized by the addition of a hydrophilic polymer brush layer (i.e., PEG). PEG stabilizes micro- and nanoparticles by introducing steric repulsion between individual particles (reducing coalescence) and between particles and cells (reducing particle uptake by macrophages).

The shells of both MBs and ELIPs may be functionalized with targeting moieties including peptides, carbohydrates, vitamins, or antibodies. For details regarding various covalent and non-covalent coupling chemistries, readers are referred to a review by Sunil Unnikrishnan et al. [32].

Targeting molecules may be conjugated to the particle shell before or after particle formation. When attaching targeting moieties prior to particle formation, the targeting molecule is synthetically attached to a subset of the shell forming subunits and the bubbles or liposomes are then prepared as usual. The targeting molecule can either be conjugated directly to the surface of the bubble or liposome [33, 34], or to a PEG spacer (Figure 3.2 A) [35, 36]. The presence of a stabilizing PEG brush layer reduces the efficiency by which ligands attached directly to the particle surface are able to bind their target [37]. For successful adhesion, it is important for the ligand to be attached to a PEG spacer longer than the equilibrium height of the stabilizing polymer layer [38, 39].

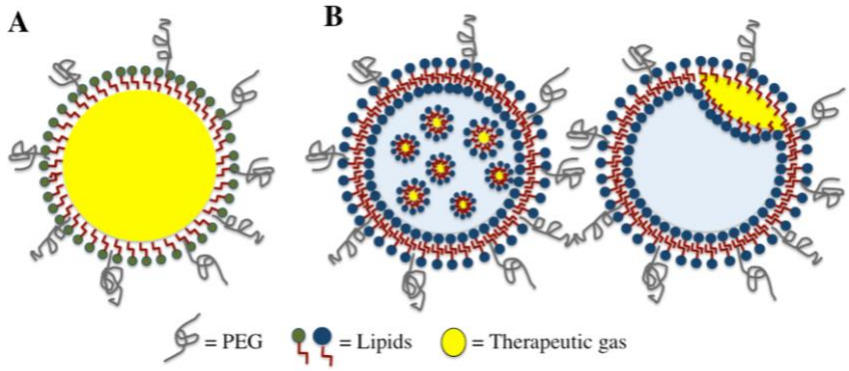

Figure 3.1: Therapeutic gas-filled microbubbles and liposomes. A) Cartoon of a microbubble stabilized by of lipid monolayer and a polymer brush layer. B) Hypothesized structures ELIPs are presented. Pockets of lipid monolayer-stabilized therapeutic gas may be encapsulated in the liposome core. Alternatively, gas pockets may form within the lipid bilayer.

Antibodies (Ab) and proteins may be sensitive to harsh particle fabrication conditions including exposure to organic solvents, vigorous mixing, elevated temperatures and shear stress. Proteins can denature when in close proximity to gases [40], which poses an additional challenge for MB and ELIP targeting. In these situations, the targeting moiety can be linked to the particle surface post-formation using a number of techniques. Demos et al. describes a method to covalently link echogenic liposomes and antibodies via thioester bonds [41, 42]. Biotin-avidin linkages are also commonly used; biotinylated bubbles or liposomes may be linked to a biotinylated antibody though an avidin bridge, as in Figure 3.2 B [43]. Alternatively, Klegerman et al. demonstrated that biotin/avidin technology can be used to form aggregates of therapeutic ELIPs and targeted liposomes. The authors found that the echogenicity of their NO-loaded particles and the targeting capabilities of the

Ab-conjugated particles were conserved upon aggregation [44]. While using biotin-avidin linkages is a powerful technique for pre-clinical studies, immunogenicity prevents its translation to humans.

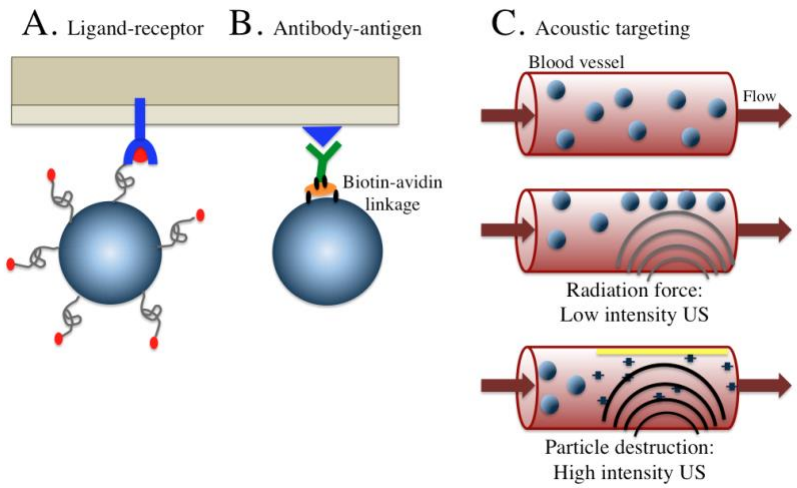

Figure 3.2: Targeting methods. A) Microbubble or liposome targeted to the receptor surface with a ligand covalently attached to a PEG spacer. B) Microbubble or liposome targeted to the receptor surface with an antibody conjugated through a biotin-avidin bridge. C) Depiction of acoustic radiation force pushing microbubbles or liposomes to the vessel wall. Ultrasound may be used to fragment the particles, releasing the therapeutic gas (yellow) in the RBC-free zone near the vessel wall.

Ultrasound may be used to target the release of a therapeutic gas in a specific area via MB or ELIP destruction at high mechanical index. Acoustic radiation force may be used to push intravenous MBs or ELIPs toward the endothelial surface. This may be used to enhance receptor-target binding efficiency [45-47] or to concentrate US-stimulated gas release near the endothelial wall, Figure 3.2 C. Considerations regarding the use of ultrasound for therapeutic gas delivery will be discussed in more detail in the following section.

3.3.4 GAS-FILLED PARTICLES RESPOND TO ULTRASOUND

In ultrasound imaging, sound waves are transmitted into the body; when these waves reach a tissue boundary, a portion of the signal is reflected and processed to form an image. The extent to which sound waves are reflected depends on the magnitude of the difference in acoustic impedance across a boundary. Acoustic impedance is defined as the product of medium density and the speed of sound in the medium. In general, soft tissues, blood, and water have similar acoustic impedances, and interfaces between these materials provide small echos. The acoustic impedance of gas however

is much lower than soft tissues, and a gas-tissue or gas-blood interface provides a large echo. Intravascular MBs and ELIPs therefore offer a high impedance mismatch and are useful as ultrasound contrast agents [48-51]. Furthermore, oscillating gas cavities such as microbubbles excited by ultrasound produce echoes with broadband frequency content not typical of tissue [52-54]. Both this characteristic, and the nonlinear response of microbubbles to acoustic pulses of varying amplitude or phase, provide methods for ultrasonic detection of microbubbles and separation of their signals from tissue background. The result is the presence of gas containing vehicles that can be detected *in vivo* with high sensitivity.

The ability to image gas-filled particles with ultrasound provides an opportunity for guidance and monitoring of therapeutic gas administration in real time. Ultrasound may be used to determine when microbubbles or ELIPs in circulation have reached the therapeutic target. Ultrasound may then be used to stimulate the release of gas contents in the region of interest via acoustic cavitation. Many researchers classify cavitation into one of two types: stable and inertial. Stable cavitation refers to persistent bubble oscillation in response to acoustic pressure and can enhance gas diffusion out of the bubble and convection into the surrounding microenvironment [55]. Inertial cavitation is defined as the rapid collapse and subsequent fragmentation of a bubble when subjected to high pressure ultrasound [56]. This can be used to rapidly release the entire contents of a bubble in a specific region subjected to ultrasound of sufficient pressure, Figure 3.3. Inducing cavitation of bubbles encapsulated within ELIPs allows for controlled rupture of the liposome and subsequent release of the liposome's therapeutic payload.

Primary acoustic radiation force propels particles in a sound field along the beam access [57, 58]. This may be used to steer MBs and ELIPs in circulation toward the endothelial wall to enhance ligand-receptor targeting or to localize gas release near the endothelial wall [45-47], as illustrated in Figure 3.2 C. Vibrating microbubbles generate a secondary radiation force that may contribute to microbubble aggregation or repulsion depending on bubble size, acoustic pressure and driving frequency [59, 60]. Bubble aggregation due to secondary radiation forces may inhibit ligand-receptor targeting, or alternatively cause increased accumulation to already adherent microbubbles. Experimental parameters may be optimized to avoid or enhance this effect.

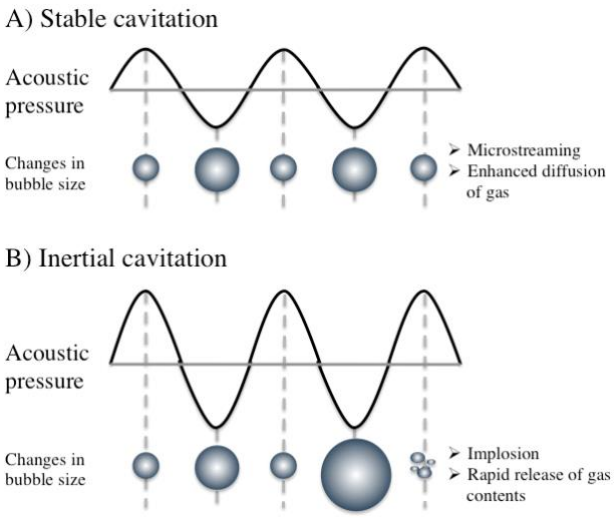

Figure 3.3: Response of bubbles to acoustic pressure. A) Stable cavitation- when subjected to low-intensity ultrasound, bubbles repeatedly oscillate around the resonant diameter. B) Inertial cavitation- when subjected to ultrasound of sufficient amplitude, bubbles rapidly grow and violently collapse.

3.3.5 ABILITY TO CO-DELIVER DRUGS FOR A SYNERGISTIC EFFECT

MBs and ELIPs may be used to co-deliver drugs for enhanced treatment effects. For example, Britton et al. suggested the co-encapsulation of tissue plasminogen activator in Xe-ELIPs to provide both clot lysis and neuroprotection for the treatment of ischemic stroke [21]. In general, the gas core and thin shell of microbubbles are not ideal for sufficient loading of organic compounds [61]. There are several techniques to circumvent this issue. For example, charged therapeutics including RNA and DNA may be coupled to the bubble shell through electrostatic interactions with charged shell molecules [62]. Alternatively, drug-containing nanoparticles may be conjugated to the bubble surface [45]. Readers are referred to a review by Steliyan Tinknov [63] for further information regarding microbubble-based drug delivery techniques.

As for microbubbles, charged molecules may be electrostatically coupled to charged ELIP surfaces [64]. Hydrophilic therapeutics may be solubilized with high loading capacity directly in the liposome core [65-68]. Hydrophobic drugs may be incorporated within the lipid bilayer, however the loading capacity and ultrasound stimulated release profiles of such drugs may be inferior to those of hydrophilic drugs [69]. The ability to simply encapsulate drugs in liposomes provides an advantage over microbubbles.

3.4 MICROBUBBLE DELIVERY OF OXYGEN AND NITRIC OXIDE

3.4.1 MICROBUBBLE PHYSICOCHEMICAL PROPERTIES

Microbubbles comprise a lipid [70-77], surfactant [78], protein [79], dextran [80], chitosan [81, 82], or polymer [83] shell surrounding a gaseous core. The bubble shell has a number of important functions. First, it provides mechanical stability for the bubble, supporting a negative pressure and allowing the gas inside the bubble to be in diffusion equilibrium with gas outside the bubble [84]. Second, the shell protects the bubble from destructive forces such as coalescence, Laplace pressure-driven dissolution and Ostwald ripening, and it therefore allows the gas bubble to persist in circulation [70, 84]. Simulations of oxygen microbubbles suggest that since the shell is gas permeable, the volume of transported oxygen may change in response to dissolved gas levels in surrounding blood [85]. For instance, bubbles can pick up oxygen in the high pO_2 environment of the lungs and release O_2 in tissues [86]. Finally, the shell may enhance the safety of bioactive gas delivery by reducing direct contact between the gas and surrounding blood and tissue. This may reduce the risk of oxygen toxicity or the potential of nitric oxide eliciting undesirable off-target effects.

Lipids are the most popular microbubble shell material. Common lipid excipients are commercially available, providing ease of microbubble formulation. Definity®, a lipid-based microbubble formulation, has proven to be safe for human use and is FDA approved as an ultrasound contrast agent for echocardiography. By altering lipid acyl chain lengths, one can optimize lipidic microbubble properties. Borden et al. modeled the dissolution behavior of lipid-stabilized oxygen microbubbles (OMBs) and found that microbubble stability is primarily controlled by the shell's resistance to gas permeation [70]. Lipid shell resistance is a function of acyl chain length; increasing hydrophobic chain length increases the attractive forces between adjacent lipids, thereby increasing the cohesion of the shell and decreasing the shell permeability to gases [70, 73]. The oxygen permeability of the lipid monolayer shell was measured to range from 10^{-4} to 10^{-3} cm/s [87, 88]. Therefore, using longer acyl chain lipids can enhance bubble stability and improve oxygen content half-life *in vivo*.

Polymer shells are ridged in comparison to the flexibility of lipid shells. This provides enhanced stability, but diminished echogenicity since the ridged bubbles resist oscillation until the shell is cracked by sufficient expansion [83]. Similarly, protein shells are relatively ridged and difficult to deform [89]. Human albumin-coated microbubbles (Optison™) are FDA approved contrast agents. However, immunogenicity is a concern when using non-human derived proteins.

Dextran is an alternative shell excipient. In a study by Cavalli et al., it was demonstrated that dextran-coated bubbles are effective oxygen carriers and can be stabilized by the co-encapsulation of a perfluorocarbon (PFC) and the addition of polyvinylpyrrolidone (PVP) in the shell [80]. An attractive feature of dextran microbubbles is their small particle size (400-550 nm). This may allow for extravasation of the dextran microbubbles from leaky tumor vasculature and enhanced depth of tumor oxygenation. Regarding therapeutic gas delivery, the best shell composition for a given application will depend on the desired *in vivo* stability, gas release profile, and acoustic properties of the microbubbles.

Microbubble properties are also dependent on their gas contents. Kwan et al. demonstrated that the stability of lipid-stabilized OMBs can be enhanced by doping the gaseous core with a poorly diffusing gas, such as a PFC. Adding just 5% decafluorobutane (DFB) to their lipidic OMBs increased stability 11-fold compared to 100% O_2 bubbles. The addition of a PFC enhances bubble stability by balancing the partial pressures between the bubble and surroundings, thus removing the chemical potential gradient for diffusion. By optimizing the relative volume of doping gas and the shell resistance, bubble stability and gas release profiles can be tuned for specific applications.

Tight control over microbubble size distribution is important for safety, shelf stability, and therefore clinical translation. Larger bubbles (>10 μm) can potentially obstruct microvasculature, and suspensions of larger lipidic OMBs are correlated with greater product loss (shorter shelf life) than those of smaller OMBs [74]. Swanson et al. demonstrated that 1,2-distearoyl-sn-glycero-3-phosphocholine (DSPC)-based OMBs are more stable than 1,2-dipalmitoyl-*sn*-glycero-3-phosphocholine (DPPC)-based OMBs [75]. DSPC-based OMBs showed a small increase in mean diameter (2 to 3 μm) and less than 20% change in volume over 3 weeks. Additionally, *in vitro*

experiments showed rapid oxygen delivery from DSPC-based OMBs to deoxygenated saline. Polizzotti et al. later demonstrated that addition of corn syrup can also aid stabilization of lipidic OMBs, following work by Dressaire et al. on sucrose-stearate stabilized microbubbles [74, 90].

3.4.2 OXYGEN MICROBUBBLES: APPLICATIONS AND RECENT STUDIES

As discussed above, the main therapeutic potential of oxygen delivery is in the reversal of oxygen depletion. This typically requires the administration of high oxygen concentrations. Oxygen content of OMBs is not continuously recycled upon passage though the high pO_2 environment of the lungs. This differentiates OMBs from classic fluorocarbon- and hemoglobin-based oxygen carriers and prevents their use as sustained oxygen delivery platforms. Continuous oxygen delivery from OMBs requires continuous infusion and may result in dose-limiting increases in serum viscosity and toxic levels of excipients. Therefore, oxygen microbubbles are limited to relatively short-term delivery. Recent studies investigating the use of OMBs for radio- and chemosensitization of hypoxic tumors and reversal of hypoxemia are summarized in Table 3.1.

Table 3.1: Summary of microbubble formulations and their proposed applications.

Shell excipients	Gas(es)	Particle sizes	Results and models used	US-stimulated release	Refs.
DSPC, DSPE-PEG2000	95% O_2 5% DFB	~ 4 μm	Simulations and *in vitro* oxygen release.	1 MHz 1200 kPa 60-240 s exposure	[73]
DSPC, PEG-40S	O_2	Polydisperse, mean particle diameter 3 μm	First demonstration of OMB stabilization by lipidic shells. *In vitro* studies showed rapid oxygen delivery to saline.	NA	[75]
DSPC, BRIJ 100	O_2	Polydisperse, mean particle diameter 3 μm	Oxygen transfer kinetics characterized *ex vivo* in human blood. *In vivo* studies show reversal of hypoxemia in rabbit models.	NA	[72]
Bovine serum albumin	O_2	Multimodal size distribution. 99% of bubbles<3 μm	*In vitro* studies demonstrate that OMBs rapidly release their oxygen content to oxygen-depleted saline upon injection.	NA	[79]

Table 3.1 cont'd **Shell excipients**	**Gas(es)**	**Particle sizes**	**Results and models used**	**US-stimulated release**	**Refs.**
Span 60 and TPGS	O_2	Polydisperse, 3.1±0.1 μm	*In vitro:* bubbles are effective contrast agents and increase oxygenation of degassed saline. *In vivo:* bubbles elevate tumor oxygen levels in mice with breast tumor xenografts.	*In vitro* studies: ~3.6 MPa, 4 MHz in power Doppler mode *In vivo* studies: 18 MHz nonlinear imaging (5s destructive pulses intermittent with 12s nondestructive)	[78]
Span 60 and TPGS	O_2	Not specified, but same methodology as in ref. [78]	*In vivo:* these bubbles elevate tumor oxygen levels in mice with breast tumor xenografts and enhance the efficacy of 5 Gy radiotherapy applied 75 s post-microbubble administration.	Microbubble destruction at 4.2 MHz and 2.5 MPa derated peak negative pressure in flash destruction-replenishment mode with intermittent low and high intensity pulses. Total exposure time = 75 s	[91]
Chitosan, palmitic acid and β-glycerol phosphate	O_2 with and without DDFP	708±51.3 nm (O_2 only) [82] 1236.5±17.5 nm (O_2/DDFP) [82] 2603.2±304.4 nm (O_2/DDFP) [81]	*In vitro* studies show the ability of these bubbles to reduce HIF-1α expression of cells grown under hypoxic conditions	45 kHz, 260 W peak power [82]	[81, 82]
Dextran, palmitic acid, +/- PVP (a stabilizing agent)	O_2 DDFP	550±30 nm (-PVP) 410±5 nm (+PVP)	*In vitro* studies demonstrate that these bubbles can effectively increase pO_2 of hypoxic media and respond to US stimulation.	2.5±0.1 MHz 2.4±0.2MPa	[80]
DSPC and PEG-40S	O_2	3.4±1.9 μm	Reversal of hypoxemia observed *in vivo* using a right pneumothorax lung injury model in rats.	NA	[71]
DSPC and PEG-40S	O_2	Not specified	Bolus injection of OMBs into the peritoneal cavity doubled survival time of rabbits experiencing complete tracheal occlusion.	NA	[92]
Phospholipid	O_2	Not specified	*In vitro* and *in vivo* studies indicate that oxygen-filled microbubbles conjugated with a sonosensitizer enhance sonodynamic therapy efficacy by increasing local oxygen concentration.	*In vitro*: 30 s exposure, 3.0 Wcm^{-2}, 1 MHz center frequency, 100 Hz pulse repetition, 50% duty cycle *In vivo*: 3.5 min, 3.5 Wcm^{-2}, 1 MHz center frequency, 100 Hz pulse repetition frequency, 30% duty cycle	[93, 94]
DBPC, DSPE-PEG2000, and DSPE-PEG2000-biotin for conjugation	O_2	1-2 μm average diameter	*In vitro* and *in vivo* studies indicate that combination therapy with oxygen-filled microbubbles conjugated with a sonosensitizer and separately 5-fluorouracil enhance treatment efficacy compared to monotherapies or treatments without oxygen delivery.	*In vitro (cells)*: 30 s exposure, 3.0 Wcm^{-2}, 1 MHz, 100 Hz pulse repetition, 50% duty cycle *In vivo*: 3.5 min, 3.5 Wcm^{-2}, 1 MHz, 100 Hz pulse repetition, 30% duty cycle	[95]

Table 3.1 cont'd **Shell excipients**	**Gas(es)**	**Particle sizes**	**Results and models used**	**US-stimulated release**	**Refs.**
DPPE-PEG2000, PC, CH	NO	Average diameter 3.85 μm	*In vivo* studies suggest that NO microbubbles promote DVT resolution in a rat model.	NA	[77]
DPPE-PEG2000 and PC	NO	Average diameter 3.85 μm	NO microbubbles coupled with US stimulation may enhance MSC homing to the myocardial infarct area and promote angiogenesis.	*In vitro* and *in vivo*: 1 MHz, 1 Wcm^{-2}	[76]
DSPC and PEG-40S	O_2	Median diameter ~4 μm	Intratumoral injection of OMBs significantly increases tumor oxygen saturation in a rat model of fibrosarcoma, improving tumor control when combined with 15 Gy radiotherapy.	NA	[96]
DPPC and DSPE	O_2 and OFP $[O_2]$ = 35 mg/L	1.7±0.1 μm	*In vitro* studies demonstrate selective, US-stimulated oxygen release from microbubble formulation. PTX loading in the oxygen microbubbles, combined with US-stimulated release, provides superior ovarian cancer cell killing.	300 kHz, 0.5 W/cm^2, 15 second exposure, continuous wave	[97]
DPPC and DSPE	O_2 and OFP $[O_2]$ = 35 mg/L	1.7±0.1 μm	In an *in vivo* model of ovarian cancer, PTX-loaded oxygen microbubbles are shown to significantly enhance therapeutic outcome when ultrasound is used for local delivery within the tumor.	300 kHz, 1.0 W/cm^2, 50% duty cycle for 6 minutes	[98]
DPPC and DSPE-PEG-Folate or DSPE-PEG2000	O_2 and OFP $[O_2]$ = 35 mg/L	1.81±0.04 μm for folate targeted 1.78±0.05 μm for untargeted	Adding a folate targeting ligand to PTX and oxygen loaded microbubbles enhances therapeutic efficacy in intraperitoneal model of ovarian cancer.	300 kHz, 1.0 W/cm^2, 10s on 10s off for 3 min	[99]

Abbreviations, Table 3.1
BRIJ 100- polyoxyethylene (100) stearyl ether
CH- cholesterol
DBPC- dibehenoylphosphatidylcholine
DPPC- 1,2-dipalmitoyl-sn-glycero-3-phosphatidylcholine
DPPE-PEG2000- 1, 2–dipalmitoyl-sn-glycero-3-phosphoethanolamine-N-[methoxy(polyethylene glycol)-2000]
DSPC- 1,2-distearoyl-sn-glycero-3- phosphocholine
DSPE- 1,2-distearoyl-sn- glycero-3-phosphoethanolamine
DSPE-PEG2000-1,2-distearoyl-sn- glycero-3-phosphoethanolamine-N-[methoxy(polyethyleneglycol)-2000]
DSPE-PEG-Folate- 1,2-distearoyl-sn- glycero-3-phosphoethanolamine-N-[folate(polyethyleneglycol)-2000]
DVT- deep vein thrombosis
HIF-1α- hypoxia inducible factor-1α
MSC- mesenchymal stem cell
OMB- oxygen microbubble
PC- phosphatidylcholine
PEG-40S- polyoxyethylene-40 stearate
DFB- decafluorobutane
DDFP- dodecafluorpentane
OFP- octofluoropropane
PTX- paclitaxel
PVP- polyvinylpyrrolidone
TPGS- alpha tocopheryl polyethylene glycol succinate
US- ultrasound

3.4.2.1 REVERSAL OF TUMOR HYPOXIA

OMBs are uniquely suited for re-oxygenation of localized tissue hypoxia; ultrasound targeted O_2 release can provide significant increases in pO_2 of a target tissue (e.g., tumor) while limiting systemic exposure to high oxygen concentrations and therefore reducing the risk of off-target oxidative stress. For this application, relatively stable microbubbles are desired that persist in circulation until fragmented by ultrasound. Kwan, et al. produced lipid-stabilized oxygen microbubbles doped with 5% PFC [73]. Through *in vitro* experimentation authors were able to increase the percent oxygen saturation of deionized water up to 15% after ultrasound-stimulated oxygen release from the bubbles.

OMBs have been prepared with a chitosan shell [81, 82]. Oxygen loading of these bubbles was again enhanced by PFC doping [82]. Administration of these chitosan OMBs to JEG-3 human carcinoma cells cultured under hypoxic conditions resulted in a 50% lower expression of hypoxia inducible factor-1α (HIF-1α) compared to untreated control cells [81, 82].

Eisenbrey et al., has demonstrated the potential of using microbubbles with a pure oxygen core for the radiosensitization of hypoxic tumors [78, 91]. They prepared bubbles stabilized by a surfactant shell composed of Span60 and water-soluble vitamin E. These bubbles were relatively stable *in vitro*, with a half-life of up to 15 minutes. They also proved to be effective ultrasound contrast agents and to significantly increase pO_2 of degassed saline upon ultrasound-stimulated O_2 release. Preliminary *in vivo* studies demonstrate the ability of these OMBs to elevate oxygen partial pressures in a murine model of breast cancer [78], and subsequent work has shown that this improves tumor control and increases median survival when combined with radiation therapy (compared to control tumors that received nitrogen-filled microbubbles) [91]. We have demonstrated similar results in our group, showing that intratumoral administration of lipid-shelled OMBs increases tumoral oxygenation and increases the tumor control offered by subsequent radiotherapy in a rat model of fibrosarcoma (see chapter 4) [96].

Sonodynamic therapy (SDT) is a method of cancer treatment that involves the use of ultrasound to activate certain chemical compounds or ‘sonosensitizers’ to generate reactive oxygen

species (ROS) that in turn damage DNA and promote apoptosis within the tumor [100]. This treatment is dependent on the presence of oxygen, and tumor hypoxia limits efficacy. McEwan et al. developed oxygen-filled microbubbles tethered to Rose Bengal (RB), a sonosensitizer, to enhance SDT treatment of hypoxic tumors [93, 94]. The investigators observed that oxygen-loaded microbubbles were able to generate significantly more singlet oxygen in a free cell system than bubbles loaded with sulfur hexafluoride, and that the oxygen loaded microbubbles also induced a greater cytotoxic effect than the sulfur hexafluoride control. *In vivo,* mice bearing human xenograft pancreatic BxPc-3 tumors treated with the oxygen-Rose Bengal conjugate and ultrasound showed a significant 45% reduction in tumor volume five days after treatment while the volume of tumors in mice treated with the conjugate only increased by 180% over the same time period, a result directly attributed to the oxygen contribution from the microbubbles. Subsequent work by the same group demonstrated that efficacy can be further enhanced by combining this oxygen-enhanced SDT with oxygen-enhanced chemotherapy (oxygen microbubbles conjugated to 5-fluorocuracil with ultrasound stimulated release) in the same *in vivo* tumor model [95].

Finally, tumor hypoxia promotes chemoresistance through a number of mechanisms. To combat this, Sun, Luo, Liu, and colleagues developed a paclitaxel-loaded oxygen microbubble formulation for the treatment of ovarian cancer [97-99]. *In vitro* testing demonstrated selective oxygen release upon ultrasound-mediated microbubble destruction. Ultrasound-mediated delivery of oxygen and paclitaxel from these microbubbles provided superior killing of ovarian cancer cells and led to reduced expression of HIF-1α compared to all control groups [97]. Translating this work *in vivo*, Liu et al. demonstrated that ultrasound-mediated destruction of oxygen and paclitaxel loaded microbubbles resulted in significantly greater tumor control compared to all control groups in a subcutaneous model of ovarian cancer [98]. More recently, the same group went on to show that therapeutic efficacy can be further enhanced by adding a folate targeting moiety to the microbubbles, which enhances uptake by ovarian cancer cells and tumor-associated macrophages [99].

3.4.2.2 REVERSAL OF HYPOXEMIA

Oxygen microbubbles may be used to increase the oxygen content of blood and extend the timeframe for effective, permanent treatment in cases of severe hypoxemia. Oxygen microbubbles offer the additional advantage of not requiring oxygen loading at the lungs and can be used in cases of respiratory injury/failure. For this application, relatively unstable OMBs that quickly transfer their O_2 contents to deoxyhemoglobin without ultrasound stimulation are desirable, Figure 3.4.

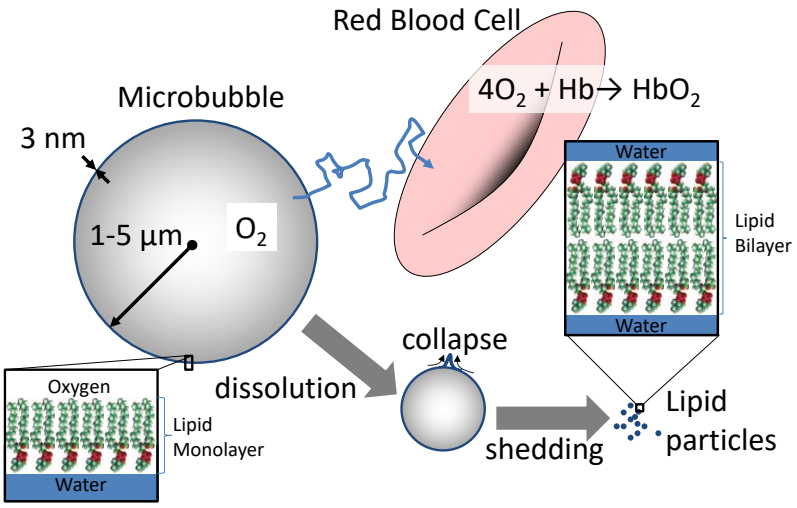

Figure 3.4: Oxygen microbubbles for the reversal of hypoxemia. Lipidic oxygen microbubbles are stabilized by a lipid monolayer approximately 3 nm thick. Oxygen can diffuse out of the microbubbles and react with deoxyhemoglobin. To accommodate the shrinking gas core, lipid is shed from the shell.

Kheir and colleagues investigated the use of pure oxygen microbubbles for intravenous delivery of oxygen in rabbit models of severe hypoxemia. Hypoxemia was induced by hypoxic ventilation of 11% oxygen, and intravenous delivery of DSPC-OMBs rapidly increased pulse oximetry (O_2 saturation) and oxyhemoglobin concentrations. Also, in a rabbit model of asphyxia, it was demonstrated that these OMBs could reduce the incidence of cardiac arrest and organ injury [72]. Authors envision similarly formulated lipid-stabilized oxygen microbubbles for rapid emergency gas delivery in critically hypoxemic patients, extending the window for safe definitive intervention (i.e., tracheal tube, intubation, etc.) before the onset of organ damage and cardiac arrest.

Feshitan et al. showed that intraperitoneal (IP) injection of OMBs can reverse hypoxemia *in vivo*. The peritoneal cavity has a large surface area and provides for efficient gas exchange. Following right pneumothorax lung injury in rats, phospholipid-stabilized O_2 microbubbles were injected into the peritoneal cavity. All rats treated with IP oxygen microbubbles survived to the predetermined 2-hour time point whereas control rats survived on average 18.5 minutes. IP delivery of O_2-microbubbles may provide an alternative for mechanical ventilation in severely hypoxemic patients. The same group showed that IP injection of OMBs significantly prolongs survival in rabbits experiencing complete tracheal occlusion [92].

3.4.3 NITRIC OXIDE MICROBUBBLES: APPLICATIONS AND RECENT STUDIES

NO elicits a wide range of biological effects, and its delivery via microbubbles may prove useful for a number of applications. To date, only two studies have been conducted investigating NO delivery via microbubbles, Table 3.1.

Stem cell-based therapies are an exciting approach for the treatment of myocardial infarction and offer the unique potential of regenerating myocardium and promoting neovascularization [101]. However, the success of this approach is limited by poor transplantation efficiency. Tong et al. recently demonstrated that intravenous delivery of NO microbubbles and mesenchymal stem cells (MSCs) coupled with ultrasound stimulation enhances MSC homing to the myocardial infarct area and promotes angiogenesis in a rat model of myocardial infarction. Ultrasound exposure may have enhanced transplantation efficiency by increasing myocardial permeability and by releasing NO, an important signaling molecule in the cardiovascular system [76].

Wang et al. proposed the use of NO microbubbles for the treatment of deep vein thrombosis (DVT) [77]. Lipid-stabilized NO microbubbles were periodically administered to rats following inferior vena cava and left common iliac vein ligation. Thrombus size of NO treated animals was approximately 40% smaller than that of control animals. Furthermore, platelet and inflammatory cell aggregation was inhibited following NO microbubble administration. Therefore, Wang et al. concluded that intravenous NO delivery via microbubbles was a promising method to stimulate DVT resolution [77].

3.5 LIPOSOMAL DELIVERY OF NITRIC OXIDE AND XENON

3.5.1 ECHOGENIC LIPOSOME PHYSICOCHEMICAL PROPERTIES

In the mid-1990s it was discovered that certain liposomes can be created with an inherent echogenicity and can be used as ultrasound contrast agents [49]. Their echogenicity was later attributed to air trapped in the liposomes during the fabrication process [50]. Since then, efforts have been made to optimize liposomes for this purpose. It has been shown that the stability of echogenic liposomes (ELIPs) can be controlled by the degree of saturation of component lipids. The inclusion of highly saturated lipids increases bilayer rigidity, decreases permeability to gases and therefore provides a stable liposome with prolonged echogenicity in circulation sufficient for use as US contrast agents [102].

Recently, echogenic liposomes have been modified for delivery of the therapeutic gasses, nitric oxide and xenon. There are two published methods to load therapeutic gases in liposomes. Huang and colleagues developed the pressurized-freeze method [24, 103]. This process involves conventional liposomal fabrication via lipid film hydration followed by the pressurized addition of the gas of interest. Suspensions are then frozen for approximately 30 minutes followed by pressure release and thawing. Resultant liposomes are approximately 800 nm in size, which is sufficiently small for safe intravascular delivery [104]. This method yields around 10% gas entrapment by volume and has proven effective for the encapsulation of NO and Xe [24]. The concentration and release profile of the therapeutic gas can be modulated by the co-encapsulation of a second, inert gas (i.e. argon) as demonstrated by Huang et al. [103].

Sutton et al. demonstrated an alternative method to encapsulate NO in liposomes [105]. They made liposome suspensions as described by Endo-Takahashi et al. [64] and replaced headspace air with a mixture of NO and octofluoropropane (OFP). The gases were then incorporated into the liposomes by vigorous shaking. A disadvantage to this method is that it yields liposomes with a bimodal size distribution with peaks at 2.5 μm and 11 μm. If used *in vivo*, the larger liposomes may become lodged in capillaries, posing safety concerns.

3.5.2 NITRIC OXIDE LIPOSOMES: APPLICATIONS AND RECENT STUDIES

The use of liposomes offers an alternative to microbubbles for the intravenous delivery of NO, and a summary of recent studies is presented in Table 3.2. Intimal hyperplasia is characterized by the thickening of the innermost layer of a blood vessel in response to vessel injury, and is a major cause of complications following angioplasty, bypass operations and stenting [106]. Huang et al. suggested the use of NO-ELIPs to inhibit intimal hyperplasia and showed that locally injected ELIPs containing 90% Ar and 10% NO effectively reduced neointimal hyperplasia in a balloon-injured arterial model in hyperlipidemic rabbits and reduced arterial wall thickening by approximately 40% compared to injured control animals [103]. This group also demonstrated that the liposomes effectively protect NO from hemoglobin scavenging *in vitro* compared to free NO in solution.

The use of NO-ELIPs has been proposed for vasodilatation [104, 105]. NO-ELIPs effectively induced arterial dilation in *ex vivo* models using rabbit and porcine carotid arteries. In both studies, this effect was enhanced by ultrasound-stimulated NO release. Kim et al. found that ultrasound stimulation induced greater NO penetration into the intima, media and adventitia, which may be due to the radiation force effects of ultrasound. When erythrocytes were included in the flow-through media, vasodilation was reduced and only observed in the presence of ultrasound. This indicates that liposomes incompletely protect NO from erythrocyte scavenging. If NO is released too far from the arterial wall, it may bind erythrocytes/hemoglobin before reaching its target.

Kim et al. also investigated cerebral vasodilitive effects of NO-ELIPs *in vivo* in rats following subarachnoid hemorrhage. NO-ELIPs effectively inhibited vasospasm and resulted in improved neurologic function in treated rats. NO-ELIP treatment coupled with ultrasound activation over the carotid artery showed further improvements in neurological function in these animals.

The cytotoxic effect of NO at high concentrations has been suggested for the treatment of breast cancer [107]. The role of NO in cancer is complex and concentration-dependent; at low concentrations NO promotes cancer cell proliferation by stimulating angiogenesis and at high concentrations NO is cytotoxic [17]. At high concentrations, NO reacts with oxygen to form the pro-apoptotic intermediate peroxynitrate, which is known to inhibit DNA repair enzymes [108]. Lee et al.

demonstrated that NO-ELIP induced breast cancer cell death *in vitro* with IC_{50} values of 0.42 mg/ml and 0.56 mg/ml for MDA-MB-468 and MDA-MB-231 cell lines, respectively [107]. Due to the diverse effects of NO in cancerous and normal cells, it is important to rigorously control the concentration and location of NO delivery to limit off-target consequences.

3.5.3 XENON LIPOSOMES: APPLICATIONS AND RECENT STUDIES

The use of echogenic liposomes has also been investigated for the intravenous delivery of Xe, Table 3.2. Britton et al. demonstrated the effectiveness of Xe-ELIPs in *in vitro* and *in vivo* models*. In vitro,* Xe-ELIPs were shown to protect PC12 cells from oxygen-glucose deprivation and subsequent hypoxic cell death. In a rat model of cerebral ischemia-reperfusion injury, intravenously delivered Xe-ELIPs resulted in 48% reduction in infarction size. Using ultrasound to stimulate Xe release enhanced the infarct reduction to 75% and restored sensorimotor function in the animals [21].

Building upon this initial success, Peng et al. investigated the effective time-window and mechanism of action for Xe-induced neuroprotection using Xe-ELIPs [109]. Using a rat model of cerebral ischemia-reperfusion injury, it was shown that Xe-ELIP administration 2, 3, and 5 hours post-stroke onset effectively reduced infarct area with greater reductions observed with earlier treatment. Significant improvements in behavioral task performance were observed with the 2- and 3-hour treatments. Peng et al. also demonstrated that Xe provides neuroprotection through NMDA antagonism and synergistic mechanisms; namely, activation of brain-derived neurotrophic factor (BDNF), protein kinase B (Akt), and mitogen-activated protein kinases (MAPK).

Table 3.2: Summary of echogenic liposome formulations and their proposed applications.

Shell excipients	Gas(es)	Particle sizes	Results and models used	US-stimulated release	Refs.
EDPPC, DOPC, CH	1:9 NO:Ar	not specified	NO-ELIP delivery inhibited intimal hyperplasia development *in vivo* following balloon injury in rabbit carotid arteries.	NA	[103]
For *in vitro/ex vivo*: EDPPC, DOPC, CH **For *in vivo*:** EDPPC, DOPC, CH, PEG2000-DPPE	1:9 NO:Ar	800 nm on average	The vasodilitive effects of NO-ELIPs were demonstrated *ex vivo* in rabbit carotid arteries and *in vivo* in a rat subarachnoid hemorrhage model.	***In vitro/ ex vivo*:** 5.7 MHz color Doppler US, MI 0.15, pulse repetition frequency 8 kHz ***In vivo*:** 1 MHz, 0.3 MPa, continuous wave US	[104]

Table 3.2 cont'd **Shell excipients**	**Gas(es)**	**Particle sizes**	**Results and models used**	**US-stimulated release**	**Refs.**
DPPC, DOTAP, PEG-2000, PEG-750	1:1 NO:OFP	Bimodal with peaks at 2.5 μm and 11 μm	NO-ELIPs effectively induced arterial dilation *ex vivo* in porcine carotid arteries.	1 MHz, 0.34 MPa peak-to-peak pressure, 30 cycles	[105]
EPC, DPPC, DPPE, DPPG, DC-CH·HCl	100% NO	not specified	NO-ELIP induced breast cancer cell death *in vitro*.	NA	[107]
DPPC, DOPC, CH	7:3 Xe:Ar	not specified	Xe-ELIPs administration reduced infarct size in a rat model of cerebral ischemia-reperfusion injury, which was enhanced when US was used to stimulate Xe release.	1 MHz, 0.18 MPa peak-to-peak pressure, continuous wave US	[21]
DPPC, Egg-PC, PEG2000-PE, DPPG, CH	7:3 Xe:Ar	not specified	Xe-ELIPs reduced infarct size when administered within 5 hours of stroke onset in a rat model.	1 MHz, 0.18 MPa peak-to-peak pressure, continuous wave US	[109]

Abbreviations, Table 3.2
Akt- protein kinase B
Ar- argon
BDNF- brain-derived neurotrophic factor
BF- bifunctionally targeted
CH- cholesterol
DOPC- 1,2-dioleoyl-sn-glycero-3-phosphocholine
DC-CH·HCl- 3β-[N-(N',N'-dimethylaminoehane)-carbamoyl] cholesterol hydrochloride
DOTAP- N-[1-(2,3-dioleoyloxy) propyl]-N,N,N-trimethylammonium
DPPC- 1,2-dipalmitoyl-sn-glycero-3-phosphocholine
DPPE- 1,2-dipalmitoyl-sn-glycero-3-phosphoethanolamine
DPPG-1,2-dipalmitoyl-sn-glycero-3- [phosphor-rac-1-glycerol]
EDPPC- 1,2-dipalmitoyl-sn-glycero-3-ethylphosphocholine
Egg-PC- egg phosphocholine
ELIP- echogenic liposome
EPC- L-α-phosphatidylcholine
IVUS- intravascular ultrasound
MAPK- mitogen-activated protein kinase
MI- mechanical index
NO- nitric oxide
OFP- octafluoropropane
PEG- polyethylene glycol
PEG2000-DPPE- carbonyl-methoxypolyethyleneglycol- 2000-2-dipalmitoyl-sn-glycero-3-phosphoethanolamine
PEG 2000-PE- 1,2- dipalmitoyl- sn- glycero-3-phosphoethanolamine-N-[methoxy(polyethylene glycol)-2000]
VSMC- vascular smooth muscle cells
Xe- Xenon

3.6 CONCLUSIONS

Microbubbles and liposomes offer unique advantages as therapeutic gas delivery vehicles. These particles are inherently echogenic, and therefore ultrasound can be used to image them and release their gas contents in a targeted region via acoustic cavitation. Targeting of these particles may also be achieved by conjugating their surfaces with ligands or antibodies. The ability to target gas release in specific regions limits the risk of off-target side effects and provides an advantage over alternative gas delivery techniques (i.e., inhalation). Future studies may exploit the potential to

coencapsulate drugs in therapeutic gas microbubbles and liposomes for enhanced treatment efficacy. The most significant difference between microbubbles and liposomes is their respective loading capacities; microbubbles are preferable when large concentrations of a gas need to be delivered and liposomes provide sufficient loading for potent bioactive gases. To date, this approach of gas delivery has only been explored for oxygen, nitric oxide and xenon. Future studies in this field may investigate delivery of other bioactive gases including carbon dioxide and hydrogen sulfide.

Microbubble and liposomal delivery of therapeutic gases must be proven to be safe prior to clinical translation. Long-term toxicity studies of shell excipients should be conducted and the concentration at which these excipients are tolerated should be established. Size distributions of therapeutic gas-filled particles are important for safety and should be characterized. Particles greater than about 10 μm can potentially occlude the microvasculature, posing a serious safety concern. In general, the concentration of therapeutic gas delivered with different microbubble and liposome formulations is not well established. Accurate dosing will be an important consideration if these particles are to be translated into humans.

REFERENCES

1. Vaupel, P., M. Hockel, and A. Mayer, *Detection and characterization of tumor hypoxia using pO2 histography.* Antioxid Redox Signal, 2007. **9**(8): p. 1221-35.

2. Siegel, R., D. Naishadham, and A. Jemal, *Cancer statistics, 2013.* CA Cancer J Clin, 2013. **63**(1): p. 11-30.

3. Bennett, M.H., et al., *Hyperbaric oxygenation for tumour sensitisation to radiotherapy.* Cochrane Database Syst Rev, 2012. **4**: p. Cd005007.

4. Henke, M., et al., *Erythropoietin to treat head and neck cancer patients with anaemia undergoing radiotherapy: randomised, double-blind, placebo-controlled trial.* Lancet, 2003. **362**(9392): p. 1255-60.

5. Bowton, D.L., P.E. Scuderi, and E.F. Haponik, *The incidence and effect on outcome of hypoxemia in hospitalized medical patients.* Am J Med, 1994. **97**(1): p. 38-46.

6. Camarata, S.J., et al., *Cardiac arrest in the critically ill. I. A study of predisposing causes in 132 patients.* Circulation, 1971. **44**(4): p. 688-95.

7. Castro, C.I. and J.C. Briceno, *Perfluorocarbon-based oxygen carriers: review of products and trials.* Artif Organs, 2010. **34**(8): p. 622-34.

8. Tao, Z. and P.P. Ghoroghchian, *Microparticle, nanoparticle, and stem cell-based oxygen carriers as advanced blood substitutes.* Trends Biotechnol, 2014. **32**(9): p. 466-73.

9. Furchgott, R.F. and J.V. Zawadzki, *The obligatory role of endothelial cells in the relaxation of arterial smooth muscle by acetylcholine.* Nature, 1980. **288**(5789): p. 373-6.

10. Ignarro, L.J., et al., *Endothelium-derived relaxing factor produced and released from artery and vein is nitric oxide.* Proc Natl Acad Sci U S A, 1987. **84**(24): p. 9265-9.

11. Ignarro, L.J., *Endothelium-derived nitric oxide: actions and properties.* Faseb j, 1989. **3**(1): p. 31-6.

12. Griffith, O.W. and D.J. Stuehr, *Nitric oxide synthases: properties and catalytic mechanism.* Annu Rev Physiol, 1995. **57**: p. 707-36.

13. Arnal, J.F., et al., *Endothelium-derived nitric oxide and vascular physiology and pathology.* Cell Mol Life Sci, 1999. **55**(8-9): p. 1078-87.

14. Loscalzo, J., *Nitric oxide insufficiency, platelet activation, and arterial thrombosis.* Circ Res, 2001. **88**(8): p. 756-62.

15. Rudic, R.D., et al., *Direct evidence for the importance of endothelium-derived nitric oxide in vascular remodeling.* J Clin Invest, 1998. **101**(4): p. 731-6.

16. Garry, P.S., et al., *The role of the nitric oxide pathway in brain injury and its treatment--from bench to bedside.* Exp Neurol, 2015. **263**: p. 235-43.

17. Mocellin, S., V. Bronte, and D. Nitti, *Nitric oxide, a double edged sword in cancer biology: searching for therapeutic opportunities.* Med Res Rev, 2007. **27**(3): p. 317-52.

18. Szabo, C. and D.J. Abraham, *Medicinal Chemistry and Therapeutic Applications of the Gasotransmitters NO, CO, and H2S and their Prodrugs*, in *Burger's Medicinal Chemistry and Drug Discovery*. 2003, John Wiley & Sons, Inc.

19. Choi, D.W., J.Y. Koh, and S. Peters, *Pharmacology of glutamate neurotoxicity in cortical cell culture: attenuation by NMDA antagonists.* J Neurosci, 1988. **8**(1): p. 185-96.

20. Ma, D., et al., *Neuroprotective and neurotoxic properties of the 'inert' gas, xenon.* Br J Anaesth, 2002. **89**(5): p. 739-46.

21. Britton, G.L., et al., *In vivo therapeutic gas delivery for neuroprotection with echogenic liposomes.* Circulation, 2010. **122**(16): p. 1578-87.

22. Liao, J.C., et al., *Intravascular flow decreases erythrocyte consumption of nitric oxide.* Proceedings of the National Academy of Sciences, 1999. **96**(15): p. 8757-8761.

23. Postema, M., et al., *Nitric oxide delivery by ultrasonic cracking: some limitations.* Ultrasonics, 2006. **44 Suppl 1**: p. e109-13.

24. Huang, S.L., D.D. McPherson, and R.C. Macdonald, *A method to co-encapsulate gas and drugs in liposomes for ultrasound-controlled drug delivery.* Ultrasound Med Biol, 2008. **34**(8): p. 1272-80.

25. Lum, H. and A.B. Malik, *Regulation of vascular endothelial barrier function.* Am J Physiol, 1994. **267**(3 Pt 1): p. L223-41.

26. Hobbs, S.K., et al., *Regulation of transport pathways in tumor vessels: role of tumor type and microenvironment.* Proc Natl Acad Sci U S A, 1998. **95**(8): p. 4607-12.

27. Gabizon, A.A., *Selective tumor localization and improved therapeutic index of anthracyclines encapsulated in long-circulating liposomes.* Cancer Res, 1992. **52**(4): p. 891-6.

28. Negishi, Y., et al., *Ultrasound-mediated gene delivery systems by AG73-modified bubble liposomes.* Peptide Science, 2013. **100**(4): p. 402-407.

29. Negishi, Y., et al., *AG73-modified Bubble liposomes for targeted ultrasound imaging of tumor neovasculature.* Biomaterials, 2013. **34**(2): p. 501-507.

30. Huang, S.L. and R.C. MacDonald, *Acoustically active liposomes for drug encapsulation and ultrasound-triggered release.* Biochim Biophys Acta, 2004. **1665**(1-2): p. 134-41.

31. Huang, S.L., *Liposomes in ultrasonic drug and gene delivery.* Adv Drug Deliv Rev, 2008. **60**(10): p. 1167-76.

32. Unnikrishnan, S. and A.L. Klibanov, *Microbubbles as ultrasound contrast agents for molecular imaging: preparation and application.* AJR Am J Roentgenol, 2012. **199**(2): p. 292-9.

33. Tardy, I., et al., *In vivo ultrasound imaging of thrombi using a target-specific contrast agent.* Acad Radiol, 2002. **9 Suppl 2**: p. S294-6.

34. Chen, X., et al., *Improved tumor-targeting drug delivery and therapeutic efficacy by cationic liposome modified with truncated bFGF peptide.* J Control Release, 2010. **145**(1): p. 17-25.

35. Ye, P., et al., *Folate receptor-targeted liposomes enhanced the antitumor potency of imatinib through the combination of active targeting and molecular targeting.* Int J Nanomedicine, 2014. **9**: p. 2167-78.

36. Chen, C.C. and M.A. Borden, *Ligand conjugation to bimodal poly(ethylene glycol) brush layers on microbubbles.* Langmuir, 2010. **26**(16): p. 13183-94.

37. Klibanov, A.L., et al., *Activity of amphipathic poly(ethylene glycol) 5000 to prolong the circulation time of liposomes depends on the liposome size and is unfavorable for immunoliposome binding to target.* Biochim Biophys Acta, 1991. **1062**(2): p. 142-8.

38. Moore, N.W. and T.L. Kuhl, *Bimodal polymer mushrooms: compressive forces and specificity toward receptor surfaces.* Langmuir, 2006. **22**(20): p. 8485-91.

39. Kim, D.K., AL; Needham, D, *The Influence of Tiered Layers of Surface-Grafted Poly(ethylene glycol) on Receptor-Ligand-Mediated Adhesion between Phospholipid Monolayer-Stabilized Microbubbles and Coated Glass Beads.* Langmuir, 2000. **16**(6): p. 2808-2817.

40. Clarkson, J.R., Z.F. Cui, and R.C. Darton, *Protein Denaturation in Foam.* J Colloid Interface Sci, 1999. **215**(2): p. 323-332.

41. Demos, S.M., et al., *In vivo targeting of acoustically reflective liposomes for intravascular and transvascular ultrasonic enhancement.* J Am Coll Cardiol, 1999. **33**(3): p. 867-75.

42. Demos, S.M., et al., *In vitro targeting of antibody-conjugated echogenic liposomes for site-specific ultrasonic image enhancement.* J Pharm Sci, 1997. **86**(2): p. 167-71.

43. Zhou, Y., et al., *Targeted Antiangiogenesis Gene Therapy Using Targeted Cationic Microbubbles Conjugated with CD105 Antibody Compared with Untargeted Cationic and Neutral Microbubbles.* Theranostics, 2015. **5**(4): p. 399-417.

44. Klegerman, M.E., et al., *Liposomal modular complexes for simultaneous targeted delivery of bioactive gases and therapeutics.* J Control Release, 2010. **142**(3): p. 326-31.

45. Lum, A.F., et al., *Ultrasound radiation force enables targeted deposition of model drug carriers loaded on microbubbles.* J Control Release, 2006. **111**(1-2): p. 128-34.

46. Dayton, P., et al., *Acoustic radiation force in vivo: a mechanism to assist targeting of microbubbles.* Ultrasound Med Biol, 1999. **25**(8): p. 1195-201.

47. Zhao, S., et al., *Radiation-force assisted targeting facilitates ultrasonic molecular imaging.* Mol Imaging, 2004. **3**(3): p. 135-48.

48. Klibanov, A.L., et al., *Detection of individual microbubbles of an ultrasound contrast agent: fundamental and pulse inversion imaging.* Acad Radiol, 2002. **9 Suppl 2**: p. S279-81.

49. Alkan-Onyuksel, H., et al., *Development of inherently echogenic liposomes as an ultrasonic contrast agent.* J Pharm Sci, 1996. **85**(5): p. 486-90.

50. Huang, S.L., et al., *Physical correlates of the ultrasonic reflectivity of lipid dispersions suitable as diagnostic contrast agents.* Ultrasound Med Biol, 2002. **28**(3): p. 339-48.

51. Wilson, S.R. and P.N. Burns, *Microbubble-enhanced US in body imaging: what role?* Radiology, 2010. **257**(1): p. 24-39.

52. Burns, P.N., *Harmonic imaging with ultrasound contrast agents.* Clin Radiol, 1996. **51 Suppl 1**: p. 50-5.

53. Chomas, J., et al., *Nondestructive subharmonic imaging.* IEEE Trans Ultrason Ferroelectr Freq Control, 2002. **49**(7): p. 883-92.

54. Kruse, D.E. and K.W. Ferrara, *A new imaging strategy using wideband transient response of ultrasound contrast agents.* IEEE Trans Ultrason Ferroelectr Freq Control, 2005. **52**(8): p. 1320-9.

55. Bader, K.B. and C.K. Holland, *Gauging the likelihood of stable cavitation from ultrasound contrast agents.* Phys Med Biol, 2013. **58**(1): p. 127-44.

56. Chomas, J.E., et al., *Threshold of fragmentation for ultrasonic contrast agents.* J Biomed Opt, 2001. **6**(2): p. 141-50.

57. Crum, L.A. and A.I. Eller, *Motion of Bubbles in a Stationary Sound Field.* The Journal of the Acoustical Society of America, 1970. **48**(1B): p. 181-189.

58. Macedo, I.C. and W.J. Yang, *Acoustic effects on gas bubbles in the flows of viscous fluids and whole blood.* J Acoust Soc Am, 1973. **53**(5): p. 1327-35.

59. Yan-Li, Z., et al., *Effect of secondary radiation force on aggregation between encapsulated microbubbles.* Chinese Physics B, 2011. **20**(11): p. 114302.

60. Dayton, P.A., et al., *A preliminary evaluation of the effects of primary and secondary radiation forces on acoustic contrast agents.* IEEE Transactions on Ultrasonics, Ferroelectrics, and Frequency Control, 1997. **44**(6): p. 1264-1277.

61. Ferrara, K., R. Pollard, and M. Borden, *Ultrasound microbubble contrast agents: fundamentals and application to gene and drug delivery.* Annu Rev Biomed Eng, 2007. **9**: p. 415-47.

62. Chen, S., et al., *Efficient gene delivery to pancreatic islets with ultrasonic microbubble destruction technology.* Proc Natl Acad Sci U S A, 2006. **103**(22): p. 8469-74.

63. Tinkov, S., et al., *Microbubbles as ultrasound triggered drug carriers.* J Pharm Sci, 2009. **98**(6): p. 1935-61.

64. Endo-Takahashi, Y., et al., *Efficient siRNA delivery using novel siRNA-loaded Bubble liposomes and ultrasound.* Int J Pharm, 2012. **422**(1-2): p. 504-9.

65. Kandadai, M.A., et al., *Plasmin-loaded echogenic liposomes for ultrasound-mediated thrombolysis.* Transl Stroke Res, 2015. **6**(1): p. 78-87.

66. Shaw, G.J., et al., *Ultrasound-enhanced thrombolysis with tPA-loaded echogenic liposomes.* Thromb Res, 2009. **124**(3): p. 306-10.

67. Tiukinhoy-Laing, S.D., et al., *Ultrasound-facilitated thrombolysis using tissue-plasminogen activator-loaded echogenic liposomes.* Thromb Res, 2007. **119**(6): p. 777-84.

68. Laing, S.T., et al., *Ultrasound-enhanced thrombolytic effect of tissue plasminogen activator-loaded echogenic liposomes in an in vivo rabbit aorta thrombus model--brief report.* Arterioscler Thromb Vasc Biol, 2011. **31**(6): p. 1357-9.

69. Kopechek, J.A., et al., *Ultrasound-mediated release of hydrophilic and lipophilic agents from echogenic liposomes.* J Ultrasound Med, 2008. **27**(11): p. 1597-606.

70. Borden, M.A. and M.L. Longo, *Dissolution Behavior of Lipid Monolayer-Coated, Air-Filled Microbubbles: Effect of Lipid Hydrophobic Chain Length.* Langmuir, 2002. **18**(24): p. 9225-9233.

71. Feshitan, J.A., et al., *Systemic oxygen delivery by peritoneal perfusion of oxygen microbubbles.* Biomaterials, 2014. **35**(9): p. 2600-6.

72. Kheir, J.N., et al., *Oxygen gas-filled microparticles provide intravenous oxygen delivery.* Sci Transl Med, 2012. **4**(140): p. 140ra88.

73. Kwan, J.J., et al., *Theranostic oxygen delivery using ultrasound and microbubbles.* Theranostics, 2012. **2**(12): p. 1174-84.

74. Polizzotti, B.D., et al., *Optimization and characterization of stable lipid-based, oxygen-filled microbubbles by mixture design.* J Biomed Mater Res B Appl Biomater, 2014. **102**(6): p. 1148-56.

75. Swanson, E.J., et al., *Phospholipid-stabilized microbubble foam for injectable oxygen delivery.* Langmuir, 2010. **26**(20): p. 15726-9.

76. Tong, J., et al., *Mesenchymal stem cell transplantation enhancement in myocardial infarction rat model under ultrasound combined with nitric oxide microbubbles.* PLoS One, 2013. **8**(11): p. e80186.

77. Wang, C., et al., *Intravenous release of NO from lipidic microbubbles accelerates deep vein thrombosis resolution in a rat model.* Thromb Res, 2013. **131**(1): p. e31-8.

78. Eisenbrey, J.R., et al., *Development of an ultrasound sensitive oxygen carrier for oxygen delivery to hypoxic tissue.* Int J Pharm, 2014. **478**(1): p. 361-367.

79. Swanson, E.J. and M.A. Borden, *Injectable oxygen delivery based on protein-shelled microbubbles.* Nano LIFE, 2010. **01**(03n04): p. 215-218.

80. Cavalli, R., et al., *Preparation and characterization of dextran nanobubbles for oxygen delivery.* Int J Pharm, 2009. **381**(2): p. 160-5.

81. Bisazza, A., et al., *Microbubble-mediated oxygen delivery to hypoxic tissues as a new therapeutic device.* Conf Proc IEEE Eng Med Biol Soc, 2008. **2008**: p. 2067-70.

82. Cavalli, R., et al., *Ultrasound-mediated oxygen delivery from chitosan nanobubbles.* Int J Pharm, 2009. **378**(1-2): p. 215-7.

83. Bloch, S.H., et al., *Optical observation of lipid- and polymer-shelled ultrasound microbubble contrast agents.* Applied Physics Letters, 2004. **84**(4): p. 631-633.

84. Van Liew, H.D. and M.E. Burkard, *Bubbles in circulating blood: stabilization and simulations of cyclic changes of size and content.* J Appl Physiol (1985), 1995. **79**(4): p. 1379-85.

85. Burkard, M.E. and H.D. Van Liew, *Oxygen transport to tissue by persistent bubbles: theory and simulations.* J Appl Physiol (1985), 1994. **77**(6): p. 2874-8.

86. Van Liew, H.D. and M.E. Burkard, *Relationship of oxygen content to PO2 for stabilized bubbles in the circulation: theory.* J Appl Physiol (1985), 1996. **81**(1): p. 500-8.

87. Borden, M.A. and M.L. Longo, *Oxygen Permeability of Fully Condensed Lipid Monolayers.* The Journal of Physical Chemistry B, 2004. **108**(19): p. 6009-6016.

88. Pu, G., M.L. Longo, and M.A. Borden, *Effect of microstructure on molecular oxygen permeation through condensed phospholipid monolayers.* J Am Chem Soc, 2005. **127**(18): p. 6524-5.

89. Dayton, P.A., et al., *Optical and acoustical observations of the effects of ultrasound on contrast agents.* IEEE Trans Ultrason Ferroelectr Freq Control, 1999. **46**(1): p. 220-32.

90. Dressaire, E., et al., *Interfacial Polygonal Nanopatterning of Stable Microbubbles.* Science, 2008. **320**(5880): p. 1198-1201.

91. Eisenbrey, J.R., et al., *Sensitization of Hypoxic Tumors to Radiation Therapy Using Ultrasound-Sensitive Oxygen Microbubbles.* Int J Radiat Oncol Biol Phys, 2018. **101**(1): p. 88-96.

92. Legband, N.D., et al., *Evaluation of Peritoneal Microbubble Oxygenation Therapy in a Rabbit Model of Hypoxemia.* Biomedical Engineering, IEEE Transactions on, 2015. **PP**(99): p. 1-1.

93. McEwan, C., et al. *Oxygen Carrying Microbubbles for Enhanced Sonodynamic Therapy of Hypoxic Tumors*. in *The 20th European Symposium on Ultrasound Contrast Imaging*. 2015. Rotterdam, the Netherlands.

94. McEwan, C., et al., *Oxygen carrying microbubbles for enhanced sonodynamic therapy of hypoxic tumours.* J Control Release, 2015. **203c**: p. 51-56.

95. McEwan, C., et al., *Combined sonodynamic and antimetabolite therapy for the improved treatment of pancreatic cancer using oxygen loaded microbubbles as a delivery vehicle.* Biomaterials, 2016. **80**: p. 20-32.

96. Fix, S.M., et al., *Oxygen microbubbles improve radiotherapy tumor control in a rat fibrosarcoma model - A preliminary study.* PLoS One, 2018. **13**(4): p. e0195667.

97. Sun, J., et al., *Ultrasound-mediated destruction of oxygen and paclitaxel loaded lipid microbubbles for combination therapy in hypoxic ovarian cancer cells.* Ultrason Sonochem, 2016. **28**: p. 319-326.

98. Liu, L., et al., *Ultrasound-mediated destruction of paclitaxel and oxygen loaded lipid microbubbles for combination therapy in ovarian cancer xenografts.* Cancer Lett, 2015. **361**(1): p. 147-54.

99. Luo, T., et al., *Ultrasound-mediated destruction of oxygen and paclitaxel loaded dual-targeting microbubbles for intraperitoneal treatment of ovarian cancer xenografts.* Cancer Lett, 2017. **391**: p. 1-11.

100. Tachibana, K., L.B. Feril, Jr., and Y. Ikeda-Dantsuji, *Sonodynamic therapy.* Ultrasonics, 2008. **48**(4): p. 253-9.

101. Abdel-Latif, A., et al., *Adult bone marrow-derived cells for cardiac repair: a systematic review and meta-analysis.* Arch Intern Med, 2007. **167**(10): p. 989-97.

102. Buchanan, K.D., et al., *Echogenic liposome compositions for increased retention of ultrasound reflectivity at physiologic temperature.* J Pharm Sci, 2008. **97**(6): p. 2242-9.

103. Huang, S.L., et al., *Nitric oxide-loaded echogenic liposomes for nitric oxide delivery and inhibition of intimal hyperplasia.* J Am Coll Cardiol, 2009. **54**(7): p. 652-9.

104. Kim, H., et al., *Nitric oxide-loaded echogenic liposomes for treatment of vasospasm following subarachnoid hemorrhage.* Int J Nanomedicine, 2014. **9**: p. 155-65.

105. Sutton, J.T., et al., *Pulsed ultrasound enhances the delivery of nitric oxide from bubble liposomes to ex vivo porcine carotid tissue.* Int J Nanomedicine, 2014. **9**: p. 4671-83.

106. Subbotin, V.M., *Analysis of arterial intimal hyperplasia: review and hypothesis.* Theor Biol Med Model, 2007. **4**: p. 41.

107. Lee, S.Y., et al., *A novel liposomal nanomedicine for nitric oxide delivery and breast cancer treatment.* Biomed Mater Eng, 2014. **24**(1): p. 61-7.

108. Hirst, D. and T. Robson, *Targeting nitric oxide for cancer therapy.* J Pharm Pharmacol, 2007. **59**(1): p. 3-13.

109. Peng, T., et al., *Therapeutic time window and dose dependence of xenon delivered via echogenic liposomes for neuroprotection in stroke.* CNS Neurosci Ther, 2013. **19**(10): p. 773-84.

CHAPTER 4[1]

IMPROVING THE EFFICACY OF RADIATION THERAPY WITH OXYGEN MICROBUBBLES

4.1 MOTIVATION AND OVERVIEW

Solid tumor microenvironments are characterized by a disorganized, leaky vasculature that promotes regions of low oxygenation (hypoxia). Hypoxia leads to resistance in all major treatment modalities, including radiation therapy, and methods of reoxygenation have long been of interest. Despite decades of research and a diversity of approaches, no methods of solid tumor reoxygenation have entered clinical practice, and controlled delivery of oxygen remains a challenge. Here, we apply the concepts explored in chapter 3 to investigate the potential of lipid-stabilized oxygen microbubbles to reoxygenate solid tumors and therefore improve the therapeutic ratio of radiation therapy.

4.2 BACKGROUND

Cancer affects 39.6% of Americans at some point during their lifetime [1]. Solid tumors are characterized by the presence of disorganized, tortuous, leaky vessels that promote regions of hypoxia, Figure 4.1. Even small tumors (<2-3mm^3) comprise 10-30% of hypoxic regions in the form of chronic and/or transient hypoxia fluctuating over the course of seconds to days [2, 3]. In fact, it has been shown repeatedly that hypoxia is a key factor in treatment failure and recurrence after treatments with radiotherapy (RT), chemotherapy and surgery [4-6]. Chronic exposure to this hypoxic environment selects for the most aggressive and resistant tumor cells and triggers the angiogenic

[1]This chapter previously appeared as an article in the journal PLOS ONE distributed under the terms of the Creative Commons License (http://creativecommons.org/licenses/by/4.0/). The original citation is as follows: Fix, S.M.* and Papadopoulou, V.*, Kasoji S., Velds, H., Borden, M.A., Chang, S., Rivera. J., Dayton, P.A. (2018). "Oxygen microbubbles improve radiotherapy tumor control in a rat fibrosarcoma model - A preliminary study." PLoS One **13**(4): e0195667. Only minor changes were made in reformatting this article into the chapter presented here.
*Samantha Fix and Dr. Virginie Papadopoulou contributed equally to the production of the original manuscript. The article was originally written by VP, but the experiments and analyses within were performed as a joint effort between SMF and VP.

signaling that contributes to the overall growth of the tumor as it develops its own blood supply network. It is therefore recognized as a hallmark of metastatic potential [7-11].

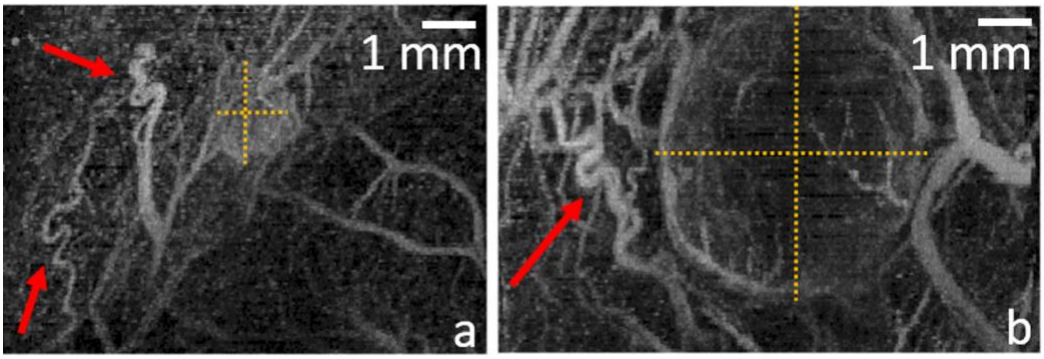

Figure 4.1: Images of tumor-associated vasculature. Example of acoustic angiography maximum intensity projections around tumors (tumor size denoted with dashed yellow lines) in a rat fibrosarcoma allograft, with tortuous angiogenesis extending beyond the tumor margins (red arrows). The small tumor (A) is also shown to be more enhanced, denoting its higher perfusion compared to the larger tumor (B).

Radiotherapy is one of the key primary treatment options for a variety of cancers and is used in over one million cancer patients yearly in the United States [12-14]. It is well-established that tumor hypoxia negatively impacts treatment outcome for RT [15]. In particular, the RT dose needed to achieve the same tumor control probability in hypoxic tissue as in normoxic tissue can be up to 3 times higher [4]. Hypoxia promotes radioresistance directly through the reduction of oxygen-dependent free radical damage and indirectly through biological HIF-1 complex signaling. The tumor re-oxygenation which occurs normally after RT also increases oxidative stress, leading to endothelial sensitization at the tumor level [16-18].

It is believed that transiently relieving tumor hypoxia during radiotherapy (RT) could significantly improve treatment outcome [19]. Previous *in vitro* studies have shown that increased oxygen presence even just a few milliseconds before or after RT significantly increases radiation-induced cancer cell damage [20]. There have been numerous previous attempts to re-oxygenate tumors to this effect, including hyperbaric oxygenation, inhaled carbogen, nitroimidazoles and other radiosensitizers. However, practical administration difficulties, vasoconstriction and normal tissue toxicity have severely limited clinical translation [21-23].

Recently, the technology of oxygen microbubbles (OMB) has made several substantial advances, with the development of high-payload OMBs similarly formulated to micrometer-sized ultrasound vascular contrast agents but comprising an oxygen gas core [24]. As such, OMBs have shown promise experimentally as an adjuvant cancer therapy in vivo to enhance the efficacy of oxygen-dependent therapies. In radiotherapy, they would offer the ability for localized oxygen delivery without the use of expensive dedicated equipment incompatible with radiation therapy rooms. The robust oxygen-delivery potential of OMBs is demonstrated by their ability to sustain animals with otherwise fatal pneumothorax for over two hours [25], and double the survival time of asphyxiated animals [26] when delivered intra-peritoneally. In a mouse model of pancreatic cancer, OMBs delivered by direct injection in the tumor have also been shown to improve the efficacy of sonodynamic therapy [27, 28]. In chemotherapy, oxygen and paclitaxel loaded microbubbles administered intravenously have shown promise as a combination therapy in an ovarian mouse xenograft model [29].

We hypothesize that these oxygen microbubbles could also be used to transiently relieve tumor hypoxia and thereby improve RT outcome if administered prior to treatment so that additional oxygen is present during radiation treatment. As a first proof of principle demonstration, in this work, we assess the potential of oxygen microbubbles to increase dissolved oxygen saturation in hypoxic solutions *in vitro*, increase tumor oxygenation in a rat fibrosarcoma *in vivo* after direct injections, and improve tumor control after RT.

4.3 MATERIALS AND METHODS

4.3.1 MICROBUBBLE MANUFACTURING AND CHARACTERIZATION

All glassware was cleaned with an Alconox detergent purchased from Sigma-Aldrich (St. Louis, MO, USA) and rinsed with 18 MΩ-cm deionized water (Direct-Q, Millipore; Billerica, MA, USA). A concentrated (10×) phosphate-buffered saline (PBS) solution from Sigma-Aldrich (St. Louis, MO, USA) was diluted to normal concentration with deionized water and vacuum filtered through a 0.2 µm nylon membrane filter (Whatman, Kent, United Kingdom). Phospholipid 1,2-distearoyl-sn-glycero-3-phosphocholine (DSPC) was purchased from NOF (Tokyo, Japan), and polyoxyethylene-40 stearate

(PEG-40S) was purchased from Sigma-Aldrich (St. Louis, MO, USA). Oxygen and nitrogen gas were purchased from Airgas (Airgas, Radnor, PA, USA).

DSPC and PEG-40S were weighed in dry form, mixed in a 9:1 molar ratio, and added to the filtered PBS solution to achieve a final lipid concentration of 12 mg/mL. A technique used by Feshitan et al. [25] was implemented to dissolve the DSPC and PEG-40S into the PBS solution and create a homogenous lipid solution. After adding the DSPC and PEG-40S, the mixture was heated to 65°C and homogenized using a Branson 450 sonifier (Danbury, CT, USA) with an output power of 25% total capability. The solution was sonicated until it appeared translucent and then stored in the refrigerator at 4°C. Oxygen microfoam was created from a process design developed by Swanson et al. [30] to produce large volumes of oxygen microbubbles. The process developed was used to create oxygen microbubbles specifically, but the methodology is the same to produce nitrogen microbubbles with the exchange of oxygen for nitrogen gas. The process comprised an ultrasonic horn reactor enclosed in a water-cooled, continuous-flow chamber (Branson, Danbury, CT, USA). The lipid solution was kept cool with ice packs and combined with room temperature oxygen in the reactor. The lipid solution flow rate was nearly double the flow rate of oxygen. Full sonication power was used in the reactor to emulsify the oxygen gas and the sonicated solution was collected in a cooling column to separate the oxygen microbubbles (bottom) from the macrofoam (top). The column was extracted into 60-mL syringes and centrifuged to further concentrate the oxygen microbubbles. The 60-mL syringes were placed in an Eppendorf 5804 centrifuge (Hauppauge, NY, USA) and centrifuged at 150 relative centrifugal force (RCF) for 4 min to yield a final concentration of ~70 vol%. The concentrated oxygen microbubble foam was transferred into 20-mL glass serum vials (Wheaton, Millville, NJ, USA), sealed with an oxygen headspace, and stored at 5°C. The remaining centrifuged lipid solution was recycled and the process was repeated until the desired volume of 70 vol% oxygen microbubbles was produced. The concentration and size distribution of the oxygen microbubbles (OMBs) (n=3 independent samples) were measured using the Coulter Counter method (Coulter Multisizer III, Beckman Coulter, Indianapolis, IN, USA). The same methodology described above was used to make concentrated nitrogen microbubbles (NMBs) by just replacing the oxygen gas with room temperature nitrogen gas.

To extract microbubbles from a vial to be used in experiments, microbubbles were slowly pulled into a syringe through a 20-gauge needle, while a bag filled with 100% oxygen was connected to another needle in the vial top (to avoid creating a vacuum in the vial that could compromise the bubbles' integrity, as well as minimize the introduction of room air into the vial).

4.3.2 *IN VITRO* OXYGEN RELEASE

A fiber-optic oxygen sensor (Oxymicro, WPI, Sarasota, FL, USA) was used to measure the dissolved oxygen content in deionized water before and after microbubble injection. Prior to use, the device was calibrated according to manufacturer's instructions for a standard two-point calibration in oxygen-free water and water vapor saturated air. Calibration for automatic temperature compensation was not performed since all experiments were performed in quick succession at room temperature (centrally maintained at 22°C).

For the measurement, a beaker with 70 mL of partially degassed deionized water containing a magnetic stirrer was placed on a stir plate for continuous mixing, and the fiber-optic measurement device recorded continuously before, during, and after OMB and NMB injections. Injections consisted of 300 µL undiluted OMBs or NMBs. Experiments were repeated thrice with independent vials of OMBs or NMBs and measurements were recorded continuously before and for at least 5 min post microbubble injection. The maximum change in dissolved oxygen saturation over the 5 min post-injection was compared between OMB and NMB groups.

4.3.3 ANIMAL MODEL FOR ALL *IN VIVO* STUDIES

All animal procedures were approved by the Institutional Animal Care and Use Committee of the University of North Carolina at Chapel Hill and performed in accordance with the Guide for the Care and Use of Laboratory Animals of the National Institutes of Health. Female Fischer 344 rats with subcutaneous fibrosarcoma (FSA) tumor allografts were used in all *in vivo* experiments. This model was chosen as the development of hypoxia in these FSA tumors has been extensively characterized [31-34]. These previous studies demonstrate hypoxia through EF5 and pimonidazole immunostaining, in addition to direct detection of pO_2 in the tumor tissue with microelectrodes. Results demonstrate

moderate hypoxia throughout much of the tumor and more severe hypoxia towards the tumor center. Briefly, tumor allografts grew after subcutaneous implantation on the right flank of 1 mm^3 fibrosarcoma (FSA) tissue freshly resected from donor tumor-bearing rats. Animals were used for experiments 2-3 weeks after implantation, when tumors were around 1 cm in diameter. The following standardized anesthesia protocol was followed for all tumor hypoxia measurements and for radiotherapy treatment studies. Anesthesia was induced by placing the animals in an induction box for 3 min to breathe 5% vaporized isoflurane with pure oxygen as the carrier gas. Anesthesia was maintained by having the animals breathe 2.0-2.5% isoflurane with medical air as the carrier gas for the remainder of the experiment. The timing of this anesthesia protocol and the use of medical air for the primary carrier gas allowed for consistent tumor hypoxia measurements and minimized changes in blood oxygenation due to pure oxygen breathing rather than microbubble intervention. The animals' temperatures were maintained throughout the experiments using a heated platform. When ultrasound imaging was used to evaluate tumor volume (unrelated to measuring tumor hypoxia), animals were anesthetized using vaporized isoflurane (initially 5% for induction, then 2.0-2.5%) with oxygen carrier gas.

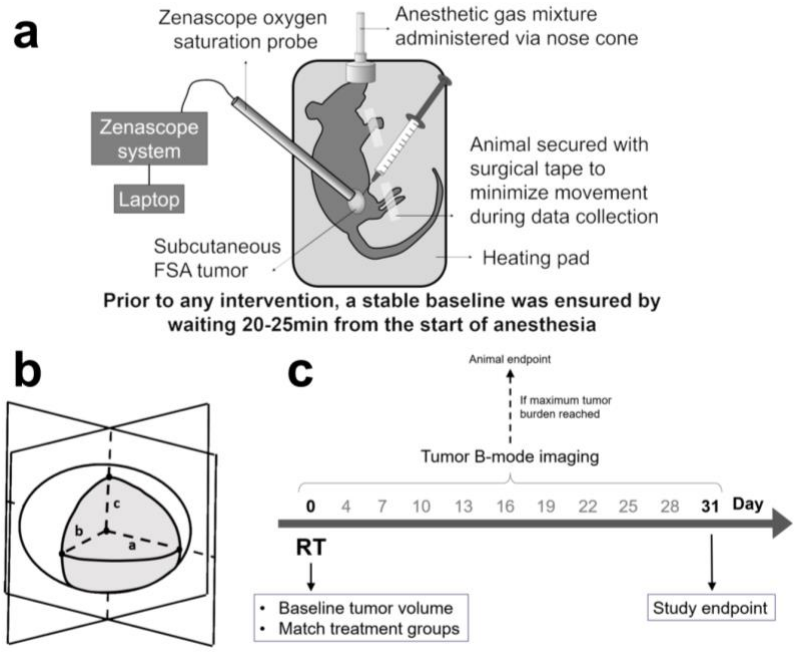

Figure 4.2: Experimental procedures. A) Schematic of the experimental setup used for *in vivo* hypoxia modulation measurements using the Zenascope system. B) Schematic of tumor volume assessment via B-mode ultrasound imaging. Two cross-sectional images were acquired, and lengths a, b and c were used to calculate tumor volume. C) Radiotherapy pre- and post-imaging experimental protocol.

4.3.4 *IN VIVO* OXYGEN RELEASE

Fischer rats with FSA tumors were anesthetized as described above, and the tumor area was shaved. Tumor oxygenation was measured continuously in real-time using a validated optical spectroscopy technique based on the absorbance of oxyhemoglobin and deoxyhemoglobin (Zenascope, Zenalux Biomedical, Durham, NC, USA). Figure 4.2 shows a schematic of the experimental setup for these measurements. Each experiment was capped at one hour from the start of anesthesia. Prior to any intervention, a stable baseline was ensured by waiting 25 min from the start of anesthesia. An oxygen challenge, defined as changing the isoflurane carrier gas from medical air to pure oxygen for 3 min, served as a positive control to ensure that an increase in blood oxygenation could be measured reliably in the tumor. Tumor hypoxia level was measured continuously before and after the following interventions.

1) OMB administration: 500 µL undiluted OMB injected intra-tumorally slowly over 30 s (n=4)
2) Nitrogen microbubble (NMB) administration (negative control): 500 µL undiluted NMB injected intra-tumorally slowly over 30 s (n=4)

The primary objective of this experiment was to characterize the ability of intratumoral OMB administration to reoxygenate FSA tumors, and a secondary objective was to confirm baseline hypoxia in this tumor model.

4.3.5 RADIOTHERAPY EXPERIMENTS

Animals were anesthetized with isoflurane and oxygen carrier gas and positioned on a heated pad, similar to Figure 4.2. Two-dimensional B-mode ultrasound imaging was used to calculate tumor volume (Acuson Sequoia 512, Mountain View, CA, USA). The largest tumor cross-sections in the sagittal and transverse planes were selected and saved after moving the transducer along these directions on a 3D motion stage. Tumor volumes were then calculated using the ellipsoid volume formula, $V = \frac{4}{3}\,\pi\,a\,b\,c$, where *V* is the calculated tumor volume, *a* is half the measured tumor width on the sagittal plane, *b* is half the measured tumor width on the transverse plane, and *c* is half the measured tumor depth (taking the average between the sagittal and transverse planes), Figure 4.2.

For a fixed dose of RT, it is well established that tumor control is strongly correlated to the initial tumor volume on the day of treatment [35-41]. Since this study aims to evaluate the feasibility of using OMBs to improve radiotherapy outcome (tumor control), a matched study design with respect to initial tumor volume on the day of radiotherapy was chosen to limit the animal numbers needed. Since both the effect size of OMB and OMB dosing per tumor size are unknown prior to the study, this strategy allows us to see how the results scale with respect to tumor volume and can then serve as a basis for a larger study (see Discussion for a full explanation).

For this reason, care was taken to match initial tumor sizes on the RT day between treatment groups. Tumor volume matching was achieved by implanting a few extra animals to allow selecting the closest tumor volumes possible and ordering animals into similarly sized groups after imaging, then randomizing treatment group assignment within these ordered categories. To minimize other biological variability within each experimental round, all animals were ordered on the same day (of similar age), had the same time to acclimatize to the vivarium before tumor implantation, were implanted on the same day from the same donor tumor, and were treated on the same day. Hydration and wet food packs were given to all animals irrespective of treatment (or no treatment) group. The experimental rounds resulting from this matching protocol are summarized in Table 4.1 and described hereafter.

Table 4.1: Experimental rounds for the radiotherapy experiments. Animals were matched according to initial tumor volume on the day of radiotherapy, and experiments were repeated in two separate rounds: round 1 consisted of n=2 animals per group and round 2 of n=4 animals per group (where the experimental group conditions of 'OMB alone' and 'No treatment' were also added). Within each experimental round, the animals were the same age, had the same amount of time to acclimatize to the vivarium before tumor implantation, were implanted on the same day from the same donor tumor, and were treated on the same day.

	RT	**RT + OMB**	**RT + NMB**	**OMB alone**	**No treatment**
ROUND 1	n=2	n=2	n=2		
ROUND 2	n=4	n=4	n=4	n=4	n=4

A total of 18 animals were matched between radiotherapy treatment groups, 1) RT alone, 2) RT+OMB and 3) RT+NMB as described above, in two rounds of experiments (n=2 per group in the first round, then n=4 per group in the second round, total of n=6 per group). Radiotherapy consisted of a single 15 Gy dose of 6 MV photons (2 cm $\times$ 2 cm field size) delivered using a clinical linear

accelerator (Siemens Healthcare, Malvern, PA, USA), following a previously described protocol from our group [42]. Animals were anesthetized as described above (standardized protocol with medical air as the carrier gas) and positioned on a heating pad on top of the clinical accelerator table. The skin around the tumor was gently extended and taped so that the tumor was positioned outward from the body to avoid irradiating vital organs, and a 1 cm thick tissue-mimicking bolus was placed on top of the tumor to correct for normal tissue attenuation of the radiation field meant for deeper tumors. The patient table height was adjusted using light field crosshair projected on paper prior to the start of radiation therapy. Animals in the groups receiving microbubbles were injected with 1 mL undiluted OMBs or NMBs intra-tumorally immediately prior to the start of RT (since we are using a clinical linear accelerator for treatment, in practice it takes 1 min to leave the treatment room and start the treatment protocol). Following RT, tumor volume was measured using B-mode ultrasound as previously described every 3 days for 31 days, as shown in Figure 4.2, or until the tumor reached 2.5 cm in the largest dimension, at which point animals were humanely sacrificed. Animals were sacrificed via isoflurane overdose followed by thoracotomy as a secondary means of euthanasia.

4.3.6 EFFECT OF OMB ADMINISTRATION IN THE ABSENCE OF RADIOTHERAPY

During the second round of radiotherapy experiments, an additional two conditions were tested: no treatment (n=4) and OMB alone without RT (n=4) and all animals in this round were also matched for initial tumor volume as previously described.

4.3.7 DATA ANALYSIS AND STATISTICAL METHODS

All data are presented as mean ± standard deviation unless otherwise stated. Statistical significance was set a priori at $p<0.05$ (*). For *in vitro* and *in vivo* oxygen release measurements, the maximum difference in dissolved oxygen content after microbubble injection was compared between the nitrogen and oxygen groups using a Student's t-test. For radiotherapy experiments, matched statistical comparison tests on the RT 'tumor control time,' defined as the time (in days) to reach maximum tumor burden, between the treatment groups were performed. Either repeated measures ANOVA with Newman-Keuls multiple comparison post-test was performed after confirming normality,

or Friedman test with Tukey's post-test was performed after negative normality test. Animals below the maximum tumor burden at day 31 were included as day 32 in these tests.

4.4 RESULTS

4.4.1 MICROBUBBLE CHARACTERIZATION AND *IN VITRO* OXYGEN RELEASE

Microbubble concentration was measured as 1.3 (±0.4) × 10^9 mL^{-1}, and median bubble size was around 4 µm, as shown in Figure 4.3 A. *In vitro* dissolved oxygen saturation measurements were significantly increased with the addition of 300 µL OMBs into 70 mL water by 14.2 ± 7.2% compared to adding NMBs (p=0.04, n=3 independent samples).

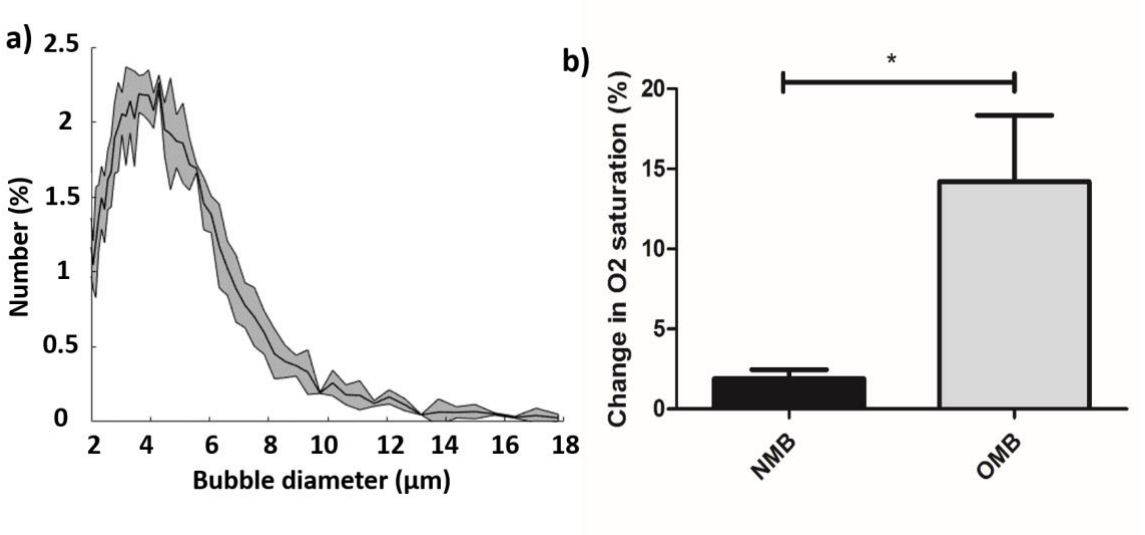

Figure 4.3: *In vitro* oxygen microbubble characterization. A) Measured oxygen microbubble size distribution, displayed with a diameter bin size of 0.032 µm, as mean ± standard deviation (gray area) from 3 independent samples; A) Measured change in oxygen % saturation *in vitro* after 300 µL OMB (n=3) or NMB (n=3) injection into 70 mL partially degassed water (p<0.05).

4.4.2 *IN VIVO* OXYGEN RELEASE RESULTS

Consistent real-time oxygenation dynamics were recorded using a non-invasive spectroscopic measurement system by assuring prior to any intervention that sufficient time was given to achieve a stable baseline during anesthesia. OMBs were shown to increase tumor oxygenation, whereas NMBs lowered tumor oxygenation (Figure 4.4). Tumors used for this study

ranged in diameter from 5 mm – 17 mm, approximately matching the range of tumor sizes used for subsequent radiotherapy experiments.

The average baseline percent hemoglobin saturation across all 8 tumors used for this experiment was 55 ± 30% (range from 0 – 83% hemoglobin saturation). These data demonstrate that the FSA model used here is indeed hypoxic. It is important to mention, however, a limitation of the Zenalux measurement system. This system measures hemoglobin saturation via optical spectroscopy. Therefore, it cannot accurately measure hypoxia deep within tissue due to the limited penetration depth of light. And thus, for large tumors we are likely measuring hemoglobin saturation only at the outer edge of the tumor rather than the center, biasing our values to be higher than what would be observed at the tumor's center. We believe that the percent hemoglobin saturation reported here is conservative, and the tumors' centers were likely more hypoxic than what we report.

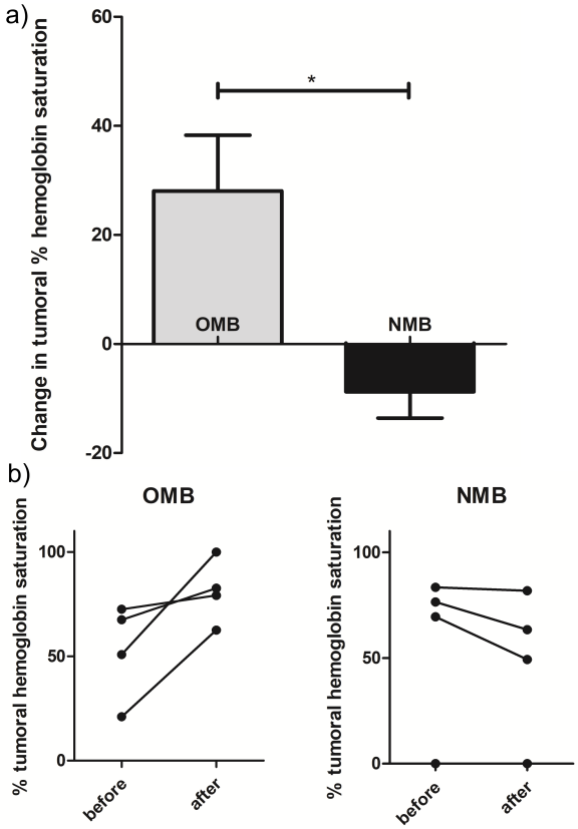

Figure 4.4: Change in tumoral oxygenation with intra-tumoral injection of OMB or NMB. The time to peak was found to be 97 s after injection on average, and the OMB-induced increase in tumoral oxygenation lasted for over 18 min on average (our protocol's maximum 1 h experiment time meant that we could not wait for a complete return to baseline in some cases). A) Average peak change in tumoral hemoglobin saturation after OMB or NMB administration (n=4/group). B) Individual data points showing pre- and post-injection values. This demonstrates baseline hypoxia in all tumors (0-83% hemoglobin saturation across all 8 tumors).

4.4.3 RADIOTHERAPY RESULTS

Table 4.2 details all results from the radiotherapy experiments, for both rounds and including all controls. In Round 2, we included two additional control groups (No treatment and OMB alone, n=4/group) to ensure that the OMB administration did not influence tumor growth in the absence of RT. Indeed, no significant difference was shown in tumor control between the animals receiving no treatment and those having received a single OMB administration in the absence of any radiation treatment, as shown in Figure 4.5. Note: these controls were not included in Round 1 of this study. Therefore, the number of animals and range of tumor sizes tested for these control groups did not match the entire range of tumor sizes used for the radiation treatment groups (RT, RT+NMB, and RT+OMB). As such, we have not drawn direct comparisons between tumor control time of the No treatment and OMB only groups (Figure 4.5) with those of the three radiation treatment groups (Figure 4.6).

Table 4.2: Individual data points for radiotherapy tumor control times (in days). Data is stratified by matched initial tumor size for each group, showing RT effect size depends on initial tumor volume.

	Matched initial tumor volume (cm^3)	Tumor control (in days) for the different treatment groups					Increase in tumor control between RT and RT+OMB	
		No treat-ment (n=4)	OMB alone (n=4)	RT + NMB (n=6)	RT (n=6)	RT + OMB (n=6)	In days: (RT+OMB) - RT	As percentage (%): (RT+OMB) / RT * 100 - 100
ROUND 2	0.1 ± 0.0	32	32	32	32	32	0	0
	0.3 ± 0.1	25	19	32	32	32	0	0
	0.6 ± 0.1	10	19	22	22[a]	31	9	41
	0.8 ± 0.1	10	10	22	22	28	6	27
ROUND 1	1.7 ± 0.2			10	16	22	6	38
	2.8 ± 0.3			7	7	10	3	43

[a]Animal died prior to experimentation end, value replaced from the NMB group since no overall difference was found between these two groups.

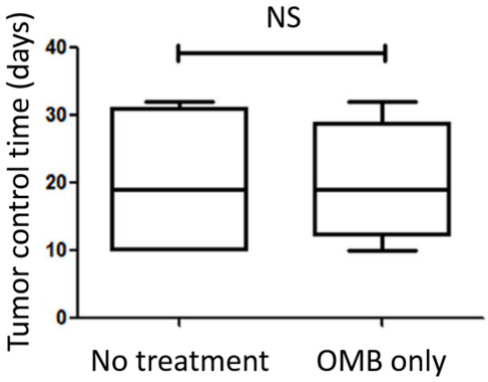

Figure 4.5: A single oxygen microbubble administration alone does not influence tumor control. No significant difference was found between the no treatment and oxygen microbubble group in the absence of any radiotherapy (n=4 per group). Box-and-whisker plots represent all data from the No treatment and OMB alone controls.

From the animals receiving RT, 17/18 successfully completed the study (one of the rats in the RT alone group died during anesthesia prior to the completion of the RT treatment protocol and was therefore excluded from the analysis). Initial RT results show that intra-tumoral OMBs improve tumor control after radiotherapy ($p<0.05$, n=6 per group), Figure 4.6, and initial tumor size significantly affects RT outcome, Table 4.2.

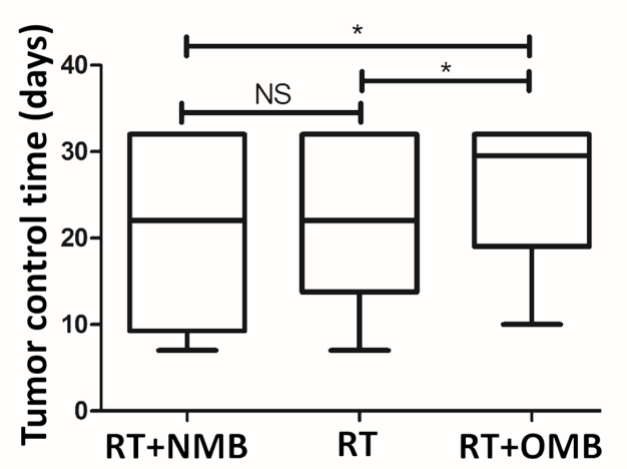

Figure 4.6: Tumor control time comparison between RT groups. OMBs significantly improve RT outcome, whereas NMBs as control do not (n=6 per group). Box-and-whisker plots show all data from the three radiotherapy treatment groups.

4.5 DISCUSSION

4.5.1 OMBs MODULATE TUMOR HYPOXIA

In this study, we demonstrate the oxygen payload of OMBs *in vitro* and *in vivo*, before showing that they can be used to significantly improve radiotherapy tumor control in a fibrosarcoma model *in vivo*. *In vitro*, the addition of OMBs to hypoxic solution increases the amount of dissolved oxygen, as expected, and has significantly higher effect than that of the NMB control. The very slight increase shown with NMBs is due to the fact that these measurements were collected over a 5 min period, so the liquid uptakes oxygen molecules through its surface area in contact with ambient air over this time (gas exchange towards equilibrium). *In vivo*, direct OMB injections into fibrosarcoma tumors are shown to significantly increase tumoral oxygenation, whereas the NMB injection control had the opposite effect. This increase is very fast (peaks around 90 s post injection) and remains

elevated for over 15 min, which is consistent with the improved tumor control observed when combining RT with OMB administration *in vivo*.

4.5.2 RADIOTHERAPY IMPROVEMENT DEPENDENCY ON INITIAL TUMOR VOLUME

The results show that for a fixed RT dose and fixed OMB dose, the gain in tumor control time depends on initial tumor volume, Table 4.2. As expected, we found that OMB administration offered the greatest benefit for intermediately sized tumors (initial volume 0.6-1.7 cm^3). Over this size range, we observed survival benefits of 6-9 days (OMB+RT vs. RT alone), Table 4.2 and Figure 4.7. Conversely, for very small tumors (<0.5 cm^3 initial volume), the tumors likely have not yet developed extensive hypoxia, and the radiotherapy dose is already very efficient for tumor control. Thus, OMBs do not significantly improve the RT efficacy for small tumors (Figure 4.7). This observation is also biased by the fact that our observation time was capped at 31 days, resulting in right censoring of all tumors that were still controlled by that time. For very large tumors (>2 cm^3 initial volume), the absolute gain in tumor control (in days) drops (Figure 4.7). Since these are likely to be very hypoxic, and we are always injecting the same OMB dose, this is probably not enough to reoxygenate these large tumors efficiently, thus limiting therapeutic gain. Interestingly, when comparing the increase in tumor control offered by OMB administration as a percentage of that offered by RT alone, we find fairly consistent improvement of ~35% for all tumors larger than a threshold initial volume of 0.5 cm^3 (Table 4.2, rightmost column).

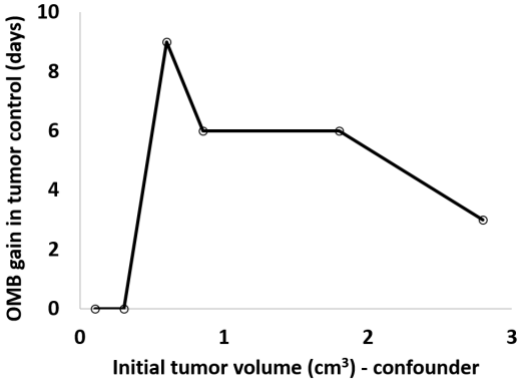

Figure 4.7: Tumor control time vs. initial tumor volume. An on/off effect (threshold) is observed around 0.5 cm^3 initial tumor volume. Below this size, tumors are controlled for 31 days with RT alone. Above this size, tumors are large enough that RT alone cannot control them for 31 days, and, therefore, OMB administration can provide a substantial improvement in tumor control time. Additionally, the benefit offered by OMB administration diminishes as initial tumor volume exceeds ~2 cm^3.

With further optimization, we do believe that OMB administration holds the potential to offer meaningful improvements in RT-mediated tumor control over a wide range of tumor volumes. Here, OMB did not improve RT outcomes for those rats with small tumors simply because the RT dose administered was already sufficient to provide a near complete response. We hypothesize that if the RT dose was reduced for this cohort of animals, we would still be able to achieve complete tumor regression through the administration of OMBs. This is attractive, since lowering the RT dose would reduce exposure of healthy tissue to radiation and limit associated side effects. Similarly, we believe that we could achieve more substantial control of large tumors by either increasing the OMB dose, RT dose, or both.

4.5.3 LIMITATIONS AND FUTURE WORK

A limitation of this study is the relatively small sample size used in the assessment of OMB administration for improved RT. Nevertheless, our results are consistent between two completely independent rounds of experiments, and the benefit offered by OMB administration is large enough to be statistically significant despite the relatively small sample size. It is reasonable to assume that optimization of the dosages and administration can result in even greater improvement in tumor control. Now that a first demonstration has been established including a comparison to NMB administration, a future study could concentrate on establishing the radiotherapy dose-modifying factor (DMF) resulting from OMBs (i.e., the reduction in RT dose required to achieve the same tumor control probability when OMBs are administered as an adjunct therapy). To do so, animals are randomized between the RT alone and RT+OMB groups, and the RT dose necessary to control 50% of tumors is calculated from logistical regression for each group; DMF is then calculated as the ratio between these RT doses. Nevertheless, we estimate that a comprehensive assessment like the one described above requires n=100 animals from the preliminary data presented here and thus is not warranted until further OMB administration optimization is undertaken (see next Discussion section *Potential for clinical translation*).

Throughout this study, we used a rat FSA tumor model previously characterized to develop hypoxic tumors. We confirmed baseline hypoxia via spectroscopic measurement of hemoglobin

saturation. However, a limitation is that we did not confirm tumor hypoxia with a second method (e.g., immunostaining of key hypoxia markers). In future work, we plan to characterize tumor-size-dependent hypoxia and the effect of OMB administration on hypoxia in more detail using histology. We are also interested in studying in more detail the effect of tumor volume on the efficiency of OMB-mediated reoxygenation.

4.5.4 POTENTIAL FOR CLINICAL TRANSLATION

Despite considerable progress in early detection and treatment options in multiple cancers over the last decade, cancer remains difficult to treat in advanced disease stages and radioresistance and recurrence at the primary tumor site are significant clinical challenges.

4.5.4.1 DIRECT TUMORAL INJECTIONS

A number of solid tumors are accessible for direct injections clinically. In particular, head and neck cancer treated with external beam radiation therapy are particularly hypoxic [43, 44] yet shallow enough for direct injections. Furthermore, more deeply seated tumors such as those of the pancreas, liver, or colon can be accessed for intratumoral injection with ultrasound, endoscopic ultrasound or computed tomography image guidance [45]. Additionally, a direct access for OMB with RT can be found in brachytherapy (clinically approved) which uses guiding tubes to feed radiation sources inside solid tumors where they irradiate for a few seconds before being retracted or are left implanted for lower irradiation over time [46]. Therefore, this direct tumoral injection of OMBs could potentially be clinically translatable in the long term through brachytherapy co-administration (through one of the guiding tubes) or some needle-accessible solid tumors with external beam radiation.

In human clinical studies, intratumoral injections of 20-40% of the total tumor volume have been reported [45, 47]. Here, we provided a consistent intratumoral OMB dose of 0.5 mL, regardless of tumor volume. It is promising that we found substantial survival benefit for intermediately sized tumors (e.g., 1.7 cm^3), where the OMB injection volume corresponded to 28% of the tumor volume and was therefore within the clinically achievable range. Future efforts will be aimed at optimizing OMB dose with respect to baseline tumor hypoxia and tumor volume, after which we anticipate being

able to achieve substantial reoxygenation with relevant OMB dose volumes across a wide range of tumor sizes.

4.5.4.2 INTRAVENOUS ADMINISTRATION

Clinically, fractionated dose RT treatment plans, where smaller doses of radiation are administered repeatedly, typically five days a week over the course of several weeks or months, were developed to spare healthy tissue toxicity, taking advantage of the better repair capability of healthy tissue compared to tumor cells. Oxygen microbubbles are similarly formulated to microbubble ultrasound contrast agents used for imaging but comprise an oxygen gas core instead of heavy molecular weight gases. Due to their micrometer size scale, similar to that of a red blood cell, microbubble contrast agents are confined to the vascular space after being intravenously administrated and serve as an ultrasound blood pool marker. Depending on the pressure of the incident ultrasound wave, microbubbles will respond by either stably oscillating or by bursting.

Therefore, local release of oxygen from OMBs following intravenous administration could be achieved using focused ultrasound in the tumor region. This would be minimally invasive and greatly advantageous in the context of fractionated dose RT. Such local reoxygenation may allow for similar tumor control with even smaller radiation doses or fewer total treatments. We have previously demonstrated *in vitro* that ultrasound application significantly enhances oxygen delivery from OMB [48].

In addition to the potential use of ultrasound for image-guided locally triggered oxygen release in the tumor, its ability to make microbubbles oscillate also offers a useful therapeutic target in relation to RT. Indeed, it has been shown that inducing stable oscillation of non-oxygen microbubbles in the vasculature of the tumor with ultrasound prior to RT increases radiation damage to these tumor vessels in a mouse model of prostate cancer treated with radiotherapy [49]. In addition to inducing tumor cell death, RT also damages the endothelium of tumor vasculature, leading to additional tumor damage as it loses its blood supply network post-treatment [50, 51]. As such, endothelial sensitization using acoustically active agents such as microbubbles could offer an additional therapeutic target, as they mechanically oscillate near vessel boundaries under appropriate ultrasound conditions.

Importantly, this promising result was achieved with non-oxygen microbubbles, so we anticipate that the additional target of hypoxia modulation would further improve these results as they target a complementary radiosensitizing pathway.

Nevertheless, intravenous administration requires OMBs that are stable enough to reach the tumor and retain their oxygen gas before being disrupted by ultrasound locally. In principle, the oxygen payload of OMBs would be retained for a longer duration in circulation if the carrier gas is pure oxygen rather than air. Additionally, the OMB formulation used in this work was designed to achieve rapid oxygen release for peritoneal microbubble oxygenation [25, 26]. The OMBs could be reformulated to increase circulation persistence and oxygen payload delivery to the tumor vasculature following intravenous administration.

4.5.4.3 PARTICULAR IMPACT IN RT

Finally, two specific radiotherapy targets merit further mention with respect to OMB hypoxia modulation. First, stereotactic radiosurgery (SRS) and stereotactic body radiotherapy (SBRT) involve delivery of one or a few large dose fractions (e.g., 8-20 Gy) to the tumor volume. This approach has shown particularly promising results for inoperable early stage tumors (e.g., lung and prostate cancers) that are small, while sparing surrounding normal tissue from irradiation. However, many tumors are hypoxic and thus radioresistant. The SRS/SBRT procedures use only a few fractions and cannot take advantage of radiotherapy-induced tumoral re-oxygenation as the conventionally fractionated RT can (with 30 daily fractions). For fractionated RT, the surviving hypoxic cancer cells after one irradiation dose are re-oxygenated and so less hypoxic at the time of the next dose [52]. Since this is not the case for SRS and SBRT, hypoxia is deemed an even more important adjuvant therapeutic target for these treatments [53].

Secondly, 40% of patients are anemic prior to receiving RT, and RT also often induces anemia [54-56]. This has important implications for tumoral hypoxia, since the decreased ability of blood to carry oxygen will also make the tumor resistant to radiation damages. It has been demonstrated that anemia is associated with lower RT local tumor control in head and neck cancers

[57]. As such, an oxygen delivery system that does not rely on red blood cells such as oxygen microbubbles could significantly benefit this patient subpopulation in particular [58, 59].

4.6 CONCLUSIONS

In conclusion, our data show that oxygen microbubbles administered by direct intra-tumoral injection in fibrosarcoma allografts *in vivo* are capable of increasing tumoral oxygenation significantly for tens of minutes, whereas control nitrogen microbubble injection reduces tumoral oxygenation. Furthermore, a preliminary study with a fixed microbubble dose and radiotherapy protocol shows that oxygen microbubbles significantly improve radiotherapy tumor control. This constitutes the first demonstration that OMBs can improve RT outcome. The tumor control time improvement is heavily dependent on the initial tumor volume as expected for any fixed dose RT study. Smaller tumors are expected to be less hypoxic and easier to control to the end of our predetermined study observation period with radiotherapy alone, whereas large tumors are likely more hypoxic.

The ability to measure the real-time dynamics of OMB-induced tumor hypoxia modulation could also be used to inform other tumor re-oxygenation adjuvant therapies, as well as optimize the dose and timings for RT. As such, future studies will concentrate on investigating administration routes and dosages. In particular, the ability to administer OMB intravenously remains most attractive due to being minimally invasive and potentially allowing for an image-guided, ultrasound-triggered release mechanism locally. This in turn offers the largest clinical translation applicability with repeated fractionated dose radiotherapy protocols and could harness endothelial sensitization as an additional therapeutic-enhancing mechanism.

REFERENCES

1. National Cancer Institute at National Institute of Health. *Cancer Statistics*. 3 May 2017]; Available from: https://www.cancer.gov/about-cancer/understanding/statistics.

2. Reinhold, H.S., B. Blachiwiecz, and A. Blok, *Oxygenation and reoxygenation in 'sandwich' tumours.* Bibliotheca Anatomica, 1977(15 Pt 1): p. 270-2.

3. Brown, J.M., *Evidence for acutely hypoxic cells in mouse tumours, and a possible mechanism of reoxygenation.* British Journal of Radiology, 1979. **52**(620): p. 650-6.

4. Rockwell, S., et al., *Hypoxia and radiation therapy: past history, ongoing research, and future promise.* Curr Mol Med, 2009. **9**(4): p. 442-58.

5. Semenza, G.L., *The hypoxic tumor microenvironment: A driving force for breast cancer progression.* Biochimica et Biophysica Acta, 2016. **1863**(3): p. 382-91.

6. Evans, S.M. and C.J. Koch, *Prognostic significance of tumor oxygenation in humans.* Cancer Letters, 2003. **195**(1): p. 1-16.

7. Rankin, E.B. and A.J. Giaccia, *Hypoxic control of metastasis.* Science, 2016. **352**(6282): p. 175-80.

8. Sullivan, R. and C.H. Graham, *Hypoxia-driven selection of the metastatic phenotype.* Cancer and Metastasis Reviews, 2007. **26**(2): p. 319-31.

9. Lu, X. and Y. Kang, *Hypoxia and hypoxia-inducible factors: master regulators of metastasis.* Clinical Cancer Research, 2010. **16**(24): p. 5928-35.

10. Branco-Price, C., et al., *Endothelial Cell HIF-1 alpha and HIF-2 alpha Differentially Regulate Metastatic Success.* Cancer Cell, 2012. **21**(1): p. 52-65.

11. Tang, N., et al., *Loss of HIF-1alpha in endothelial cells disrupts a hypoxia-driven VEGF autocrine loop necessary for tumorigenesis.* Cancer Cell, 2004. **6**(5): p. 485-95.

12. American Society for Radiation Oncology. *Fast Facts About Radiation Therapy.* . 3 May 2017]; Available from: https://www.astro.org/News-and-Media/Media-Resources/FAQs/Fast-Facts-About-Radiation-Therapy/Index.aspx.

13. Smith, B.D., et al., *The future of radiation oncology in the United States from 2010 to 2020: will supply keep pace with demand?* Journal of Clinical Oncology, 2010. **28**(35): p. 5160-5.

14. Barnett, G.C., et al., *Normal tissue reactions to radiotherapy: towards tailoring treatment dose by genotype.* Nature Reviews Cancer, 2009. **9**(2): p. 134-142.

15. Gray, L.H., et al., *The Concentration of Oxygen Dissolved in Tissues at the Time of Irradiation as a Factor in Radiotherapy.* British Journal of Radiology, 1953. **26**(312): p. 638-648.

16. Moeller, B.J., R.A. Richardson, and M.W. Dewhirst, *Hypoxia and radiotherapy: opportunities for improved outcomes in cancer treatment.* Cancer and Metastasis Reviews, 2007. **26**(2): p. 241-8.

17. Semenza, G.L., *Hypoxia-inducible factors: mediators of cancer progression and targets for cancer therapy.* Trends in Pharmacological Sciences, 2012. **33**(4): p. 207-14.

18. Vishwanath, K., et al., *Quantitative optical spectroscopy can identify long-term local tumor control in irradiated murine head and neck xenografts.* Journal of Biomedical Optics, 2009. **14**(5).

19. Overgaard, J., *Hypoxic radiosensitization: Adored and ignored.* Journal of Clinical Oncology, 2007. **25**(26): p. 4066-4074.

20. Hodgkiss, R.J., et al., *Rapid-mixing studies of radiosensitivity with thiol-depleted mammalian cells.* International Journal of Radiation Biology and Related Studies in Physics, Chemistry and Medicine, 1987. **52**(5): p. 735-44.

21. Kaanders, J.H.A.M., J. Bussink, and A.J. van der Kogel, *Clinical studies of hypoxia modification in radiotherapy.* Seminars in Radiation Oncology, 2004. **14**(3): p. 233-240.

22. Dunn, T.J., et al., *The effects of hyperoxic and hypercarbic gases on tumour blood flow.* British Journal of Cancer, 1999. **80**(1-2): p. 117-126.

23. Mendenhall, W.M., et al., *Radiotherapy breathing for and neck alone or combined with carbogen squamous cell carcinoma of the head - A prospective, randomized trial.* Cancer, 2005. **104**(2): p. 332-337.

24. Fix, S.M., M.A. Borden, and P.A. Dayton, *Therapeutic gas delivery via microbubbles and liposomes.* J Control Release, 2015. **209**: p. 139-49.

25. Feshitan, J.A., et al., *Systemic oxygen delivery by peritoneal perfusion of oxygen microbubbles.* Biomaterials, 2014. **35**(9): p. 2600-6.

26. Legband, N.D., et al., *Evaluation of peritoneal microbubble oxygenation therapy in a rabbit model of hypoxemia.* IEEE Transactions on Biomedical Engineering, 2015. **62**(5): p. 1376-82.

27. McEwan, C., et al., *Oxygen carrying microbubbles for enhanced sonodynamic therapy of hypoxic tumours.* J Control Release, 2015. **203**: p. 51-6.

28. McEwan, C., et al., *Combined sonodynamic and antimetabolite therapy for the improved treatment of pancreatic cancer using oxygen loaded microbubbles as a delivery vehicle.* Biomaterials, 2016. **80**: p. 20-32.

29. Liu, L., et al., *Ultrasound-mediated destruction of paclitaxel and oxygen loaded lipid microbubbles for combination therapy in ovarian cancer xenografts.* Cancer Letters, 2015. **361**(1): p. 147-54.

30. Swanson, E.J., et al., *Phospholipid-stabilized microbubble foam for injectable oxygen delivery.* Langmuir, 2010. **26**(20): p. 15726-9.

31. Yuan, H., et al., *Intertumoral differences in hypoxia selectivity of the PET imaging agent 64Cu(II)-diacetyl-bis(N4-methylthiosemicarbazone).* Journal of Nuclear Medicine, 2006. **47**(6): p. 989-98.

32. Schroeder, T., et al., *Spatial heterogeneity and oxygen dependence of glucose consumption in R3230Ac and fibrosarcomas of the Fischer 344 rat.* Cancer Research, 2005. **65**(12): p. 5163-71.

33. Cardenas-Navia, L.I., et al., *Tumor-dependent kinetics of partial pressure of oxygen fluctuations during air and oxygen breathing.* Cancer Research, 2004. **64**(17): p. 6010-7.

34. Cardenas-Navia, L.I., et al., *The pervasive presence of fluctuating oxygenation in tumors.* Cancer Research, 2008. **68**(14): p. 5812-9.

35. Rwigema, J.C.M., et al., *The Impact of Tumor Volume and Radiotherapy Dose on Outcome in Previously Irradiated Recurrent Squamous Cell Carcinoma of the Head and Neck Treated With Stereotactic Body Radiation Therapy.* American Journal of Clinical Oncology-Cancer Clinical Trials, 2011. **34**(4): p. 372-379.

36. Doweck, I., D. Denys, and T. Robbins, *Tumor volume predicts outcome for advanced head and neck cancer treated with targeted chemoradiotherapy.* Laryngoscope, 2002. **112**(10): p. 1742-1749.

37. Krause, M., et al., *Cancer stem cells: Radioresistance, prediction of radiotherapy outcome and specific targets for combined treatments.* Advanced Drug Delivery Reviews, 2017. **109**: p. 63-73.

38. Dubben, H.H., H.D. Thames, and H.P. Beck-Bornholdt, *Tumor volume: a basic and specific response predictor in radiotherapy.* Radiotherapy and Oncology, 1998. **47**(2): p. 167-174.

39. Bradley, J.D., et al., *Gross tumor volume, critical prognostic factor in patients treated with three-dimensional conformal radiation therapy for non-small-cell lung carcinoma.* International Journal of Radiation Oncology, Biology, Physics, 2002. **52**(1): p. 49-57.

40. Chen, M., et al., *Prognostic factors for local control in non-small-cell lung cancer treated with definitive radiation therapy.* American Journal of Clinical Oncology-Cancer Clinical Trials, 2002. **25**(1): p. 76-80.

41. Pitson, G., et al., *Tumor size and oxygenation are independent predictors of nodal disease in patients with cervix cancer.* International Journal of Radiation Oncology Biology Physics, 2001. **51**(3): p. 699-703.

42. Kasoji, S.K., et al., *Early Assessment of Tumor Response to Radiation Therapy using High-Resolution Quantitative Microvascular Ultrasound Imaging.* Theranostics, 2018. **8**(1): p. 156-168.

43. Curtis, K.K., W.W. Wong, and H.J. Ross, *Past approaches and future directions for targeting tumor hypoxia in squamous cell carcinomas of the head and neck.* Critical Reviews in Oncology/Hematology, 2016. **103**: p. 86-98.

44. Walsh, J.C., et al., *The clinical importance of assessing tumor hypoxia: relationship of tumor hypoxia to prognosis and therapeutic opportunities.* Antioxid Redox Signal, 2014. **21**(10): p. 1516-54.

45. Sangro, B., et al., *Phase I trial of intratumoral injection of an adenovirus encoding interleukin-12 for advanced digestive tumors.* Journal of Clinical Oncology, 2004. **22**(8): p. 1389-97.

46. Gerbaulet, A., et al., *The GEC ESTRO handbook of brachytherapy*. 2002, Leuven, Belgium: European Society for Therapeutic Radiology and Oncology.

47. Shirley, L.A., et al., *Therapeutic endoscopic ultrasonography: intratumoral injection for pancreatic adenocarcinoma.* Gastroenterol Res Pract, 2013. **2013**: p. 207129.

48. Kwan, J.J., et al., *Theranostic Oxygen Delivery Using Ultrasound and Microbubbles.* Theranostics, 2012. **2**(12): p. 1174-1184.

49. Kwok, S.J.J., et al., *Ultrasound-Mediated Microbubble Enhancement of Radiation Therapy Studied Using Three-Dimensional High-Frequency Power Doppler Ultrasound.* Ultrasound in Medicine and Biology, 2013. **39**(11): p. 1983-1990.

50. Garcia-Barros, M., et al., *Tumor response to radiotherapy regulated by endothelial cell apoptosis.* Science, 2003. **300**(5622): p. 1155-9.

51. Fuks, Z. and R. Kolesnick, *Engaging the vascular component of the tumor response.* Cancer Cell, 2005. **8**(2): p. 89-91.

52. Kallman, R.F., *The phenomenon of reoxygenation and its implications for fractionated radiotherapy.* Radiology, 1972. **105**(1): p. 135-42.

53. Chang, J.Y., et al., *Stereotactic body radiation therapy in centrally and superiorly located stage I or isolated recurrent non-small-cell lung cancer.* International Journal of Radiation Oncology, Biology, Physics, 2008. **72**(4): p. 967-71.

54. Hirst, D.G., *What Is the Importance of Anemia in Radiotherapy - the Value of Animal Studies.* Radiotherapy and Oncology, 1991. **20**: p. 29-33.

55. Harrison, L., et al., *Prevalence of anemia in cancer patients undergoing radiation therapy.* Seminars in Oncology, 2001. **28**(2 Suppl 8): p. 54-9.

56. Harrison, L.B., et al., *Radiotherapy-Associated Anemia: The Scope of the Problem.* The Oncologist, 2000. **5 Suppl 2**: p. 1-7.

57. Dubray, B., et al., *Anemia is associated with lower local-regional control and survival after radiation therapy for head and neck cancer: A prospective study.* Radiology, 1996. **201**(2): p. 553-558.

58. Span, P.N., J. Bussink, and J.H.A.M. Kaanders, *Engineered microparticles delivering oxygen to enhance radiotherapy efficacy.* Proceedings of the National Academy of Sciences of the United States of America, 2016. **113**(50): p. E8009-E8009.

59. Kheir, J.N. and B.D. Polizzotti, *Rational design of oxygen microparticles for radiation therapy REPLY.* Proceedings of the National Academy of Sciences of the United States of America, 2016. **113**(50): p. E8010-E8010.

CHAPTER 5[1]

OVERCOMING BIOLOGICAL BARRIERS TO DRUG DELIVERY WITH ULTRASOUND-STIMULATED CONTRAST AGENTS

5.1 MOTIVATION AND OVERVIEW

In general, the goal drug delivery research is to maximize efficacy while minimizing systemic toxicity, thereby widening the therapeutic window of a drug (Figure 5.1). This is often attempted through targeting, which refers to any method that enriches drug accumulation specifically at the disease site while sparing other tissues. Targeting can be accomplished through a number of mechanisms including (1) covalent attachment of ligands or antibodies that bind to disease-site-specific receptors, (2) formulation of the pharmaceutical in nano- or microparticles that are preferentially taken up by the tissue or cells of interest, and (3) physical methods where biological barriers are disrupted through the application of external stimuli [1, 2]. This chapter introduces the use of ultrasound-stimulated contrast agents as a physical drug targeting method.

This approach offers a number of unique advantages compared to other drug delivery methods. First, it is widely applicable across disease states and for a diverse range of pharmaceuticals. This method can be used to deliver small molecule drugs [3, 4], proteins [5], nanoparticles [6], and genetic material [7] in diseases ranging from cancer [3] to Alzheimer's disease

[1]Portions of this chapter have been adapted from previously published and submitted journal articles. The original citations are as follows:

Fix, S.M., Koppolu, B.P., Novell, A., Hopkins, J., Kierski, T.M., Zaharoff, D.A., Dayton, P.A., Papadopoulou, V. (2018), "Ultrasound-stimulated low boiling point phase-change contrast agents for epithelial permeabilization towards ultrasound-mediated gastrointestinal drug delivery." (Under Revision, Ultrasound in Medicine and Biology)

Fix, S.M., Novell, A., Yun, Y., Dayton, P.A., Arena, C.B. (2017). "An evaluation of the sonoporation potential of low-boiling point phase-change ultrasound contrast agents in vitro." J Ther Ultrasound **5**: 7. This article was distributed under the terms of the Creative Commons License (http://creativecommons.org/licenses/by/4.0/).

[5]. The versatility of this platform is afforded by the fact that ultrasound is used to locally disrupt a specific biological barrier that would otherwise impede drug delivery. Acoustic parameters can be tailored with respect to the physicochemical properties of the cargo being delivered and physiologic features of the target tissue.

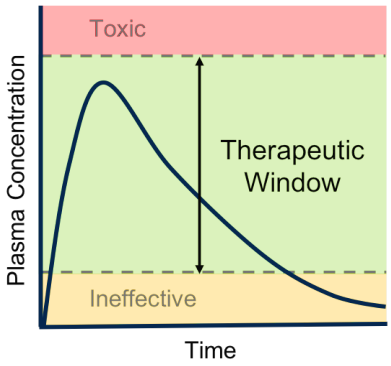

Figure 5.1: Therapeutic window. The therapeutic window is defined as range of drug concentrations that fall between the minimum required dose for efficacy and maximum concentration before which toxicity is observed.

A second key advantage is the opportunity for image guidance. Standard B-mode ultrasound imaging can be used to locate and align an anatomical feature before applying the therapeutic ultrasound pulses [8]. This allows for precise treatment planning in real-time, increasing accuracy and ultimately reducing the risk of off-target damage and toxicity. In some cases, ultrasound image guidance and therapy can be achieved with the same transducer, while other applications require alignment of two separate transducers for imaging and drug delivery.

The purpose of this chapter is to introduce key biological barriers to drug delivery and provide an overview of the mechanisms by which ultrasound-stimulated contrast agents can be used to overcome them. We conclude by considering advantages of using novel phase change contrast agents (PCCAs) in this context and the expanded drug delivery applications that they may provide.

5.2 BIOLOGICAL BARRIERS TO DRUG DELIVERY

5.2.1 GASTROINTESTINAL TRACT

The gastrointestinal (GI) tract has evolved to efficiently breakdown food products, allow nutrient uptake, and simultaneously provide a robust defense against ingested toxins and

pathogens [9, 10]. This presents a complex barrier for both local and systemic drug delivery through the GI tract, particularly for biologics [11]. The first hurdle is maintaining drug stability in the degradative environment. This often requires specialized formulations to protect the active pharmaceutical ingredient from (1) the harsh and fluctuating acidic pH and (2) an array of degradative species and enzymes [12]. If drug integrity is maintained, the second hurdle is permeability. The GI tract is blanketed with mucus that traps and protects the underlying epithelium from foreign particles [13]. Furthermore, GI epithelial cells are linked by tight junctions that restrict paracellular transport of large molecules (> 200 Da), and the hydrophilic nature of most biologic drugs limits passive transcellular diffusion [11]. In general, these challenges limit GI drug delivery to small molecules.

While a few reports exist, therapeutic ultrasound has yet to be extensively explored as a method for improving GI drug delivery [14-16]. This application would involve drug administration to the GI tract via oral or enema routes, followed by local ultrasound stimulation with an endoscopic probe. This technology has the potential improve treatment options for a number of GI diseases including ulcerative colitis, cancers of the GI tract, infection, and Crohn's disease, and offers the following unique benefits [9, 14, 15]. First, rapid delivery would limit concerns of drug degradation by intestinal enzymes, eliminating the need for complex protective formulations. Second, this technique may allow for local GI delivery of biologic drugs previously restricted to intravenous administration (including peptides, proteins, monoclonal antibodies, RNA, and DNA), which would expand therapeutic options for GI diseases. Third, concentrated local delivery has the potential to enhance drug efficacy and reduce systemic toxicities. Finally, this technique is theoretically drug-independent and may be applicable for a wide range of molecules, independent of molecular weight and physicochemical properties.

5.2.2 VASCULATURE

For systemic drugs (e.g., following intravenous (IV) administration or absorption through the GI barrier), the vasculature presents key barrier to efficient delivery. The vasculature is lined with a continuous layer of endothelial cells [17] that are linked by protein complexes, and the ability of molecules to transverse this barrier and enter the surrounding tissue varies with respect to the

molecule's physicochemical properties/formulation and the local vascular physiology [18]. The barrier function of vasculature varies substantially from tissue to tissue and can be affected by local disease [18, 19]. Extreme examples include the tightly regulated blood brain barrier, and the leaky, disorganized vasculature characteristic of solid tumors.

The brain requires a stable chemical composition for proper neuronal function, and as such, its vasculature is highly specialized to shield the brain from circulating blood components. This so-called 'blood brain barrier (BBB)' is comprised of specialized endothelial cells, astrocytes and pericytes, which work together to prevent extravasation of foreign molecules and selectively promote up take of essential nutrients [20]. This vascular network is substantially more restrictive than vasculature in peripheral tissue, with the tight junctions between endothelial cells being 50-100× tighter in in the BBB [21]. This presents a major challenge with respect to local drug delivery to the brain, and it is estimated that 98% of small molecule drugs and 100% of macromolecular therapeutics are unable to penetrate [22]. Methods to circumvent the BBB include direct trans-cranial drug delivery, administration via the nasal pathway, and physical/chemical disruption of BBB function [22]. Ultrasound-stimulated contrast agents present an opportunity to transiently open the BBB non-invasively and with tight spatial control, and this technology is currently being explored as an option to improve the treatment of brain cancers and neurodegenerative diseases such as Parkinson's and Alzheimer's [23].

The vascular physiology of solid tumors represents the other end of the spectrum in terms of leakiness, which comes with its own unique delivery challenges. Angiogenesis is a hallmark feature of cancer, as a functional nutrient and oxygen supply is necessary to support continued tumor growth [24]. To keep up with the rapid growth, tumor-associated angiogenesis is often chaotic leading to disorganized and poorly formed vessels [24]. These vessels often have large fenestrations between individual endothelial cells, which makes them particularly leaky. This, combined with the characteristically poor lymphatic drainage of solid tumors, results in to the so-called 'enhanced permeability and retention (EPR) effect', which describes the phenomenon of enhanced accumulation of macromolecules and nanoparticles within solid tumors [25]. It is important to note that the degree to which a tumor will demonstrate EPR is heterogeneous among different cancer types and even

between individuals with the same disease. Thus, EPR alone may be insufficient for effective tumoral drug delivery [25, 26].

While the leakiness of solid tumor vasculature can aid in drug delivery for certain tumor types and cargos, it also presents paradoxical challenges. First, the EPR effect leads to fluid build-up and therefore excessive interstitial fluid pressure within solid tumors [26, 27]. This can in turn lead to vascular collapse, poor perfusion, and hampered penetration of drugs from the vasculature into surrounding tissue, all contributing to poor drug delivery efficiency. Growth of dense stroma within the tumor microenvironment can exacerbate these issues, limiting drug permeation through tumor tissue and preventing drugs from accessing deeply situated tumor cells [26, 27]. Finally, the same challenges that hinder drug delivery also limit tumor oxygenation, and solid tumors often exhibit marked hypoxia [28]. This presents additional challenges associated with hypoxia-induced chemoresistance and the increased risk of metastasis.

In the context of solid tumors, ultrasound stimulated contrast agents can be used to enhance the permeability of existing vasculature [29], which may be valuable especially in cases of poor EPR or where large drugs/particles are being delivered. It has also been postulated that acoustic radiation force and streaming can enhance local drug diffusion and promote deep drug penetration independent of permeability concerns [29, 30]. This may be particularly useful in cases where elevated interstitial fluid pressure and stromal bulk prevent thorough drug distribution within a tumor.

5.2.3 CELL MEMBRANE

After entering the interstitial space of a tissue, most drugs must pass the cell membrane to exert their pharmacologic activity within the cytosol or nucleus. This is a notoriously difficult barrier for therapeutic proteins and genetic material, due to their typically large size, high surface charge, and sensitivity to degradation in biological environments [31, 32]. Extensive research effort has been devoted to devising methods for efficient intracellular delivery of these molecules, each offering advantages and limitations. For example, biologics can be formulated in nanoparticles, which protects them from degradation in circulation. Here, targeting ligands can be used to promote site-specific delivery and intracellular accumulation via receptor-mediated endocytosis. However, to finally enter

the cytosol, the therapeutic molecule must be able to escape both the nanoparticle and endosome before being degraded in the lysosome, which can be a major hurdle [33]. For gene delivery, viral vectors offer an alternative approach [34]. Viral vectors offer inherent mechanisms for passing the cell membrane, escaping the endosome, and entering the nucleus [35]. However, the use of viral vectors poses safety concerns regarding vector immunogenicity and delivery specificity.

Ultrasound-stimulated contrast agents can be used to physically disrupt cell membranes and enhance intracellular delivery of wide variety of therapeutic molecules, including biologics [36]. Furthermore, drugs and genes can be loaded onto the contrast agents, offering protection from enzymatic degradation and enhancing site specific delivery [37]. Importantly, cell membrane perforation by ultrasound is a transient process, and the cell can rapidly repair and reseal itself.

While this technique has shown great promise in the *in vitro* setting, *in vivo* translation is complicated by the fact that traditional ultrasound contrast agents (microbubbles) are too large to extravasate from the vasculature following intravenous administration. This limits the utility of cellular perforation to drug delivery into vascular endothelial cells, unless microbubbles are invasively injected into the disease site (e.g., solid tumor), which presents addition risks and limitations.

5.3 SONOPORATION: PROPOSED MECHANISMS AND OVERVIEW OF ACOUSTIC PARAMETERS

5.3.1 PROPOSED MECHANISMS OF SONOPORATION

Sonoporation is a term used to describe the process of using ultrasound-stimulated contrast agents to permeabilize biological barriers, typically for drug or gene delivery purposes [36]. The bulk of literature surrounding this topic describes either cell membrane perforation *in vitro* [36, 38] or permeabilization of vascular barriers *in vivo* [23, 29], however, the same principals can be applied to other biological barriers such as the GI epithelium. Despite decades of research, a consensus has yet to be reached regarding the precise mechanisms involved in sonoporation. This is partly due to the wide range of acoustic parameters and experimental designs used within the literature, which makes it difficult to draw generalizable mechanistic conclusions. Nevertheless, the primary mechanisms driving sonoporation are thought to all stem from physical or chemical effects of cavitation. In this

section, we provide a brief overview of phenomena surrounding acoustic cavitation and a sampling of biological responses that these phenomena may induce.

Traditional ultrasound contrast agents are micron-range gas filled bubbles (microbubbles), which typically comprise a gas core and a stabilizing shell of lipids, protein, or polymers [37]. When interrogated with relatively low amplitude ultrasound, microbubbles will oscillate with the expansion and contraction phases of the passing acoustic wave. This is referred to as stable cavitation [39]. As amplitude is increased, the inertia of the surrounding fluid compressing the microbubble during the contraction phase becomes so great that the microbubble will violently collapse upon itself, in a process called inertial cavitation.

Under the stable cavitation regime, a number of physical phenomena occur. First, microbubble oscillations cause microstreaming or flow in the surrounding fluid [36, 38]. This exerts shear stress on surrounding biological structures, which may ultimately disrupt their integrity and may result in the formation of small membrane pores. Furthermore, when a microbubble oscillates while in direct contact with a cell or microvessel, the push and pull from the expansion and contraction phases will directly deform the cell or vessel, contributing to cell membrane or vascular permeabilization [36, 38].

In addition to these mechanical stresses, stable cavitation can induce sonoporation through chemical means. The shear stress of microstreaming is thought to generate reactive oxygen species (ROS) [36, 40], which can (1) modulate the function of ion channels with downstream signaling effects or (2) directly induce cellular injury by lipid peroxidation [36]. Cell membrane perforation also leads to an influx of Ca^{+2} into the cell [41], which may enhance intracellular drug accumulation via the induction of endocytosis [42].

Inertial cavitation is associated with more intense physical forces, including the generation of shock waves and the production of micro fluid jets towards nearby surfaces [43]. These strong physical forces can mechanically disrupt cell membranes and vascular barriers, creating membrane pores that are in general larger than then pores created through stable cavitation. Both *in vitro* and *in vivo* studies have demonstrated an increased risk of cell death / tissue damage with increasing inertial cavitation energy [44-47].

Complimentary to permeabilizing drug delivery barriers, acoustic phenomena can independently enhance the drug transport and distribution in tissue. Particles can be pushed in the direction of the acoustic beam via acoustic radiation force [29, 30, 48]. One report shows that this may be responsible for the greater permeation of liposomal doxorubicin through tumor tissue when ultrasound stimulation is applied in the absence of microbubbles [30]. Additionally, the microstreaming around oscillating microbubbles can greatly enhance the transport of drugs in the surrounding fluid [48, 49]. Finally, microbubbles oscillating within the brain vasculature can enhance the perivascular pump effect, promoting thorough distribution of extravascular drugs through brain tissue [50].

5.3.2 ACOUSTIC PARAMETERS FOR SONOPORATION

It is difficult to describe a single set of “best” acoustic parameters for sonoporation, as optimization will depend on a number of non-acoustic experimental criteria including (1) physicochemical properties of the drug / particle being delivered, (2) biology of the barrier being disrupted (e.g., tumor vasculature vs. BBB vs. cell membrane), and (3) the concentration and properties of the microbubbles being used as cavitation nuclei. Furthermore, the interplay between acoustic parameters is important, and it is likely that several parameter combinations could result in similar levels of drug delivery enhancement for a given application. These considerations make acoustic parameter optimization both difficult to perform and not necessarily generalizable among diverse applications. As a result, a wide range of successful acoustic parameters have been reported in the literature, with little consensus in the field regarding best practices. Below we have summarized general considerations for key acoustic parameters, including a range of reported values.

Frequency (0.3 ~ 2.5 MHz): The likelihood of inducing cavitation is inversely related to frequency [51], and as such, relatively low frequencies tend to be best for sonoporation. Another important consideration is the resonant frequency of the microbubbles being used, which varies as a function of microbubble size [52]. Exiting microbubbles near resonance will lead to more pronounced oscillatory behavior, and therefore enhanced biological effects [53].

Pressure (0.1 ~ 2.5 MPa): Pressure has been considered one of the most important acoustic variables dictating sonoporation outcome. Cavitation activity is directly proportional to rarefactional pressure [51]. At low pressure, stable cavitation is dominant. As pressure is increased, so is the likelihood of microbubble destruction via inertial cavitation. In general, the severity of biological effects will increase with increasing pressure, initially enhancing drug delivery but eventually leading to undesired tissue damage [54]. Furthermore, rapid microbubble destruction may negatively impact cavitation persistence during treatment (see section ***Importance of Cavitation Persistence*** below). For these reasons, intermediate pressures (on the order of a few hundred kilopascals) may be best.

Pulse length (4 ~ 50,000 cycles): Sonoporation protocols vary substantially with respect to pulse length. As with increasing pressure, drug delivery has been shown to increase with increasing pulse length, eventually at the price of increased cell death/damage [55]. Furthermore, the effects of acoustic radiation force increase with increasing pulse length [56], which may be an important consideration for some applications.

Duty cycle (1 ~ 100%): Duty cycle is defined as the percent “on” time of the ultrasound pulse (pulse length divided by time interval between pulses). This parameter varies substantially among literature reports. Combining high duty cycles with high intensity ultrasound can lead to tissue heating. To emphasize the mechanical effects of cavitation and minimize heating, it has been suggested that duty cycle is kept low when high ultrasound intensities are used and may be increased when low intensities are employed [29].

Exposure time (10 s ~ 30 min): Exposure time is kept short for *in vitro* studies, typically 1 min or less. For *in vivo* studies, exposure time typically ranges from 1.0 – 10 minutes. *In vivo,* it is important to consider the pharmacokinetics of the drug and microbubbles when choosing an exposure time [8]. Microbubbles must be present for the duration of the treatment, which may require continuous IV infusion or repeat bolus dosing since microbubbles have short half-lives in circulation.

Importance of cavitation persistence: Recent reports regarding vascular permeabilization with microbubbles emphasize the importance of achieving *persistent* cavitation activity. If microbubble-

destructive ultrasound pulses are used, it is important to allow microbubbles to re-enter the focal zone via blood flow, such that sonoporation effects are produced for the duration of the treatment. Reperfusion into the focal zone can be achieved by alternating sonication with rest time [6, 57] or theoretically by using short pulses and long pulse repetition periods [58]. To this end, Pouliopoulos and colleagues have demonstrated the value of using low pressures and short pulses to provide sustained, controllable, and safe cavitation activity for vascular permeabilization [59, 60].

5.4 MOTIVATION FOR USING LOW BOILING POINT PCCAs FOR SONOPORATION

While microbubbles have seen success as sonoporation initiators for cellular perforation *in vitro* and vascular disruption *in vivo,* their large size prevents expanded *in vivo* applications. Microbubbles are relatively large (1-10 μm) and therefore cannot escape the vasculature following intravenous administration [61]. Therefore, extravascular cell membrane perforation for the purpose of improved drug or gene delivery within a target tissue is not feasible. Furthermore, GI drug delivery applications would be challenging with microbubbles, as they would not be able to efficiently permeate the GI mucus mesh to interrogate the underlying epithelium.

PCCAs are nanometer scale, liquid-filled droplets that can be vaporized into microbubbles when subjected to ultrasound of sufficient amplitude through a process termed acoustic droplet vaporization (ADV). Their nanometer-scale size distributions may allow for (1) passive accumulation in leaky tumors via the EPR effect [62, 63] and (2) permeation through GI mucus for sonoporation of the GI epithelial barrier. Furthermore, since PCCAs are nearly invisible to ultrasound in their liquid state, high concentrations can be used without the shielding effects characteristic of high microbubble concentrations. PCCA-derived microbubbles destroyed in one acoustic pulse may be replenished through subsequent vaporization events, thereby allowing sustained generation of cavitation energy and enhanced sonoporation [64]. PCCAs therefore offer a solution to the major limitations previously given for microbubble-mediated sonoporation and hold the potential for extravascular and GI sonoporation *in vivo*.

PCCA formulations are commonly filled with perfluorocarbons with boiling points near body temperature, such as dodecafluoropentane (DDFP, b.p. = 29°C), and a few laboratories have

demonstrated the sonoporation potential of such agents in vitro [57, 64-66]. While these initial studies show promise, the high negative pressures required to vaporize nano-scale DDFP-filled PCCAs (3-6 MPa [63, 64]) may cause unwanted bioeffects such as heating or cell lysis in an *in vivo* setting. Our laboratory has developed a class of low-boiling point PCCAs filled with octofluoropropane (OFP, b.p. = -36.7°C), which are characterized by far lower pressure requirements for vaporization when compared to DDFP-filled PCCAs (~20× lower). Therefore, we hypothesize that our formulation will offer greater control over the bioeffects caused by ADV and subsequent microbubble cavitation.

5.5 CONCLUSIONS

Sonoporation is a promising physical drug targeting method that has the potential to enhance the therapeutic efficacy of a diverse range of pharmaceuticals in a number of disease states. Current approaches use microbubbles as cavitation nuclei, and applications are for the most part restricted to cell membrane perforation *in vitro* and vascular disruption *in vivo.* We believe low boiling point PCCAs offer a solution to the limitations associated with conventional microbubbles and their use as sonoporation initiators may allow expanded *in vivo* applications.

The following chapters explore the sonoporation potential of low boiling point PCCAs *in vitro*. First, PCCAs are used to permeabilize pancreatic cancer cell membranes, representing a first step towards the goal of extravascular cell membrane disruption in solid tumors (chapter 6). We next demonstrate the ability to overcome chemoresistance in a colon cancer cell line using PCCA-mediated sonoporation (chapter 7). Finally, through chapter 8, we explore the ability of PCCAs to enhance drug delivery through Caco-2 epithelial monolayers, as a proof-of-principal demonstration supporting the eventual the goal of GI drug delivery with PCCAs.

REFERENCES

1. Torchilin, V.P., *Passive and active drug targeting: drug delivery to tumors as an example.* Handb Exp Pharmacol, 2010(197): p. 3-53.

2. Mitragotri, S., *Devices for overcoming biological barriers: the use of physical forces to disrupt the barriers.* Adv Drug Deliv Rev, 2013. **65**(1): p. 100-3.

3. Kotopoulis, S., et al., *Sonoporation-enhanced chemotherapy significantly reduces primary tumour burden in an orthotopic pancreatic cancer xenograft.* Mol Imaging Biol, 2014. **16**(1): p. 53-62.

4. Escoffre, J.M., et al., *Irinotecan delivery by microbubble-assisted ultrasound: in vitro validation and a pilot preclinical study.* Mol Pharm, 2013. **10**(7): p. 2667-75.

5. Jordão, J.F., et al., *Antibodies targeted to the brain with image-guided focused ultrasound reduces amyloid-beta plaque load in the TgCRND8 mouse model of Alzheimer's disease.* PLoS One, 2010. **5**(5): p. e10549.

6. Mullick Chowdhury, S., et al., *Ultrasound-guided therapeutic modulation of hepatocellular carcinoma using complementary microRNAs.* J Control Release, 2016. **238**: p. 272-280.

7. Shapiro, G., et al., *Multiparameter evaluation of in vivo gene delivery using ultrasound-guided, microbubble-enhanced sonoporation.* J Control Release, 2016. **223**: p. 157-164.

8. Dimcevski, G., et al., *A human clinical trial using ultrasound and microbubbles to enhance gemcitabine treatment of inoperable pancreatic cancer.* J Control Release, 2016. **243**: p. 172-181.

9. Schoellhammer, C.M. and G. Traverso, *Low-frequency ultrasound for drug delivery in the gastrointestinal tract.* Expert Opin Drug Deliv, 2016. **13**(8): p. 1045-8.

10. Barrett, K.E., *Epithelial biology in the gastrointestinal system: insights into normal physiology and disease pathogenesis.* J Physiol, 2012. **590**(Pt 3): p. 419-20.

11. Goldberg, M. and I. Gomez-Orellana, *Challenges for the oral delivery of macromolecules.* Nature Reviews Drug Discovery, 2003. **2**: p. 289.

12. Moss, D.M., et al., *The biological challenges and pharmacological opportunities of orally administered nanomedicine delivery.* Expert Rev Gastroenterol Hepatol, 2017: p. 1-14.

13. Cone, R.A., *Barrier properties of mucus.* Advanced Drug Delivery Reviews, 2009. **61**(2): p. 75-85.

14. Schoellhammer, C.M., et al., *Ultrasound-mediated gastrointestinal drug delivery.* Sci Transl Med, 2015. **7**(310): p. 310ra168.

15. Schoellhammer, C.M., et al., *Defining optimal permeant characteristics for ultrasound-mediated gastrointestinal delivery.* J Control Release, 2017. **268**: p. 113-119.

16. Schoellhammer, C.M., et al., *Ultrasound-Mediated Delivery of RNA to Colonic Mucosa of Live Mice.* Gastroenterology, 2017. **152**(5): p. 1151-1160.

17. Pugsley, M.K. and R. Tabrizchi, *The vascular system. An overview of structure and function.* J Pharmacol Toxicol Methods, 2000. **44**(2): p. 333-40.

18. Claesson-Welsh, L., *Vascular permeability--the essentials.* Ups J Med Sci, 2015. **120**(3): p. 135-43.

19. Marsden, P.A., M.S. Goligorsky, and B.M. Brenner, *Endothelial cell biology in relation to current concepts of vessel wall structure and function.* J Am Soc Nephrol, 1991. **1**(7): p. 931-48.

20. Serlin, Y., et al., *Anatomy and physiology of the blood-brain barrier.* Semin Cell Dev Biol, 2015. **38**: p. 2-6.

21. Abbott, N.J., *Astrocyte-endothelial interactions and blood-brain barrier permeability.* J Anat, 2002. **200**(6): p. 629-38.

22. Pardridge, W.M., *The blood-brain barrier: bottleneck in brain drug development.* NeuroRx, 2005. **2**(1): p. 3-14.

23. Burgess, A. and K. Hynynen, *Microbubble-Assisted Ultrasound for Drug Delivery in the Brain and Central Nervous System.* Adv Exp Med Biol, 2016. **880**: p. 293-308.

24. Hanahan, D. and R.A. Weinberg, *Hallmarks of cancer: the next generation.* Cell, 2011. **144**(5): p. 646-74.

25. Maeda, H., *Toward a full understanding of the EPR effect in primary and metastatic tumors as well as issues related to its heterogeneity.* Adv Drug Deliv Rev, 2015. **91**: p. 3-6.

26. Nakamura, Y., et al., *Nanodrug Delivery: Is the Enhanced Permeability and Retention Effect Sufficient for Curing Cancer?* Bioconjug Chem, 2016. **27**(10): p. 2225-2238.

27. Miao, L. and L. Huang, *Exploring the tumor microenvironment with nanoparticles.* Cancer Treat Res, 2015. **166**: p. 193-226.

28. Weinmann, M., C. Belka, and L. Plasswilm, *Tumour hypoxia: impact on biology, prognosis and treatment of solid malignant tumours.* Onkologie, 2004. **27**(1): p. 83-90.

29. Qin, J., T.Y. Wang, and J.K. Willmann, *Sonoporation: Applications for Cancer Therapy.* Adv Exp Med Biol, 2016. **880**: p. 263-91.

30. Eggen, S., et al., *Ultrasound improves the uptake and distribution of liposomal Doxorubicin in prostate cancer xenografts.* Ultrasound Med Biol, 2013. **39**(7): p. 1255-66.

31. Juliano, R., *Challenges to macromolecular drug delivery.* Biochem Soc Trans, 2007. **35**(Pt 1): p. 41-3.

32. Walker, B.J., G.V. Stan, and K.M. Polizzi, *Intracellular delivery of biologic therapeutics by bacterial secretion systems.* Expert Rev Mol Med, 2017. **19**: p. e6.

33. Guo, S. and L. Huang, *Nanoparticles Escaping RES and Endosome: Challenges for siRNA Delivery for Cancer Therapy.* Journal of Nanomaterials, 2011. **2011**: p. 12.

34. Gonçalves, G.A.R. and R.d.M.A. Paiva, *Gene therapy: advances, challenges and perspectives.* Einstein, 2017. **15**(3): p. 369-375.

35. Daya, S. and K.I. Berns, *Gene therapy using adeno-associated virus vectors.* Clin Microbiol Rev, 2008. **21**(4): p. 583-93.

36. Lentacker, I., et al., *Understanding ultrasound induced sonoporation: definitions and underlying mechanisms.* Adv Drug Deliv Rev, 2014. **72**: p. 49-64.

37. Ferrara, K., R. Pollard, and M. Borden, *Ultrasound microbubble contrast agents: fundamentals and application to gene and drug delivery.* Annu Rev Biomed Eng, 2007. **9**: p. 415-47.

38. Bouakaz, A., A. Zeghimi, and A.A. Doinikov, *Sonoporation: Concept and Mechanisms.* Adv Exp Med Biol, 2016. **880**: p. 175-89.

39. Bader, K.B. and C.K. Holland, *Gauging the likelihood of stable cavitation from ultrasound contrast agents.* Phys Med Biol, 2013. **58**(1): p. 127-44.

40. VanBavel, E., *Effects of shear stress on endothelial cells: possible relevance for ultrasound applications.* Prog Biophys Mol Biol, 2007. **93**(1-3): p. 374-83.

41. Juffermans, L.J., et al., *Transient permeabilization of cell membranes by ultrasound-exposed microbubbles is related to formation of hydrogen peroxide.* Am J Physiol Heart Circ Physiol, 2006. **291**(4): p. H1595-601.

42. Qin, P., et al., *Mechanistic understanding the bioeffects of ultrasound-driven microbubbles to enhance macromolecule delivery.* Journal of Controlled Release.

43. Postema, M., et al., *Ultrasound-induced encapsulated microbubble phenomena.* Ultrasound Med Biol, 2004. **30**(6): p. 827-40.

44. Hwang, J.H., et al., *Correlation between inertial cavitation dose and endothelial cell damage in vivo.* Ultrasound Med Biol, 2006. **32**(10): p. 1611-9.

45. Tung, Y.S., et al., *In vivo transcranial cavitation threshold detection during ultrasound-induced blood-brain barrier opening in mice.* Phys Med Biol, 2010. **55**(20): p. 6141-55.

46. Qiu, Y., et al., *The correlation between acoustic cavitation and sonoporation involved in ultrasound-mediated DNA transfection with polyethylenimine (PEI) in vitro.* J Control Release, 2010. **145**(1): p. 40-8.

47. McDannold, N., N. Vykhodtseva, and K. Hynynen, *Targeted disruption of the blood-brain barrier with focused ultrasound: association with cavitation activity.* Phys Med Biol, 2006. **51**(4): p. 793-807.

48. Mo, S., et al., *Ultrasound-enhanced drug delivery for cancer.* Expert Opin Drug Deliv, 2012. **9**(12): p. 1525-38.

49. Pitt, W.G., G.A. Husseini, and B.J. Staples, *Ultrasonic drug delivery--a general review.* Expert Opin Drug Deliv, 2004. **1**(1): p. 37-56.

50. Chen, H., et al., *Focused ultrasound-enhanced intranasal brain delivery of brain-derived neurotrophic factor.* Sci Rep, 2016. **6**: p. 28599.

51. Apfel, R.E. and C.K. Holland, *Gauging the likelihood of cavitation from short-pulse, low-duty cycle diagnostic ultrasound.* Ultrasound Med Biol, 1991. **17**(2): p. 179-85.

52. Doinikov, A.A., J.F. Haac, and P.A. Dayton, *Resonance frequencies of lipid-shelled microbubbles in the regime of nonlinear oscillations.* Ultrasonics, 2009. **49**(2): p. 263-8.

53. McLaughlan, J., et al., *Increasing the sonoporation efficiency of targeted polydisperse microbubble populations using chirp excitation.* IEEE Trans Ultrason Ferroelectr Freq Control, 2013. **60**(12): p. 2511-20.

54. O'Reilly, M.A. and K. Hynynen, *Blood-brain barrier: real-time feedback-controlled focused ultrasound disruption by using an acoustic emissions-based controller.* Radiology, 2012. **263**(1): p. 96-106.

55. Fix, S.M., et al., *An evaluation of the sonoporation potential of low-boiling point phase-change ultrasound contrast agents in vitro.* Journal of Therapeutic Ultrasound, 2017. **5**: p. 7.

56. Dayton, P.A., J.S. Allen, and K.W. Ferrara, *The magnitude of radiation force on ultrasound contrast agents.* J Acoust Soc Am, 2002. **112**(5 Pt 1): p. 2183-92.

57. Gao, D., et al., *Ultrasound-Triggered Phase-Transition Cationic Nanodroplets for Enhanced Gene Delivery.* ACS Appl Mater Interfaces, 2015. **7**(24): p. 13524-37.

58. Shamout, F.E., et al., *Enhancement of non-invasive trans-membrane drug delivery using ultrasound and microbubbles during physiologically relevant flow.* Ultrasound Med Biol, 2015. **41**(9): p. 2435-48.

59. Pouliopoulos, A.N., S. Bonaccorsi, and J.J. Choi, *Exploiting flow to control the in vitro spatiotemporal distribution of microbubble-seeded acoustic cavitation activity in ultrasound therapy.* Phys Med Biol, 2014. **59**(22): p. 6941-57.

60. Pouliopoulos, A.N., et al., *Rapid short-pulse sequences enhance the spatiotemporal uniformity of acoustically driven microbubble activity during flow conditions.* J Acoust Soc Am, 2016. **140**(4): p. 2469.

61. Sirsi, S. and M. Borden, *Microbubble Compositions, Properties and Biomedical Applications.* Bubble science engineering and technology, 2009. **1**(1-2): p. 3-17.

62. Rapoport, N., et al., *Ultrasound-mediated tumor imaging and nanotherapy using drug loaded, block copolymer stabilized perfluorocarbon nanoemulsions.* J Control Release, 2011. **153**(1): p. 4-15.

63. Reznik, N., et al., *The efficiency and stability of bubble formation by acoustic vaporization of submicron perfluorocarbon droplets.* Ultrasonics, 2013. **53**(7): p. 1368-76.

64. Burgess, M.T. and T.M. Porter, *Acoustic Cavitation-Mediated Delivery of Small Interfering Ribonucleic Acids with Phase-Shift Nano-Emulsions.* Ultrasound Med Biol, 2015. **41**(8): p. 2191-201.

65. Fabiilli, M.L., et al., *Delivery of Chlorambucil Using an Acoustically-Triggered Perfluoropentane Emulsion.* Ultrasound in Medicine & Biology, 2010. **36**(8): p. 1364-1375.

66. Liu, W.W., et al., *Nanodroplet-Vaporization-Assisted Sonoporation for Highly Effective Delivery of Photothermal Treatment.* Sci Rep, 2016. **6**: p. 24753.

CHAPTER 6[1]

AN EVALUATION OF THE SONOPORATION POTENTIAL OF LOW-BOILING POINT PHASE-CHANGE CONTRAST AGENTS *IN VITRO*

6.1 MOTIVATION AND OVERVIEW

The primary objective of this chapter is to characterize the potential of low-boiling point phase-change contrast agents (PCCAs) to induce transient cell membrane perforation *in vitro.* The precise mechanisms involved in PCCA-mediated sonoporation remain unknown, and likely depend on a number of factors including the contrast agent formulation, specific acoustic parameters (frequency, peak negative pressure [1], duty cycle, etc.), and non-acoustic parameters (microbubble size and bubble-to-cell distance [2], cell culture conditions, size of sonoporation indicator [1], etc.). It is conceivable that PCCA-induced sonoporation is driven by the same mechanisms that mediate microbubble sonoporation, with membrane permeabilization being a product of microbubble cavitation following acoustic droplet vaporization. However, the rapid expansion of an individual droplet as it phase-converts into a microbubble may itself influence cell permeability. A secondary objective of this study is to determine if the vaporization event of low-boiling point PCCAs contributes to sonoporation and/or effects cell viability.

[1]This chapter previously appeared as an article in the Journal of Therapeutic Ultrasound distributed under the terms of the Creative Commons License (http://creativecommons.org/licenses/by/4.0/). The original citation is as follows: Fix, S.M., Novell, A., Yun, Y., Dayton, P.A., Arena, C.B. (2017). "An evaluation of the sonoporation potential of low-boiling point phase-change ultrasound contrast agents in vitro." J Ther Ultrasound **5**: 7. The introduction of this work was abbreviated in this chapter as to not be redundant with prior chapters in this thesis. Otherwise, only minor changes were made in reformatting this article into the chapter presented here.

6.2 MATERIALS AND METHODS

6.2.1 FABRICATION AND CHARACTERIZATION OF PHASE-CHANGE ULTRASOUND CONTRAST AGENTS

Low boiling point PCCAs containing liquid octafluoropropane (OFP, b.p. = -36.7°C) were generated as described elsewhere [3]. First, lipid-shelled, OFP-filled microbubbles were prepared. Briefly, 90 mol% 1,2-distearoyl-*sn*-glycero-3-phosphocholine (DSPC) and 10 mol% 1,2-distearoyl-*sn*-glycero-3-phosphoethanolamine-N-methoxy(polyethylene-glycol)-2000 (mPEG-DSPE) (Avanti Polar Lipids, Alabaster, AL, USA) were combined and dissolved in a phosphate-buffered saline (PBS)-based solution containing 15% propylene glycol (v/v) and 5% glycerol (v/v) for a final lipid concentration of 1.0 mg/mL. This lipid solution (1.5 mL) was aliquoted into 3.0 mL glass vials and the headspace air was exchanged with OFP gas (Fluoromed, Round Rock, TX, USA). Finally, microbubbles were generated by vigorous shaking of the lipid vials using a VialMix (Bristol-Myers-Squibb, New York, NY, USA).

The OFP microbubbles were condensed into liquid-filled nanodroplets (i.e., PCCAs) [3]. Microbubble vials were cooled in an isopropanol/CO_2 bath maintained between -10 and -13°C. Simultaneously, the headspace pressure of the vials was gradually increased through the addition of excess OFP gas until microbubble condensation was observed. Phase transition is visually apparent, as the initially opaque microbubble solution turns translucent when condensed into liquid-filled particles.

The size distribution and concentration of the PCCAs were characterized using a NanoSight NS500 (Malvern Instruments, Westborough, MA, USA) capable of detecting nanoparticles between 50-2000nm. PCCAs were diluted 3000-fold in HPLC-grade, 20 nm filtered water. Four, 30 second recordings were captured per sample to calculate an average size distribution and concentration for each sample. This procedure was repeated in triplicate for three separate vials of PCCAs and averaged to get a representative size distribution and concentration. The particles were characterized by a polydisperse size distribution, as in Figure 6.1, with a mean size of 143±13 nm and concentration of 1.7 (±0.1) × 10^{12} particles/ml (see Appendix B for error estimation).

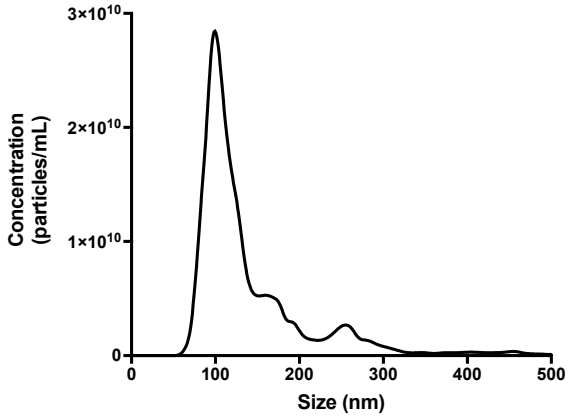

Figure 6.1: Nanosight results for OFP-filled PCCAs (N=3 vials). The mean particle size (±SD) was found to be 140 ± 10 nm and the average concentration (±SD) was 1.7 (± 0.1) × 10^{12} particles/mL.

6.2.2 VISUALIZATION OF PCCA VAPORIZATION AND SECONDARY MICROBUBBLE AFFECTS USING OPTICAL MICROSCOPY AND HIGH-SPEED PHOTOGRAPHY

High-speed optical microscopy was used to detect PCCA vaporization following ultrasound stimulation using a previously described experimental setup [4, 5]. Briefly, an inverted microscope with a 100× water immersion objective (Olympus IX71, Center Valley, PA, USA) was interfaced with a high-speed camera (FastCam SA1.1, Photron USA, Inc., San Diego, CA, USA). The objective was submerged in a temperature-controlled water bath fixed on top of the microscope. The water bath was filled with degassed water and held at 37°C. A solution of PCCAs diluted in PBS (6.7% v/v) was injected into a microcellulose tube (200 µm inner diameter) (Spectrum Labs, Inc., Rancho Dominguez, CA, USA) positioned over the optical focus. This injection was followed by a brief waiting period to allow the flowing particles to become nearly stationary. This enabled clear visualization of vaporization events as images become blurred when particles are flowing.

A 1.0 MHz spherically focused piston transducer (diameter = 19 mm, focal distance = 38 mm, IL0106HP, Valpey Fisher Corp., Hopkinton, MA, USA) was submerged in the water bath and positioned such that the acoustic focus was aligned with the microcellulose tube at the optical focus as described previously [5]. Briefly, a calibrated needle hydrophone (HNA-0400, Onda Corp., Sunnyvale, CA, USA) was aligned with the microscope focus and used to subsequently align the focus of the transducer to that location. The hydrophone was then used to calibrate the pressure

output of the transducer at various excitation voltages. The transducer was excited with sinusoidal pulses generated with an arbitrary waveform generator (AFG3021C, Tektronix, Inc., Beaverton, OR, USA) and amplified approximately 60 dB with a power amplifier (A500, ENI, Rochester, NY, USA). Following calibration, the hydrophone was replaced with a microcellulose tube, which was aligned with the microscope focus. In this way, we ensured that the plane of the tube visible in the optical focus was subjected to the calibrated acoustic pressures aligned to that location.

PCCAs flowing through the microcellulose tube were exposed to acoustic pulses with lengths of 5, 10, 20, and 50 cycles and peak negative pressures of 125, 300, 600, 1000, and 2000 kPa to observe the effect of pulse length and pressure on PCCA vaporization. In subsequent experiments, pre-vaporized PCCAs were stimulated with a second identical acoustic pulse to observe how ultrasound affected the generated microbubbles.

A synchronization pulse from the waveform generator was used to trigger the high-speed camera. Video recordings were set to begin just before the manually triggered ultrasound pulse such that vaporization or microbubble manipulations would be recorded in their entirety. A frame rate of 500 frames per second was employed. Images and videos were stored on a computer using proprietary camera software (PFV; Photron USA, Inc., San Diego, CA, USA) and analyzed using ImageJ (NIH, Bethesda, MD, USA).

6.2.3 DETECTION OF CAVITATION SIGNALS FOLLOWING PCCA VAPORIZATION

Similar to the high-speed microscopy experiments, PCCAs solutions were perfused through a microcellulose tube (200 µl/min) aligned with the focus of a 1.0 MHz, piston transducer. The transducer was calibrated at the focus using a needle hydrophone, and PCCAs were activated with sinusoidal ultrasound pulses using a pulse repetition frequency (PRF) of 5.0 Hz, peak negative pressures ranging from 125-2000 kPa, and pulse lengths between 5-50 cycles. Three concentrations of PCCAs were tested: 0.067%, 0.67%, and 6.7% (v/v) in PBS. All conditions and concentrations were tested in triplicate using three independent vials of PCCAs. Control trials with a water-filled tube were used as a reference to estimate stable and inertial cavitation generated by the vaporized PCCAs.

To detect cavitation signals, a separate, spherically focused receive transducer (7.5 MHz center frequency, diameter = 19 mm, focal distance = 50 mm) (V321, Panametrics, Inc., Waltham, MA, USA) was positioned perpendicular to the transmit transducer such that the microcellulose tube was aligned with both transducer foci. Signals from the receive transducer were acquired using a 14-bit analog to digital conversion card with a sampling frequency of 100 MHz (PDA14, Signatec, Corona, CA, USA) installed in a computer (Dell, Round Rock, TX, USA) running a custom acquisition program (LabVIEW, National Instruments Corp., Austin, TX, USA). A total of 50 individual signals were captured for each combination of pressure, pulse length, and PCCA concentration. These signals were saved and post-processed using MATLAB (Mathworks Inc., Natick, MA, USA).

A custom MATLAB script was developed to quantify the energy of stable and inertial cavitation generated for each condition. First, a window from 50-110 μs referenced to the beginning of the acoustic pulse was applied to select the signal emitted by the PCCAs. The 50 individual RF signals from each exposure condition were converted into the frequency domain. Detection of the second harmonic component was used to estimate the stable cavitation level by filtering the data from 1.8 MHz to 2.2 MHz (Butterworth filter, order 3). The broadband signal resulting from inertial cavitation was detected by filtering the signals from 5.25 MHz to 7.75 MHz (Butterworth filter, order 3) and by simultaneously excluding the harmonic components at 6 MHz and 7 MHz. Finally, energies of these stable and inertial cavitation signals were calculated, averaged among the 50 individual signals for each condition, and normalized by the energy calculated for a water-filled tube exposed to the same acoustic conditions. This procedure was repeated for three independent vials of PCCAs. The average, normalized cavitation energies are reported with the inter-vial standard deviation.

6.2.4 CELL CULTURE

Human pancreatic adenocarcinoma cells (PANC-1) were purchased from American Type Culture Collection (ATCC, VA, USA) and cultured in Dulbecco's Modified Eagle's Medium (DMEM) supplemented with 10% fetal bovine serum (FBS) and 1% penicillin-streptomycin (Sigma-Aldrich Co., MO, USA) at 37°C and 5% CO_2 atmosphere. For all experiments, cells between passages 5-24 were

used. Cells were harvested using trypsin-EDTA (Sigma-Aldrich Co., MO, USA) and counted using a hemocytometer for use in sonoporation and viability experiments.

6.2.5 SONOPORATION OF CELLS IN SUSPENSION

PANC-1 cells (1.0×10^6 cells) were suspended in serum-free DMEM containing PCCAs (8.5×10^8 particles) and propidium iodide (PI, 30 µM) (Sigma-Aldrich Co., MO, USA) for a final volume of 1.5 mL. PI was used as a sonoporation indicator as it is impermeable to intact cell membranes. The cell suspension was added to a custom plastic cuvette with nearly acoustically transparent windows made of 20 µm thick polyolefin film (Rajashrink, Roissy, France) as previously described by Escoffre et al. [6]. The cuvette was then held in a 37°C degassed water bath with constant magnetic stirring and positioned 5 cm in front of the transducer for sonoporation treatment, as shown in Figure 6.2.

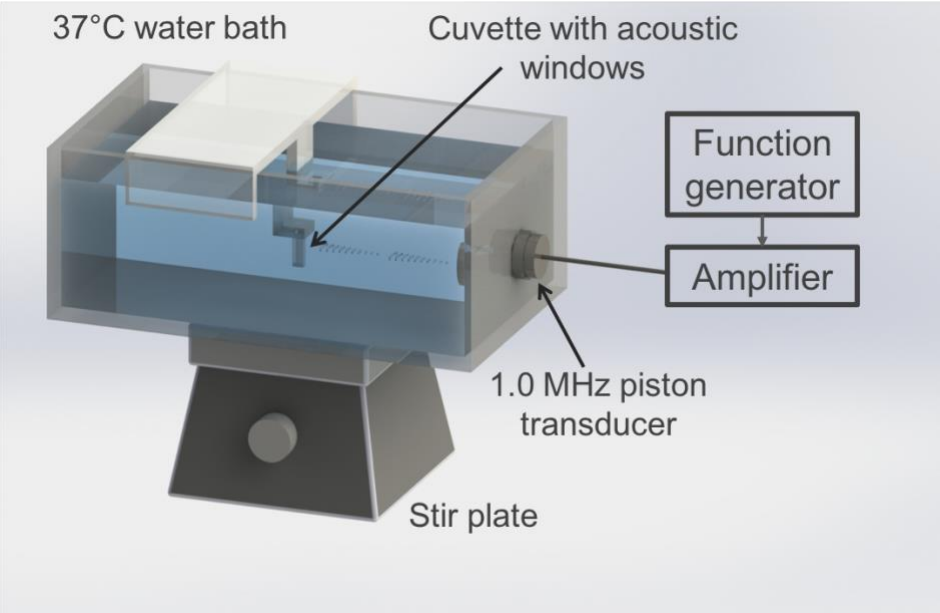

Figure 6.2: Setup designed for the sonoporation of cells in suspension with PCCAs.

To generate ultrasound pulses, a 1.0 MHz unfocused piston transducer (diameter = 1.0 in, IL0108HP, Valpey Fisher Corp., Hopkinton, MA, USA) was excited by a sinusoidal arbitrary function generator signal (AFG3021C, Tektronix, Inc., Beaverton, OR, USA) amplified approximately 55 dB by an RF power amplifier (3100LA, ENI, Rochester, NY, USA). The pressure output of the transducer at various excitation voltages was characterized using a calibrated needle hydrophone placed 5 cm in

front of the transducer, matching the distance of the cuvette in sonoporation experiments. The cell suspensions were insonified for 30 seconds with peak negative pressures of 125, 300, or 600 kPa, pulse lengths of 5, 10, 20 or 50 cycles, and a constant PRF of 5.0 kHz, as summarized in Table 6.1. As controls, cells underwent (1) sham treatment (without PCCAs or ultrasound exposure) and (2) ultrasound only treatment (without PCCAs) using the highest energy condition – 600 kPa and 50 cycles.

Post-treatment, cells were transferred to plastic tubes and incubated at 37°C for at least 15 minutes to ensure membrane resealing processes were completed prior to further manipulation of the cells [7]. Subsequently, the viability stain calcein-AM (0.8 μM) (Thermo Fisher Scientific Inc., MA, USA) was added and the cells were allowed to incubate for at least an additional 30 min at 37°C. Cells were filtered through 44 μm nylon mesh (Component Supply Co., FL, USA) before being analyzed by flow cytometry. Cells showing both PI uptake and calcein-AM cleavage by flow cytometry were considered to be successfully sonoporated. These experiments were repeated in triplicate on independent days. All sonoporation conditions were also performed in triplicate without the addition of dye to monitor changes in autofluorescence due to treatment.

Table 6.1: Experimental and control conditions for sonoportion.

Conditions	PCCAs (Y/N)	Cycles (#)	PRF (kHz)	Pressure (kPa)
1-4	Y	5, 10, 20, 50	5	125
5-8	Y	5, 10, 20, 50	5	300
9-12	Y	5, 10, 20, 50	5	600
US only control	N	50	5	600
Sham control	N	NA	NA	NA

6.2.6 ASSESSMENT OF SONOPORATION EFFICIENCY BY FLOW CYTOMETRY

Flow cytometry was used to quantify the number of sonoporated cells for each treatment group, i.e., those cells displaying both PI uptake (permeabilization) and calcein-AM cleavage (viability). An LSRFortessa cytometer equipped with 561 nm and 488 nm excitation lasers (Becton Dickinson, Franklin Lakes, NJ, USA) was used for acquisition, and 30,000 events were recorded for

each sonoporation treatment. For further details regarding acquisition settings, please see Appendix B, Table B.2.

The gating strategy employed to isolate sonoporated cells is described in full in the Appendix B and displayed in Figure B.1. Briefly, singlet cells were isolated from debris and doublet cells through initial gating steps. The viability of the chosen cell population was then confirmed by calcein fluorescence. Curly quadrant gates were applied to the calcein vs. PI fluorescence dot plots, with thresholds determined such that unstained control cells would be classified as both calcein and PI negative. The percent of cells in quadrant two (calcein and PI positive) was taken to be the sonoporation efficiency (i.e., percent of viable cells that were sonoporated). All data analysis was performed using FlowJo Data Analysis Software (FlowJo, LLC., Ashland, OR, USA).

6.2.7 ASSESSING VIABILITY POST-SONOPORATION TREATMENT

Through our flow cytometry experiments, we found that dead cells and cellular debris were characterized by elevated autofluorescence in the calcein (viability) channel (data not shown). Therefore, we were unable to accurately quantify cell viability based on the flow cytometry results alone. As such, we performed an additional cell viability assay. Cells suspended in serum-supplemented DMEM were subjected to the sonoporation protocol as described above without the addition of PI or calcein-AM. Following treatment, 1.0×10^5 cells per treatment group were transferred to 24-well plates and allowed to incubate for 24 hours at 37°C and 5% CO_2 atmosphere. Subsequently, cell viability was assessed using a resazurin-based toxicology assay according to the manufacturer's protocol (Sigma-Aldrich Co., MO, USA).

Briefly, a volume of resazurin dye equal to 10% of the culture media was added to the cells and allowed to incubate for 3 hours. A 200 µL sample from each culture well was then transferred to a 96-well plate for analysis. The fluorescence increase at 590 nm (F_{590}) due to reduction of the resazurin dye by viable cells was detected using a plate reader (Synergy 2, BioTek Instrument, Inc., Winooski, VT, USA) with excitation and emission filters of 530/25nm and 590/35nm, respectively. The fluorescence intensity of a blank sample containing complete media but no cells was subtracted from

that of each sample. Cell viability was then calculated as the percent resazurin reduction of the sham control. Viability experiments were repeated in triplicate on independent days.

6.2.8 STATISTICAL ANALYSES

All statistical analyses were performed in GraphPad Prism 7 (GraphPad Software, Inc., La Jolla, CA, USA), and data are presented as average ± standard deviation throughout this work. Sonoporation efficiencies and cell viabilities were compared among treatment groups using one-way ANOVA followed by Dunnett's multiple comparison testing on significant results. Each treatment group was compared to the sham control, and p-values of < 0.05 were considered statistically significant. Pearson correlation coefficients (r) were computed in GraphPad Prism 7 to analyze the correlation between (1) sonoporation efficiency and stable cavitation and (2) sonoporation efficiency and inertial cavitation. Correlations were considered statistically significant if the two-tailed p-values were < 0.05.

6.3 RESULTS

6.3.1 DETECTION OF PCCA VAPORIZATION AND SUBSEQUENT CAVITATION SIGNALS

Through optical high-speed microscopy and the detection of cavitation signals, we investigated the effect of acoustic pulse length and peak negative pressure on PCCA vaporization (a.k.a. acoustic droplet vaporization – ADV) and the behavior of resultant microbubbles. At a frequency of 1.0 MHz, we found that our PCCAs undergo ADV at and above peak negative pressures of 300 kPa but never at or below 125 kPa, regardless of pulse length. This is consistent with previous reports demonstrating that ADV is a pressure-dependent, threshold phenomenon that is independent of pulse length when short, microsecond pulses are used [8, 9]. Representative photos showing PCCAs before and after ultrasound stimulation above and below the activation threshold are displayed in Figure 6.3 A. Note: 300 kPa does not represent an absolute pressure threshold for vaporization; rather, we conclude that the vaporization threshold is between 125 kPa and 300 kPa under the conditions studied.

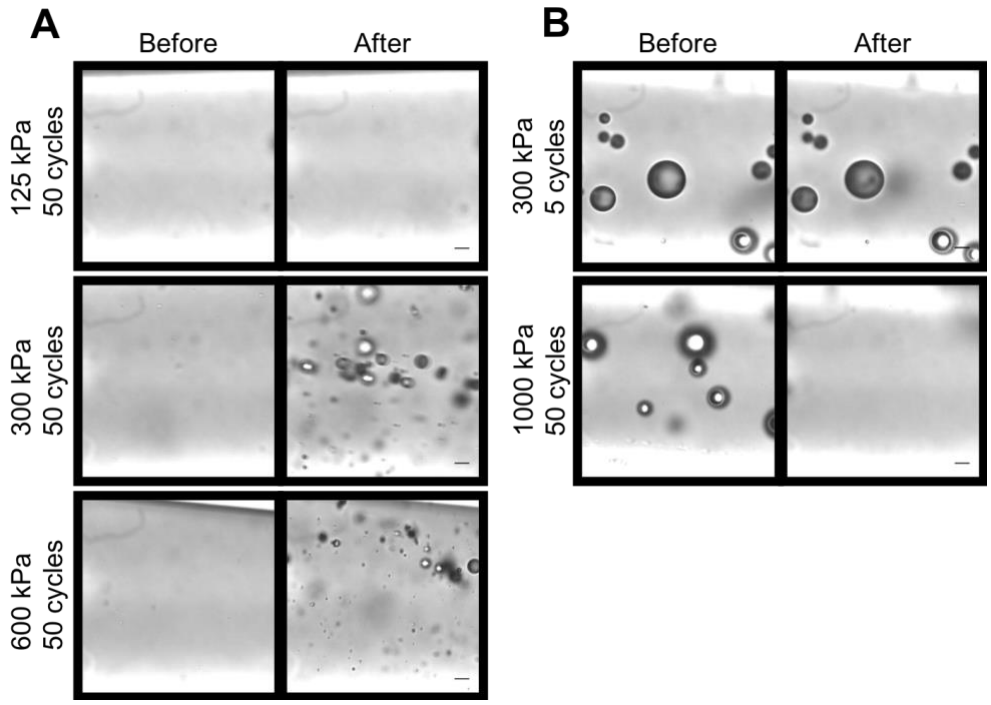

Figure 6.3: Observation of PCCA vaporization and secondary microbubble effects using high speed photography. Representative photos are displayed of PCCAs or resultant microbubbles before and after ultrasound stimulation (1.0 MHz center frequency). A) The nanoscale, liquid-filled PCCAs are difficult to observe before vaporization. A peak negative pressure of 125 kPa is not sufficient to vaporize the PCCAs (top). With a peak negative pressure of 300 kPa, efficient vaporization of the PCCAs into microbubbles is observed (bottom). B) Secondary effects are observed when generated microbubbles are subjected to a second acoustic pulse. At 300 kPa and 5 cycles, the second acoustic pulse appears to have no effect on the generated microbubbles (top). With high acoustic energies, complete microbubble destruction is observed (bottom). Scale bar = 10 μm.

While pulse length did not affect whether or not vaporization would occur, it did influence the behavior of resultant microbubbles. When generated microbubbles were stimulated with a second ultrasound pulse, microbubble destruction occurred on a continuum. No destruction was observed with low-pressure pulses (300 kPa) and complete destruction of all microbubbles in the field of view occurred with long pulses (20 and 50 cycles) at high pressure (1000 and 2000 kPa) (Figure 6.3 B).

Microbubble sizes were estimated from the captured images. Microbubbles generated from ADV at 300 kPa were polydisperse and ranged in size between 2-10 μm. When the peak negative pressure was increased to 600 kPa and above, generated microbubbles were observed in the 1-10 μm range; however, we note an increase in the number small (~1 μm) microbubbles present. This is consistent with previous reports from our laboratory detailing the dependence of generated microbubble size on various acoustic parameters, including peak negative pressure [10]. The shift

towards smaller resultant microbubbles with increased pressure is due inverse relationship between vaporization threshold and PCCA size [10, 11]. When generated microbubbles were allowed to rest before being subjected to a second acoustic pulse (Figure 6.3 B), we noticed microbubble sizes shift to be larger (approximately 3-20 μm). This is likely due to coalescence of the generated microbubbles.

The generation of stable and inertial cavitation signals depended on peak negative pressure and pulse length. Very little stable and no inertial cavitation was observed at pressures of 125 kPa regardless of pulse length; the slight stable cavitation may be due to oscillations of microbubbles that arose from spontaneous vaporization. Cavitation energy was observed from 300-2000 kPa, with very little cavitation achieved with peak negative pressures of 300 kPa and short (5 and 10 cycle) pulse lengths (Figure 6.4). The amount of stable cavitation produced reached a plateau between 24-29 dB for 50 cycle pulses with pressures between 300-2000 kPa. Alternatively, inertial cavitation continued to increase with increasing pressure. Interestingly, the concentration of PCCAs did not significantly influence the amount of stable or inertial cavitation detected (data not shown) and obtained graphs for all tested concentrations were nearly identical to the one presented in Figure 6.4 for 0.67% (v/v) PCCAs in PBS.

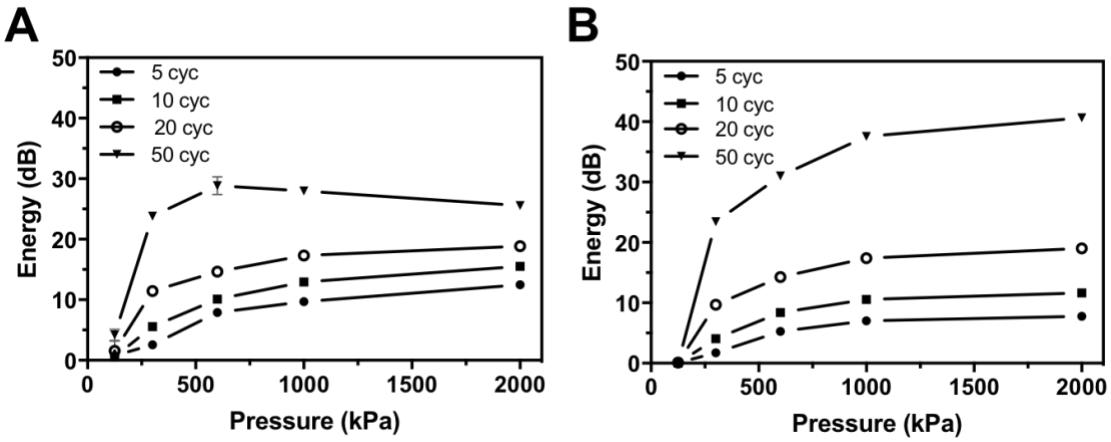

Figure 6.4: Stable and inertial cavitation. Quantification of the (A) stable and (B) inertial cavitation energy generated by PCCAs subjected to ultrasound of various peak negative pressures and pulse lengths. Note: while error bars (SD) are plotted, they are not visible on all data points due to their small size.

6.3.2 SONOPORATION EFFICIENCY

Flow cytometry was used to analyze the effect of acoustic pressure and pulse length on PCCA-facilitated PI uptake through sonoporation. Dead cells were discarded from the analysis through an initial gating step to remove cellular debris (Appendix B, Figure B.1). The viability of remaining cells was confirmed using calcein-AM staining. While the viability of gated cells was near 100% for all conditions, the percentage of cellular debris was observed to increase with increasing acoustic energy, implying elevated cell death.

Sonoporation efficiency, the percent of viable cells displaying PI fluorescence, was quantified as the percent of cells in quadrant 2, as shown in Figure 6.5. A small percentage of cells (2 – 4.5%) appeared in quadrant two for the sham control, likely due to the prolonged exposure of cells to PI. This was defined as the false positive rate and was subtracted from the sonoporation efficiency of all other treatment groups. The autofluorescence analysis demonstrated slight spreading of unstained cell populations along the PI axis due to ultrasound treatment with PCCAs (Appendix B, Figure B.2). The average percent of cells classified as PI positive due to autofluorescence never exceeded 2%, but these values were subtracted from the final sonoporation efficiencies of all groups.

Statistically significant elevation in PI uptake was observed at 300 kPa with pulse lengths of 20 and 50 cycles and at 600 kPa with 5-50 cycle pulse lengths compared to the sham control. Sonoporation efficiency increased with peak negative pressure and pulse length, reaching a maximum of 36±4% at 600 kPa and 50 cycles (Figure 6.6). As expected, we did not observe sonoporation below the vaporization threshold of the PCCAs (at 125 kPa) or when cells were insonified in the absence of PCCAs.

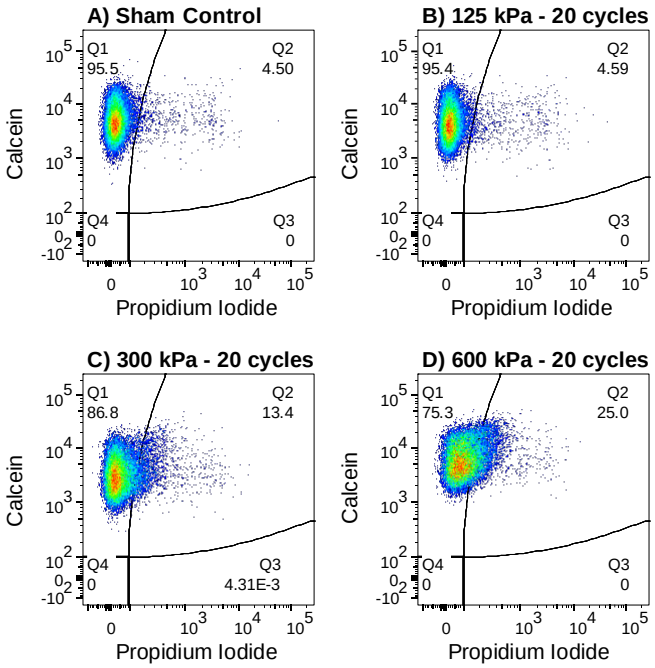

Figure 6.5: Representative flow cytometry dot plots used to quantify sonoporation efficiency. Cells were classified as sonoporated if they showed calcein fluorescence (viability) and uptake propidium iodide (membrane permeability). These cells appear in quadrant 2 (Q2) in the above dot plots. A) The small percentage of cells that appear in Q2 for the sham treatment group was defined as the false positive rate and was subtracted from the percent of cells in Q2 for all treatment groups. B) Ultrasound exposure below the PCCA activation threshold did not result in sonoporation. C-D) Sonoporation is observed above the PCCA activation threshold and increases with increasing pressure.

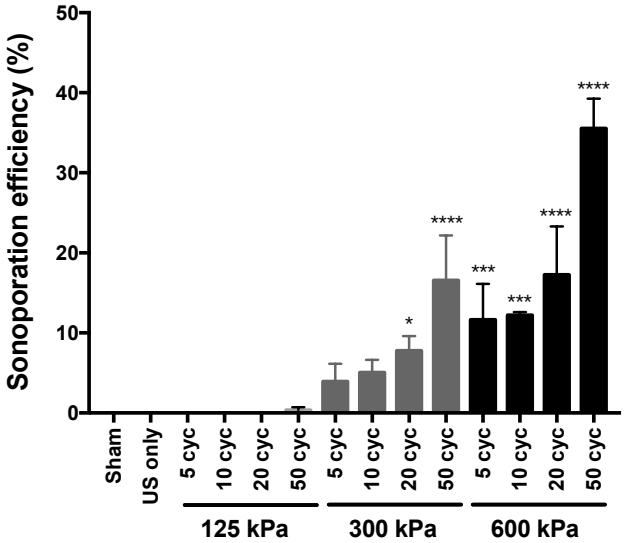

Figure 6.6: Sonoporation efficiency of PANC-1 cells at various acoustic pressures and pulse lengths. As expected, we do not observe sonoporation below the vaporization threshold of the PCCA (at 125 kPa) or when cells are insonified in the absence of PCCA (US alone). One-way ANOVA was used followed by Dunnett's multiple comparisons test compare each treatment to the sham control.
* p≤0.05, **p≤0.01, ***p≤0.001, ****p≤0.0001

6.3.3 CELL VIABILITY 24 HOURS POST-TREATMENT

To test the effect of sonoporation treatment on cell viability, cells were treated using a protocol identical to that employed for sonoporation but without the addition of PI or calcein-AM. Twenty-four hours post-treatment, viability was assessed using a resazurin-based metabolic assay. Ultrasound exposure in the absence of PCCA did not affect cell viability. Furthermore, the PCCAs themselves did not have a toxic effect on cells as evidenced by the high viability in treatment groups below the PCCA activation threshold (125 kPa treatment groups). We did observe decreasing cell viability with increasing cycle number and pressure above the activation threshold. In general, fairly high viability was recorded for those cells treated with 300 kPa ultrasound of various pulse lengths (84±7% – 94±7% viability) and cells treated with 600 kPa ultrasound with pulse lengths between 5-20 cycles (85±12% – 93±6%) (Figure 6.7). A statistically significant drop in viability (70±5%) was observed in cells treated with 600 kPa and 50 cycles compared to sham treated cells.

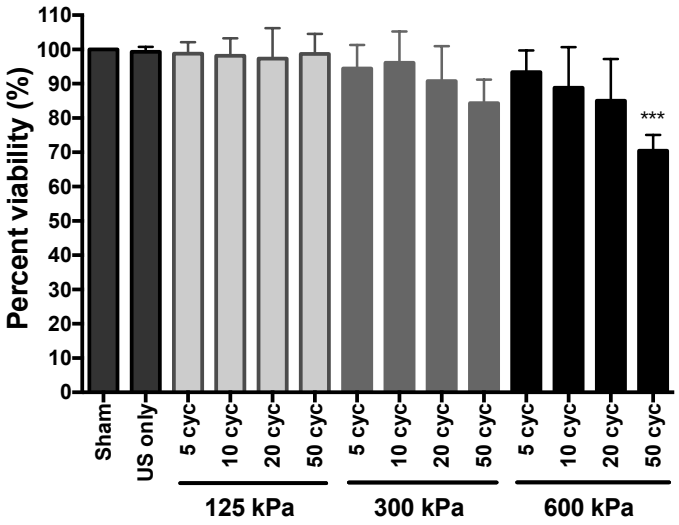

Figure 6.7: Cell viability 24 hours post-sonoporation treatment. Here we observe decreasing cell viability with increasing pulse length and pressure. As expected, ultrasound exposure in the absence of PCCAs does not affect cell viability. Furthermore, the PCCAs themselves to not have a toxic effect on cells as evidenced by the high viability in treatment groups below the PCCA activation threshold (125 kPa groups). One-way ANOVA was used followed by Dunnett's multiple comparisons test to compare each treatment to the sham control. ***$p \leq 0.001$

6.4 DISCUSSION

6.4.1 ACOUSTIC OR TEMPERATURE-INDUCED DROPLET VAPORIZATION CAN BE ACHIEVED WITHOUT MEMBRANE PERFORATION OR IMPAIRED CELL VIABILITY

Our PCCAs are comprised of a very low boiling point PFC and undergo some spontaneous vaporization when incubated at 37°C. Therefore, cells incubated with PCCAs and exposed to ultrasound below the activation threshold (at 125 kPa) felt the effects of temperature-induced vaporization alone. The membrane permeability and viability of cells treated in this way was unaltered. Additionally, cells treated with PCCAs at 300 kPa with pulse lengths of 5 or 10 cycles demonstrated insignificant sonoporation efficiencies and no change in cell viability. These cells were exposed to acoustic droplet vaporization but minimal cavitation of the resultant microbubbles. These data indicate that vaporization events do not affect cellular membrane permeability or cause any detrimental cellular bioeffects.

This is in contrast to the bioeffects observed following the vaporization of micron-sized, DDFP-filled PCCAs used for vascular occlusion. Seda, et al. have demonstrated that vaporization of DDFP-filled droplets results in extensive cell death even when using acoustic parameters designed to minimize secondary mechanical effects from the resultant bubbles [12]. Differences in experimental setups (cells treated in adherent culture vs. in suspension) and size distributions of PCCAs (1.6±0.5 μm vs. 143±13 nm mean size) make it difficult to directly compare these results. However, the difference in severity of bioeffects observed is likely due to the difference in pressure required to vaporize the PCCAs. Rarefactional pressures of at least 6 MPa were required for vaporization of DDFP-filled PCCAs, while 300 kPa was sufficient for vaporization of our PCCAs. By using a highly volatile formulation with lower pressure requirements for ADV, we can safely induce vaporization without immediately and irreparably damaging surrounding cells.

6.4.2 PCCA-INDUCED SONOPORATION IS CORRELATED WITH STABLE AND INERTIAL CAVITATION

Sonoporation efficiency was found to be significantly and positively correlated with both stable ($r = 0.9352$, $p < 0.0001$) and inertial ($r = 0.9456$, $p<0.0001$) cavitation (Figure 6.8). While it is difficult to ascertain a cavitation threshold for sonoporation from these data, we note that all statistically significant sonoporation treatments were associated with stable cavitation energies greater than 7.9 dB and inertial cavitation energies greater than 5.2 dB. This study was not designed to elucidate the mechanisms driving PCCA-mediated sonoporation, but our data suggest that the mechanical effects due to microbubble-ultrasound interactions are necessary for significant sonoporation. Therefore, it is likely that the same mechanisms that drive conventional microbubble-mediated sonoporation also drive PCCA-mediated sonoporation.

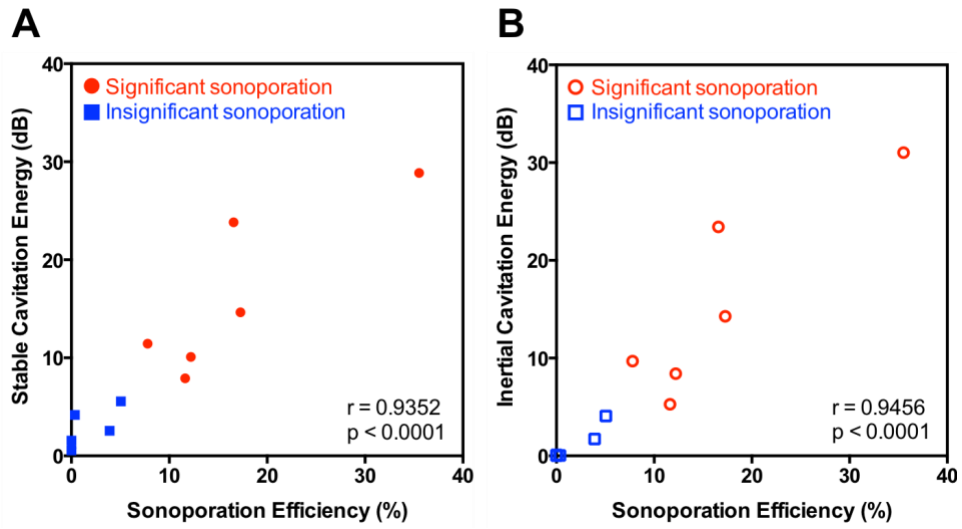

Figure 6.8: Correlations between sonoporation efficiency and stable or inertial cavitation. We observe a strong, positive correlation between sonoporation efficiency and (A) stable cavitation and (B) inertial cavitation. The Pearson correlation coefficients for sonoporation efficiency vs. stable and inertial cavitation are 0.9352 and 0.9456, respectively, and both correlations are statistically significant with p-values < 0.0001. Data points corresponding to statistically significant sonoporation efficiencies (compared to sham control) are shown in red circles, while data points corresponding to statistically insignificant sonoporation efficiencies are shown in blue squares.

The peak sonoporation efficiency we achieved (36%) is similar to what has previously been reported for microbubble sonoporation (28-39% efficiency) [13-15], albeit with lower cell viability (70%

viability for PCCA sonoporation vs. 90-96% viability for MB sonoporation [13-15]). However, these microbubble sonoporation studies employ unique strategies to increase sonoporation efficiency and minimize cell death, making it difficult to make direct comparisons. For example, McLaughlan et al. achieved their highest viable sonoporation using a combination of (1) targeted microbubbles that increase cell-microbubble interactions and (2) chirp frequency excitation to maximize the response of their polydisperse microbubbles [14]. Song et al. found that using monodisperse 2.0 μm microbubbles resulted in the highest sonoporation and viability after a single ultrasound treatment [15]. We believe that with further optimization of our PCCA-mediated sonoporation methods, we will be able to match the sonoporation efficiencies and viabilities achieved with microbubbles. Future studies will be designed to apply the aforementioned techniques developed by the microbubble sonoporation community to PCCA-mediated sonoporation.

6.5 CONCLUSIONS

In conclusion, our data show that low-boiling point PCCAs are capable of inducing sonoporation without causing detrimental cellular bioeffects *in vitro*. Furthermore, the low pressure required to activate such PCCAs allows us to fine-tune the severity of cellular bioeffects simply by modifying pulse length. This provides flexibility in future applications imaginable and allows for acoustic droplet vaporization to be achieved safely and with existing diagnostic imaging hardware. Here we demonstrate the ability to cause (1) vaporization with no cellular damage – ideal for diagnostic imaging applications, (2) reversible sonoporation – desirable for therapeutic applications such as drug or gene delivery where cell death is to be avoided, or (3) irreversible sonoporation – useful in augmenting tumor killing through high intensity focused ultrasound treatment.

A limitation of this study is that we did not control for differences in PCCA vaporization efficiency at each acoustic condition. In other words, more bubbles were likely generated using the highest energy conditions compared to the lowest energy conditions as a constant PCCA concentration was used throughout. This makes it difficult to draw conclusions about sonoporation mechanism and parameter optimization. The increases in sonoporation efficiency with increasing pressure and pulse length may have been due to (1) increased cavitation and associated mechanical

effects, (2) increased concentration of generated microbubbles, or (3) a combination thereof. Future studies will be designed to quantify the vaporization efficiency of PCCAs at each acoustic condition to allow for concentration matching of generated microbubbles. Other important parameters to consider are contrast agent size distribution, ultrasound exposure duration, and center frequency. Future studies will be designed to optimize these parameters and provide a thorough comparison between the sonoporation potential of microbubbles, low-boiling point PCCAs, and high-boiling point PCCAs.

One of the main advantages of using PCCAs for reversible sonoporation compared to microbubbles is the potential for their extravasation from a tumor's leaky vasculature. While we note that the mean size of our PCCAs is smaller than the pore sizes in many permeable tumor lines (200 nm – 1.2 μm) [16], the extravasation and accumulation of our particles in tumors has yet to be confirmed. Studies are currently ongoing towards this end. Nevertheless, our data warrant further investigation into the use of PCCAs to induce extravascular sonoporation *in vivo* for the purpose of enhancing local drug or gene delivery, particularly within solid tumors.

REFERENCES

1. De Cock, I., et al., *Ultrasound and microbubble mediated drug delivery: acoustic pressure as determinant for uptake via membrane pores or endocytosis.* J Control Release, 2015. **197**: p. 20-8.

2. Qin, P., et al., *Effect of non-acoustic parameters on heterogeneous sonoporation mediated by single-pulse ultrasound and microbubbles.* Ultrason Sonochem, 2016. **31**: p. 107-15.

3. Sheeran, P.S., et al., *Design of ultrasonically-activatable nanoparticles using low boiling point perfluorocarbons.* Biomaterials, 2012. **33**(11): p. 3262-9.

4. Sheeran, P.S., et al., *Formulation and acoustic studies of a new phase-shift agent for diagnostic and therapeutic ultrasound.* Langmuir, 2011. **27**(17): p. 10412-20.

5. Sheeran, P.S., et al., *Decafluorobutane as a phase-change contrast agent for low-energy extravascular ultrasonic imaging.* Ultrasound Med Biol, 2011. **37**(9): p. 1518-30.

6. Escoffre, J.M., et al., *Focused ultrasound mediated drug delivery from temperature-sensitive liposomes: in-vitro characterization and validation.* Phys Med Biol, 2013. **58**(22): p. 8135-51.

7. Hu, Y., J.M. Wan, and A.C. Yu, *Membrane perforation and recovery dynamics in microbubble-mediated sonoporation.* Ultrasound Med Biol, 2013. **39**(12): p. 2393-405.

8. Fabiilli, M.L., et al., *The role of inertial cavitation in acoustic droplet vaporization.* IEEE Trans Ultrason Ferroelectr Freq Control, 2009. **56**(5): p. 1006-17.

9. Lo, A.H., et al., *Acoustic droplet vaporization threshold: effects of pulse duration and contrast agent.* IEEE Trans Ultrason Ferroelectr Freq Control, 2007. **54**(5): p. 933-46.

10. Sheeran, P.S., T.O. Matsunaga, and P.A. Dayton, *Phase-transition thresholds and vaporization phenomena for ultrasound phase-change nanoemulsions assessed via high-speed optical microscopy.* Phys Med Biol, 2013. **58**(13): p. 4513-34.

11. Sheeran, P.S. and P.A. Dayton, *Phase-Change Contrast Agents for Imaging and Therapy.* Curr Pharm Des, 2012. **18**(15): p. 2152-65.

12. Seda, R., et al., *Characterization of Bioeffects on Endothelial Cells under Acoustic Droplet Vaporization.* Ultrasound Med Biol, 2015. **41**(12): p. 3241-52.

13. Karshafian, R., et al., *Sonoporation by ultrasound-activated microbubble contrast agents: effect of acoustic exposure parameters on cell membrane permeability and cell viability.* Ultrasound Med Biol, 2009. **35**(5): p. 847-60.

14. McLaughlan, J., et al., *Increasing the sonoporation efficiency of targeted polydisperse microbubble populations using chirp excitation.* IEEE Trans Ultrason Ferroelectr Freq Control, 2013. **60**(12): p. 2511-20.

15. Song, K.H., et al., *High Efficiency Molecular Delivery with Sequential Low-Energy Sonoporation Bursts.* Theranostics, 2015. **5**(12): p. 1419-27.

16. Hobbs, S.K., et al., *Regulation of transport pathways in tumor vessels: role of tumor type and microenvironment.* Proc Natl Acad Sci U S A, 1998. **95**(8): p. 4607-12.

CHAPTER 7[1]

IN VITRO DELIVERY OF BLEOMYCIN INTO RESISTANT CANCER CELL LINE USING SONOPORATION WITH LOW BOILING POINT PCCAs

7.1 MOTIVATION AND OVERVIEW

Bleomycin (BLM) is a potently cytotoxic glycopeptide used to treat several cancer types including ovarian, cervical, and testicular cancers, non-Hodgkin's lymphoma, and head and neck carcinoma [1, 2]. When BLM chelates metal ions, the activated complex reacts with molecular oxygen to create free radicals that cleave DNA and damage other cellular components, resulting in cell death [2]. Given this mechanism of action, BLM must be sufficiently internalized by target cells for it to have the desired effect. BLM is cell membrane impermeable and therefore relies on receptor-mediated endocytosis for internalization. Cancer types with poor expression of the BLM-binding receptor are resistant to this treatment [1, 3].

Technologies that permeabilize cell membranes for localized drug delivery present a promising method to broaden the utility of BLM to resistant cancer types. This may be achievable with ultrasound-stimulated microbubbles through sonoporation. As described in the previous two chapters, PCCAs provide considerable advantages over microbubbles for *in vivo* sonoporation applications that require extravascular cell membrane perforation, as would be the case for sonoporation-enhanced BLM therapy. Thus, the objective of this work is to demonstrate the ability to improve intracellular accumulation and efficacy of BLM in a resistant colon cancer cell line *in vitro* through sonoporation with PCCAs. A secondary objective is to compare the sonoporation efficiency of PCCAs to that of

[1]© 2017, IEEE. Reprinted with permission from Fix, S.M., Novell, A., Escoffre, J.M., Tsuruta, J.K., Dayton, P.A., Bouakaz, A. "In-vitro delivery of BLM into resistant cancer cell line using sonoporation with low-boiling point phase change ultrasound contrast agents." Sept., 2017

standard lipid-shelled microbubbles. This work represents a first step towards extravascular sonoporation-mediated BLM delivery with PCCAs *in vivo.*

7.2 MATERIALS AND METHODS

7.2.1 FABRICATION OF LIPID-SHELLED MICROBUBBLES AND PHASE-CHANGE CONTRAST AGENTS

Lipid-shelled microbubbles and PCCAs were generated in-house as described in chapter 6 and pervious work [4]. This process yielded microbubbles with a mean diameter of 1.01 ± 0.02 μm and concentration of 1.11 (±0.08) × 10^{10} microbubbles/mL, as characterized by single particle optical sizing (Accusizer 780AD, Particle Sizing Systems, Port Richey, FL, USA). PCCAs were generated via condensation of these microbubbles and were characterized by dynamic light scattering (DLS) (Zetasizer Nano ZS, Malvern, Worcestershire, UK). The PCCAs were found to have an average size of 179 ± 13 nm and a single-peak size distribution, as displayed in Figure 7.1. The DLS was unable to provide particle concentration data. Therefore, throughout this work, we assumed that the microbubble condensation efficiency was 100%, and we considered the concentration of droplets to be equal to that of their precursor microbubbles (*i.e.,* 1.11x10^{10} particles/mL).

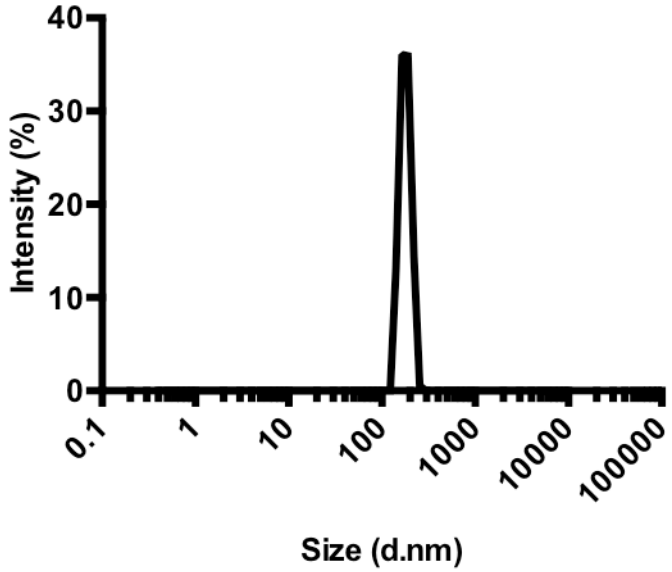

Figure 7.1: PCCA size distribution as assessed using dynamic light scattering. The average diameter of these particles was found to be 179 ± 13 nm.

7.2.2 CELL CULTURE

Human colon adenocarcinoma cells (HT-29, European Collection of Cell Cultures, Salisbury, UK) were cultured in McCoy's 5A medium (with sodium bicarbonate and L-glutamine) (Sigma-Aldrich, Saint-Louis, MO, USA) supplemented with 10% (v/v) fetal bovine serum (FBS) and 1% penicillin/streptomycin (Fisher Scientific, Illkirch, France). Cells between passage numbers 20 – 22 were used for all experiments. Cells were harvested using trypsin and suspended in OptiMEM High W/GlutaMax-I medium (Fisher Scientific, Illkirch, France) supplemented with 1% FBS for sonoporation treatments.

7.2.3 DRUG DELIVERY AND VIABILITY ASSESSMENT

Sonoporation was performed according to the previously published protocol described in chapter 6 [5]. Briefly, HT-29 cells (500,000 cells) were suspended in 1.5 mL OptiMEM High W/GlutaMax-I supplemented with 1% FBS, transferred to a plastic cuvette, and positioned 3 cm in front of the face of a 1.0 MHz unfocused piston transducer (IM 013, Imasonic, Besançon, France) in a 37°C water bath (Grant Instruments Ltd. Cambridge, UK). The cells were held in suspension by constant magnetic stirring throughout the sonoporation procedure. Microbubbles or PCCAs were added to the cell suspension at an agent to cell ratio of 5.6 agents: 1.0 cell. Bleomycin (0.01-10 μM) was added to assess the potential of microbubbles and PCCAs to improve drug delivery. Cells were insonified for 30 seconds with a peak negative pressure of 400 kPa and duty cycle of 40%, which is sufficient acoustic energy to vaporize our PCCAs into microbubbles.

Post-sonoporation treatment, cells suspensions (0.5 mL) were transferred to 24 well plates and incubated at 37 °C for 4 hours at which point the cell media was supplemented to contain a final concentration of 10% FBS and 1% P/S. Cell viability was evaluated 48 hours post-sonoporation.

Cell viability was assessed using an MTT viability assay (Invitrogen, Carlsbad, CA, USA). Culture media was replaced with OptiMEM containing MTT (0.5 mg/ml) and FBS (10% v/v). Cells were allowed to incubate at 37°C for 1 hour at which point the MTT-containing media was replaced with DMSO (Sigma-Aldrich, Saint-Louis, MO, USA). To release reduced MTT dye, the plates were protected from light and shaken at 20 rpm for 10 minutes. Reduced MTT was measured via

absorbance at 570 nm using a Nanodrop Spectrophotometer (NanoDrop 2000, Thermo Fisher Scientific, Waltham, MA, USA), and percent viability was calculated in reference to cells treated with ultrasound alone (without contrast agents or BLM) unless otherwise specified.

7.2.4 STATISTICAL ANALYSES

Data throughout this work are presented as the average ± standard deviation of three replicates. The toxicities of 0 – 10 μM BLM in the absence of ultrasound exposure were compared using one-way ANOVA followed by Dunnett's multiple comparison test comparing the viability data for each BLM concentration to that of control cells exposed to 0.0 μM BLM. Similarly, the viability of cells exposed to sonoporation conditions in the absence of BLM were compared using one-way ANOVA followed by Dunnett's multiple comparison test to compare results to that of the ultrasound only control (i.e., sonoporation without contrast agents). Cell viability after sonoporation with MBs or PCCAs at a range of BLM concentrations were compared using two-way ANOVA followed Dunnett's multiple comparison testing (comparing cell viability of MB-sonoporation and PCCA-sonoporation to that of ultrasound alone at each BLM concentration).

7.3 RESULTS AND DISCUSSION

First, we confirmed that the HT-29 cell line is resistant to BLM over the tested concentration range. As shown in Figure 7.2, incubating these cells with 0.01 – 10 μM BLM for 48 hours has no effect on viability compared to untreated cells (Figure 7.2) (data normalized to untreated control cells). Next, we characterized the effect of our sonoporation protocol on cell viability in the absence of BLM. Here we observe that ultrasound exposure alone (without contrast agents) has a stimulatory effect on cell proliferation (ultrasound exposed vs. sham treated cells, normalized to viability of ultrasound treated cells). Neither sonoporation with MBs nor with PCCAs reduced cell viability 48 hours post-treatment compared to the ultrasound only control (Figure 7.3). These results confirmed that our sonoporation protocol was reversible and not harmful to the cells.

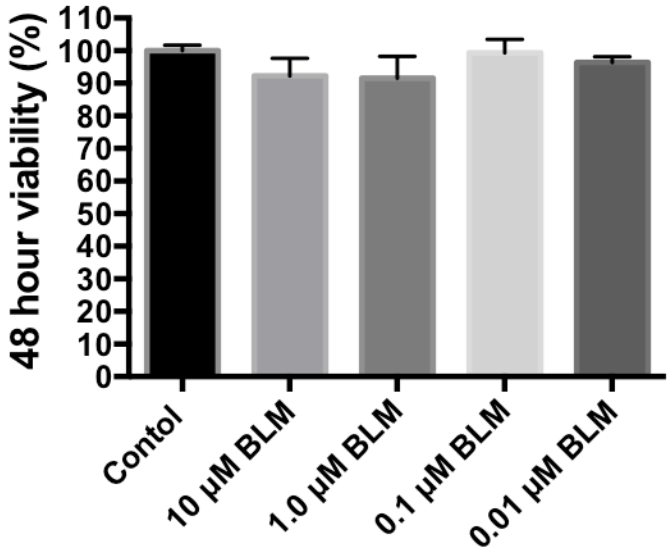

Figure 7.2: Exposing HT-29 cells to a range of BLM concentrations for 48 hours has no effect on viability. Data normalized to viability of control cells not exposed to BLM. One-way ANOVA followed by Dunnett's multiple comparison testing shows no statistical difference between BLM exposure groups and the untreated control (all p-values > 0.05).

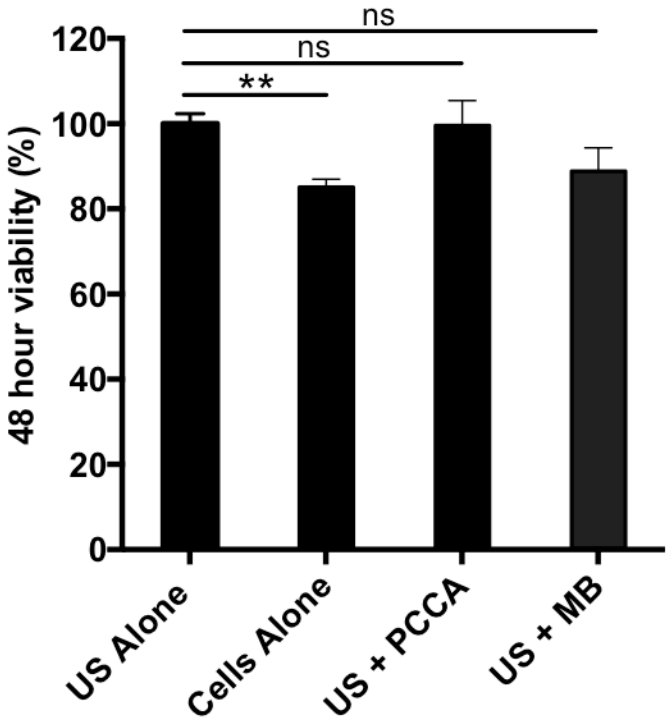

Figure 7.3: Exposing cells to ultrasound (US alone, *i.e.* sonoporation without contrast agents) stimulated growth compared to the sham treated control. The sonoporation procedure with PCCAs or MBs did not result in significant cell death compared to the US only control, indicating that sonoporation was reversible and not harmful to the cells. All groups normalized to the viability of the US only control. ** $p \leq 0.01$, ns $p > 0.05$

We were able to achieve significantly improved toxicity over the entire BLM concentration range through sonoporation with microbubbles and PCCAs (agents:cell ratio: 5.6:1.0) (Figure 7.4). We achieved the greatest cell death at the highest BLM concentration (53 ± 4% and 54 ± 13% viability for MB- and PCCA-mediated sonoporation, respectively). MBs and PCCAs performed similarly, resulting in comparable cell death over a range of BLM concentrations. Since the sonoporation protocol alone does not negatively impact cell viability, we conclude that sonoporation results in improved intracellular accumulation of BLM allowing efficacy in resistant HT-29 cells.

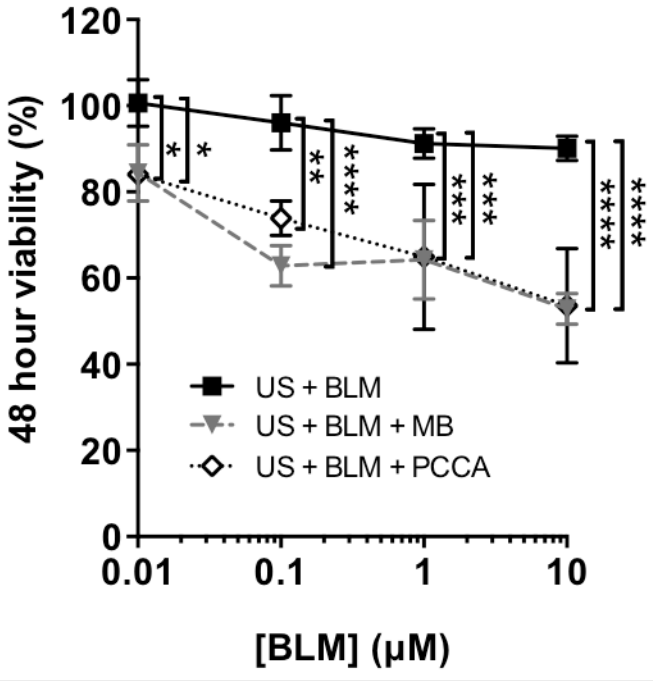

Figure 7.4: Sonoporation with PCCAs or microbubbles (MBs) resulted in enhanced cytotoxicity of BLM at all tested concentrations compared to the respective ultrasound (US) alone control. All groups normalized to the viability of cells exposed to US alone in the absence of BLM. * $p \leq 0.05$, ** $p \leq 0.01$, *** $p \leq 0.001$, **** $p \leq 0.0001$

7.4 CONCLUSIONS

Here we have demonstrated the ability to improve the toxicity of BLM in a resistant cancer cell line through sonoporation-mediated intracellular drug delivery. Furthermore, we were able to achieve comparable results with PCCAs and conventional lipid-shelled microbubbles. Future studies will be aimed at translating this technique *in vivo.* Contrary to regular microbubbles, we anticipate that PCCAs will be able to extravasate into solid tumors via the enhanced permeability and retention

(EPR) effect, and therefore may be used to sonoporate extravascular tumor tissue. This would be an attractive method to non-invasively enhance BLM efficacy in resistant cancer types and improve tumor regression.

REFERENCES

1. Aouida, M. and D. Ramotar, *A new twist in cellular resistance to the anticancer drug bleomycin-A5.* Curr Drug Metab, 2010. **11**(7): p. 595-602.

2. Escoffre, J.M. and M.P. Rols, *Electrochemotherapy: progress and prospects.* Curr Pharm Des, 2012. **18**(23): p. 3406-15.

3. Pron, G., et al., *Internalisation of the bleomycin molecules responsible for bleomycin toxicity: a receptor-mediated endocytosis mechanism.* Biochemical Pharmacology, 1999. **57**(1): p. 45-56.

4. Sheeran, P.S., et al., *Design of ultrasonically-activatable nanoparticles using low boiling point perfluorocarbons.* Biomaterials, 2012. **33**(11): p. 3262-9.

5. Fix, S.M., et al., *An evaluation of the sonoporation potential of low-boiling point phase-change ultrasound contrast agents in vitro.* Journal of Therapeutic Ultrasound, 2017. **5**: p. 7.

CHAPTER 8[1]

ULTRASOUND-STIMULATED PCCAs FOR EPITHELIAL PERMEABILIZATION TOWARDS ULTRASOUND-MEDIATED GASTROINTESTINAL DRUG DELIVERY

8.1 MOTIVATION AND OVERVIEW

Therapeutic ultrasound *without* contrast agents has recently been proposed as a universal method to physically enhance GI permeability to macromolecular drugs [1-5]. This technique involves colonic insertion of an ultrasound probe with co-administration of a medicated enema [5]. Low-frequency (≤ 100 kHz) ultrasound exposure for one minute or less has been shown to significantly enhance macromolecule delivery into surrounding GI tissue preclinically [1, 3], and this technology has the potential to transform the treatment landscape for several GI diseases.

In the absence of contrast agents, ultrasound-mediated drug delivery relies on bioeffects produced by cavitation much like the sonoporation mechanisms described in chapter 5 [5, 6]. First, however, *in situ* generation of vapor cavities is required. When a fluid is subjected to ultrasound of sufficient energy, small gas pockets are created. These bubbles subsequently oscillate (stable cavitation) or violently implode (inertial cavitation) in subsequent acoustic cycles much like injected contrast agents. These phenomena enhance the permeability of nearby boundaries.

The likelihood of ultrasound to induce cavitation is related to the wave's mechanical index (MI) which is defined as the peak rarefactional pressure (in MPa) divided by the square root of the center frequency (in MHz) [7]. To achieve ultrasound-mediated drug delivery in the absence of contrast agents, low frequencies (≤ 100 kHz) and consequently high MIs (>2) are often

[1]This chapter under revision for publication in Ultrasound in Medicine and Biology with the following citation: Fix, S.M., Koppolu, B.P., Novell, A., Hopkins, J., Kierski, T.M., Zaharoff, D.A., Dayton, P.A., Papadopoulou, V. (2018), "Ultrasound-stimulated low boiling point phase-change contrast agents for epithelial permeabilization towards ultrasound-mediated gastrointestinal drug delivery." (Under Revision)

needed [1, 3, 4]. However, introducing exogenous cavitation nuclei (e.g., microbubble contrast agents) into the acoustic field substantially lowers the energy required to induce cavitation-mediated bioeffects as initial bubble formation is no longer required [7].

The use of ultrasound-stimulated microbubbles for drug delivery has been studied extensively for the disruption of vascular barriers [8]. For applications such as opening the blood brain barrier [9-11] or enhancing vascular permeability within solid tumors [12, 13], microbubbles are administered intravenously and are stimulated with an external ultrasound source. We envision an adaptation of this technology for GI drug delivery, which would involve co-administration of contrast agents with a medicated enema in the colon followed by ultrasound stimulation using an endoscopic probe. With the use of contrast agents, we believe that higher frequencies and lower pressures may be used compared to the previously described, contrast-free methods of ultrasound-mediated GI drug delivery. This approach may theoretically localize bioeffects more precisely, as permeabilization would only occur where contrast agents are present (e.g., at the GI wall). This would reduce concerns of unsuppressed cavitation activity outside the desired treatment area (e.g., surrounding tissues).

As a first step towards this goal, we studied the dynamics of epithelial monolayer disruption and recovery *in vitro* using low boiling point phase-change ultrasound contrast agents (PCCAs) stimulated with 1.0 MHz ultrasound pulses. PCCAs are liquid perfluorocarbon-filled particles that can be vaporized into acoustically active microbubbles with the application of an ultrasound pulse of sufficient amplitude. In the liquid state, PCCAs are characterized by nanometer-range size distributions (100-300 nm) that may allow more thorough permeation through the GI mucus mesh compared to microbubbles (0.5-10 μm [14]). Once vaporized, PCCAs form microbubbles several microns in diameter that can be utilized to enhance drug delivery.

The primary objective of this study is to demonstrate the potential of using ultrasound-stimulated PCCAs to cause transient disruption of confluent colorectal adenocarcinoma (Caco-2) epithelial monolayers and enhance the permeation of a model macromolecular drug. This represents a first step towards the goal of *in vivo* GI drug delivery applications.

8.2 MATERIALS AND METHODS

8.2.1 PHASE-CHANGE ULTRASOUND CONTRAST AGENT (PCCA) FABRICATION AND CHARACTERIZATION

PCCAs were generated via microbubble condensation as described in chapter 6 and previous publications [15, 16]. The size distribution of resultant PCCAs was characterized using a NanoSight NS500 (Malvern Instruments, Westborough, MA, USA) (detection capability 50-2000 nm) (n=3 representative vials).

8.2.2 PCCA VAPORIZATION CAPTURED VIA HIGH-SPEED OPTICAL MICROSCOPY

PCCA vaporization events were captured at a range of acoustic settings using high-speed optical microscopy, as described in chapter 6 and prior work [17]. Briefly, a temperature-controlled water bath (37°C) was mounted on an inverted microscope with a 100× water immersion objective (Olympus IX71, Center Valley, PA, USA), and the microscope was interfaced with a high-speed camera to capture vaporization events (FastCam SA1.1, Photron USA, Inc., San Diego CA, USA).

PCCAs were diluted 1:4 in PBS and perfused through a 200-μm inner-diameter microcellulose tube (Spectrum Labs, Inc., Rancho Dominguez, CA, USA) positioned at the optical focus of the microscope and within the calibrated pressure field of an unfocused 1.0 MHz transducer (IP0102HP, Valpey Fisher Corp., Hopkinton, MA, USA). Injection of the PCCAs was followed by a brief waiting period to allow particles in the field of view to become nearly stationary, which minimized blurring in the captured images. Previous work has shown that PCCA vaporization is a pressure-threshold dependent phenomenon, independent of pulse length when sub-millisecond pulses are used [18, 19]. Therefore, to determine an approximate pressure threshold for vaporization, PCCAs were exposed to single 20-cycle acoustic pulses with PNPs of 100, 200, 300, 400, 500, or 600 kPa.

A synchronization pulse from the function generator was used to trigger the high-speed camera and initiate video recording at 500 frames per second. Videos were set to begin recording just before the triggered ultrasound pulse, which allowed complete PCCA vaporization events within the

optical field of view to be captured. Images were analyzed offline using ImageJ (National Institutes of Health, Bethesda, MD, USA).

8.2.3 CELL CULTURE

Colorectal adenocarcinoma (Caco-2) cells were chosen as an *in vitro* model of intestinal absorption. When Caco-2 monolayers are grown to confluence, they differentiate, developing polarity and tight junctions between cells. This accurately mimics the human intestinal epithelial barrier, making Caco-2 permeability testing a reliable tool for predicting *in vivo* intestinal absorption of various compounds [20]. Note that while these cells were derived from cancerous tissue, they are used to model normal intestinal barrier function.

Caco-2 cells were purchased from the American Type Culture Collection (ATCC) and cultured using minimum essential medium without L-glutamine (Corning Inc., Corning, NY, USA) supplemented with 100 U/mL penicillin/streptomycin, 1× NEAA, 1× sodium pyruvate, 1× L-glutamate, and 20% heat-inactivated FBS (VWR, Radnor, PA, USA) in a humidified, 37°C incubator with 5% CO_2 atmosphere. Low passage number (passage 15) Caco-2 cells were seeded at 150,000 cells per well onto Transwell supports with 0.4 μm pores (12-well plate, 12 mm membrane diameter, 1.12 cm^2 cell growth area, Corning Inc., Corning, NY, USA) and allowed to grow for approximately 10 days to form confluent monolayers. Monolayer integrity was regularly monitored via the measurement of transepithelial electrical resistance (TEER) (World Precision Instruments, Sarasota, FL, USA). Monolayers were used for permeability experiments after TEER values had reached at least 500 Ohm (560 $Ohm \cdot cm^2$), which is similar to TEER values reported in the literature for this model [21, 22]. Furthermore, above this threshold, macromolecular tracers (e.g., the 70 kDa dextran used here) are unable to permeate through the Caco-2 monolayers.

8.2.4 ULTRASOUND ALIGNMENT STRATEGY

Caco-2 monolayers were sonicated from the apical side using a 1.0 MHz unfocused piston transducer (diameter = 8 mm, -6 dB ‘focal spot’ = ~6 mm diameter, IP0102HP, Valpey Fisher Corp., Hopkinton, MA, USA). A custom water bath was designed to (1) facilitate consistent alignment of the

transducer above the center of each well and (2) reduce acoustic reflections from the base of the well plate (Figure 8.1). The 14 cm×10 cm×8.5 cm (L×W×H) water bath was created using 3.2 mm acrylic sheets. For each experiment, a 12-well culture plate was placed on an internal ledge within the bath, providing coupling between the bottom of the well plate and the pre-heated 37°C water below. Such coupling was designed to minimize acoustic reflections that would have otherwise occurred at the air-plastic interface. A lid for the water bath was created with 1.0 cm-diameter circular holes centered above each well. This served as a method to hold the ultrasound transducer centered within each well at a consistent height above the cells (6 mm).

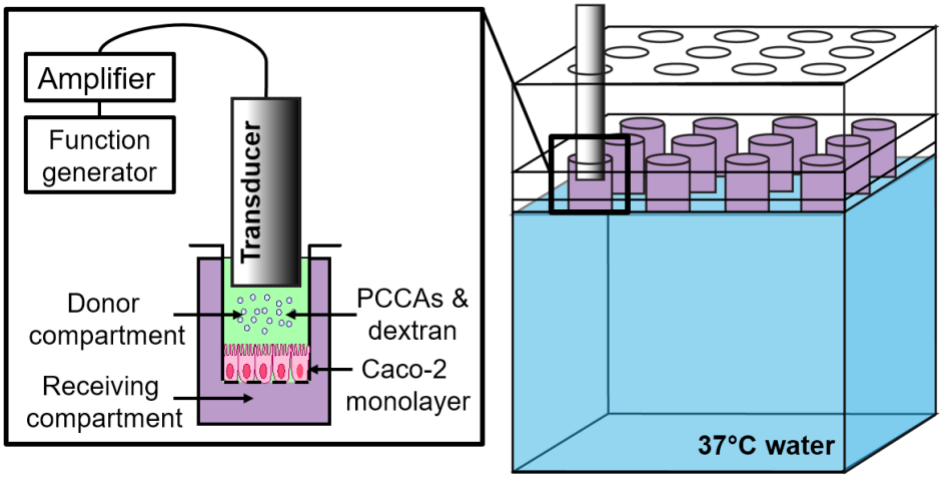

Figure 8.1: Sonication strategy. Colorectal adenocarcinoma (Caco-2) cells were cultured on permeable Transwell supports. Phase-change contrast agents (PCCAs) and dextran were added to the donor chamber before sonication and samples were collected from the receiving compartment over the following 72 hours post-ultrasound treatment. The twelve-well culture plates were positioned in a custom water bath and coupled to the 37°C water below before treatment. A lid with circular holes was used to align the ultrasound transducer in the center of each well at a consistent height above the cells.

8.2.5 ULTRASOUND-MEDIATED FITC-DEXTRAN DELIVERY THROUGH EPITHELIAL MONOLAYERS

Twelve-well plates containing confluent Caco-2 monolayers on Transwell® supports were positioned in the custom water bath as described above. Cell media (400 µl) containing PCCAs (0.5 µl; 1.75×10^9 particles/ml) and 70 kDa FITC-dextran (50 µg; 0.125 mg/ml) was added to the donor chamber (apical side) of a well to simulate absorption from the intestinal lumen. The 70 kDa dextran

was chosen to model macromolecular drugs (e.g., moderately-sized proteins) typically unable to pass the GI epithelial barrier. Subsequently, the 1.0 MHz transducer was placed in center of the well and excited with amplified sinusoidal signals from an arbitrary function generator (AFG3021C, Tektronics, Inc., Beaverton, OR, USA and 3100LA Power Amplifier, ENI, Rochester, NY, USA) (Figure 8.1). A pulse repetition frequency of 5000 Hz and exposure time of 30 seconds was used for all conditions. Pulse lengths of 20 cycles (10% duty cycle) or 40 cycles (20% duty cycle) were employed, and peak negative pressures were varied from 300 to 600 kPa. Control samples were exposed to (1) sham treatment (without PCCAs or ultrasound), (2) PCCAs only, and (3) ultrasound only (using the highest energy condition of 600 kPa and 40 cycle pulse length). A summary of the conditions tested can be found in Table 8.1, including experimental replicates for each group.

Table 8.1: Summary of conditions tested. Summary of the acoustic conditions tested for ultrasound-mediated Caco-2 permeabilization with PCCAs, including the number of experimental replicates performed. Abbreviations: PCCA – phase change contrast agent; kPa – kilopascal; kDa – kilodalton; US – ultrasound; Y – yes; N – no; NA – not applicable

Condition	PCCA (Y/N)	Pressure (kPa)	Cycles (#)	Dextran size (kDa)	Experimental replicates
1	Y	300	20	70	3
2		400			3
3		500			3
4		600			3
5	Y	300	40	70	6
6		400			3
7		500			3
8		600			3
9 - sham	N	NA	NA	70	3
10 - US only	N	600	40	70	3
11 - PCCA only	Y	NA	NA	70	3

Samples (100 µl) were collected from the receiving chamber (basolateral side) at the following time points after treatment and replaced with cell media: ~5 min, 3 hr, 8 hr, 24 hr, 48 hr, and 72 hr. Dextran concentration was determined via fluorescence intensity (excitation: 485 nm, emission: 528 nm) using a Cytation 5 Plate Reader (BioTek, Winooski, VT, USA). Percent dextran delivery was calculated based on the mass initially added to the donor compartment, correcting for the mass

removed through sampling at each time point and considering 100% to be the receiving well concentration if equilibrium had been established between both compartments.

TEER values were recorded at the same time points and used to monitor monolayer disruption and recovery dynamics. For all experiments, monolayers with a TEER value of at least 560 Ohms·cm^2 were considered intact, and monolayers below this threshold were considered disrupted. "Time to monolayer recovery" was calculated as a summary metric to quantify the degree of monolayer disruption caused by sonication. For monolayers that recovered by the last measurement time point (72 hours), time to recovery was calculated as the time that TEER values remained below 560 Ohms·cm^2, using a linear interpolation between measured time points. Monolayers that never dropped below 560 Ohms·cm^2 therefore had a time to monolayer recovery of 0 hours.

8.2.6 DETECTION OF CAVITATION SIGNALS AND THEIR PERSISTENCE DURING 30 SECOND ULTRASOUND EXPOSURES

Cavitation is thought to be the main mechanical driver of biological barrier permeabilization with ultrasound. As such, we were interested in characterizing the generation and persistence of stable and inertial cavitation energy generated by ultrasound-stimulated PCCAs during 30 second exposures.

We detected cavitation signals using a method adapted from our previous work described in chapter 6 [23]. PCCAs (1.75×10^9 particles/ml) were suspended in 800 µl of 37°C PBS in a disposable plastic cuvette (FisherBrand, Thermo Fisher Scientific, Waltham, MA, USA). The unfocused 1.0 MHz transducer was shallowly submerged in the PCCA suspension and set to transmit the same ultrasound pulses that were used for monolayer permeabilization (Table 8.1) with the only difference being that the pulse repetition frequency was reduced to 2000 Hz. Unfortunately, hardware limitations prevented us from saving data with a pulse repetition frequency of 5000 Hz to match the cell experiments. We do not believe that this discrepancy significantly alters the interpretation of our results, as discussed in subsequent sections.

A separate, single element, spherically focused transducer (7.5 MHz nominal frequency, measured center frequency = 8.740 MHz, diameter = 19 mm, focal distance = 50 mm, -6 dB

bandwidth = 1.270 MHz) (IL0706HP, Valpey Fisher Corp., Hopkinton, MA, USA) was arranged perpendicular to the transmit transducer with its focus positioned within the PCCA solution. Acoustic signals received by this transducer were passed through a receive amplifier (BR-640A, RITEC, Inc., Warwick, RI, USA) with 27 dB gain and a 500 kHz high pass filter. Signals were subsequently digitized using a 12-bit analog-to-digital conversion card with a sampling rate of 200 MHz (GaGe model #CSE1222, DynamicSignals LLC, Lockport, IL, USA) installed in a computer (Dell, Round Rock, TX, USA) running a custom acquisition program (LabVIEW, National Instruments Corp., Austin, TX, USA).

We saved signals over a total of 30 seconds to monitor the dynamics of cavitation energy generated from the acoustically-stimulated PCCAs. Ultrasound was transmitted continuously throughout the 30-second period; however, signals were saved intermittently to reduce data to a manageable size. Each second, 20 individual signals (i.e., 10 ms of data) were saved followed by a 990 ms saving delay. This was repeated every second for a total of 30 seconds.

All saved data was post-processed using an adaptation of the MATLAB (MathWorks Inc., Natick, MA, USA) post-processing analysis script described in chapter 6 to quantify stable and inertial cavitation doses [23]. Briefly, for each individual radiofrequency line, the PCCA signal was selected by applying a 30 μs window from the point corresponding to the beginning of the acoustic pulse. Fast Fourier transform was used to convert individual time-domain signals to the frequency domain in order to estimate the level of stable and inertial cavitation. For stable cavitation, the area under curve (AUC) of the second harmonic component was calculated considering a spectral window from 1.9 to 2.1 MHz. For inertial cavitation, the broadband emission was quantified by calculating the AUC of frequency content ranging from 5.25 to 7.75 MHz (while excluding the 6 and 7 MHz harmonic components). Stable and inertial cavitation doses were then calculated by normalizing AUC values obtained for PCCAs with those calculated for a PBS-filled cuvette (without PCCAs) exposed to the same acoustic parameters. This was repeated for three independent vials of PCCAs; average cavitation doses (relative AUC) with inter-vial standard deviation are reported. Finally, average of relative AUC for stable and inertial cavitation are plotted over the 30 second period, and total cavitation dose for each was calculated by taking the area under these curves.

8.2.7 STATISTICAL ANALYSES

All statistical analyses were performed in GraphPad Prism 6 (GraphPad Software, Inc., La Jolla, CA, USA). P-values of <0.05 were considered statistically significant, and data are presented as average ± standard deviation throughout this work.

To evaluate which ultrasound parameters resulted in statistically significant dextran delivery, we performed a two-way repeated-measures ANOVA with respect to time and acoustic treatment. At each timepoint, the mean of each treatment group was compared to the mean of the sham control at the same time point via Dunnett's multiple comparisons testing. The same statistical procedure was applied to analyze changes in TEER values over time in various ultrasound treatment groups vs. time point-respective sham controls.

Cumulative dextran delivery achieved at 72 hours was analyzed via an additional two-way ANOVA with respect to acoustic pressure and pulse length. The purpose of this test was to evaluate the extent to which dextran delivery is affected by these factors (i.e., the percent of variability in dextran delivery that can be attributed to pressure vs. number of cycles). Following this two-way ANOVA, two multiple comparisons tests were performed. First, a Sidak multiple comparison test was used to compare mean delivery efficiency between 20 and 40 cycle cases at each pressure. Second, a Tukey multiple comparison test was used to compare mean delivery efficiency between all rarefactional pressures separately for the 20 and 40 cycle cases.

The relationship between monolayer disruption and percent dextran delivery was assessed by calculating the correlation between time to monolayer recovery and cumulative percent dextran delivery at the 72-hour time point. Spearman correlation coefficients (r) and p-values are reported.

Linear regressions were performed to assess the relationships between pressure and (1) total stable cavitation dose, (2) total inertial cavitation dose, and (3) the sum of total stable and inertial cavitation. This was done separately for 20-cycle and 40-cycle conditions. Again, goodness-of-fit (r^2) and p-values are reported.

8.3 RESULTS AND DISCUSSION

8.3.1 PCCA CHARACTERIZATION

The PCCA formulation was characterized by a polydisperse size distribution with an average concentration of 1.4 (±0.2) × 10^{12} particles/ml and mean particle size of 170±20 nm (n=3 independent vials) (Figure 8.2 A). Figure 8.2 B shows representative optical microscopy images captured before (t = -2 ms) and after (t = 8 ms) a single 20-cycle ultrasound pulse at t = 0 ms. We found that PCCAs consistently vaporized into microbubbles at and above a peak negative pressure of 300 kPa, but showed little to no activation at lower pressures (at 1.0 MHz), which is consistent with our previous findings [23]. Qualitatively, we observed an increase in the number of bubbles generated with a single ultrasound pulse as pressure was increased from 300 kPa to 600 kPa (Figure 8.2 A). From these experiments, we concluded that the pressure threshold for PCCA vaporization is between 100 – 300 kPa at 1.0 MHz, and therefore pressures at or above 300 kPa were used for all subsequent experiments.

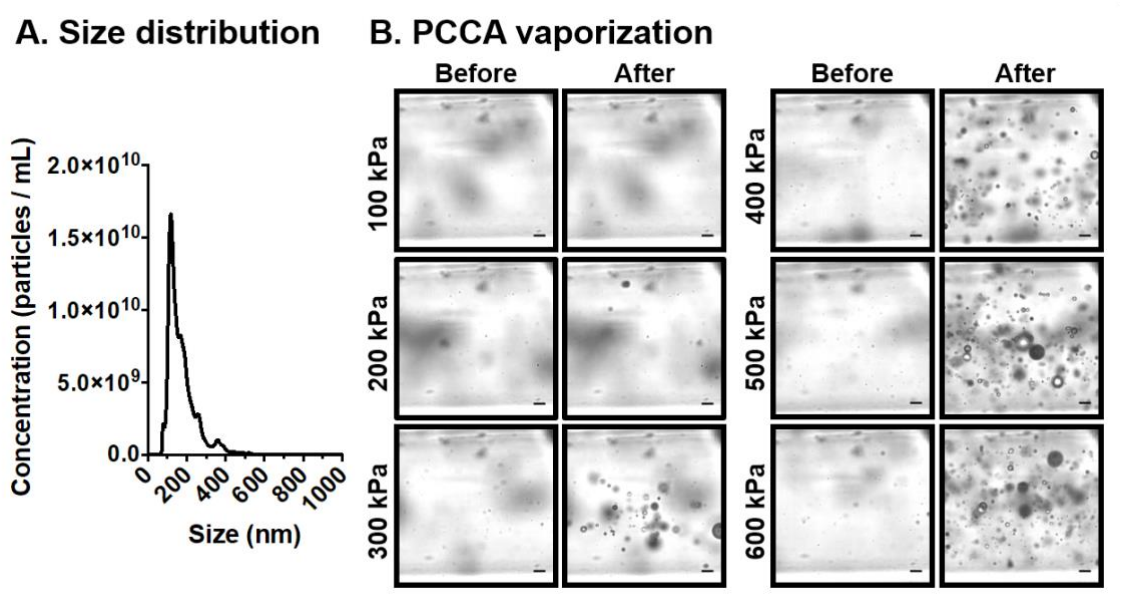

Figure 8.2: Characterization of PCCA size distribution and vaporization. (A) The size distribution and concentration of PCCAs were characterized using a Nanosight. The PCCA formulation was characterized by a polydisperse size distribution with an average concentration of 1.4 (±0.2) × 10^{12} particles/ml and mean particle size of 170±20 nm (n=3 independent vials). (B) Acoustic PCCA vaporization. Representative high speed optical microscopy images showing PCCA vaporization as a function of rarefactional pressure. Considerable PCCA vaporization is observed at and above 300 kPa, with the number of generated microbubbles increasing with increasing pressure. Scale bar = 10 μm.

8.3.2 ULTRASOUND-MEDIATED FITC-DEXTRAN DELIVERY THROUGH EPITHELIAL MONOLAYERS

As expected, 70 kDa dextran was not able to penetrate sham-treated Caco-2 monolayers over the 72 hr incubation period, confirming that effective barrier function had been established in our model (Figure 8.3 A). Similarly, we did not observe appreciable delivery through control monolayers treated with (1) PCCAs only (no ultrasound) or (2) ultrasound only (no PCCAs, ultrasound stimulation at the highest setting of 600 kPa and 40 cycles) (Figure 8.3 A). This indicated that neither our agents nor ultrasound alone altered monolayer integrity with the parameters used in our study. Correspondingly, TEER values for all control groups remained well above the previously chosen threshold for an intact monolayer (560 Ohm·cm^2) throughout the 72-hour observation period, further demonstrating that control treatments did not significantly alter membrane integrity (Figure 8.4 A). Neither PCCAs alone nor ultrasound alone resulted in statistically significant changes in TEER values at any time point compared to the time-point respective sham controls (Table 8.2).

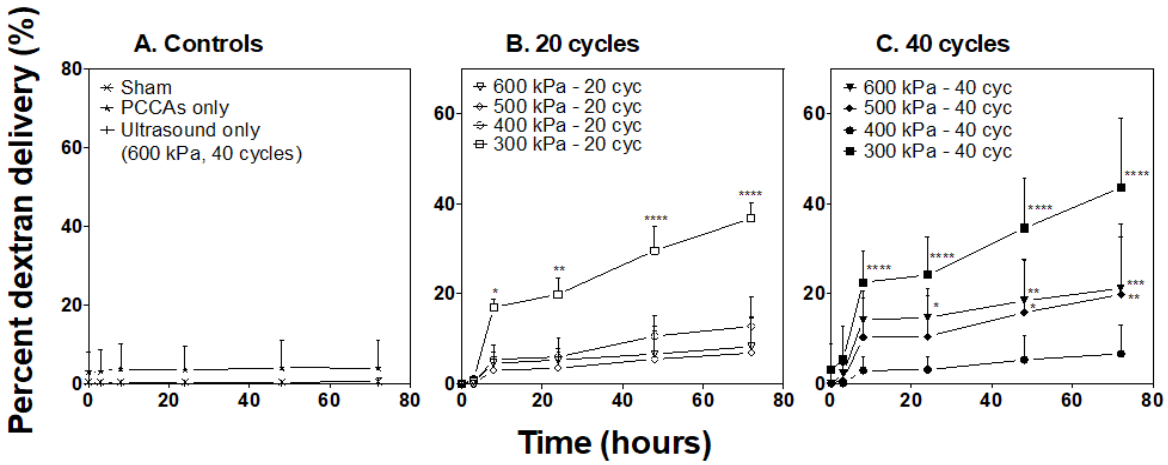

Figure 8.3: Dextran delivery through Caco-2 monolayers. Dextran delivery is presented as a percentage of the maximum dextran mass that would have been found in the receiving compartment if equilibrium had been achieved between the donor and receiver Transwell compartments (i.e., if there was no barrier between chambers). (A) Negligible amounts of the 70 kDa dextran permeated through control treated monolayers over the 72-hour incubation period. When monolayers were sonicated in the presence of PCCAs, significant delivery was achieved with select acoustic parameters (B and C). Stars indicate the results of Dunnett's multiple comparison testing at each timepoint comparing mean percent dextran delivery of each group to that of the sham control for that timepoint after two-way ANOVA.
Key: * $p \leq 0.05$; ** $p \leq 0.01$; *** $p \leq 0.001$; **** $p \leq 0.0001$

When ultrasound was combined with PCCAs we were able to achieve significant delivery (vs. time-point respective sham controls) of 70 kDa dextran with select parameter combinations (Figure

8.3 B and 8.3 C). When substantial delivery was achieved, it most often reached statistically significant levels between 8-24 hours post-treatment with cumulative percent delivery increasing slightly thereafter. These results correspond with TEER values indicating significant monolayer disruption (Figure 8.4 and Table 8.2). For all ultrasound-stimulated PCCA treatments, we observed an immediate and statistically significant reduction in TEER, with all groups characterized by average TEER values in the range of 200-280 Ohm·cm^2 approximately 5 minutes post-treatment (Figure 8.4 and Table 8.2). TEER values tended to recover within 24-48 hours post-treatment, regaining values ≥560 Ohm·cm^2. The 300-kPa treatment groups were the only conditions that did not show 100% recovery of all monolayers by the 72-hour time point. For the 300 kPa treatment groups, we achieved 33% and 50% recovery for the 20 and 40 cycle cases, respectively.

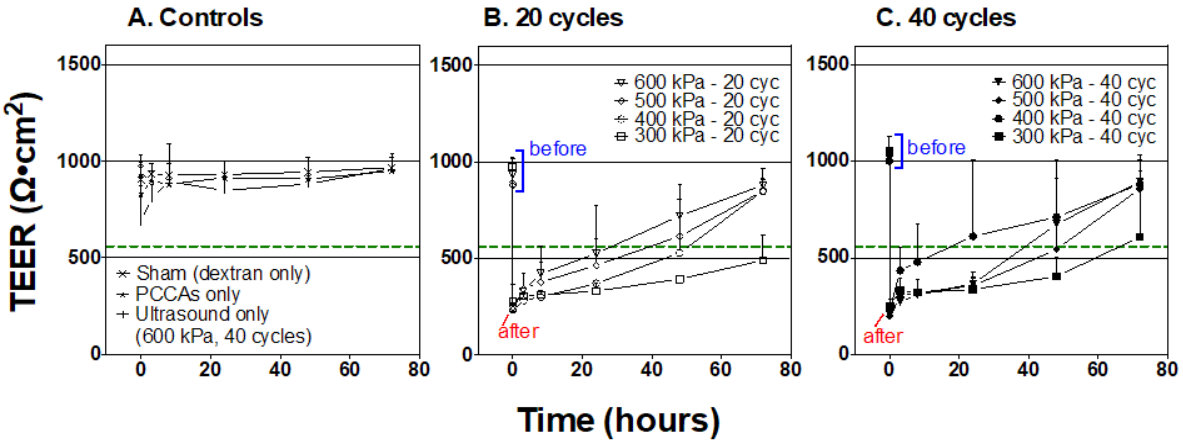

Figure 8.4: Transepithelial resistance (TEER) values before and after monolayer sonication. Control treated cells did not show any significant change in TEER values after manipulation, and TEER values remained above 560 Ohm·cm^2 (green dashed line) throughout the 72-hour observation period, indicating maintained monolayer integrity (A). For all monolayers treated with ultrasound and PCCAs, a significant decrease in TEER values was recorded immediately (~5 min) after treatment (B and C). Most of these monolayers recovered (regained TEER values ≥ 560 Ohm·cm^2 within 24-48 hours, with the exception of some monolayers treated with 300 kPa and either 20 or 40 cycle pulse lengths.

Treatment groups diverged with respect to monolayer recovery time. To investigate this further, we interpolated “time to monolayer recovery” for each treatment (i.e., time for a monolayer to regain a TEER value ≥560 Ohm·cm^2). This summary value, which captures the monolayer recovery dynamics, correlated well with the cumulative percent dextran delivered ($r = 0.8475$, $p < 0.0001$)

(Figure 8.5). Biologically, the main factor dictating dextran delivery efficiency appears to be how long the monolayers remain leaky.

In terms of acoustic parameters, rarefactional pressure has a greater influence on dextran delivery outcome than pulse length. To test this observation statistically, we performed a two-way ANOVA to quantify the relative contributions of acoustic pressure and pulse length to overall variation in cumulative dextran delivery (72 hr time point). We found that pressure ($p = 0.0002$) but *not* pulse length ($p = 0.1476$) was a significant source of variability in percent dextran delivery, with pressure accounting for 53.5% of the total variation compared to 3.5% attributed to pulse length. This can be assessed visually in Figure 8.6 A, where the cumulative percent delivery varies substantially with respect to pressure but remains fairly consistent between pulse lengths. Indeed, multiple comparison testing showed that differences in cumulative dextran delivery between 20 and 40 cycle conditions were statistically insignificant at each rarefactional pressure.

Table 8.2: Statistics describing transepithelial resistance (TEER) values before and after monolayer sonication. Stars indicate the results of Dunnett's multiple comparison testing at each timepoint comparing mean TEER value of each group to that of the sham control for that timepoint after two-way ANOVA.
Key: * $p \leq 0.05$; ** $p \leq 0.01$; *** $p \leq 0.001$; **** $p \leq 0.0001$
Abbreviations: PCCA – phase change contrast agent; kPa – kilopascal; US – ultrasound; cyc – cycles.

	Significantly different than respective sham control?						
	Time point (hours)						
Group	**pre**	**0**	**3**	**8**	**24**	**48**	**72**
US only	ns	ns	ns	ns	ns	ns	ns
PCCA only	ns	ns	ns	ns	ns	ns	ns
600 kPa - 20 cyc	ns	****	****	****	***	ns	ns
500 kPa - 20 cyc	ns	****	****	****	****	**	ns
400 kPa - 20 cyc	ns	****	****	****	****	****	ns
300 kPa - 20 cyc	ns	****	****	****	****	****	****
600 kPa - 40 cyc	ns	****	****	****	****	*	ns
500 kPa - 40 cyc	ns	****	****	****	****	***	ns
400 kPa - 40 cyc	ns	****	****	****	**	ns	ns
300 kPa - 40 cyc	ns	****	****	****	****	****	****

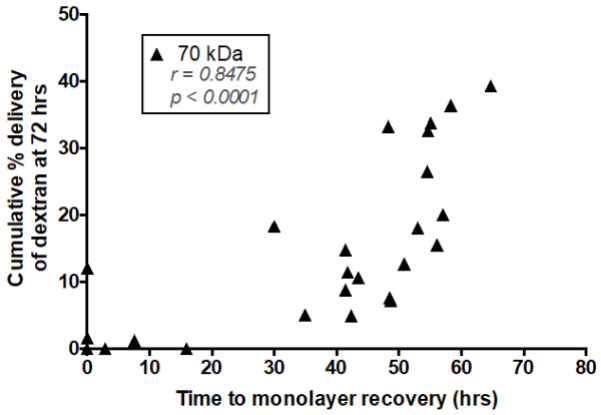

Figure 8.5: Correlation between cumulative dextran delivery and time to monolayer recovery. A significant correlation was found between percent dextran delivery at 72 hours and interpolated time to monolayer recovery.

The most interesting and unexpected finding was that the 300 kPa exposure conditions consistently provided significantly greater dextran delivery compared to higher-pressure groups, while the higher-pressure conditions (400, 500, and 600 kPa) provided similar results (statistically insignificantly different) (Figure 8.6 B and 8.6 C). These findings are counter to our initial hypothesis that as acoustic energy was increased, a greater proportion of PCCAs would vaporize into microbubbles and cavitation dose would be more pronounced, together leading to more dramatic biological effects and ultimately greater dextran delivery efficiency. We hypothesize that these unexpected findings may be explained by differences in cavitation *persistence* between ultrasound exposure conditions, as is explored in the subsequent section.

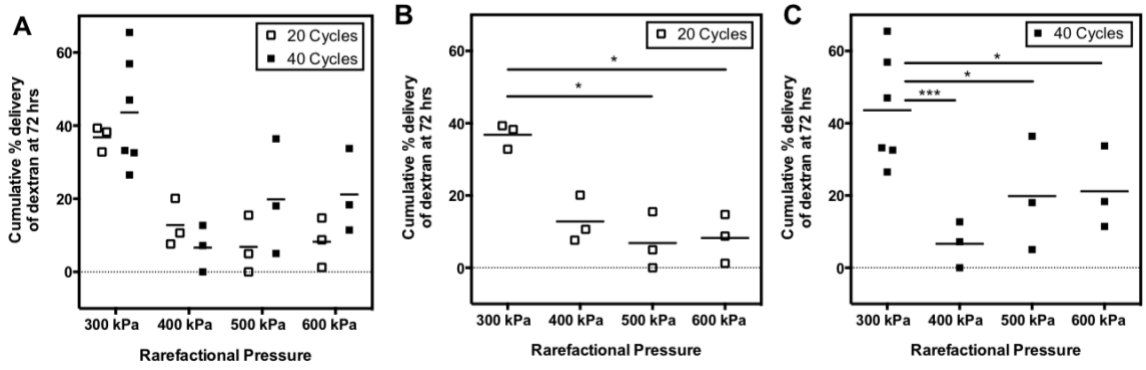

Figure 8.6: Influence of pulse length and rarefactional pressure on overall dextran delivery outcome. Dextran delivery efficiency was comparable for 20 cycle and 40 cycle groups at each rarefactional pressure, as depicted in (A). The 300 kPa conditions consistently provided the greatest dextran delivery outcomes compared to all higher-pressure conditions (B and C). Higher pressure conditions (400 – 600 kPa) provided similar delivery outcomes to each other.

8.3.3 PERSISTENCE OF CAVITATION OVER 30 SECOND EXPOSURES

In our experiments, as would be the case for GI drug delivery applications, the same sample of PCCAs were stimulated for the duration of the ultrasound exposure time (30 seconds in this study). Therefore, at high pressure, PCCAs may be rapidly converted to microbubbles but also subsequently destroyed via inertial cavitation. This would limit the effective cavitation duration to a fraction of the ultrasound on time (30 s). Conversely, if PCCAs were being vaporized more slowly and were able to persist for longer at lower pressures, the effects of microbubble cavitation would have been felt by the cells for a longer period of time, enhancing the biological effect.

To test this hypothesis, we quantified stable and inertial cavitation dose generated from acoustically-stimulated PCCAs *in vitro* over the course of 30 seconds. All parameters matched those of our dextran delivery experiments except for pulse repetition frequency, which was reduced to 2000 Hz.

For all acoustic exposure conditions (300-600 kPa with 20 and 40 cycle pulse lengths), we observed substantial stable and inertial cavitation immediately after the ultrasound transmission was initiated (Figure 8.7 A-D). For 20 cycle pulse lengths, there is a clear separation in cavitation dynamics with respect to rarefactional pressures, with lower pressures resulting in more sustained stable and inertial cavitation compared to the higher pressures. The lower pressures (especially 300 kPa) provide sustained stable and inertial cavitation activity over the entire 30 second exposure, while cavitation dose decreases dramatically within the first 15 s for the higher pressures (especially 600 kPa) (Figure 8.7 A & 8.7 C). This trend is also observed for stable cavitation dose with respect to pressure at 40 cycles (Figure 8.7 B). This is less pronounced for inertial cavitation dose at 40 cycles, as cavitation dose decreases more rapidly for all pressures (Figure 8.7 D). In general, these data demonstrate that both peak rarefactional pressure and pulse length influence cavitation persistence for PCCAs, as has previously been reported for microbubbles [24]. The lower pulse repetition frequency used for these experiments compared to the dextran delivery experiments may have biased results slightly. At a higher pulse repetition frequency, cavitation dose would be expected to decrease more rapidly for all conditions, thus this effect is likely more pronounced in our cell experiments at higher pulse repetition frequency.

In general, we hypothesize that two main factors contribute to the inverse trend between total cavitation dose and pressure. First, we qualitatively observed that PCCA vaporization efficiency increases with increasing pressure. This can be observed in the representative images shown in Figure 8.2, where more bubbles are generated after a single ultrasound pulse at 600 kPa vs. 300 kPa. This qualitative finding is supported by previous work showing that relative PCCA vaporization efficiency increases with increasing pressure [25, 26]. As a result, it will take longer to vaporize all PCCAs in the sample with lower pressures, contributing to sustained cavitation activity over the 30-second exposure time. Secondly, as pressure increases, we believe that generated microbubbles will be destroyed more rapidly, ultimately limiting microbubble lifetime and cavitation persistence. A similar inverse trend between generated microbubble stability/survival and pressure has previously been described by Reznik et al. [26].

To quantitatively analyze the trends in acoustic cavitation with respect to pressure, we first calculated the cumulative stable cavitation dose (SCD) and cumulative inertial cavitation dose (ICD) by calculating the area under each of the cavitation curves over the 30 s ultrasound exposure. This provided single values summarizing the total SCD and ICD generated by each condition. We also summed these cumulative SCD and ICD values to provide an estimate of the overall cavitation dose generated per condition (SCD+ICD). Linear regressions were performed between each of these summary values and acoustic pressure (Figure 8.7 E-F). For the 20 cycle cases, we find statistically significant inverse trends between pressure and total SCD+ICD and total SCD ($p = 0.0007 – 0.0100$). For the 40 cycle cases, all three summary cavitation metrics were found to significantly and inversely trend with pressure ($p = 0.0049 – 0.0100$). For both pulse lengths, 300 kPa qualitatively provided the greatest cumulative SCD, ICD and SCD+ICD compared to all higher-pressure groups, which corresponds with our finding that 300 kPa results in the greatest dextran delivery efficiency.

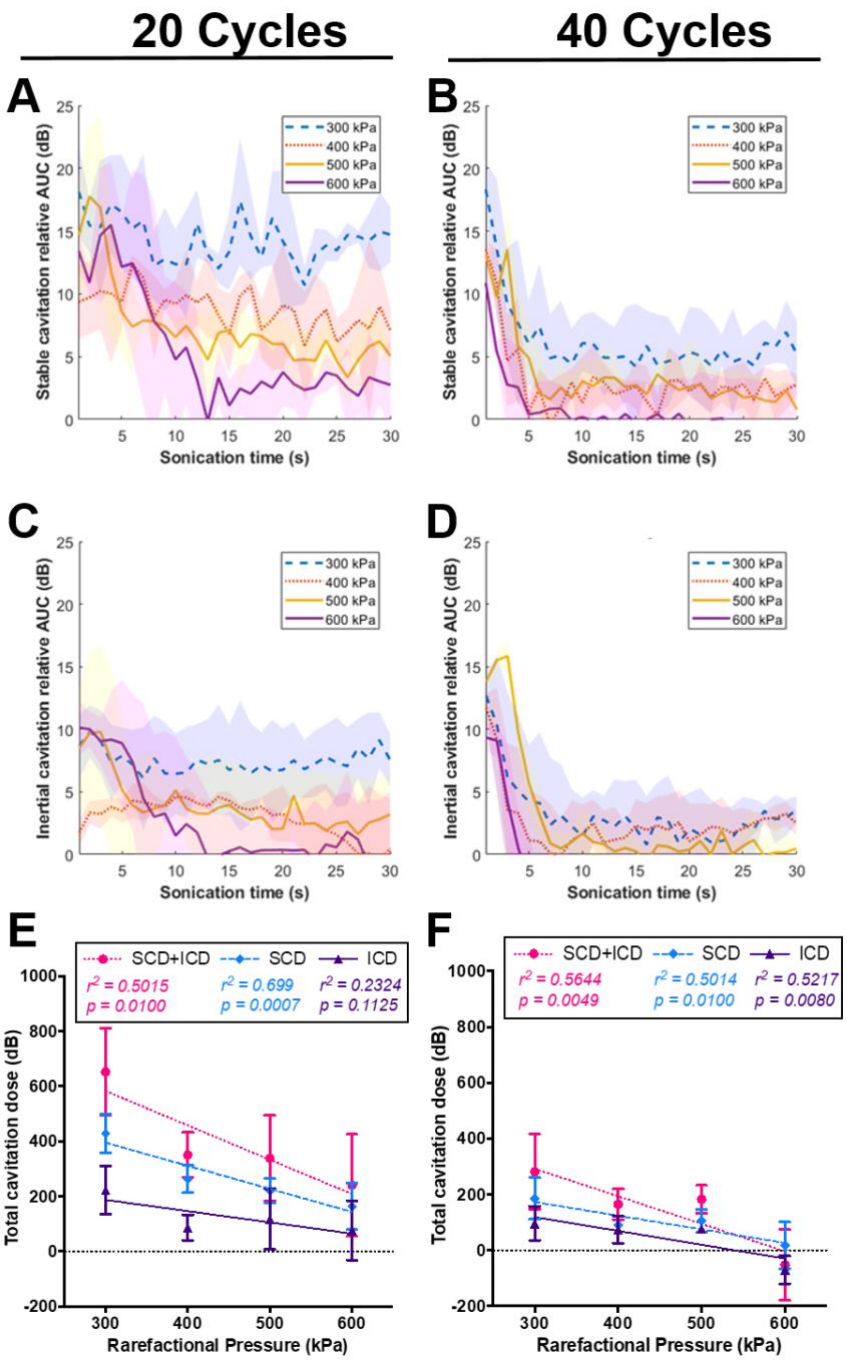

Figure 8.7: Generation of stable and inertial cavitation and trends with rarefactional pressure. (A-D) Acoustic stimulation of PCCAs resulted in the generation of substantial stable cavitation (SCD) and inertial cavitation (ICD) for all acoustic conditions tested. The persistence of this cavitation over 30 seconds varied between conditions. In general, SCD and ICD was most persistent at the low-pressure conditions (300 or 400 kPa) with short pulse length (20 cycles). Total SCD and ICD dose was calculated as the area under the cavitation curves over 30 seconds. (E) For the 20 cycle conditions, we found significant inverse trend between rarefactional pressure and total SCD+ICD dose and SCD dose. (F) This trend held true for SCD+ICD, SCD and ICD doses for the 40 cycle conditions.

8.3.4 LIMITATIONS

Total cavitation dose alone cannot predict dextran delivery efficiency as evidenced by the discrepancy we find between 20 and 40 cycle conditions: dextran delivery outcomes are comparable across pulse lengths, while total cavitation doses were in general lower for 40 cycle conditions compared to respective 20 cycle conditions. For the 20 cycle conditions, we find a significant correlation between cumulative dextran delivery and (1) total SCD (Pearson $r = 0.9624$, $p = 0.0376$) and (2) total SCD+ICD (Pearson $r = 0.9638$, $p = 0.0362$). However, for the 40 cycle cases we do not find significant correlations between dextran delivery and any of the total cavitation metrics. This discrepancy may be due to various confounding variables that were not captured by the total cavitation dose metric. For instance, we hypothesize that peak cavitation dose and the balance between stable and inertial cavitation may be important variables contributing to biological outcome. An additional confounding variable may be acoustic radiation force and its influence on microbubble-to-cell distance. The magnitude of biological effects is expected to increase with decreasing distance between cavitating microbubbles and underlying cells, as observed in the literature surrounding ultrasound-mediated drug delivery into cells [27, 28]. Despite their buoyancy, we expect that microbubbles were pushed towards the cell boundary in our set up via primary radiation force [29, 30]. Therefore, any differences in radiation force between groups (e.g., due to pulse length or pressure) may have influenced microbubble-to-cell distance and therefore dextran delivery efficiency.

Furthermore, acoustic pressure and pulse length are known to influence the stability and size distribution of microbubbles generated by PCCA vaporization [17, 26], and differences in microbubble populations may have influenced dextran delivery efficiency. The proportion of small microbubbles generated by PCCA vaporization has previously been show to increase with increasing acoustic pressure [17, 23], which is attributed to the inverse relationship between vaporization pressure threshold and PCCA size [17, 31]. Additionally, the likelihood of microbubble fusion (i.e., generation of larger microbubbles) increases with increasing pulse length [17]. These expected differences in microbubble size distribution as a function of acoustic excitation parameters may influence monolayer disruption efficiency.

After ultrasound-mediated monolayer disruption, TEER value analysis indicated that it typically took 24-48 hours for the epithelial cells to regain their integrity. While recovery mechanism was not explicitly studied in this work, this rather long recovery time may indicate that recovery is due to cell repopulation and growth rather than resealing of transiently opened tight junctions between cells. A limitation of this study is that we did not quantify cell death after treatment. Furthermore, not all monolayers treated with the 300 kPa conditions recovered within the 72-hour observation window. We do not claim that we have found optimal acoustic parameters for *in vitro* intestinal permeabilization. Rather, this study provides an encouraging proof of principle demonstration that epithelial monolayer disruption is feasible with ultrasound stimulated PCCAs and supports further optimization of acoustic parameters to maximize transient disruption while minimizing recovery time and cell death.

It is important to note that cell-based assays of intestinal permeabilization are known to overestimate damage compared to what would be observed in viable intestinal tissue (in the context of chemically induced permeability enhancement) [32, 33]. This is attributed to the lack of complete intestinal repair mechanisms and protective mucus in simple cell culture assays. As a result, any future optimization of acoustic parameters should be carefully validated (e.g., through the *in situ* intestinal perfusion [34]) to ensure that the chosen parameters are effective and safe when working with viable intestinal tissue. One of the greatest safety concerns for intestinal barrier disruption *in vivo* is the risk of facilitating absorption of harmful bystanders such as bacteria, viruses, and toxins [32]. This risk should be carefully evaluated and minimized upon *in vivo* translation.

8.3.5 FUTURE DIRECTIONS: POTENTIAL FOR ULTRASOUND-MEDIATED GI DRUG DELIVERY WITH PCCAs

The data presented herein represent a first step towards the ultimate goal of ultrasound-mediated GI drug delivery with PCCAs, and the finding that lower pressure results in greater delivery efficiency is important for successful *in vivo* translation. In the *in vivo* setting, we envision co-administering a medicated enema with a solution of PCCAs. Subsequently, an endoscopic ultrasound probe would be inserted and used to stimulate PCCAs for GI permeabilization. Without natural

replenishment of the PCCAs (e.g., through blood flow), achieving persistent cavitation by limiting the destruction of generated microbubbles will be of utmost importance.

This is in contrast to an analogous application where ultrasound-stimulated contrast agents are used to enhance drug delivery through vascular barriers. For vascular disruption, microbubbles are administered intravenously, and blood flow provides continuous replenishment of intact microbubbles. Indeed, delivery efficiency has been shown to increase with increasing pressure for this application [35-37], and microbubble reperfusion into the focal zone can be achieved by alternating sonication with rest time [36, 38] or theoretically by using short pulses and long pulse repetition periods [39]. However, using high pressures for vascular permeabilization is associated with an increased risk of undesirable bioeffects [40], pointing to another motivation for using reduced pressures for any drug delivery application. To this end, Pouliopoulos and colleagues have demonstrated the value of redefining the acoustic pulses typically used for vascular permeabilization to provide sustained, controllable, and safe cavitation activity with low pressures and short pulse lengths [24, 41].

The likelihood that ultrasound will induce cavitation is related to the mechanical index (MI = peak rarefactional pressure divided by center frequency) of the transmitted pulse. The United States Food and Drug Administration stipulates that MI cannot exceed 1.9 for clinical diagnostic ultrasound, which is intended to prevent cavitation-mediated biological effects in the absence of exogenous contrast agents. Therefore, when ultrasound-mediated GI permeabilization is performed in the absence of contrast agents, MIs above this threshold (MI~2.2 – 3.3) are often employed to generate the cavitation activity necessary for permeabilization [1, 3, 4]. (Note: these MIs were estimated based on the reported acoustic intensities for *ex vivo* experiments, assuming plane wave transmission, an acoustic impedance of water of 1.48×10^{6} $kg\cdot m^{-2}\cdot s^{-1}$, negligible tissue attenuation, and that the reported intensity represented instantaneous acoustic intensity.) While these protocols have generally been described as safe in preclinical studies [3, 4], cavitation-mediated biological effects could be induced in tissues beyond the GI epithelium. Conversely, we were able to achieve efficient drug delivery at a mechanical index of 0.3 (300 kPa at 1.0 MHz), which is well below the FDA limit of MI = 1.9, indicating that biological effects will likely only be induced in areas with direct contact to the

contrast agents. This claim is supported by the absence of monolayer disruption (as evidenced by stably high TEER values and impermeability to dextran) when cells were stimulated with ultrasound alone in our experiments. This offers an opportunity for improved treatment localization and the potential for enhanced safety compared to ultrasound-mediated GI drug delivery in the absence of contrast agents.

In the GI space, we believe low boiling point PCCAs will provide greater success than standard microbubbles. Unlike microbubble contrast agents, the small size of PCCAs may allow permeation through the GI mucus mesh and permeabilization of the underlying GI epithelium. In future studies, we will test the penetration of PCCAs through mucus and optimize acoustic parameters for GI drug delivery in a model that more accurately captures the *in vivo* setting (e.g., *in situ* intestinal perfusion).

The use of ultrasound for drug delivery offers an opportunity for simultaneous image guidance. This will be particularly important for GI drug delivery applications where site-specific (e.g., immunotherapy delivery to a colon tumor) rather than global GI drug delivery is desired. Ultrasound image guidance could be achieved in one of two ways. First, it may be possible to achieve low-resolution ultrasound imaging and subsequent drug delivery with clinically available endoscopic ultrasound probes (e.g., with 5 MHz center frequency). A similar approach has been published for externally applied ultrasound for drug delivery to pancreatic tumors with a clinically available machine [42, 43]. Perhaps more exciting is the prospect of developing dual frequency endoscopic ultrasound probes that incorporate aligned low frequency elements for optimal drug delivery and high frequency elements for high-resolution ultrasound imaging. Dual frequency transducers are currently under development for contrast-enhanced intravascular and intracavity imaging [44-46], which could be modified for image-guided therapy purposes. A dual frequency approach can also be employed to initiate PCCA phase change at high frequency and detect the unique acoustic signature of PCCA vaporization at low frequency [47]. This would offer a method to image the efficiency and duration of PCCA vaporization events during the treatment.

8.4 CONCLUSIONS

We have demonstrated efficient delivery of a macromolecular drug mimic (70 kDa FITC-dextran) through otherwise impermeable Caco-2 epithelial monolayers using ultrasound-stimulated PCCAs. We found that the lowest pressure conditions (300 kPa) consistently provided the greatest dextran delivery efficiency (vs. 400-600 kPa), which is explained in part by the observation that cavitation is more persistent during ultrasound exposure at lower pressures. While we believe that persistent cavitation activity is important for achieving efficient epithelial disruption, we have not fully explored other acoustic metrics that may also play a role, such as acoustic radiation force, peak cavitation dose, and variable size distributions of acoustically generated microbubbles. Further experimentation should be conducted to evaluate the relative importance of these variables and their contribution to dextran delivery outcome. Insight gleaned from these experiments will allow for rational and thorough optimization of acoustic parameters for *in vivo* drug delivery through the GI epithelial barrier.

REFERENCES

1. Schoellhammer, C.M., et al., *Defining optimal permeant characteristics for ultrasound-mediated gastrointestinal delivery.* J Control Release, 2017. **268**: p. 113-119.

2. Schoellhammer, C.M., R. Langer, and G. Traverso, *Of microneedles and ultrasound: Physical modes of gastrointestinal macromolecule delivery.* Tissue Barriers, 2016. **4**(2).

3. Schoellhammer, C.M., et al., *Ultrasound-Mediated Delivery of RNA to Colonic Mucosa of Live Mice.* Gastroenterology, 2017. **152**(5): p. 1151-1160.

4. Schoellhammer, C.M., et al., *Ultrasound-mediated gastrointestinal drug delivery.* Sci Transl Med, 2015. **7**(310): p. 310ra168.

5. Schoellhammer, C.M. and G. Traverso, *Low-frequency ultrasound for drug delivery in the gastrointestinal tract.* Expert Opin Drug Deliv, 2016. **13**(8): p. 1045-8.

6. Lentacker, I., et al., *Understanding ultrasound induced sonoporation: definitions and underlying mechanisms.* Adv Drug Deliv Rev, 2014. **72**: p. 49-64.

7. Bhatnagar, S., H. Schiffter, and C.C. Coussios, *Exploitation of acoustic cavitation-induced microstreaming to enhance molecular transport.* J Pharm Sci, 2014. **103**(6): p. 1903-12.

8. Martin, K.H. and P.A. Dayton, *Current Status and Prospects for Microbubbles in Ultrasound Theranostics.* Wiley Interdiscip Rev Nanomed Nanobiotechnol, 2013. **5**(4).

9. Burgess, A. and K. Hynynen, *Drug delivery across the blood-brain barrier using focused ultrasound.* Expert Opin Drug Deliv, 2014. **11**(5): p. 711-21.

10. Zhao, Y.Z., et al., *Ultrasound-mediated strategies in opening brain barriers for drug brain delivery.* Expert Opin Drug Deliv, 2013. **10**(7): p. 987-1001.

11. Wu, S.K., et al., *Characterization of Different Microbubbles in Assisting Focused Ultrasound-Induced Blood-Brain Barrier Opening.* Sci Rep, 2017. **7**: p. 46689.

12. Mullick Chowdhury, S., T. Lee, and J.K. Willmann, *Ultrasound-guided drug delivery in cancer.* Ultrasonography, 2017. **36**(3): p. 171-84.

13. Qin, J., T.Y. Wang, and J.K. Willmann, *Sonoporation: Applications for Cancer Therapy.* Adv Exp Med Biol, 2016. **880**: p. 263-91.

14. Sirsi, S. and M. Borden, *Microbubble Compositions, Properties and Biomedical Applications.* Bubble science engineering and technology, 2009. **1**(1-2): p. 3-17.

15. Sheeran, P.S., et al., *Design of ultrasonically-activatable nanoparticles using low boiling point perfluorocarbons.* Biomaterials, 2012. **33**(11): p. 3262-9.

16. Sheeran, P.S., et al., *Formulation and acoustic studies of a new phase-shift agent for diagnostic and therapeutic ultrasound.* Langmuir, 2011. **27**(17): p. 10412-20.

17. Sheeran, P.S., T.O. Matsunaga, and P.A. Dayton, *Phase-transition thresholds and vaporization phenomena for ultrasound phase-change nanoemulsions assessed via high-speed optical microscopy.* Phys Med Biol, 2013. **58**(13): p. 4513-34.

18. Fabiilli, M.L., et al., *The role of inertial cavitation in acoustic droplet vaporization.* IEEE Trans Ultrason Ferroelectr Freq Control, 2009. **56**(5): p. 1006-17.

19. Lo, A.H., et al., *Acoustic droplet vaporization threshold: effects of pulse duration and contrast agent.* IEEE Trans Ultrason Ferroelectr Freq Control, 2007. **54**(5): p. 933-46.

20. van Breemen, R.B. and Y. Li, *Caco-2 cell permeability assays to measure drug absorption.* Expert Opin Drug Metab Toxicol, 2005. **1**(2): p. 175-85.

21. Kudsiova, L. and M.J. Lawrence, *A comparison of the effect of chitosan and chitosan-coated vesicles on monolayer integrity and permeability across Caco-2 and 16HBE14o-cells.* J Pharm Sci, 2008. **97**(9): p. 3998-4010.

22. Srinivasan, B., et al., *TEER measurement techniques for in vitro barrier model systems.* J Lab Autom, 2015. **20**(2): p. 107-26.

23. Fix, S.M., et al., *An evaluation of the sonoporation potential of low-boiling point phase-change ultrasound contrast agents in vitro.* Journal of Therapeutic Ultrasound, 2017. **5**: p. 7.

24. Pouliopoulos, A.N., et al., *Rapid short-pulse sequences enhance the spatiotemporal uniformity of acoustically driven microbubble activity during flow conditions.* J Acoust Soc Am, 2016. **140**(4): p. 2469.

25. Wu, S.Y., et al., *Focused ultrasound-facilitated brain drug delivery using optimized nanodroplets: vaporization efficiency dictates large molecular delivery.* Phys Med Biol, 2018. **63**(3): p. 035002.

26. Reznik, N., et al., *The efficiency and stability of bubble formation by acoustic vaporization of submicron perfluorocarbon droplets.* Ultrasonics, 2013. **53**(7): p. 1368-76.

27. McLaughlan, J., et al., *Increasing the sonoporation efficiency of targeted polydisperse microbubble populations using chirp excitation.* IEEE Trans Ultrason Ferroelectr Freq Control, 2013. **60**(12): p. 2511-20.

28. Wang, M., et al., *Sonoporation-induced cell membrane permeabilization and cytoskeleton disassembly at varied acoustic and microbubble-cell parameters.* Sci Rep, 2018. **8**(1): p. 3885.

29. Dayton, P.A., J.S. Allen, and K.W. Ferrara, *The magnitude of radiation force on ultrasound contrast agents.* J Acoust Soc Am, 2002. **112**(5 Pt 1): p. 2183-92.

30. Zhao, S., et al., *Radiation-force assisted targeting facilitates ultrasonic molecular imaging.* Mol Imaging, 2004. **3**(3): p. 135-48.

31. Sheeran, P.S. and P.A. Dayton, *Phase-Change Contrast Agents for Imaging and Therapy.* Curr Pharm Des, 2012. **18**(15): p. 2152-65.

32. McCartney, F., J.P. Gleeson, and D.J. Brayden, *Safety concerns over the use of intestinal permeation enhancers: A mini-review.* Tissue Barriers, 2016. **4**(2): p. e1176822.

33. Petersen, S.B., et al., *Colonic absorption of salmon calcitonin using tetradecyl maltoside (TDM) as a permeation enhancer.* Eur J Pharm Sci, 2013. **48**(4-5): p. 726-34.

34. Escribano, E., et al., *Single-pass intestinal perfusion to establish the intestinal permeability of model drugs in mouse.* Int J Pharm, 2012. **436**(1-2): p. 472-7.

35. Chen, H. and E.E. Konofagou, *The size of blood-brain barrier opening induced by focused ultrasound is dictated by the acoustic pressure.* J Cereb Blood Flow Metab, 2014. **34**(7): p. 1197-204.

36. Wang, T.Y., et al., *Ultrasound-guided delivery of microRNA loaded nanoparticles into cancer.* J Control Release, 2015. **203**: p. 99-108.

37. Liu, H.L., et al., *Low-pressure pulsed focused ultrasound with microbubbles promotes an anticancer immunological response.* J Transl Med, 2012. **10**: p. 221.

38. Mullick Chowdhury, S., et al., *Ultrasound-guided therapeutic modulation of hepatocellular carcinoma using complementary microRNAs.* J Control Release, 2016. **238**: p. 272-280.

39. Shamout, F.E., et al., *Enhancement of non-invasive trans-membrane drug delivery using ultrasound and microbubbles during physiologically relevant flow.* Ultrasound Med Biol, 2015. **41**(9): p. 2435-48.

40. Baseri, B., et al., *Multi-modality safety assessment of blood-brain barrier opening using focused ultrasound and definity microbubbles: a short-term study.* Ultrasound Med Biol, 2010. **36**(9): p. 1445-59.

41. Pouliopoulos, A.N., S. Bonaccorsi, and J.J. Choi, *Exploiting flow to control the in vitro spatiotemporal distribution of microbubble-seeded acoustic cavitation activity in ultrasound therapy.* Phys Med Biol, 2014. **59**(22): p. 6941-57.

42. Dimcevski, G., et al., *A human clinical trial using ultrasound and microbubbles to enhance gemcitabine treatment of inoperable pancreatic cancer.* J Control Release, 2016. **243**: p. 172-181.

43. Kotopoulis, S., et al., *Treatment of human pancreatic cancer using combined ultrasound, microbubbles, and gemcitabine: a clinical case study.* Med Phys, 2013. **40**(7): p. 072902.

44. Kim, J., et al., *Phantom evaluation of stacked-type dual-frequency 1-3 composite transducers: A feasibility study on intracavitary acoustic angiography.* Ultrasonics, 2015. **63**: p. 7-15.

45. Lindsey, B.D., et al., *Dual-Frequency Piezoelectric Endoscopic Transducer for Imaging Vascular Invasion in Pancreatic Cancer.* IEEE Trans Ultrason Ferroelectr Freq Control, 2017. **64**(7): p. 1078-1086.

46. Wang, Z., et al., *Contrast Enhanced Superharmonic Imaging for Acoustic Angiography Using Reduced Form-factor Lateral Mode Transmitters for Intravascular and Intracavity Applications.* IEEE Trans Ultrason Ferroelectr Freq Control, 2017. **64**(2): p. 311-9.

47. Arena, C.B., et al., *Dual-frequency acoustic droplet vaporization detection for medical imaging.* IEEE Trans Ultrason Ferroelectr Freq Control, 2015. **62**(9): p. 1623-33.

CHAPTER 9

SUMMARY

Throughout this thesis, we applied concepts from molecular pharmaceutics to the study of ultrasound contrast agents, and in the process, we have strengthened our understanding of how contrast agents interact with biological environments and how they can be used for therapeutic purposes.

In chapter 2, we explored dynamic changes in microbubble pharmacokinetics when these agents were administered repeatedly over several weeks. This challenges the long-standing assumption that microbubbles behave as static sources of contrast in ultrasound imaging and highlights the importance of pharmacokinetic characterization in quantitative contrast-enhanced imaging studies as well as therapeutic ultrasound applications where stable microbubble concentrations are important.

We went on to characterize the potential of microbubbles to be adapted as carriers for therapeutic gasses in chapters 3 and 4. Chapter 3 provided a thorough review of the literature surrounding this topic. In chapter 4, we demonstrated that oxygen-filled microbubbles can be used to reoxygenate hypoxic tumors using a rat model of fibrosarcoma and that this reoxygenation improves the efficacy of subsequent radiotherapy. Ongoing work on this project is aimed at translating this technology to improve radiotherapy outcomes for patient dogs with sarcomas.

The final chapters of this thesis demonstrated ways in which a new class of contrast agents – phase-change contrast agents (PCCAs) – can be used to overcome biological barriers to drug delivery. Chapter 5 provided an introduction to ultrasound-mediated drug delivery in general and described the motivation for using PCCAs for this application. We went on to show that ultrasound-stimulated PCCAs can be used to transiently permeabilize cell membranes, increasing the intracellular accumulation of model drugs (chapter 6). In chapter 7, we applied this technique to

deliver bleomycin into otherwise resistant colon cancer cells, providing significant improvements in chemotherapeutic efficacy. Ongoing work related to this project is focused on *in vivo* translation to improve the delivery of cytotoxic drugs and immunotherapy in difficult-to-treat tumor models. Finally, in chapter 8, we demonstrated that ultrasound-stimulated PCCAs can be used to improve drug delivery through epithelial monolayers. These results represent a first step towards improved gastrointestinal delivery of macromolecular drugs *in vivo*, which would substantially improve treatment options for a number of gastrointestinal diseases.

APPENDIX A[1]

SUPPLEMENTARY MATERIAL FOR CHAPTER 2

A.1 ELISA WITH PLATES COATED WITH MICROBUBBLE COMPONENTS

Enzyme-linked immunosorbant assays (ELISAs) were repeated as described in the body of chapter 2 (experiment 1) using plates coated with our microbubble components. Briefly, 96-well, half-area plates were coated via incubation overnight at 4°C with a PBS based solution containing 50:50 molar ratio of DSPC:mPEG-DSPE (final mPEG-DSPE concentration of 100 μg/ml). Secondary antibodies (anti-rat IgM-HRP and anti-rat IgG-HRP) provided with the Life Diagnostics anti-PEG IgM and anti-PEG IgG ELISA kits were used to detect anti-microbubble IgM and IgG, respectively.

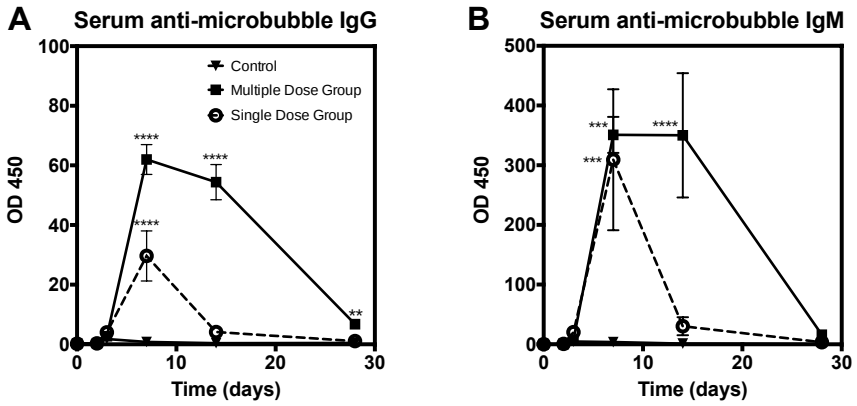

Figure A.1: Anti-microbubble antibody detection. Levels of anti-microbubble IgG and anti-microbubble IgM follow similar trends to anti-PEG IgG and anti-PEG IgM reported in the body of the text. Both isotypes are found to peak between 7-14 d after the initial microbubble dose and decrease considerably by day 28.

[1]This chapter previously appeared as supplementary material for an article in Ultrasound in Medicine and Biology. The original citation is as follows: Fix, S. M., Nyankima, A.G., McSweeney, M.D., Tsuruta, J.K., Lai, S.K., Dayton, P.A. (2018). "Accelerated Clearance of Ultrasound Contrast Agents Containing Polyethylene Glycol is Associated with the Generation of Anti-Polyethylene Glycol Antibodies." Ultrasound in Medicine & Biology **44**(6): 1266-1280.

A.2 ANTI-PEG ANTIBODY DETECTION VIA KIT ELISA AFTER IN VIVO COMPETITION

We immunized rats by dosing them with PEGylated microbubbles on days 0, 1, 2, and 3. On day 7 (when antibody concentrations were likely near their peak) we attempted free PEG competition with a 550 mg/kg dose of PEG20 kDa. This did not result in prolonged microbubble dwell time. However, ELISA analysis of serum collected before and 3hrs after the PEG dose showed no decrease in detected anti-PEG IgM and IgG antibodies (Figure A.2 A and A.2 B). Conversely, running a competitive ELISA assay with 0.9mg/ml PEG20 kDa reduced detected anti-PEG IgG and IgM antibodies (i.e. generated anti-PEG antibodies bind to free PEG20 kDa) (Figure A.2 C and A.2 D). Therefore, we concluded that the free PEG dose provided *in vivo* was simply not enough to occupy a large fraction of the circulating anti-PEG antibodies and recover microbubble dwell time.

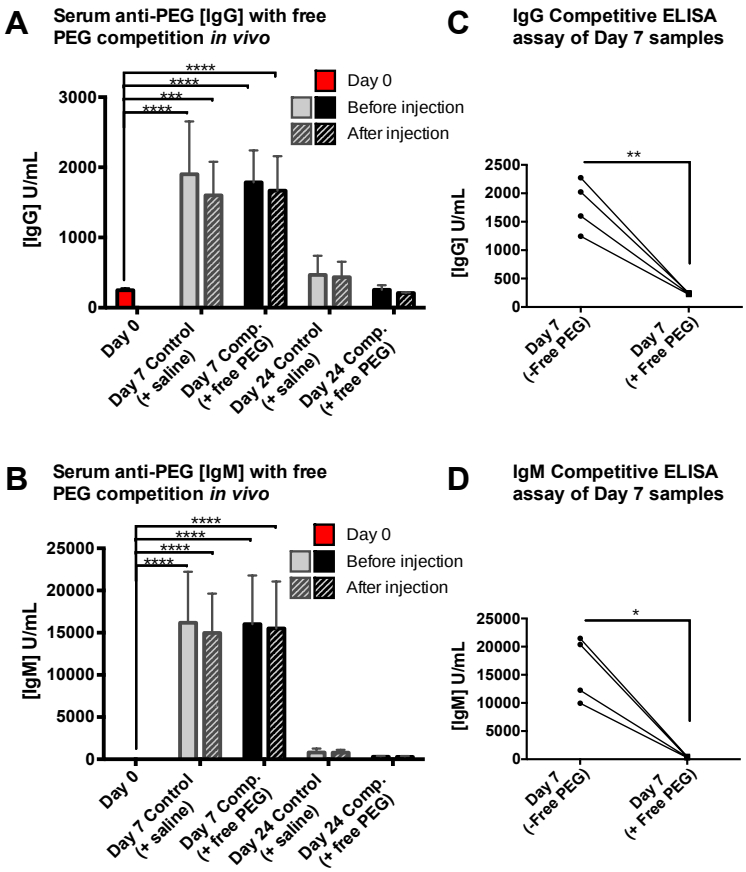

Figure A.2: Anti-PEG antibody detection after *in vivo* competition. Anti-PEG IgG (A) and anti-PEG IgM (B) concentrations detected on day 0, day 7, and day 24. On day 7, significant anti-PEG antibody concentrations are detected, but no change is observed after the administration of saline or free PEG for either IgM or IgG. A competitive ELISA showed that incubating serum with free PEG does result in decreased antibody signal for both IgG (C) and IgM (D).

We repeated the free PEG competition experiment using a higher dose of free PEG (2200 mg/kg) on Day 24 when the antibody concentrations were significantly lower (Figure A.2 A and A.2 B). Here we did see nearly complete recovery of microbubble dwell time. The ELISA data for serum collected before and after PEG administration showed that antibody concentrations at this time point were below the limit of detection (LOD) of the assay. Limit of detection was defined as the IgG or IgM concentration calculated based on the average absorbance at 450 nm of blank samples plus three times the standard deviation of the blank samples. LODs were found to be 663 U/ml and 2014 U/ml for anti-PEG IgG and IgM, respectively. Therefore, we were unable to see a drop in detectable antibodies in response to the PEG competition.

APPENDIX B[1]

SUPPLEMENTARY MATERIAL FOR CHAPTER 6

B.1 ERROR ESTIMATION FOR PCCA SIZE AND CONCENTRATION

Each individual PCCA sample was measured four times to give a representative size distribution and concentration, each with an associated standard deviation (intra-sample SD). This was repeated for three independent vials of PCCAs giving an overall average size and concentration with an associated standard deviation (inter-vial SD). The intra-sample SD for both size and concentration was found to be greater than the corresponding inter-vial SDs (Table B.1). As such, slight variations between vials were negligible given the uncertainty associated with measurement, and vials used throughout the experiments were assumed to be identical and to be characterized by the size distribution and concentration presented. In the body of this text, average size and concentration was reported with their associated intra-sample SDs.

Table B.1: Error estimation for PCCA size and concentration.

Characteristic	Intra-sample SD	Inter-vial SD
Size (nm)	± 13	± 3.5
Concentration (#/mL)	$\pm 1.2\times10^{11}$	$\pm 0.67\times10^{11}$

B.2 DETAILS REGARDING FLOW CYTOMETRY ANALYSIS

All flow cytometry experiments were run using an LSRFortessa cytometer equipped with 488 nm and 561 nm excitation lasers to detect calcein and propidium iodide (PI) fluorescence, respectively (Becton Dickinson, Franklin Lakes, NJ, USA). Detector voltages (gains) were kept consistent throughout the experiments and are presented in Table B.2.

[1]This appendix previously appeared as supplementary material for an article in the Journal of Therapeutic Ultrasound distributed under the terms of the Creative Commons License (http://creativecommons.org/licenses/by/4.0/). The original citation is as follows: Fix, S.M., Novell, A., Yun, Y., Dayton, P.A., Arena, C.B. (2017). "An evaluation of the sonoporation potential of low-boiling point phase-change ultrasound contrast agents in vitro." J Ther Ultrasound **5**: 7. Only minor changes were made in reformatting this material into the chapter presented here.

Table B.2: Detector voltages used for all flow cytometry acquisitions

Detector	Voltage (V)
Front scatter (FSC)	162
Side scatter (SSC)	164
Calcein	130
Propidium Iodide	242

There is very little spectral overlap between calcein and PI; nevertheless, compensation matrices were calculated for each experiment. The following were used as compensation controls: (1) untreated, unstained cells, (2) untreated cells stained only with calcein-AM, and (3) ethanol-killed cells stained only with PI. Ten thousand events were recorded for each. Compensation matrices were calculated using FlowJo Data Analysis Software (Ashland, OR, USA) and were used to compensate all sonoporation data.

To quantify the number of viable sonoporated cells the following gating strategy was employed. First, cells were isolated from debris using front scatter area (FSC-A) vs. side scatter area (SSC-A) characteristics. Second, singlet cells were isolated using FSC-A vs. front scatter height (FSC-H). Third, viability of the isolated cell population was confirmed by calcein fluorescence. Finally, a curly quadrant gate was drawn on the calcein vs. PI dot plot to quantify the percent of sonoporated cells as those displaying both calcein-AM cleavage (viable) and PI uptake (permeabilized) (quadrant two (Q2)). Curly quadrant gates (those with curved arms) were employed in effort to minimize error associated with spread of intensely fluorescent populations (due to proton counting error). See Figure B.1 for gating hierarchy.

A nearly identical gating strategy was employed to detect changes in autofluorescence following treatment, with the only exception being that viable cells were not gated based on calcein fluorescence (as these cells were un-dyed) (Figure B.2 A). Cells that were untreated and undyed (sham control) showed no autofluorescence in the calcein or the PI channels. However, slight spreading along the PI axis was observed in cells treated with ultrasound and PCCAs. The percentage of cells in Q3 was subtracted from final sonoporation efficiencies for each condition.

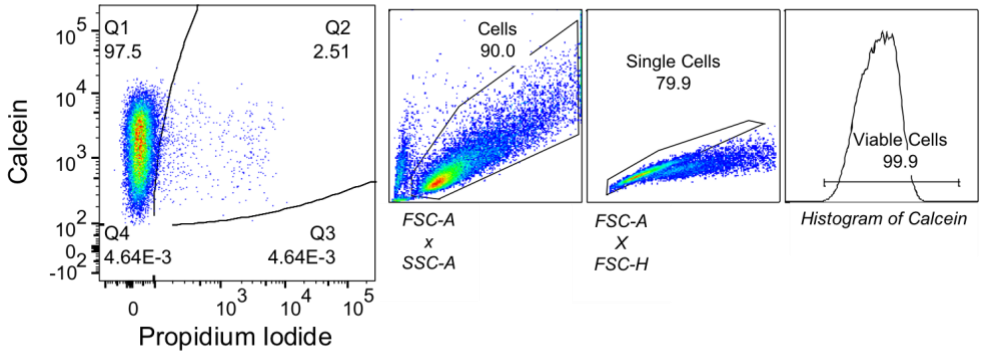

Figure B.1. Gating hierarchy used for sonoporation detection.

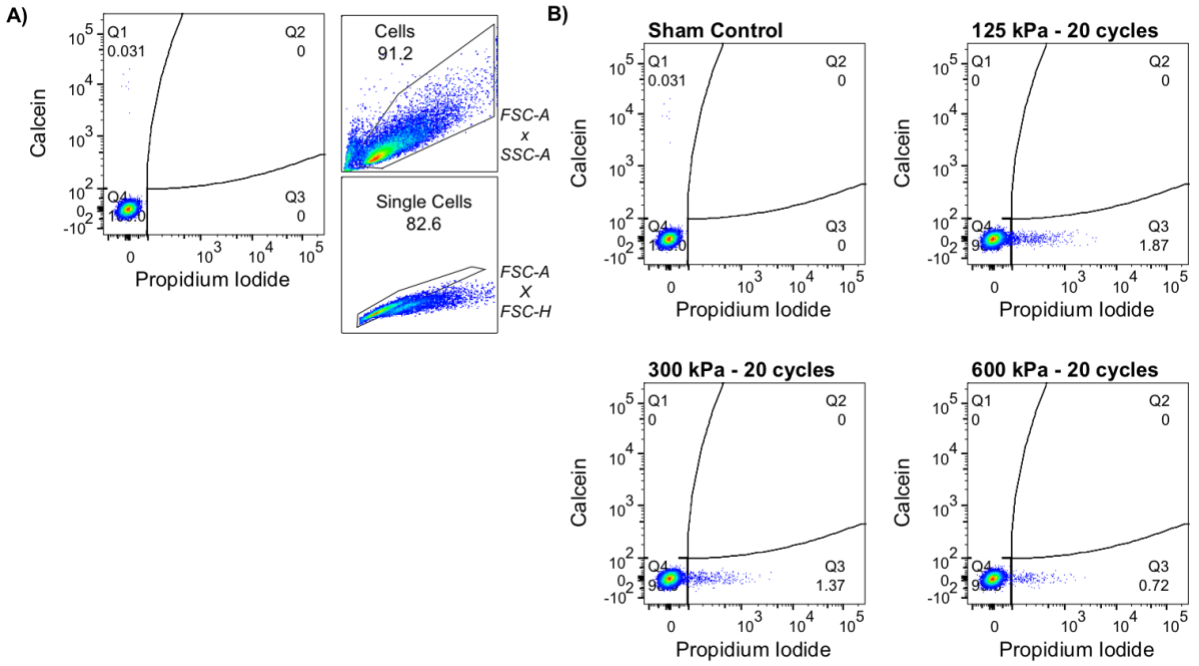

Figure B.2: Detecting autofluorescence in sonoporation-treated cells. A) Gating hierarchy for detecting autofluorescence in treated cells. First, cells were isolated from debris using FSC-A vs. SSC-A. Second, singlet cells were isolated using FSC-A vs. FSC-H. Third, quadrant gates were drawn identical to those used for quantifying sonoporation. B) Representative dot plots demonstrating slight spreading (autofluorescence) of cells treated with ultrasound and PCCAs.